SOFT X-RAY SPECTROMICROSCOPY OF RADIATION

DAMAGED PERFLUOROSULFONIC ACID

SOFT X-RAY SPECTROMICROSCOPY OF RADIATION

DAMAGED PERFLUOROSULFONIC ACID

By

Lis Guimarães de Azeredo Melo, M.Sc.

A Thesis

Submitted to the School of Graduate Studies

In Partial Fulfillment of the Requirements

For the Degree of

Doctor of Philosophy

McMaster University

DOCTOR OF PHILOSOPHY (2018)　　　　　McMaster University

(Chemistry)　　　　　　　　　　　　　　Hamilton, Ontario

TITLE:　　　　　　Soft X-ray Spectromicroscopy of Radiation Damaged Perfluorosulfonic Acid

AUTHOR:　　　　　 Lis Guimarães de Azeredo Melo, M.Sc. (McMaster University)

SUPERVISOR:　　　Professor Adam Percival Hitchcock

NUMBER OF PAGES:　 xxvi, 246

Lay Abstract

Polymer electrolyte membrane fuel cells are an alternative, environmentally friendly power source for transportation and stationary applications. Major challenges for mass production include cost competitiveness, improved durability and performance. A key component to enhance the performance and lower costs involves understanding and improving the spatial distribution of the perfluorosulfonic acid (PFSA) polymer in the catalyst layer. The ionizing nature of electrons and X-rays used in microscopy characterization tools challenges PFSA characterization since this material is radiation sensitive. This thesis developed measurement protocols and methods for quantitative studies of radiation damage to PFSA and other polymers using scanning transmission X-ray microscopy. The chemical changes to PFSA films irradiated with photons, electrons and ultraviolet (UV) photons were studied. The quantitative results identify limits to analytical electron and soft X-ray microscopy characterization of PFSA. The results are used to optimize methods for soft X-ray microscopy characterization of PFSA in fuel cell applications.

Abstract

Climate change has propelled the development of alternative power sources that minimize the emission of greenhouse effect gases. Widespread commercialization of polymer electrolyte membrane fuel cell (PEM-FC) technology for transportation and stationary applications requires cost-competitiveness with improved durability and performance. Advantages compared to battery electric vehicles include fast refueling and long distance range. One way to improve performance and minimize costs of PEM-FC involves the optimization of the nanostructure of the catalyst layer. The rate limiting oxygen reduction reaction occurs at a triple-phase interface in the cathode catalyst layer (CL) between the proton conductor perfluorosulfonic acid, PFSA, the Pt catalyst particles decorating the electron conductor carbon support and gaseous O_2 available through the porous framework of the carbon support. Visualization and quantitation of the distribution of components in the CL requires microscopy techniques. Electron and X-ray microscopy have been used to characterize the distribution of the PFSA relative to the carbon support and porosity in CLs. Understanding and limiting the analytical impact of radiation damage, which occurs due to the ionizing nature of electrons and X-rays, is needed to improve quantitation, particularly of PFSA. This thesis developed scanning transmission X-ray microscopy (STXM) methods for quantitation of damage due to electron and soft X-ray irradiation in PFSA materials. Chemical damage to PFSA when irradiated by photons and electrons is dominated by fluorine loss and CF_2-CF_2 amorphization. The quantitative results are used to set maximum dose limits to help optimize characterization and quantitation of PFSA in fuel cell cathode catalyst layers using: analytical electron microscopy, X-ray microscopy, spectromicroscopy, spectrotomography, spectro-ptychography and spectro-ptycho-tomography.

Acknowledgements

First and foremost, I am extremely grateful to my supervisor Dr. Adam Hitchcock. He trusted me and offered me a position to pursue research at a time when even I doubted myself. He never ceases to amaze me with his patience (which was crucial for the completion of this thesis and for the development of all our manuscripts), his hands-on experience in the lab, operating the microscope and analyzing the data, excellent organizational, and critical thinking skills. The most impressive is his energy – for traveling, working, revising our work and doing science! He has set such a good example for the kind of professional I want to become. I also truly appreciate his support for letting me pursue two three-months research internship at AFCC. Being able to see the importance of my research in an industrial setting catalyzed my motivation! I am also very grateful for the independency and freedom he gave me to pursue side-projects and additional collaborations. I am eternally grateful for him helping me achieve my dream of getting a PhD and for all the amazing opportunities I had during my degree.

Second, I offer my sincerest gratitude to Dr. Viatcheslav Berejnov. I have never met someone more passionate about science! His drive to pursue the scientific truth in all aspects of our projects certainly enriched our work. He has also helped me truly understand what science really is. His patience and innumerous inputs have greatly improved the work in this thesis.

I am very grateful for the advice, suggestions and support from the two members of my committee: Drs. Gillian Goward and Gianluigi Botton. Thank you for your time and attention!!

I wanted to thank the research group and all the amazing people I met during my internship at AFCC. A special thanks to Dr. Darija Susac for helping me settle in Vancouver and for all the discussions and insights in the projects we developed together. I also thank Dr. Juergen Stumper

Finalmente, eu não tenho palavras pra expressar a gratidão que tenho pela minha família e meus amigos queridos do meu Brasil. Sem o apoio, carinho, e atenção de cada um deles, eu não estaria onde estou hoje! Serei eternamente grata a cada um deles: Mamita, Papito, Theo, Catarina, meus avós, meus primos, meus tios e tias, Lucas, Gabriela, Raquel.

A PhD thesis is not only 4 years of your life, it is a journey of self-discovery and self-reflection. I am so very grateful and very fortunate for the opportunity of learning and working with all these amazing people during my PhD!   **Thank you each and every one of you!!!**

Table of Contents

List of Figures

Chapter 5

List of Tables

List of Abbreviations and Symbols

Å	Angstrom
a_c	Critical dose
A_o	Distance between sample and OSA
A_s	Exposed area in TEM
AES	Auger Electron Spectroscopy
AFM	Atomic Force Microscopy
ALS	Advanced Light Source
CCD	Charge Coupled Device
CCEM	Canadian Centre for Electron Microscopy
CCM	Catalyst Coated Membrane
CDI	Coherent Diffractive Imaging
CL	Catalyst Layer
CLS	Canadian Light Source
COP21	21st Conference of Parties
CS	Central Stop
Δr	Outer zone width of the ZP
D	Zone plate width
doF	Depth of focus
DLSR	Diffraction Limited Storage Ring
E	Energy
E_A	Analysis energy
ECA	Electrocatalyst active area
E_D	Damage energy
EDS	Energy Dispersive X-ray Spectroscopy
EELS	Electron Energy Loss Spectroscopy
E_p	Pre-edge energy
EPU	Elliptically Polarized Undulator
EXAFS	Extended X-ray Absorption Fine Structure

EW	Equivalent weight
f	Focal length
FC	Fuel Cell
FEG	Field Emission Gun
FEI	Field Electron and Ion Company
FEL	Free Electron Laser
FIB	Focused Ion Beam
FTIR	Fourier Transform InfraRed
γ	Lorentz Factor
GDL	Gas Diffusion Layer
h	Thickness
HAADF	High angle annular dark field
HPLC	High performance liquid chromatography
I	Transmitted intensity through sample
I_0	Incident Photon Intensity
ICE	Internal Combustion Engine
ID	Insertion Device
IP	Ionization Potential
IPA	Isopropanol
λ	Wavelength
LINAC	Linear Accelerator
$\mu(E)$	Energy dependent mass absorption coefficient
M	Magnification
M	Molecular weight
MEA	Membrane Electrode Assembly
MIBK	4-methyl-2-pentanone
n	Diffraction order
N_A	Avogadro's constant
NEXAFS	Near Edge Fine Structure Spectroscopy

NIST	National Institute for Science and Technology
NMR	Nuclear Magnetic Resonance
OD	Optical density
OD1	Optical density per nm of material
OD_∞	OD after infinite damage
ORR	Oxygen Reduction Reaction
OSA	Order Sorting Aperture
PAAm	Polyacrylamide
PC	Polycarbonate
PE	Polyethylene
PEEM	X-ray Photoemission Electron Microscope
PFA	Polytetrafluoroethylene-co-perfluoropropyl vinyl ether
PGM	Plane Grating Monochromator
PMMA	Poly(methyl methacrylate)
PEM-FC	Polymer Electrolyte Membrane Fuel Cell
PET	Polyethylene terephthalate
PFSA	Perfluorosulfonic Acid
PS	Polystyrene
PTFE	Polytetrafluoroethylene
PU	Polyurethane
PVMK	Poly(vinyl methyl ketone)
RF	Radio Frequency
r	Radius of small fluorescent screen in TEM
RT	Room temperature
ρ	Density
σ_a	Mass absorption coefficient
S,s	Beam diameter / spot size
SASE	Spontaneously generated seed
SDD	Silicon drift detectors

SE	Secondary Electrons
SF-OD1	Composition based on μ and ρ
SGM	Spherical grating monochromator
SPEM	Scanning Photo-emission X-ray Microscopy
SR	Synchrotron radiation
STEM	Scanning Transmission Electron Microscopy
STXM	Scanning Transmission X-ray Microscopy
SSNMR	Solid State Nuclear Magnetic Resonance
SVD	Singular Value Decomposition
SXFM	Scanning X-ray Fluorescence Microscopy
θ_h	Horizontal spread
h	Thickness
TEM	Transmission Electron Microscopy
TTE	Amine epoxy resin
TXM	Transmission X-ray Microscopy
US	United States
UV	Ultraviolet
UV-SR	Ultraviolet Spectral Reflectance
XANES	X-ray Absorption Near-Edge Structure
XAS	X-ray Absorption
XMCD	X-ray Magnetic Circular Dichroism
XPS	X-ray Photoelectron Spectroscopy
XRF	X-ray Fluorescence
ZP	Zone Plate

Declaration of academic achievements

This dissertation was written as a 'sandwich' style consisting of two published peer-reviewed papers as a partial requirement for the degree of Doctor of Philosophy in Chemistry at McMaster University. The research was performed between September 2014 and July 2018 with a six-month internship at Automotive Fuel Cell Corporation (AFCC) in Burnaby, BC. The contributions of the following authors are as follows:

- Lis G.A. Melo was the primary author of all published papers (Chapters 4 and 7), and the material presently under preparation for submission (Chapters 5 and 6).

- Dr. Adam P. Hitchcock was the supervisor in all projects related to this thesis. He gave ideas, guided measurements, assisted with data analysis, and revised all manuscripts.

- Dr. Viatcheslav Berejnov was the day-to-day supervisor during the author's internship at AFCC. He gave the idea for Chapter 4 and provided guidance for the development of Chapters 5 and 7. He revised and is a co-author of three manuscripts (Chapter 4, 5 and 7).

- Dr. Darija Susac was the industrial supervisor at AFCC. She provided ideas and guided the projects developed during the internship. She revised and is co-author of two manuscripts (Chapter 4 and 7).

- Dr. Jasna Jankovic performed the STEM-EDS measurements and helped analyze the data. She is a co-author for the manuscript based on material presented in Chapter 7.

- Dr. Juergen Stumper was the industrial supervisor at AFCC for all STXM related projects. He is co-author of two manuscripts (Chapter 4 and 7).

- Marcia West prepared all ultramicrotomed sections used in this thesis and is co-author of the paper based on material presented in Chapter 5.

The publications included verbatim in this thesis are:

Chapter 4: L.G.A. Melo, A. Hitchcock, D. Susac, J. Stumper, V. Berejnov: Effect of UV radiation damage in air on polymer film thickness, studied by soft X-ray spectromicroscopy. Physical Chemistry Chemical Physics, **2018**, 20, 16625 – 16640. doi: 10.1039/c7cp08621k

Chapter 7: L.G.A. Melo, A. Hitchcock, J. Jankovic, J. Stumper, D. Susac, V. Berejnov: Quantitative Mapping of Ionomer in Catalyst Layers by Electron and X-ray Spectromicroscopy. ECS Transactions, **2017**, 80(8) 275-282. doi: 10.1149/08008.0275ecst

The following manuscripts are being prepared for submission:

(Results are reported in Chapter 5) L.G.A. Melo, V. Berejnov, M. M. West, A. P. Hitchcock: Soft X-ray damage of perfluorosulfonic acid, studied by soft X-ray spectromicroscopy. *To be submitted to J. Phys. Chem. C*

(Results are reported in Chapter 6) L.G.A. Melo, A. Hitchcock: STXM evaluation of electron beam damage to PFSA. *To be submitted to Micron.*

The author also contributed to the following publications but the materials are not directly included in this thesis:

1. LGA Melo; G. A. Botton, A.P. Hitchcock, Quantification of the critical dose for radiation damage to perfluorosulfonic acid membranes using soft X-ray microscopy. Microscopy and Microanalysis, 21, 2443-2444, **2015**. 10.1017/S1431927615012994

2. LGA Melo; A.P. Hitchcock, V. Berejnov, D. Susac, J. Stumper, G. Botton. Evaluating focused ion beam and ultramicrotome sample preparation for analytical microscopies of the cathode layer of a polymer electrolyte membrane fuel cell. Journal of Power Sources (Print), 312, 23-35, **2016** 10.1016/j.jpowsour.2016.02.019

3. Z.H. Yan.; R. Hayes; LGA Melo; G. Goward; A.P. Hitchcock; X-ray absorption and solid state NMR Spectroscopy of fluorinated proton conducting polymers. The Journal of Phys.Chem.C **2018**, 122 (6) 3233-3244 10.1021/acs.jpcc.7b11592

4. Juan Wu; LGA Melo; X. Zhu; M. M West; V. Berejnov; D. Susac; J. Stumper; A.P. Hitchcock. 4D imaging of polymer electrolyte membrane fuel cell catalyst layers by soft X-ray spectro-tomography. J. Power Sources, **2018**, 381, 72-83 10.1016/j.jpowsour.2018.01.074

5. V. Berejnov; B. Rubinstein; LGA Melo; A.P. Hitchcock; First principles X-ray Absorption dose calculation for time dependent mass and optical density. J. Synch. Rad. 25 part 3 May **2018**, 833-847

6. LGA Melo; Hitchcock, A.P.; Talpalaru, C.; Jankovic, J.; Susac, D.; Stumper, J.; Berejnov, V. Effect of focused ion beam cryo-milling on component distribution and chemistry in fuel cell dispersed catalyst electrodes. Journal of Power Sources *Manuscript in preparation*

7. <u>LGA Melo</u>, Isaac Martens, M. West, D. P. Wilkinson, D. Bizzotto and A.P. Hitchcock. Understanding X-ray induced beam damage in perfluorosulfonic acid using correlative microscopy. J. Phys. Chem. C *Manuscript in preparation*

8. <u>LGA Melo</u>, A.P. Hitchcock. Comparison of electron and X-ray microscopies for characterizing perfluorosulfonic acid ionomer for fuel cell applications. Microscopy and Microanalysis, **2018**, in press.

9. <u>LGA Melo</u>, A.P. Hitchcock. Optimizing Soft X-ray Spectromicroscopy for Fuel Cell studies: X-ray Damage of ionomer. Microscopy and Microanalysis, **2018**, 24 (Suppl. 2), 460-461.

Chapter 1

Introduction

This chapter describes polymer electrolyte membrane fuel cells, their importance in the context of global climate change, and the reasons why improved characterization of perfluorosulfonic acid ionomer is important. This is followed by introducing radiation damage, which is the main limitation for ionomer characterization, and why soft X-ray microscopy is a useful tool for studying damage caused by ionizing radiation. The chapter ends by outlining the main goals of this work and the chapters of this thesis.

1.1   Global climate change and challenge to de-carbonize mobile power

At the Conference of Parties (COP21) global meeting in Paris in 2015, a world consensus was reached that human based-activities resulting in CO_2 emission needed to be greatly curtailed to minimize the rise in temperature to a target of 2 ^{o}C (Rhodes, 2016). Burning of fossil fuels is a major source of CO_2 emission. The internal combustion engine (ICE) used in most automobiles and other vehicles accounts for ~ 20 % of fossil fuel use world-wide (The World Bank, 2014). In the United States (US), the CO_2 emissions related to transportation is projected to exceed that of electric power, industrial and residential consumption (Sieminski, 2017). Therefore, the urgent need to reduce CO_2 emissions is motivating the development of several power conversion technologies for mobile applications that will replace the ICE (Ehsani, Gao, & Emadi, 2009). Two alternatives are batteries and fuel cells, both of which are forms of electric vehicles

(Sieminski, 2017; Thomas, 2009). Major challenges for these technologies include cost, refueling facilities and resource implications for mass adoption (Li and Pt are both scarce) (Gröger, Gasteiger, & Suchsland, 2015; Curtin & Gangi, 2017; Hujsak, Roth, Kellogg, Li, & Dravid, 2018). Both batteries and fuel cells rely on clean power sources, which is electricity in the case of batteries and hydrogen, in the case of fuel cells. For each of these technologies, they are as 'clean' as their source of primary power (Campanari, Manzolini, & Garcia de la Iglesia, 2009; Biello, 2016).

1.2   *Polymer Electrolyte Membrane Fuel Cells for automotive use*

Fuel cells were invented nearly 200 years ago (Grove, 1839). Today, different types of fuel cells exist, with their chemistry optimized for different applications. Polymer electrolyte membrane fuel cells (PEM-FC) have much higher theoretical efficiencies and lower pollution compared to the ICE (Barbir, 2005; Carrette, Friedrich, & Stimming, 2001). In 2016, PEM-FC dominated the fuel cell (FC) market and are the preferred technology for transportation applications including light and heavy weight vehicles and forklifts (Curtin & Gangi, 2017). Several major automobile companies have recently launched FC cars (i.e. Honda Clarity, Toyota Mirai, Hyundai Tucson, Mercedes GLC F-Cell) and thus, FC cars are now commercialized albeit on a limited scale (Suzuki, 2016).

The main challenges for widespread commercialization and adoption of FCs are cost competitiveness while maximizing the performance, power density and durability. According to the US Department of Energy, the ultimate goal for FCs is power production at \$30/kW. Recent calculations show that the FC stack makes up for nearly half of the cost (Wilson, Marcinkoski, & Papageorgopoulos, 2016). The stack is made up of a set of interconnected membrane electrode

assemblies (MEAs). The most common configuration consists of connecting the cathode with the anode of another cell, separated by the bi-polar plates (Barbir, 2005).

PEM-FCs react gaseous hydrogen as a fuel and oxygen from air to generate electricity and water (**Figure 1.1**). The electrochemical reactions responsible for converting chemical energy into electricity takes place in the MEA, which consists of a proton conductive membrane coated with two electrodes (**Figure 1.1a**) (Barbir, 2005; Carrette et al., 2001). Each electrode consists of a catalyst layer (CL) and a gas diffusion layer, GDL, as shown in **Figure 1.1b**. The anode and cathode CLs are located between the electrically conductive porous GDLs and the proton conductive membrane.

The reactions taking place in PEM-FC occur simultaneously at both electrodes. At the anode, hydrogen is oxidized, generating electrons and protons. The protons are transported to the cathode through the membrane while the electrons pass through an external electrical circuit, powering the device. The rate limiting step is the oxygen reduction reaction (ORR) which occurs in the cathode CL at the interface of three components: the proton conducting ionomer, the Pt catalyst particles attached to the electron conducting carbon support particles, and gaseous O_2 transported through a porous network, as illustrated in **Figure 1.1b**. State-of-the-art cathode CLs consist of 1-5 nm Pt or Pt-alloy nanoparticles decorating a support, typically high surface area graphitized carbon black particles, that are held together by a perfluorosulfonic acid (PFSA) ionomer proton conductive layer, as shown in **Figure 1.1b**. Reactant gas transport and product water removal occurs through the porous network.
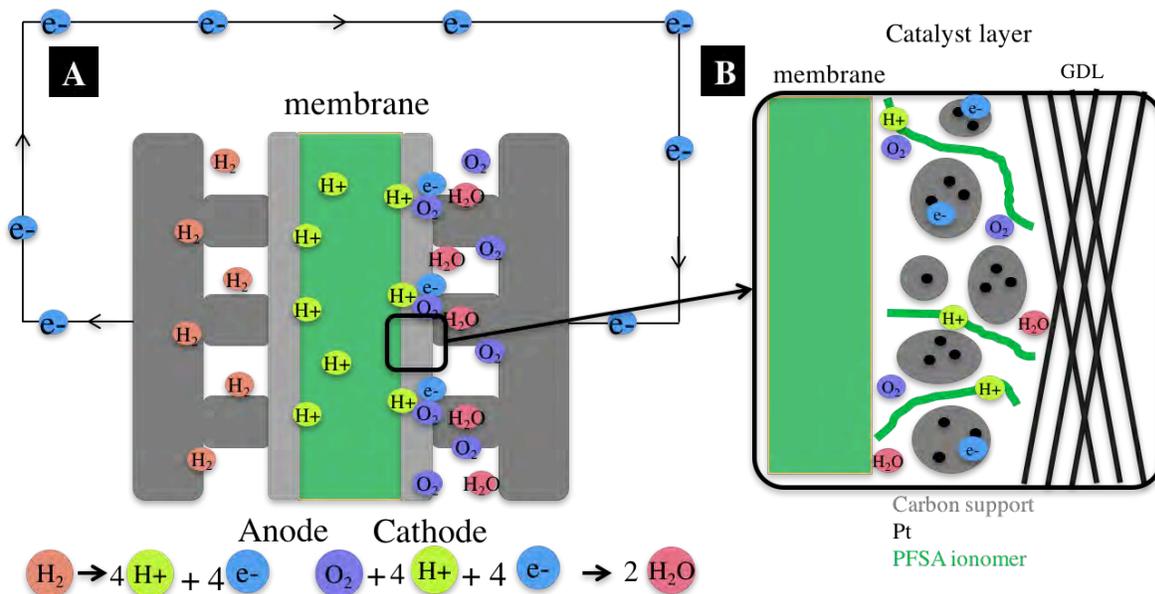
Figure 1.1 Conversion of chemical energy to electrical energy during operation of a PEM-FC. **(A)** The FC stack consists mainly of a membrane electrode assembly (MEA), where the membrane separates the two electrodes. The H_2 and O_2 gases are introduced by channels in the bipolar plates on opposite ends of the MEA, **(B)** the chemical reactions occur in the catalyst layer, situated between the GDL and the membrane.

One way to maximize the performance and minimize cost consists of increasing the efficiency of the expensive Pt catalyst particles, and also the fraction of those particles that are positioned at the triple interface. The latter property depends strongly on the morphology of the cathode CL structure. Optimization of the CL layer thickness, particle size, distribution of catalyst nanoparticles, spatial distribution of the ionomer, nano and micro scale porosity, and the interfacial area between each of the three main components continue to be key targets for improvement of PEM-FC technology (Xing, 2008; Holdcroft, 2013; Karan, 2017). The CL structure is also strongly implicated in water management, mass transport and catalyst dispersion (Huang, Li, & Zhang, 2017).

A major breakthrough increasing the performance while minimizing Pt loading (and hence cost) was made in the 1990's when PFSA ionomer was mixed with catalyst coated support particles in a solution (called 'catalyst ink') which was then deposited on the membrane (Wilson & Gottesfeld, 1992). Since then, there has been significant effort into understanding how the aggregation of each component in the catalyst ink translates into the morphology of the dried CL. The initial ink composition, including the loading of each component, solvent(s) and concentration(s) shapes the CL morphology, which directly affects mass transport resistance and conductivity of the electrons and protons and the device performance (Eikerling, Malek, & Wang, 2008). The morphology also depends on uniformity, viscosity and content of the ink dispersion (Holdcroft, 2013; Eslamibidgoli, Huang, Kadyk, Malek, & Eikerling, 2016; Zamel, 2016). After the solvents are dried, the contact between the ionomer and the catalyst particles is crucial since it provides a pathway for the flow of electrons to the reaction interface and transport of O_2 to the reaction sites. Thus, the ionomer layer thickness and spatial distribution will affect electronic conductivity and access of the reactant gases to the reaction sites (Holdcroft, 2013).

The structure of Nafion^{TM}, a typical PFSA ionomer, is shown in **Figure 1.2a.** It consists of a hydrophobic backbone with CF_2-CF_2 main chains (similar to polytetrafluoroethylene, PTFE) and ether-linked hydrophilic side chains with terminal sulfonic acid groups. The latter are responsible for proton conductivity. The proton conductivity depends on the acidic side chains, the hydration state of the PFSA and its nanomorphology (i.e. formation and connection of the hydrophilic channels) (Holdcroft, 2013). Insights into the actual structure of CL have been provided by coarse-grained molecular dynamic simulations (Malek, Mashio, & Eikerling, 2011). These simulations predict there is a distinct ionomer layer only 2-5 nm thick and ~10 nm in length over

the carbon agglomerates with a water layer (by-product of ORR reaction) in-between, as

presented in **Figure 1.2b**. The orientations and density of the hydrophilic side-chains relative to

the Pt catalyst particles and the carbon support particles depends on the wettability of the Pt/C

interface in the agglomerates (Malek et al., 2011).
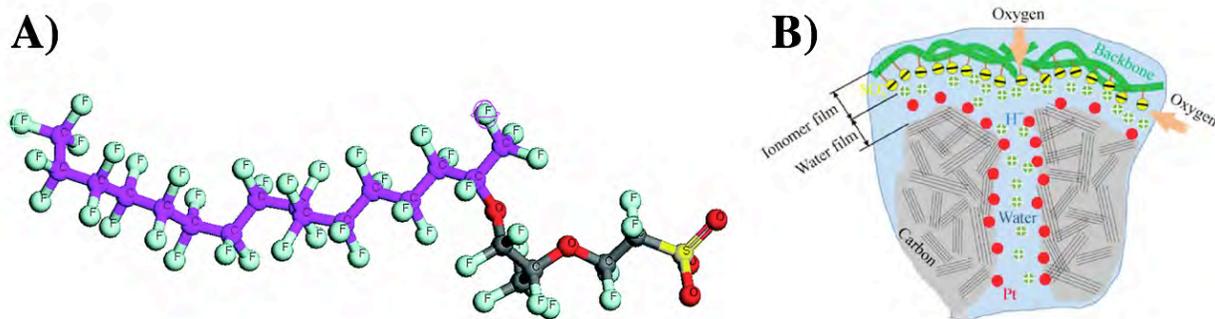
Figure 1.2 (A) Molecular structure of PFSA ionomer **(B)** Aggregate model of the CL showing
that the ionomer does not impregnate pores of the carbon agglomerates. The hydrophilic side-
chains of the ionomer face toward the catalyst particles and are separated by a thin water layer as
described in Malek et.al. 2011. © *Springer Nature, 2017 from Huang et al. 2017.*

The exact nanomorphology of the hydrophobic framework and hydrophilic pockets and

channels, including the size and shape of ionic domains or clusters, their distribution and

connectivity, remains unknown despite extensive research over the past few decades. Much of

what we know about PFSA ionomer comes from studies of the membrane [see reviews by:

Kusoglu & Weber, 2017; Mauritz & Moore, 2004)]. Different casting conditions and solvents

affect the final properties of the membrane material, including its mechanical robustness, water

uptake and proton conductivity (Kusoglu & Weber, 2017). It is possible that the bulk membrane's

properties and morphology do not reflect that of the ionomer thin film that exists in the CL (Paul,

Fraser, & Karan, 2011; Siroma et al., 2009).

Although molecular dynamic simulations give some understanding of the structure of PFSA at the molecular level, the interactions among, and the spatial correlations of support particles, ionomer phases and (Pt-C-PFSA) interfaces, still lack experimental validation (Eikerling et al., 2008). This requires characterization tools that can reliably quantify each component within the CL. However, non-destructive characterization of the CL from the nano to micron-scale in three dimensions is very challenging since ionizing probes, such as electron, ion and X-ray beams rapidly destroy the ionomer as the membrane (Almeida & Kawano, 1998; Schulze, Lorenz, Wagner, & Guelzow, 1999; Yakovlev, Balsara, & Downing, 2013), and in the CL (Cullen et al., 2014; Melo et al., 2016; Wu et al., 2018).

1.3   Methods to characterize PFSA in PEM-FC cathode CL

1.3.1   Electron microscopy

Due to its high spatial resolution (down to the atomic level), electron microscopy seems like a suitable candidate for direct visualization of PFSA nanostructure of pure films (e.g. membranes) as well as in the CL. Recently, novel techniques and methods that combine information from electron microscopy with multiple techniques have been developed towards this goal. These include: multi-scale characterization using focused ion beam (FIB) combined with electron tomography (Thiele et al., 2013); nano-scale X-ray computed tomography combined with electron microscopy, X-ray scattering and porosimetry (Cetinbas et al., 2017); staining of the ionomer to enhance contrast in electron tomography (Uchida et al., 2006; Lopez-Haro et al., 2014); development of new algorithms for electron tomographic reconstruction (Lopez-Haro et al., 2014); and mapping of the CL using spectroscopic techniques in the electron

microscope (Cullen et al., 2014; Scheiba, Benker, Kunz, Roth, & Fuess, 2008). In fact, some of

the results have been consistent with simulations and the proposed morphology models of PFSA.

By staining the ionomer component with Cs^+, electron tomography enabled visualization of a thin

ionomer layer covering the carbon support (Lopez-Haro et al., 2014) as predicted from molecular

dynamic simulations (Eikerling et al., 2008; Malek et al., 2011). However, it is not clear how

staining affects the chemical structure of the ionomer. Also, the proportion of the PFSA that

reacts with the staining compound is not known. Theoretically, there is an exchange between the

heavy metal from the staining solution with the proton in the end groups of the side-chains of the

PFSA. However, there has not been a systematic study showing that this is in fact the only

reaction occurring. Does the entire layer or only a few nm of the ionomer react?

The thin ionomer layer surrounding the Pt/C particles was also supposedly visualized using

transmission electron microscopy (TEM) bright field images as an amorphous component

surrounding crystalline carbon particles (More & Reeves, 2005). Although the structure could be

ionomer, it could also be non-crystalline carbon, either adventitious or damaged PFSA. A

spectroscopic analysis of the thin layer is needed to confirm it is ionomer. To date, there are no

publications where a similar structure in a cathode has been identified as fluorinated material by a

direct analytical electron microscopy method such as electron energy loss spectroscopy (EELS)

or energy dispersive X-ray spectroscopy (EDS). In addition, an alleged visualization by cryo

electron tomography of hydrophilic channels of dry and hydrated 100 nm PFSA films (Allen et

al., 2015) was consistent with the interconnected domain model. However, the cumulative

electron fluence of approximately 220 $e^-/Å^2$ for the tomo series (Allen et al., 2015) is orders of

magnitude higher than that used in another study that claimed fluences higher than 10 $e^-/Å^2$

resulted in noticeable damage in hydrated PFSA films fabricated in a similar manner (Yakovlev et al., 2013).

There have been substantial advances in electron microscopy instrumentation in the last decade. Atomic resolution images are now routinely achieved for metallic or ceramic materials (Kirkland, Chang, & Hutchison, 2007), which has enabled atomic resolution chemical maps using EELS (Kimoto et al., 2007) and EDS (Chu, Liou, Chang, Choa, & Chen, 2010). On the other hand, the resolution of materials sensitive to the electron beams is dose-limited due to radiation damage (Egerton, 2012).

It is surprising that a technique known to result in elemental and morphological changes to PFSA, even in ultra-low fluence conditions (Yakovlev et al., 2013), would enable fine-scale characterization of PFSA without severe radiation damage artifacts. In a recent attempt to chemically map the ionomer in the CL using analytical microscopy, EELS and EDS were used to quantify fluorine loss in PFSA due to electron irradiation (in terms of fluence) (Cullen et al., 2014). For both EDS (cathode sample) and EELS (5-25 nm thick PFSA films), the fluorine content measured using 1 e-/$Å^2$ with the sample at cryo-conditions was taken as the pristine condition. Due to the different thicknesses of the PFSA thin film and cathode sample, this does not result in the same dose (MGy). The accuracy and precision for the fluorine quantitation using only 1 e-/$Å^2$ for both techniques are unclear.

There is general confusion about the expression of radiation dose for electron microscopy. Most users in the electron microscopy community express electron irradiation as **fluence** (e⁻/area), instead of absorbed **dose** (MGy). In the context of radiation damage, dose is the energy absorbed per unit mass of the sample (Carlsson, 1981), in units of Grays, where 1 Gy = 1J/kg.

Sample thickness, sample temperature and conductive substrates all affect the material damage with electron irradiation (Egerton, 2013). Because of the lack of quantitation of electron dose, the maximum absorbed dose using an electron beam for meaningful analysis of PFSA is not well known. The same fluence will not result in the same damage in samples with different analysis temperature, or different substrates. One of the contributions of this thesis work is to place dose determination for electron microscopy on a more scientific basis.

1.3.2   X-ray microscopy

Scanning Transmission X-ray Microscopy (STXM) is a synchrotron based technique that combines microscopy and spectroscopy capabilities (Ade et al., 1992; Ade, 1998; Hitchcock, 2012). A beam of monochromated soft X-rays tuned to the energy of interest is incident upon a sufficiently thin sample. The intensity of the transmitted signal depends on the X-ray absorption properties of the chemical species present. The energy and spatial resolution is typically 0.1 eV and 30 nm (Kilcoyne et al., 2003). Technique and instrumentation developments are driving the spatial resolution down to the sub-10 nm range (Hitchcock & Toney, 2014).

STXM is an alternative to analytical electron microscopy for analytical studies of soft materials. It has been shown to result in less radiation damage per analytical (spectroscopic) information output than TEM-EELS (Rightor et al. 1997; Wang, et al. 2009). In this thesis, I have made the same observation: STXM results in significantly less radiation damage per analytical information (elemental and/or spectroscopic) output compared to TEM-EDS (see Chapter 7) if spatial resolution is not a constraint. STXM spectromicroscopy (imaging at multiple photon energies) has enabled quantitative mapping of ionomer relative to carbon support in real catalyst coated membrane samples, using only a few images, chemically specific to each component

(Susac, Berejnov, Hitchcock, & Stumper, 2011; Susac, Berejnov, Stumper, & Hitchcock, 2012; Berejnov, Susac, Stumper, & Hitchcock, 2013). With the development of more efficient reconstruction techniques, 3D analysis using multiple energy STXM tomography has resulted in 4D images with a resolution of ~80 nm (Wu et al., 2018). This was the first time both the carbon support and the ionomer have been quantitatively and chemically mapped with a microscopic technique without relying on staining to improve contrast, and by limiting the dose to cause minimal damage to the PFSA. Nonetheless, X-ray irradiation can result in significant chemical damage to the PFSA.

1.4   Radiation damage

Most high resolution microscopy techniques (resolution ranging from Å to microns) are based on ionizing radiation, including X-rays, electrons, and ions (Henderson, 1995). All types of ionizing radiation interact with the sample and generate a variety of additional electrons, photons and sometimes particles, which can further ionize the sample. Both the primary event and inelastic scattering of the secondary particles transfer energy to the sample causing bond breakage, which results in the chemical changes called radiation damage.

1.4.1   Types of ionizing radiation

Ionizing radiation is characterized by a transfer of sufficient kinetic energy to excite (energy transfer) and ionize (electron removal) valence or inner shell electrons of atoms of the sample of interest (Attix, 1986). For most elements, this requires at least 4 eV. Some argue that ultraviolet (UV) is not considered ionizing radiation (Attix, 1986) since all molecules are modified by high-energy radiation (i.e. electrons, photons, gamma-rays etc.), whereas UV

radiation results in selective absorption by molecules (Dole, 1972). Absorption of ionizing radiation results in chemical changes such as bond cleavage and dissociation (Anderson, 1984). This may produce molecule fragments and free radicals. The types of ionizing radiation encountered in this thesis were: UV photons, X-rays, electrons, and gallium ion beams.

1.4.1.1   *Ultraviolet (UV) photons*

UV radiation is the part of the electromagnetic spectrum ranging from 3.1 (400 nm) to 5.0 (250 nm) eV. After UV radiation is absorbed by the material, the excited species transfers the absorbed energy to its local surroundings resulting in chemical reactions. Some polymers that are not sensitive to UV may suffer photodegradation due to the presence of impurities (Andrady, 2007). When the damage occurs in air, oxygen can play a significant role in the degradation process (Andrady, 2007). Polymers sensitive to UV usually form CO and CO_2 upon irradiation, typically resulting in chain scission, crosslinking and formation of other components (Andrady, 2007). The mechanisms of UV degradation in polymers are generally a controversial topic in part due to the complex nature of radical reactions, and in part due to the challenges of deducing elementary mechanistic steps from integrated changes.

The absorption of a UV photon can be described with an energy diagram as shown in **Figure 1.3** (Srinivasan, 1986). The ground state (bottom curve) has lower energy compared to the excited state (top curve). Each horizontal line represents a vibrational mode with a specific energy (Srinivasan, 1986). When a UV photon is absorbed the system is excited from the ground to a specific excited state (line 1). In some excited states the upper potential curve is dissociative and bond breaking occurs.
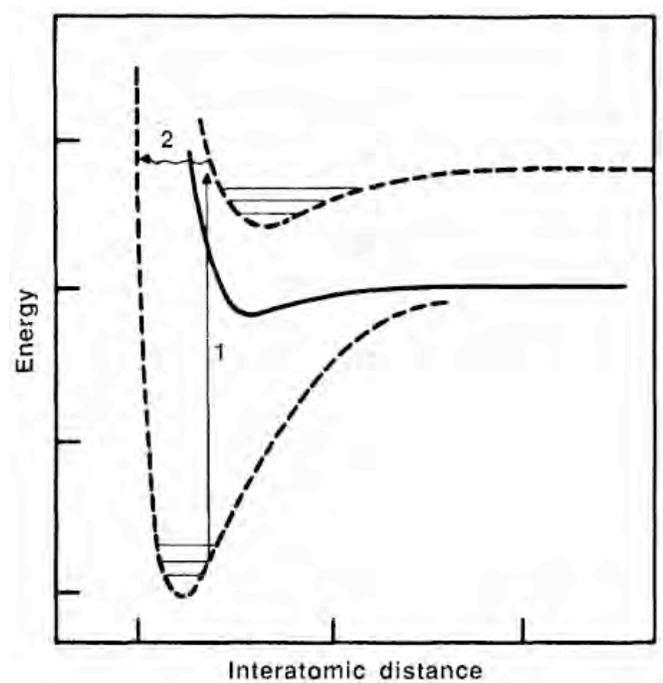
Figure 1.3 Energy diagram depicting the excitation of an electron due to UV absorption. An electron from the ground state (bottom curve) is excited (upper curve) – © *Science AAAS, 1986 from Srinivasan 1986.*

1.4.1.2   X-rays photons

X-ray photons interact with matter through several processes, with probabilities which depend on the X-ray energy and the properties of the material. In order of energy at which they become important, the processes include: Rayleigh scattering (elastic), photoelectric effect, Compton effect, pair production, and photo-nuclear interactions (Attix, 1986). Compton scattering and pair production are the dominant processes for MeV and higher energy photons (Attix, 1986). In the photoelectric effect (called photoabsorption in this thesis) a photon is absorbed, which results in the photon energy being transferred completely into internal energy of the target (Attix, 1986). That energy can cause both excitation and ionization. For inner-shell ionization to occur, the photon energy must be greater than the binding energy of the ionized electron. The photon ceases to exist after photoabsorption (Attix, 1986). Since photoabsorption

is the dominant process that occurs with soft X-rays, the other processes will not be discussed further.

After photoabsorption, an inner-shell electron may be excited to an unoccupied molecular orbital (basis for X-ray Absorption, XAS also called Near Edge Fine Structure Spectroscopy, NEXAFS – see **section 2.3**). The photoelectron ejected from the atom has a characteristic kinetic energy, which is the incident photon energy minus the binding energy of the electron. The detection of the energy of this electron is the basis of X-ray Photoelectron Spectroscopy (XPS). The ionized atom will then stabilize by an outer-shell electron falling into the vacancy left by the ejected electron, accompanied by either ejection of an Auger electron (basis for Auger Electron Spectroscopy, AES) or emission of a characteristic X-ray (basis for X-ray Fluorescence, XRF which is typically called EDS in electron microscopy), as depicted in **Figure 1.4.**

The probability of Auger versus X-ray emission depends on the photon energy. Auger decay is much more probable than X-ray fluorescence for the soft X-ray photon energies used in this thesis. Energetic photoelectrons, either from the primary or secondary ionization processes, cause further excitation and ionization through inelastic scattering (Dole, 1972) which is ultimately the source of most radiation damage effects (Egerton, Konstantinova, & Zhu, 2015).
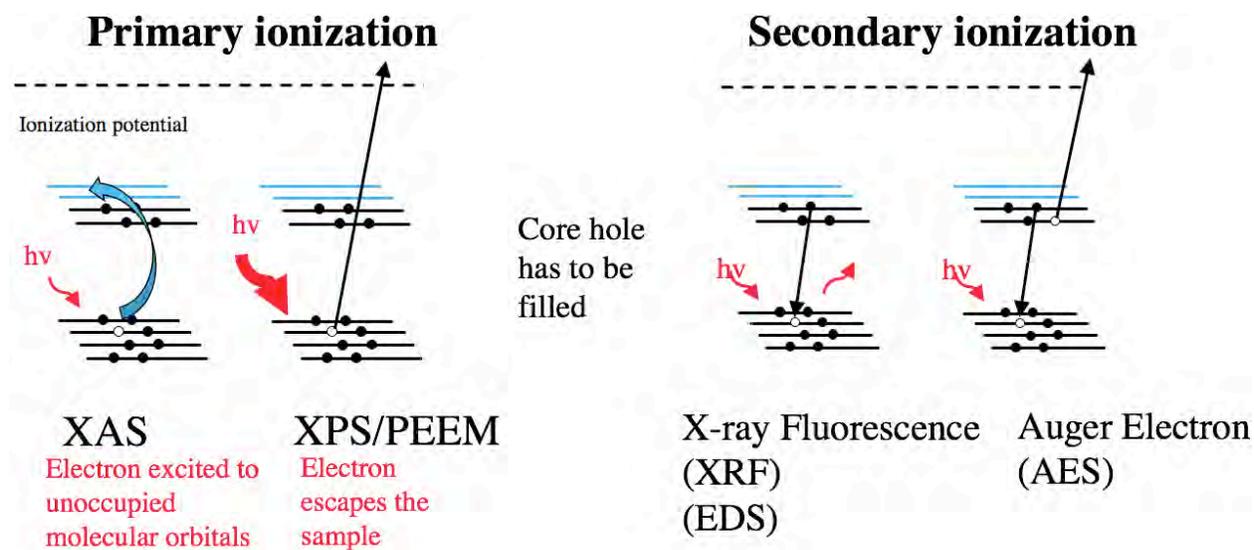
Figure 1.4 Depiction of primary and secondary ionization that occurs after photoabsorption of a soft X-ray photon (*hv*). If the energy of the incident photon is lower than the binding energy of an inner-shell electron, the electron will be ejected to an unoccupied molecular orbital (shown in blue). If the incident energy is higher than the binding energy, then the electron will be ejected. Consequent stabilization results in an outer-shell electron filling the core hole with emission of an Auger electron or characteristic X-ray.

1.4.1.3   High energy electrons

When an incident electron beam interacts with a sample, both elastic and inelastic scattering occur (Egerton, 2011; Williams & Carter, 2009). There are four main processes of inelastic scattering: knock-on damage (dominant in conducting materials; involves the displacement of atoms from a crystalline lattice), heating, charging, and ionization damage or radiolysis. Most of the energy transfer results in thermal vibrations [the temperature rise due to sample heating is usually negligible (Egerton, Li, & Malac, 2004)] and some goes into generation of secondary electrons (SE), which results in charging of the insulating materials (Egerton, 2011). The combination of the SE production and heating can soften and tear polymeric samples

(Egerton, 2012). Damage from ionization (radiolysis) includes collective multiple valence excitations (also known as plasmons) and to a smaller degree, inner-shell ionization of the core-hole. Valence ionization typically requires a few tens of eV (much less than 100 eV), while inner shell ionization requires 50 to a few thousand eV. Plasmons rapidly transfer their energy to surrounding electrons, generating additional SE that can further excite and ionize the sample (Egerton et al., 2015).

For both X-rays and electrons, the initial interaction generates excited and ionized electronic states that generate energetic Auger electrons which can cause further excitation and ionization. Although the primary processes are different, the secondary processes are quite similar and are dominated by the effects of SE, radicals and ions that diffuse into the sample and cause further generation of similar species. SE travel only a few nm through the sample due to inelastic interactions with the sample. Radicals are probably responsible for longer range damage processes since their reaction with other entities can generate new radical species, resulting in a chain reaction that generates damage far away from the interaction site (Wang, 2008).

1.4.1.4 Focused ion beams

Damage caused by focused ion beams (FIB) has been studied extensively for Si and other materials since FIB became an attractive method for site-specific sample preparation. Gallium contamination, generation of defects, amorphization of the surface of the FIB lamella, and unintentional sputtering of the sample are common artifacts when using FIB (Lehrer et al., 2000). Damage to soft materials is less studied perhaps since there are easier and cheaper ways to prepare thin films. Nonetheless, Raman Spectroscopy has been used to quantify the decrease of C=C bonds of an unsaturated polymer irradiated with a Ga ion beam at room and cryo

temperatures (Sezen et al., 2009). It was shown that cryo-temperature does not influence the damage compared to room temperature ion irradiation (Sezen et al., 2009, 2011). EELS analysis of FIB damaged conjugated polymers (polyfluorene and poly-3-hexylthiophene) showed amorphization at the C 1s edge and shifting of the $\pi^*_{C=C}$ and σ^*_{C-C} related peaks to higher energies (Sezen et al., 2011). Changing the patterning strategy mitigates FIB damage on soft materials while keeping the same processing time as conventional raster scanning (Orthacker et al., 2014).

1.4.2   *Soft X-ray spectromicroscopy to study damage*

STXM has been used to study chemical changes due to radiation damage in a variety of soft materials. This includes studies where the damage was generated by UV (Klein, Fischer, & Lenhart, 2008), electrons (Rightor et al. 1997; Wang, Morin, et al., 2009; Le Guillou, Remusat, Bernard, Brearley, & Leroux, 2013), ion beams (Bernard et al. 2009; Bassim et al. 2012; Melo et al. 2016), and X-rays (Zhang, Jacobsen, Lindaas, & Williams, 1995; Coffey, Urquhart, & Ade, 2002; Beetz & Jacobsen, 2003; Zubavichus et al., 2004; Braun, Kubatova, Wirick, & Mun, 2009; Schäfer et al., 2009; Wang, Botton, et al., 2009; Wang, Morin, et al., 2009; Leontowich et al., 2012; Leontowich, 2013; Tzvetkov, Späth, & Fink, 2014; Gianoncelli et al., 2015; Leontowich, Hitchcock, & Egerton, 2016). See **Table 1.1** for a summary of STXM-based radiation damage studies.

Table 1.1 STXM characterization of radiation damaged materials

Material	Ionizing radiation	Qualitative characterization*	Quantitative characterization	Reference
Polyethylene terephthalate (PET)	80 kV electrons	O 1s NEXAFS spectra	Critical dose of Ph-COOR & COOR damage (400 MGy) & mass loss	Wang, Botton, et al., 2009
Kerogen	200 kV electrons		Standard deviation of deconvoluted peak area 284-287 eV	Le Guillou et al. 2013
Araldite	30 kV Ga ion beam		None	Bernard et al. 2009
Lignite coal	2-30 kV Ga ion beam		None	Bassim et al. 2012
Polyacrylamide (PAAm)	2-30 kV Ga ion beam		None	Bassim et al. 2012
Cathode catalyst membrane sample	10-30 kV Ga ion beam	F 1s NEXAFS spectra	None	Melo et al. 2016
Cysteine (amino acid)	C 1s, O 1s, N 1s and S 2p photons	O 1s, N 1s and S 2p NEXAFS spectra	None	Zubavichus et al. 2004
Fibrinogen	300 eV photons	N 1s and O 1s NEXAFS & PEEM spectra	Critical dose of C=O loss (300-350 MGy)	Wang, Morin, et al., 2009
Kidney cells	1000 eV photons		None	Gianoncelli et al. 2015
Polysaccharides	C1s photons		None	Cody et al. 2009
Argillite	C1s photons	K 1s, Ca 1s, O 1s, Fe 1s NEXAFS spectra	Critical dose of C=O (2.5 GGy)	Schäfer et al. 2009
Polyethylene terephthalate (PET)	300, 302, 315 eV photons	O 1s NEXAFS spectra	Critical dose of Ph-COOR and COOR (400 MGy; 2.2×10^4 eV/nm^3) damage and mass loss (5.9×10^4 eV/nm^3)	Rightor et al. 1997; Wang, Botton, et al., 2009; Coffey et al. 2002
Poly(methyl methacrylate) (PMMA)	315, 317 eV photons	C 1s PEEM spectra	Critical dose of C=O damage (70-150 MGy; 5.2×10^2 eV/nm^3) and C=C growth (75 MGy), mass loss (3.5×10^2 eV/nm^3), cryo temperature	Zhang et al. 1995; Coffey et al. 2002; Beetz & Jacobsen 2003; Wang, Morin, et al., 2009
Poly(bisphenol-A-carbonate) (PC)	315 eV photons		Critical dose of C=O loss (5.8×10^2 eV/nm^3),mass loss (none)	Coffey et al., 2002
Nylon6	315 eV photons		Critical dose of C=O decay (2.3×10^3 eV/nm^3), mass loss (8×10^2 eV/nm^3)	Coffey et al., 2002
Poly(vinyl methyl ketone) (PVMK)	315 eV photons		Critical dose of C=O decay (1.6×10^3 eV/nm^3), mass loss (1.4×10^3 eV/nm^3)	Coffey et al., 2002
Polyurethane (PU)	315 eV photons		Critical dose of C=O (7.4×10^2 eV/nm^3), mass loss (none)	Coffey et al., 2002

Table 1.1 Continued

Material	Ionizing radiation	Qualitative characterization	Quantitative characterization	Reference
Poly(ethylene succinate) (PES)	315 eV photons		Critical dose of C=O decay (5.3×10^2 eV/nm^3), mass loss	Coffey et al., 2002
Polystyrene (PS)	315 & 285.1 eV photons	PEEM spectra	Critical dose of C=C decay (1200 MGy), mass loss (none)	Coffey et al., 2002; Wang, Morin, et al., 2009
Polyethylene (PE)	315 eV photons		C=C, mass loss (none in He versus air)	Coffey et al., 2002
Poly(propylene oxide) (PPO)	315 eV photons		Critical dose of C=O decay, mass loss (4.3×10^2 eV/nm^3)	Coffey et al., 2002
Soot	Energy scan 270-340 eV		None	Braun et al., 2009

* All references studied the qualitative characterization using C1s NEXAFS spectra

For polyethylene terephthalate (PET), soft X-ray and electron irradiation result in similar chemical changes and rate of damage measured by STXM-NEXAFS (Wang, Botton, et al., 2009). The peaks related to the C 1s(C=C) $\rightarrow \pi*_{C=C}$ transitions of the phenyl ring decay and merge due to bond scission between the ester and phenyl ring. Peaks related to the C=O bonds decreased (O=C-OR) and increased (C=O) as the ester C-O dissociated and generated benzaldehyde (Wang, Botton, et al., 2009). All the transitions, including carbon mass loss, decayed at similar rates (Wang, Botton, et al., 2009).

By using a model system and photon irradiation, scientists have simulated conditions to study the evolution of organic matter in outer space (Le Guillou et al., 2013). STXM-NEXAFS was used to understand radiation damage mechanisms due to electron irradiation in kerogen. Electron irradiation resulted in amorphization and chemical damage of kerogen (Le Guillou et al., 2013). STXM enabled verification that the cryo-holder significantly slowed the rate of chemical changes when the same electron fluence as room temperature irradiation was used (Le Guillou et al., 2013).

When using Ga-FIB, some soft materials such as araldite (Bernard et al., 2009) and lignite coal (Bassim et al., 2012) do not exhibit significant chemical damage compared to their microtomed counterparts. On the other hand, polymers such as polyacrylamide (PAAm) (Bassim et al., 2012) and PFSA ionomer in the cathode (Melo et al., 2016) experience extensive chemical changes due to FIB milling compared to microtomed sample preparation. For araldite sample preparation, STXM C 1s NEXAFS showed some small changes to peak intensities related to C=C bonds in aromatic/olefinic groups, resulting in some amorphization (Bernard et al., 2009). There were no significant changes to the phenolic group (Ar-OH) or alcoholic groups (C-OH). Aromatic polymers are generally more robust towards ionizing radiation (Glaeser & Taylor, 1978). Compared to microtomed sections, Ga ion beam milling results in slight changes to the relative peak heights in the C 1s spectrum of lignite coal (Bassim et al., 2012). On the other hand, the C 1s spectrum of PAAm is completely modified, with formation of peaks at energies typical of C=C and C=O. These changes were attributed to the electron irradiation rather than the ion beam during FIB milling (Bassim et al., 2012).

Upon soft X-ray radiation, poly(methyl methacrylate) (PMMA) suffers main and side-chain scission with a decay of C 1s $\rightarrow \pi*_{C=O}$ transitions and growth of C 1s $\rightarrow \pi*_{C=C}$ transitions (Zhang et al., 1995). In general, polymers that have carbonyl groups show decay of the C 1s (C=O) $\rightarrow \pi*_{C=O}$ peak (Coffey et al., 2002). Polyethylene (PE), poly(vinyl methyl ketone) (PVMK) and Nylon-6 show growth of C 1s (C=C) $\rightarrow \pi*_{C=C}$ peaks (Coffey et al., 2002). Polymers with phenyl groups, including polystyrene (PS), polycarbonate (PC) and polyurethane (PU), show a growth of peaks related to C 1s (C-R) $\rightarrow \pi*_{C=C}$ transitions due to phenyl modification and did not present any mass loss upon irradiation (Coffey et al., 2002). For PS, photon

irradiation results in damage to the phenyl ring and dehydrogenation of the backbone (Wang, Morin, et al., 2009). Polymers that do not lose significant mass likely cross-link, as was suggested for PC, PE, PU and PS (Coffey et al., 2002).

STXM has been used to study damage to soot (carbonaceous material) (Braun et al., 2009) and amino acids (Zubavichus et al., 2004). The amino acid cysteine suffers decarboxylation and formation of C=C when X-ray damaged (Zubavichus et al., 2004). Decay of the carbonyl group was also noted for protein (fibrinogen) under X-ray irradiation, in addition to formation of C=N and probable elimination of water (Wang, Morin, et al., 2009). STXM-NEXAFS has identified different minerals and acids in an argillite rock sample (Schäfer et al., 2009). Quantification of the photon irradiation damage to the mineral components showed carbon and oxygen mass loss due to bond breaking with an increase of C=C bonds, which the authors linked to polymerization crosslinking (Schäfer et al., 2009).

1.4.3   Kinetics of radiation damage

In the case of soft X-ray damage generated using STXM, the quantitative kinetics and damage mechanisms of several polymers (Zhang et al., 1995; Rightor et al., 1997; Coffey et al., 2002; Wang, 2008; Wang, Botton, et al., 2009; Zhang et al., 2009; Leontowich, 2013), mineralogical (Schäfer et al., 2009) and biological materials (Cody et al., 2009; Gianoncelli et al., 2015) have been studied. In addition to spectroscopic changes (see previous section), these studies report quantitation of the damage as a function of dose. This enables one to estimate measurement limits (in terms of dose) before the material suffers significant chemical damage. This ensures that analytical measurements are from an undamaged material, and not an artifact due to radiation damage. The decay (sometimes, growth) of the intensity of spectral peaks with

dose has typically been analyzed assuming first order kinetics, and thus fit to an exponential decay function:

$$y = y_o + a \cdot exp^{-bx}$$ Equation 1.1

where y is a signal related to damage, such as a peak intensity, relative or absolute amount of undamaged or damaged material, x is the dose (in MGy), and y_o, a and b are constants derived from the fit. y_o is the signal remaining after infinite irradiation dose (also symbolized as OD_∞ elsewhere in this thesis), and b is the inverse of the critical dose, a_c^{-1} , where a_c is the critical dose at which a damage signal has changed by 63% (1/e) of the difference between the 0 and ∞ damage signal. Plotting $ln(y-y_o)$ versus dose (x) for such processes yields a linear function, where the slope is equal to 1/b. This has been shown to be the case for X-ray damage to a variety of polymeric materials, including PMMA (Wang, 2008; Wang, Morin, et al., 2009) – see **Figure 1.5**.

The critical dose (a_c) is a useful parameter for comparing the rate of damage to different materials and different processes (e.g. damage to different functional groups) within the same material. Such comparisons have helped understand damage mechanisms for PMMA, PS and fibrinogen (Wang, Morin, et al., 2009). Aromatic polymers (PET, PS, PC, PU) are very resistant to soft X-ray damage compared to PMMA, Nylon-6 and others (Coffey et al., 2002). The a_c values for those polymers for which they have been reported are listed in **Table 1.1**.
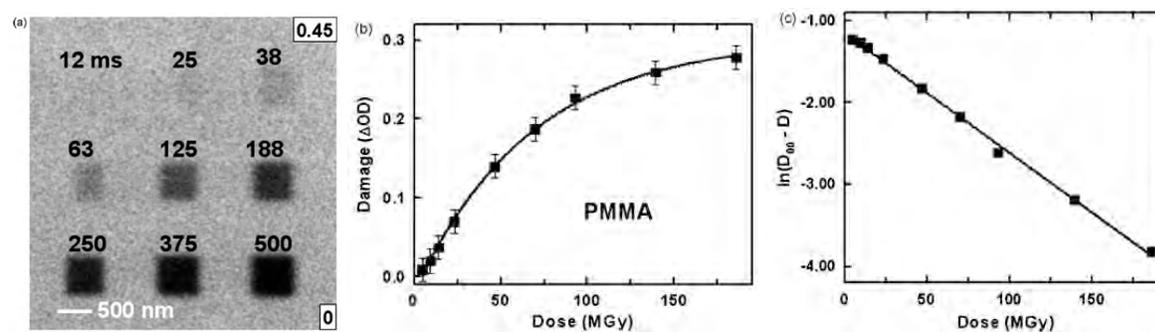
Figure 1.5 Dose damage relationship for PMMA where **(a)** shows a 288.4 eV STXM image of a 9-pad template burned into a thin film of PMMA, with the exposure time at each pad indicated, **(b)** quantifies the damage in each pad as a function of dose and **(c)** plots the linearized data from (b) (*© American Chemical Society, 2009 from Wang, Morin et al., 2009*).

1.5   Thesis research – approaches and hypotheses

There are several major challenges impeding the widespread commercialization of PEM-FC powered automobiles. These include (1) lack of refueling stations (Curtin & Gangi, 2017), (2) significant CO_2 production by the most economical method of generating clean H_2 (natural gas) (Hino, Matsui, & Yan, 2011), (3) finite amount of Pt in the world (Gordon, Bertram, & Graedel, 2006) and (4) limited durability, performance and high costs of the existing PEM-FC technology. Although the first three issues are not dealt with in this thesis, optimization of PEM-FC performance, durability, and reducing costs are all impacted by my research. The ionomer does not play a direct role in the reaction kinetics, but its layer thickness and 3D spatial distribution in the CL affects the access of protons and O_2 to the very expensive Pt or Pt alloy nanoparticles that catalyze the reaction, and the ease with which the product water can be removed. One of the ultimate goals in FC technology is to visualize and quantify the particle size distribution, the morphology of all components, the porosity and its connectivity, and the interfacial area between

each component in the CL in 3D. Ideally this information should be measured before, during and after performance testing. Correlating the nanostructural evolution of each component with properties of the FCs such as the performance and electrocatalyst active area (ECA) will allow the design of a structurally optimized CL with maximum efficiency. Understanding how the nanostructure and morphology of each component changes during operating conditions of FC will help design new materials with improved durability. Therefore, techniques that can measure the required information with minimal modification to the sample are needed.

STXM has been used routinely to quantitatively map ionomer in CL in 2D and 3D and to evaluate chemical changes caused by FC operation (Berejnov et al., 2012; Lee et al., 2013; George, Wang, Banerjee, & Bazylak, 2016). It is also a useful tool to quantify radiation damage (see **section 1.4.2**). This is because: 1) it is easier to control the damage compared to electron microscopy; 2) it is a bulk analysis technique and not as sensitive to surface contamination such as XPS, and 3) quantitation of the damage is done with just a few images (Zhang et al., 1995; Coffey et al., 2002; Wang, Morin, et al., 2009). It is also extremely useful as it records X-ray absorption spectra (XAS) of the damaged material and thus allows studies of the chemical changes caused by radiation damage.

The current understanding of the structure of ionomer in the CL is limited due to the difficulty in characterizing and quantifying ionomer because of radiation damage. In order to improve this situation, it is important to understand radiation damage both qualitatively and quantitatively. My thesis research has developed new and improved soft X-ray microscopy methods for quantifying damage due to ionizing irradiation (by ions, electrons, UV photons, and X-rays). Since the context is PEM-FC optimization, my research has emphasized studies of

radiation damage to the proton conducting ionomer, perfluorosulfonic acid (PFSA), but the methodology developed is general, and several other polymers were studied in the course of the research.

Quantitation of radiation damage due to a characterization method allows one to design measurement protocols that 1) minimize the damage and 2) accurately quantify the material of interest. In order to study radiation damage to polymers, thin uniform films of PFSA and other polymers were fabricated and exposed beams of ions, UV light, electrons and X-rays. The localized nature of probes is an important aspect – without that the controlled damage would be harder to study. STXM coupled with XAS was used to quantify the chemical and elemental changes to the PFSA. The quantitative results identified severe challenges to ion beam sample preparation and (analytical) electron microscopy for PFSA (quantitation and) characterization. The results were used to optimize X-ray microscopy characterization of PFSA for fuel cell applications and set an upper limit for dose where the damage becomes significant.

1.6   Outline of thesis chapters and summary of key results

This thesis developed and optimized methods for quantifying radiation induced changes of any polymer, with the main interest in PFSA. These methods were also used to evaluate the suitability of low-dose electron microscopy characterization of PFSA films and PFSA in cathodes.

Chapter 2 describes the principles of synchrotron radiation, STXM and NEXAFS, including the instrumentation, beamline set-up etc. Chapter 2 concludes with a brief description of electron microscopy, EDS and general aspects of the sample preparation techniques used.

Chapter 3 describes the thin film sample preparation, and methods developed for STXM quantitation used throughout this thesis. Methods for electron dose calculation are also reported.

Chapter 4 presents a comparison of ultraviolet spectral reflectance (UV-SR) and STXM for quantifying the thickness of thin polymer films. The accuracy of quantitation by STXM was evaluated by comparing STXM results to thickness determination of the same films with UV-SR. This work showed that STXM can determine film thickness with an accuracy of 10% when compared to UV-SR. STXM was used to verify chemical changes to the polymer films caused by UV light and guide conditions of UV/air exposure for minimal damage. While polystyrene, PS, and PMMA are significantly sensitive to UV/air exposure and suffer extensive damage including thickness decay, PFSA is robust under similar exposure conditions (L.G.A. Melo, A. Hitchcock, D. Susac, J. Stumper, V. Berejnov, Physical Chemistry Chemical Physics, 2018, 20(24) 16625-16640 doi: 10.1039/C7CP08621K)

Chapter 5 reports spectroscopic studies of chemical changes to PFSA caused by soft X-ray irradiation. The critical doses for several damage processes were measured. The results gave insight into damage mechanisms. It was observed that fluorine mass loss follows the same rate as amorphization of the CF_2-CF_2 chains. S 2p, C 1s, O 1s and F 1s spectra were measured as a function of dose and used to quantify i) the decay and formation of spectral transitions associated with specific bonds (e.g. C-F and C=O); and ii) changes to the elemental composition of PFSA irradiated with soft X-rays. Other fluoropolymers (PTFE and Teflon®AF) were also studied to gain a better understanding of how the main and side chains degrade with photon irradiation. The results were used to design measurement protocols minimizing damage during X-ray microscopy

characterization of PFSA for fuel cell applications (in preparation for submission to J. Phys. Chem.C).

Chapter 6 addresses the STXM characterization of electron irradiated PFSA films. Thin PFSA films were exposed to ultra-low dose in the transmission electron microscopy (TEM) using similar conditions as used in the biological sciences, including cryo temperatures. The dose was correlated with the cross-over from positive to negative lithography of PMMA. STXM showed that even ultra-low dose conditions (corresponding to 20 MGy) resulted in chemical changes to the PFSA. The dose-limited spatial resolution was calculated (in preparation for submission to J. Phys. Chem.C).

Chapter 7 compares quantitative mapping of PFSA in the CL by STXM and EDS in a scanning TEM (STEM). The chemical changes and fluorine loss of the PFSA in the cathode was characterized under different exposures. It was found that STEM-EDS underestimates fluorine loss compared to STXM NEXAFS. Although both techniques result in radiation damage, medium quality STXM images quantify the ionomer with negligible damage whereas there are unacceptable levels of damage when recording STEM-EDS maps to the level of visualizing detail at a similar spatial scale (L.G.A. Melo, A. Hitchcock, J. Jankovic, J. Stumper, D. Susac, V. Berejnov, ECS Transactions, 2017, v80(8) 275-282, doi: 10.1149/08008.0275ecst).

Chapter 8 summarizes all contributions of this thesis and concludes with suggestions of future work.

Chapter 2

Methods

This chapter describes the principles of synchrotron radiation with emphasis on third generation storage rings. It describes the beamline instrumentation and principles of scanning transmission X-ray microscopy. Basic principles and instrumentation of transmission electron microscopy is presented for both parallel and convergent beam modes. Energy Dispersive X-ray Spectroscopy is explained. Sample preparation methods (ultramicrotomy, spin-coating and focused ion beam milling) are described. Explicit details of how these methods were applied in this work, including some novel extensions, are given in Chapter 3.

2.1   *Synchrotron radiation*

Synchrotron radiation (SR) is naturally produced by cosmic sources and can be man-made in particle accelerators. In synchrotron facilities, electromagnetic radiation is produced by accelerating high energy charge particles (typically electrons, sometimes positrons) at relativistic speeds (Balerna & Mobilio, 2015; Willmott, 2011). The first generation synchrotron facilities were parasitic on accelerators designed and built for experiments in nuclear or high-energy physics in the 1960s. Aside from the early dedicated SURF ring at the National Institute for Science and Technology (NIST, Maryland, US – still in operation), the Tantalus ring in Stoughton, WI, US and the Accelerator Circulaire d'Orsy (ACO, France) built in the 1960s, the first dedicated synchrotron facilities with long-term operation as SR sources were the second-

generation storage rings, such as NSLS_I, super-ACO, Bessy-I, MaxI, II, etc, built in the 1970-80s. Third generation facilities, build in the 1990s and 2000s, reduced the electron beam source size and beam divergence relative to 2nd generation rings. The electron beam emittance is defined as the product of the source area and beam divergence (Willmott, 2011). The third generation facilities incorporated insertion devices (ID), which are arrays of magnets which dramatically improve the X-ray brilliance. Brilliance depends on the spatial and angular distribution of the radiation as well as the energy width and time of emission (SR is pulsed). Brilliance has units of flux/area/solid angle/unit spectral bandwidth (Willmott, 2011).

A modern third generation synchrotron facility consists of five main components depicted in **Figure 2.1**: electron source, booster ring, storage ring, radio frequency (RF) supply and beamlines. The electrons are usually generated by high intensity electron guns. The electrons are initially accelerated in a LINAC – Linear Accelerator. They are then injected into a booster ring, which accelerates the electrons to near the speed of light using synchro-cyclotron (also known as synchrotron) principles (Bryant & Johnsen, 1993). The electrons are then injected into a storage ring in specific time frames (3x a day at the Canadian Light Source, CLS, and every few minutes in the top-up mode at the Advanced Light Source, ALS). The top-up current is 500 mA at the ALS while the CLS starts at 220 mA and is allowed to decay to ~150 mA over an 8 hour period. In top-up mode, when the current drops to some preset value (498 mA at ALS) additional electrons are injected (Willmott, 2011). **Table 2.1** compares the properties of the beam at both the CLS and ALS.

Table 2.1 Properties of the ALS and CLS.

Facility (beamline)	Beam energy (GeV)	Beam current (mode)	Beam emittance (horizontal/ vertical nm.rad)	Beam size (horizontal/ vertical μm)
Advanced Light Source	1.9	500 mA (Top-up)	2.0 / 0.04	251/8
Canadian Light Source	2.9	220 mA (reinjection 3x/day)	18 / 0.09	~1000/300

The storage ring is made up of an array of different types of magnets which serve to i) bend the electron trajectory, ii) focus or steer the electron beam, and iii) correct chromatic aberrations (Willmott, 2011). The most intense synchrotron radiation is generated by the wiggler and undulator IDs, which are periodic series of magnets in long straight sections placed between the curved sections of the storage ring. The bend magnets also emit radiation, orders of magnitude more intense than laboratory sources, but with lower brilliance compared to ID radiation (Willmott, 2011). The electrons inherently lose energy due to synchrotron light emission and the energy is replenished by a RF supply, where a high frequency (typically 500 MHz) electric field accelerates the electrons (Balerna & Mobilio, 2015). Beamlines are placed tangentially to the storage ring, aligned either with IDs or bend magnets (Willmott, 2011). Beamlines have some common components: apertures to define angular spread of the radiation; radiation safety components to prevent harmful γ-radiation passing into end stations when the storage ring beam hits a vacuum wall close to a beamline take-off port; blocks or filters to remove higher-order or low-energy stray light; monochromators and focusing elements.
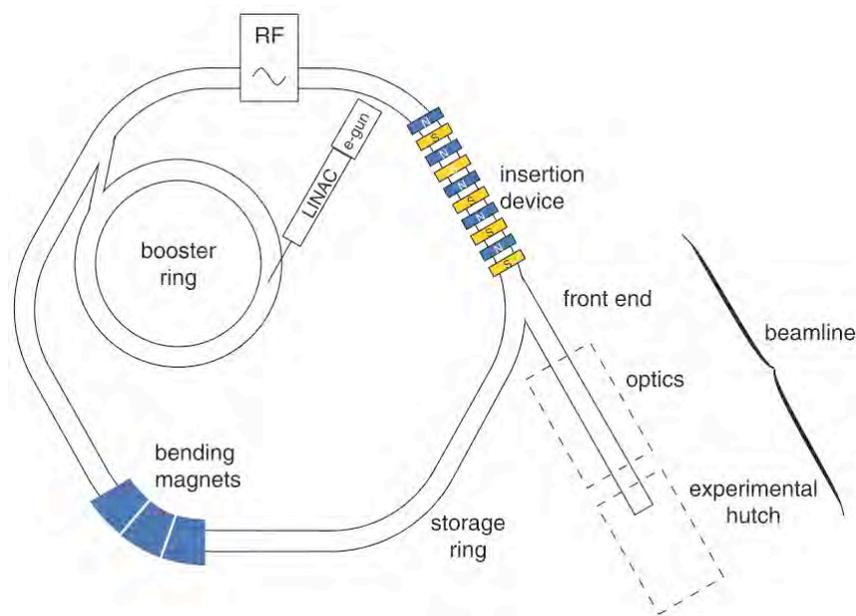
Figure 2.1 Schematics of the major components in modern synchrotron facilities (*© John Wiley and Sons 2011, from Willmott, 2011*).

Third generation facilities generally have a brilliance in the range of 10^{21} photons/mm^2/mrad^2/0.1% bandwidth (Willmott, 2011). This brilliance is many orders of magnitude higher than laboratory sources and only a few orders of magnitude lower than visible lasers. The low emittance in third generation facilities, which is the reason for the high brilliance, is enabled by advanced design of the magnets, the beam energy (between 0.6-8 GeV) and the circumference (between 30-1200 meters), which sets the range of photon energy available (Willmott, 2011). High beam energies, such as the 8 GeV Spring8 facility in Japan, are important for generating hard X-rays in the >50 keV range (Aquilanti, Vaccari, Plaisier, & Goldoni, 2015).

Fourth generation diffraction limited storage rings (DLSR) are currently operational in Sweden (MAX-IV) and under construction in Brasil (SIRIUS). Due to use of a multibend achromat lattice and compact magnet design (several compact magnets with small bending angle combined with focusing magnets with small gaps in between), DLSR light sources have a very

low emittance (pm/rad range) reaching the fundamental limit of diffraction at lower X-ray energies (Tavares, Leemann, Sjöström, & Andersson, 2014). The ALS is currently in design phase of ALS-U, a DLSR which will have by far the lowest emittance of all storage rings [but larger than Free Electron Lasers (FEL)]. Improved performance of STXM and ptychography microscopes is the most compelling argument for the ALS upgrade. FEL sources use very long undulators, which reinforce emission from either a spontaneously generated seed (SASE) or from a UV laser seed, to generate few femto-second X-ray pulses (Geloni, 2018). The resulting beam is highly focused, has ultrahigh brightness, and power density. The main issues with FELs are related to power density which gives challenges to focusing optics, and to sample integrity (Yumoto et al., 2013).

2.1.1 Properties of synchrotron radiation

The Lorentz factor, γ, which governs the properties of SR, is related to the storage ring energy, E in (GeV) by (Willmott, 2011):

$$\gamma = \frac{E}{mc^2} = 1957\, E \qquad \text{Equation 2.1}$$

Electrons traveling at low speed (low energy) that are accelerated emit radiation nearly isotropically. When electrons are accelerated to speeds near that of light, the radiation is emitted in a narrow cone in the direction of motion (Willmott, 2011). The angular divergence of the beam is related to the storage ring energy by: $\theta \sim \gamma^{-1}$ (Willmott, 2011). The flux of the emitted synchrotron radiation depends on the speed of the electrons and is proportional to γ^4 (Willmott, 2011). The angular distribution of bending magnet radiation is broader than that of ID radiation (Balerna & Mobilio, 2015). The flat-cone radiation (**Figure 2.2a**) of bending magnets allows

several beamlines to be placed after the magnet (Willmott, 2011). The spatially alternating transverse magnetic fields in wigglers and undulators force the electrons to follow an oscillating path and emit light after each oscillation (**Figure 2.2b**) (Balerna & Mobilio, 2015; Willmott, 2011). In the case of undulators, there are many periods of alternating magnetic field and the emission from successive periods interfere with each other, greatly amplifying the emission. The horizontal spread, θ_h of the generated radiated is (Willmott, 2011):

$$\theta_h = \frac{2K}{\gamma}$$

Equation 2.2

Wigglers have relatively few magnetic periods with a value of K (dimensionless) between 10-20. Wigglers increase flux over a broad spectrum rather than forming the relatively narrow intense peaks characteristic of undulators. In fact, **Equation 2.2** shows there is a continuum of operation between wigglers and undulators (K ~ 1) and intermediate devices have been developed. Flux and brilliance is enhanced compared to bending magnets due to the reinforcement of radiation emitted by each magnetic pole in IDs (Balerna & Mobilio, 2015).
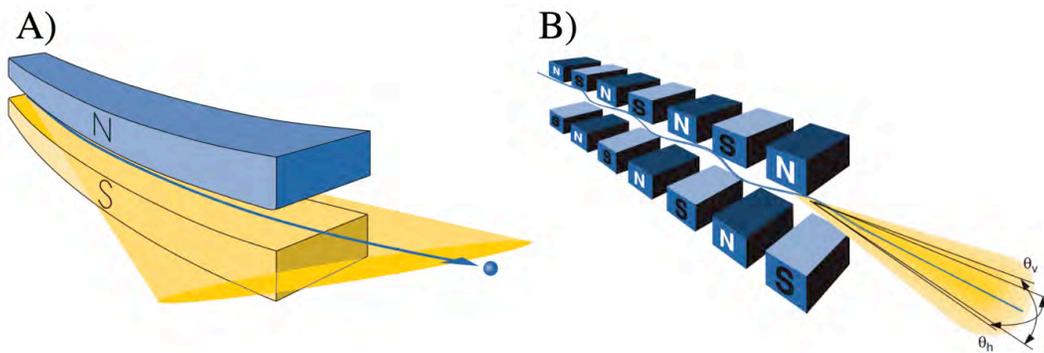
Figure 2.2 Schematic diagram of (**A**) bending magnet and (**B**) insertion device radiation, where the angular spread is defined in the horizontal, θ_h and vertical planes, θ_v. © *John Wiley and Sons 2011, from Willmott, 2011*.

2.1.2   *Soft X-ray beamlines: monochromation and focusing*

After the ID or bending magnet, there is a 'front end' which includes heat and radiation baffles, apertures to define the angular acceptance of the beam, and radiation protection components (Willmott, 2011). The X-ray optical system consists of a monochromator, various types of mirrors (to optimize energy resolution and curved mirrors to focus the beam), slits and filters (Willmott, 2011).

A schematic of the polymer bending magnet beamline 5.3.2.2 at ALS is shown in **Figure 2.3a** (Warwick et al. 1998, 2002). The beamline has a particularly simple optical design, consisting of a toroidal mirror, an entrance slit, a spherical grating monochromator (SGM) with a single grating, and a (x,y) variable exit slit at a fixed Z-position. It was designed for the energy range 270 – 560 eV, but in fact performs quite well from 150 – 1100 eV. **Figure 2.3a** presents the intensity curve measured in the STXM at ALS BL 5.3.2.2.

A) Bend magnet
Toroidal mirror
($R_s = 0.695$ m, $R_t = 181$ m)

10.0 m

9.0 m

174°

Exit slit/pinhole

173°

Zone plate
(200 µm diameter)

Entrance slit

4.4 m

Plan view

6.4 m   1.0 m

Spherical grating
(300 l/mm, $R = 88.0$ m)

B)

N 1s

O 1s

C 1s

N 1s
2nd ord

STXM 5322

Ni 2p

measured March 2006
slits 30 um x 30 um

Log_{10}(flux (photons/sec))

7.0
6.5
6.0
5.5
5.0
4.5
4.0

200   400   600   800   1000   1200
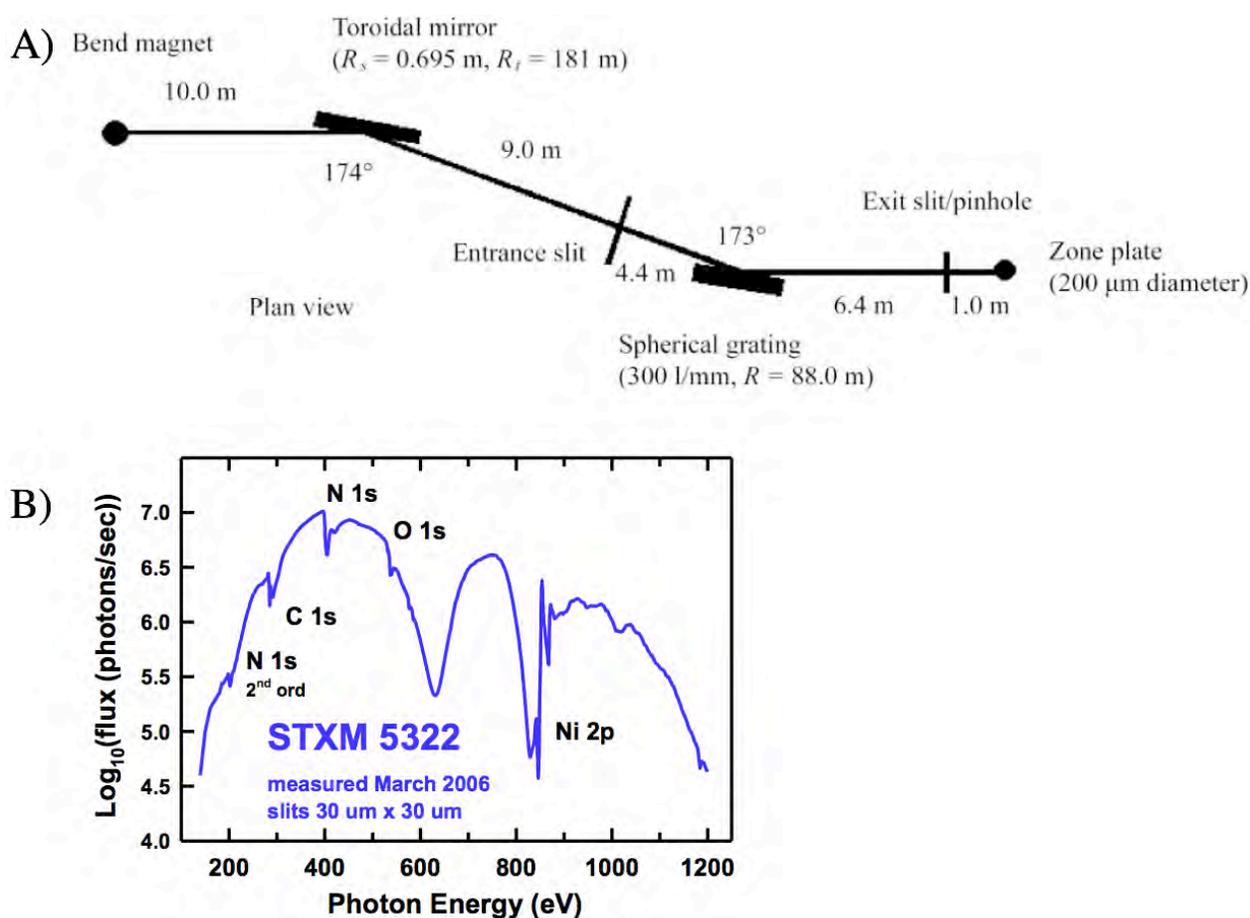
Photon Energy (eV)

Figure 2.3 (A) STXM beamline schematics of the bending magnet at 5.3.2.2. at the ALS (*Reprinted with permission from the International Union of Crystallography, Warwick 2002*) and **(B)** Intensity as a function of photon energy measured in the STXM at 5.3.2.2. Note the detector efficiency drops as the energy decreases so this curve significantly underestimates the intensity at lower energies. Since this measurement was made, the performance at 5.3.2.2 has been increased by more than 1 order of magnitude by changing optics and improving optical alignment.

The monochromator disperses the photon energy distribution horizontally at the 5.3.2.2 beamline, rather than vertically, as is the case in almost all storage ring beamlines. This was done to compress the beam horizontally and thus increase the flux illuminating the zone plate (ZP). (It was also convenient as this design allowed the beamline to 'wrap around' a building support

pillar, directly in line with the path of the beam). The energy resolution of the SGM is controlled by the entrance slit and the horizontal exit slit, typically set to 50 μm and 25 μm respectively. The spatial resolution is affected by the horizontal and vertical exit slits, typically set to 25 μm and 25 μm, which act to define the virtual source for the microscope, and control the transverse coherence. With these slit values (50/25/25 μm), a 240 μm diameter ZP is just filled in the vertical and significantly overfilled in the horizontal direction (i.e. the beam just before the ZP is about 500 μm x 300 μm (H x V). The exit slits can be opened to increase flux but at the cost of either spatial resolution (V) or energy resolution (H) (Warwick et al., 2002).

A special feature of the 5.3.2.2 beamline is an inline N_2 gas filter which is a differentially pumped gas cell. When the ~1 m path length is filled to a pressure of ~0.7 torr of N_2, the second order harmonics light in the C 1s region is very effectively suppressed. 2nd order harmonics light is much more intense in the bending magnet spectrum from the storage ring (peak output of the ALS 1.9 GeV ring is at about 1000 eV) and is very effectively diffracted by the SGM (Warwick, Padmore, & Ade, 1998). **Figure 2.4** shows the influence of the N_2 filter on reduction of 2nd order harmonics light (seen as the O 1s spectrum of CO_2 at ~262 eV) and dramatic enhancement in the peak optical density (OD) that can be measured in the C 1s region (seen at the C 1s $\rightarrow \pi^*$ peak of CO_2 at 290.7 eV).
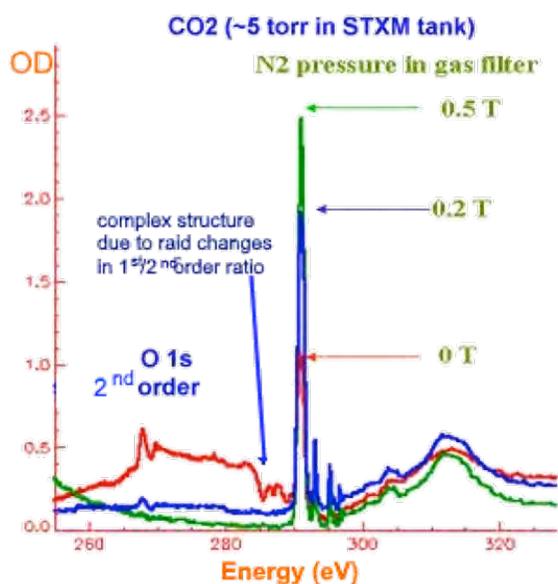
Figure 2.4 Effect of pressure of N_2 in the N_2 gas filter at STXM 5.3.2.2 on the 2nd order harmonics light and on the 1st order spectrum of CO_2 (measurement made in ~2007).

Usually STXM microscopes are installed in undulator beamlines (such as the 10ID1 at the CLS). The elliptically polarized undulator (EPU) beamline at the CLS [see **Figure 2.5**-(Kaznatcheev et al., 2007)] is entrance-slit-less and uses a plane grating monochromator (PGM), which increases the energy range and resolution of the beamline (Aquilanti et al., 2015). The EPU delivers left and right circular polarized light and linear polarized light from -90° to 90° (Kaznatcheev et al., 2007). At the CLS, the 10ID1 beamline is shared by three endstations: ambient-STXM and cryo-STXM (in line) and X-ray photoemission electron microscope (PEEM) on a branch line.
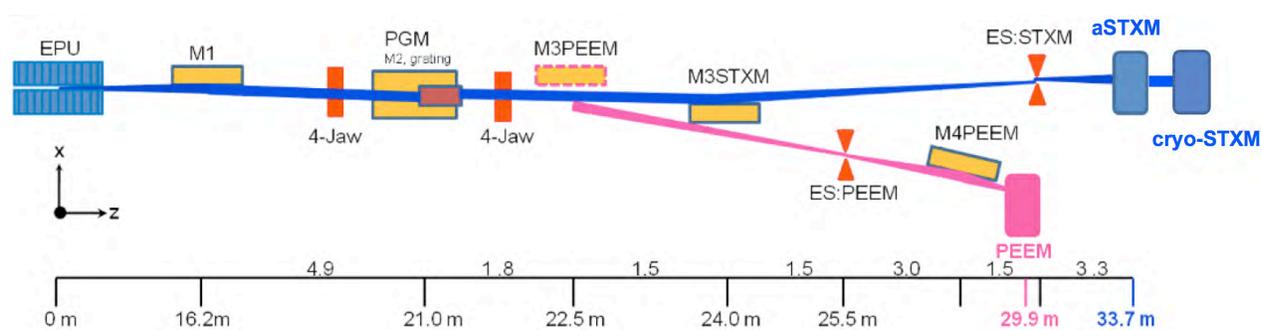
Figure 2.5 STXM beamline schematics of the undulator beamline 10ID1 at the CLS.

2.1.3   *Synchrotron X-ray microscopy – comparison of TXM, STXM and ptychography*

SR is ideal for X-ray microscopy since it provides a tunable incident photon beam, which is necessary for X-ray Absorption Spectroscopy (XAS, more in section 2.3), and a high brightness with considerable coherence that allows zone plate (ZP) lenses to perform at full potential. There are four main synchrotron-based X-ray microscopy techniques that use zone plate (ZP) lenses: transmission X-ray microscopy (TXM), scanning transmission X-ray microscopy (STXM), scanning photo-emission X-ray microscopy (SPEM) and scanning X-ray fluorescence microscopy (SXFM). STXM and TXM are in the domain of soft X-ray, photon-in and photon-out microscopes and are described in more detail here.

TXM has an optical layout very similar to modern optical microscopes, with a condenser ZP to define the illuminated area (1 – 20 μm) and a post-sample objective lens to expand the transmitted light into the far field where it is detected in parallel using an X-ray camera. The magnification is controlled by changing the distance from the imaging ZP lens to the detector. TXM provides fast (1-10 s) acquisition of 2-D images, which allows rapid collection of tomography data by changing the tilt angle of the sample to build 3-D images (Howells, Jacobsen, Warwick, & Van den Bos, 2007). To date, most of the science done using soft X-ray

TXMs has been 2D imaging and 3D tomography of biological samples at 520 eV in the water window (e.g. see papers by Caroline Larabel (Hitchcock, 2018)) and for static and dynamic imaging of artificial magnetic structures (e.g. see papers by Peter Fischer (Hitchcock, 2018)). There are two operational soft X-ray TXMs on proper dispersing beamlines [Bessy II (Guttmann et al., 2003), Alba (Sorrentino et al., 2015)] and several more are under commissioning. In principle, TXMs on these beamlines should out-compete STXM for throughput. In practice, STXM has been (and still is) the preferred tool for analytical spectromicroscopy studies due to the problems of TXM which include: the excessive dose, non-uniform illumination, no interferometers (and wandering samples), and inability to do coarse scanning to navigate to areas of interest. In the case of 3D imaging, TXM results in faster acquisition times but much higher doses compared to STXM.

STXM combines both microscopy and spectroscopy (Near-Edge X-Ray Absorption Fine Structure or NEXAFS). The main advantage over other spectroscopy techniques is that it provides quantitative spatial distribution of compounds or phases with detailed speciation capability (Ade & Hitchcock, 2008; Hitchcock, 2012). It provides contrast based on the unoccupied electronic structure of the sample (McNeill et al., 2008). Samples studied by STXM includes gaseous, solid and liquid samples, including polymers (Ade & Hitchcock, 2008), hydrated biological and environmental sciences samples (Hitchcock et al., 2002) and in-situ experiments at variable voltages (Guay, Stewart-Ornstein, Zhang, & Hitchcock, 2005), temperatures (Tzvetkov & Fink, 2008) and polarization (Ade, 1998).

The resolution in X-ray microscopy based on Fresnel ZP lenses is currently limited by imperfect image-forming optics. A set of techniques called Coherent Diffractive Imaging (CDI)

have been developed to overcome this limitation. A (partially) coherent beam is used to provide coherent scattering from non-repeating structures. Basically, CDI methods exploit the same light-sample interaction that gives rise to X-ray diffraction patterns, but the signal appears 'blurry' and can change in time (speckles), due to the lack of periodic repeat structure of the sample. A direct method is used to invert the scattering signal to determine the complex index of refraction of a sample and the characteristics of the probe beam. Both absorption (amplitude) and phase are measured quantitatively (Thibault, Guizar-Sicairos, & Menzel, 2014). Ptychography is a CDI approach that has been developed to take advantage of the dramatically improved convergence and stability of the mathematical processing, when the data is in the form of multiple measurements sampled in overlapping spatial regions (Thibault et al., 2008). Basically, the requirement greatly constrains the convergence of the algorithms used, as the phase and amplitude in the overlapping regions must be the same.

STXM is an ideal platform for ptychography since modern STXMs have optimized sample stability, and are equipped with interferometric monitoring and control of the relative position of the light source and the sample. In ptychography, overlapping areas of the sample are scanned with a focused X-ray beam while measuring the diffraction patterns. High-quality reconstruction with appropriate algorithms recovers the illumination profile simultaneously with the complex-valued image of the sample (Thibault et al., 2008). Advantages relative to real space X-ray imaging include (i) improved spatial resolution (world record at present is **3 nm** using 1500 eV photon energy, and a 45 nm outer zone plate (Shapiro et al., 2014)), (ii) determination of spatial maps of the full complex refractive index response of the sample, and (iii) characterization of the illumination beam. It is expected that, when combined with the new generation of diffraction

limited storage rings (e.g. Max IV (Tavares et al., 2014) and SIRIUS), there will be further
dramatic performance improvements in ptychography (Hitchcock, 2015).

2.2   Scanning Transmission X-ray Microscopy

2.2.1   Diffraction focusing using a Fresnel Zone Plate Lens

Fresnel Zone plates (ZP) focus X-rays by diffraction (Attwood, 1999; Howells et al., 2007).
The ZP is made up of a series of concentric X-ray opaque rings fabricated on a thin membrane
partially transparent to X-rays (typically silicon nitride). As the X-ray beam passes through the
ZP, a portion is diffracted by the alternating opaque / transparent zones. After the ZP, several
orders of diffracted light are produced as shown in **Figure 2.6**. The zero-order component must
be blocked to allow use of one of the diffraction orders as a focused probe. ZPs are based on
constructive interference, where the first order diffracted beam consist of reinforced signals from
the successive radial zones of radius r_n with a path length defined as $n\lambda/2$, where n is the
diffraction order and λ is the X-ray wavelength (Attwood, 1999) for a perfect ZP. The even orders
of diffraction cancel at focus due to the symmetry between the successive zones (Attwood, 1999).
The diffraction efficiency of higher order light is much lower compared to the first order light due
to a much higher requirement of perfection of fabrication (Attwood, 1999). After the
monochromated photons diffract through the ZP, approximately 50% of the photons are absorbed,
25% are transmitted without diffraction (zero-order light), 10% form first order light, 10% form
negative first order light and 1% forms third order light (Attwood, 1999).
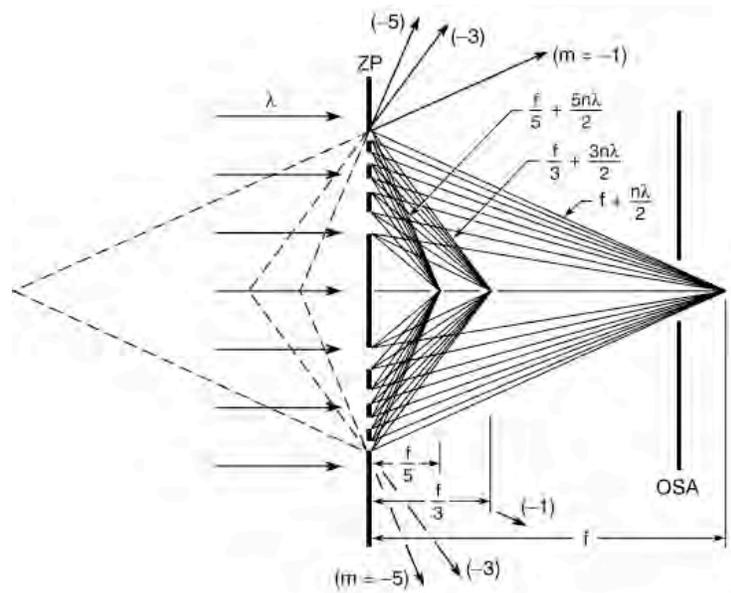
Figure 2.6 Diffraction focusing of ZP lenses showing 1st, 3rd and 5th order light. The OSA blocks all light except for the 1st order light. The negative orders are also shown (dashed lines) with virtual foci behind the lenses (© *Cambridge University Press, 1999 from Attwood 1999*).

2.2.2   Principles of STXM

A monochromated X-ray beam is focused on the sample. Transmission images at a single photon energy are generated by positioning the sample at the focal point of the ZP, and (x,y) raster scanning the sample. The transmitted flux is recorded using an X-ray sensitive detector consisting of a phosphor (P43) to down-convert the X-ray into a shower of visible photons which are then detected using a high performance photomultiplier tube (Hamamatsu R647) (Kilcoyne et al., 2003). The (x,y) positions of the sample relative to the ZP lens are controlled by interferometry (Kilcoyne et al., 2003) which uses the fast piezoelectric sample scanning stage to maintain position within ~10 nm with a ~100 Hz response.

The ZP has an X-ray opaque central stop (CS) to suppress zero order and higher order light (Kilcoyne et al., 2003). Together with the CS or C, the order selection aperture (OSA), placed

between the ZP and the sample, allows only the first-order light to illuminate the sample – see

Figure 2.7. The focal length of the ZP, f, increases linearly with the incident photon energy and

the outer-zone width of the ZP, Δr, and is defined as (Attwood, 1999; Jacobsen, Wirick, Flynn, &

Zimba, 2000):

$$f = \frac{D \cdot \Delta r}{\lambda} \qquad\qquad \text{Equation 2.3}$$

where D is the ZP width [µm], Δr is in [nm], and the wavelength, λ, of the incident beam can be

transformed into energy by:

$$\lambda = \frac{1240}{E} \qquad\qquad \text{Equation 2.4}$$

Where E is the incident photon energy in [eV]. Substituting Equation 2.4 into 2.3 gives:

$$f = \frac{D \cdot \Delta r \cdot E}{1240} \qquad\qquad \text{Equation 2.5}$$

where f is calculated in µm. The fully focused beam diameter and hence the spatial resolution is

determined by Δr of the ZP. The diffraction-limited resolution of a ZP, according to the Rayleigh

criterion, is given by $\sim 1.22\Delta r$. Typically, when scanning the photon energy by 40 eV around an

elemental edge, the ZP-z position must change several hundreds of µm in order to maintain the

focus at the sample. The distance between the sample and the OSA, called A_0 in the

STXM_Control and pySTXM data acquisition programs, can be set by the user and is selected to

be 50 – 100 µm less than the point at which the 1st order beam just starts to be clipped by the

OSA. For a ZP with D = 240 µm, C = 90 µm, Δr = 25 nm, and an OSA diameter of 60 µm, the

OSA starts to clip the first order light at an A_0 of 327 µm at 270 eV and thus an $A_0 \leq 260$ µm is

used at the C1s edge (the OSA is not perfectly round). The advantage of using ZPs with lower

spatial resolution and larger Δr is that f is larger and the A_0 can be set to higher values, allowing

greater sample to OSA distances, and less risk of collisions, which are undesirable. This is

particularly useful for tilted samples which are used in X-ray Magnetic Circular Dichroism

(XMCD), X-ray Fluorescence (XRF) detection, some types of linear polarization studies, and for

tomography which requires sample rotation.
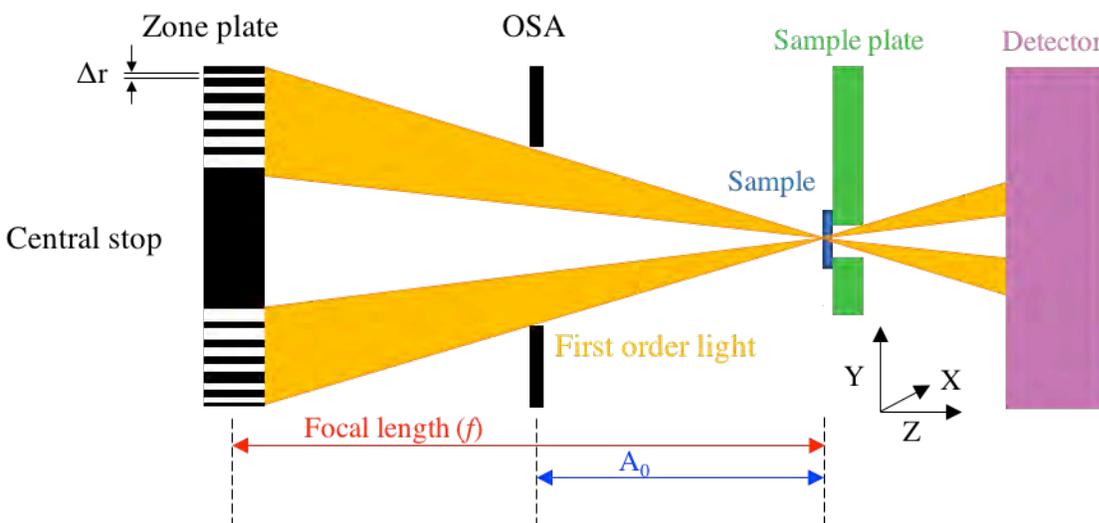
Figure 2.7 Schematics of a STXM microscope depicting the ZP, CS, OSA, sample and detector.
The focal length and A_0, the position of the sample relative to the OSA, are also shown.

The transmitted signal at each (X,Y) pixel and photon energy, E, is converted to absorption

(optical density, OD) using Beer Lambert's Law:

$$OD(E) = -\ln(I(E)/I_o(E)) \qquad\qquad \text{Equation 2.6}$$

where $I_o(E)$ is the transmitted signal without the sample but through any other material at the

position of the sample (windows, substrate, filters, etc) and $I(E)$ is the transmitted intensity. The

OD is directly related to the sample properties through $OD(E) = \mu(E)\,\rho\,h$ where $\mu(E)$ is the

photon energy dependent mass-absorption coefficient, ρ is the density and h is the thickness of

the material. For further details please see the original paper describing the instrument (Kilcoyne

et al., 2003) and STXM reviews (Ade et al., 1995; Ade & Urquhart, 2002; Hitchcock, 2012).

2.2.3   Limiting radiation damage by defocusing

In the case of samples that are sensitive to ionizing radiation, the radiation damage caused

by measurements with a fully focused beam can invalidate the measurement. In such cases, it is

desirable to reduce the dose given to the sample by increasing the beam diameter, S, by

displacing the ZP from its position of perfect focus, thereby defocusing the beam and reducing

the spatial resolution. At a certain level of defocus the incident beam diameter will become an

annulus. The defocused spot size or beam diameter, S, that causes the illumination to form an

annulus shape on the sample can be calculated. Its value depends on what one considers to be the

depth of focus, doF. The doF is the displacement away from the focal point for which the quality

of focus is unchanged and is defined as (Howells et al., 2007):

$$doF = \frac{8 \cdot \Delta r^2}{\lambda}$$
<div align="right">Equation 2.7</div>

When S is larger than the depth of focus (doF), the incident beam forms an annulus on the

sample. The inner diameter of the annulus (x) is given by simple trigonometry as:

$$\frac{D}{C} = \frac{S}{x}$$
<div align="right">Equation 2.8</div>

For a 500 nm beam diameter and a ZP with D=240 μm and C=90 μm, x is 0.19 μm, as shown in

Figure 2.8a,b. 86% of the area will be illuminated by the incident beam with any selected beam

diameter or defocus larger than the doF, with a central 14% area non-illuminated. The necessary

defocus to form an annulus spot is:

$$S_{annulus} = \frac{D \cdot doF}{f}$$

Equation 2.9

For a 25 nm ZP at 320 eV $S_{annulus}$ is ~ 200 nm. Due to significant damage spread of soft materials

(Wang, Stöver, Hitchcock, & Tyliszczak, 2007), the experimental $S_{annulus}$ may be much larger.

As discussed in Chapter 3, many of the pattern generation and most of the damage

measurements used a beam defocused by manually adjusting the A_0 value. The change in A_0

(δA_0) needed to change to a beam diameter of S (see **Figure 2.8c**) is given by:

$$\frac{\delta A_o}{f} = \frac{S}{D}$$

Equation 2.10

or, combining Eqn. 2.5 and Eqn. 2.10:

$$\delta A_o = \left[\frac{E \cdot \delta r}{1240}\right] S$$

Equation 2.11
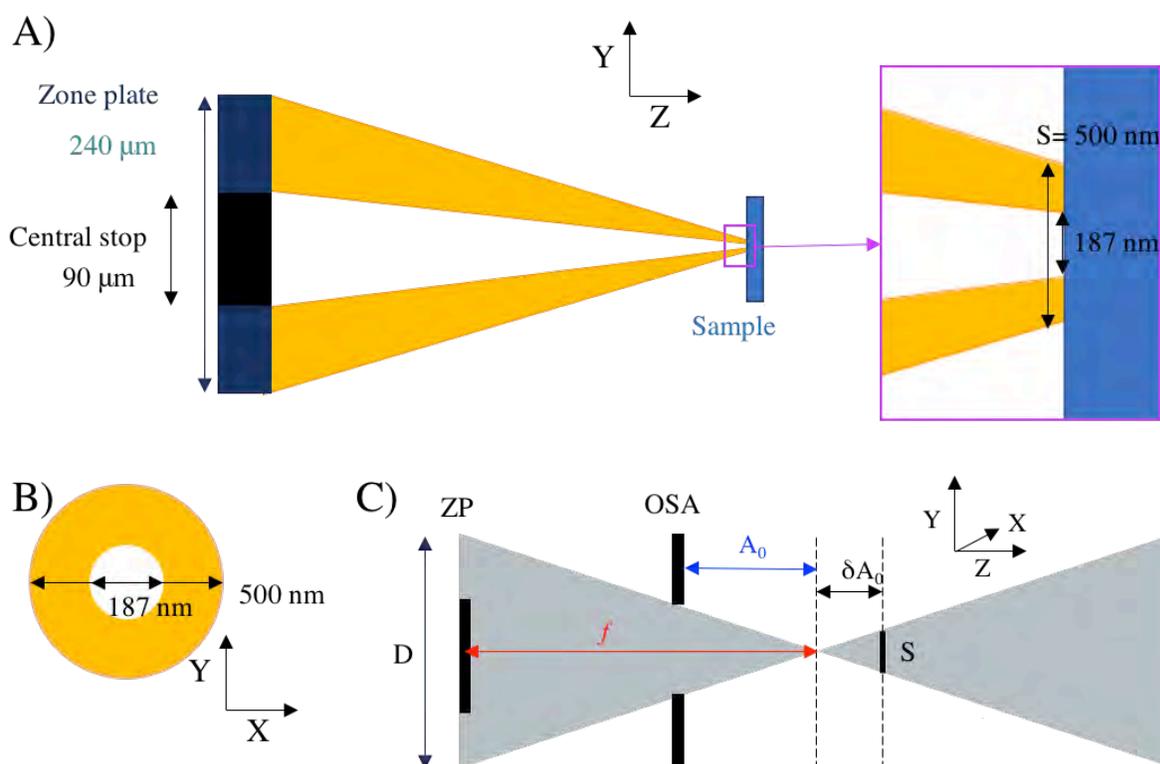
Figure 2.8. (A) A side-view depiction of how the actual incident beam diameter changes as a function of beam diameter (S) due to the relationship between the ZP width, D, and the central stop width for defocus larger than the doF in the Y and Z directions and **(B)** A cross-sectional view in the Y and X directions showing the area illuminated by the incident photons is an annulus (for defocus larger than 200 nm). **(C)** STXM optics indicating how the position of the ZP affects the beam diameter, S, on the sample, δA_0 is the calculated parameter that is added to the A_0 to set the position of the ZP to the desired beam diameter (S).

2.3   *X-ray absorption spectroscopy (XAS)*

The main interaction between soft X-ray photons and a sample is absorption (discussed in section 1.4.1.2) (Stöhr, 1992), in which the photon disappears and its energy is deposited into the sample, which in most cases can be described by the excitation of a single electron. X-ray Absorption (XAS) spectra have sharp features due to absorption at specific energies, related to

specific electronic excitations. The absorption of photons results in the excitation and ionization of inner-shell electrons and creation of a high energy excited state from the ground state of the system. If the photon energy is greater than the ionization potential (IP) for a given inner-shell level, the electron is promoted to the continuum states above the vacuum level. The ionized electron has excess translational kinetic energy which can, in turn, cause inelastic scattering and excitation or ionization of neighboring electrons (Yano & Yachandra, 2009). If the photon energy is lower than the ionization potential, the electron is excited to unoccupied orbitals (molecular picture) or bands (solid state picture). This is the basis for X-ray Absorption Near-Edge Structure (XANES) also called Near Edge Fine Structure Spectroscopy (NEXAFS). The details of an inner-shell spectrum, both below and above the IP, depend on the electronic structure of the sample, including the occupied and empty electronic states, which are related to the geometric and chemical structure. This makes NEXAFS a highly specific technique to study the chemical structure of materials (Stöhr, 1992).

Figure 2.9 shows the F 1s NEXAFS spectrum of PFSA and its spectroscopic interpretation in terms of an energy level diagram. The assignment of the spectral features was based on polytetrafluoroethylene (PTFE). The two peaks at the F 1s edge are attributed to the F 1s $\rightarrow \sigma^*_{F-C}$ ($\perp$) and F 1s $\rightarrow \sigma^*_{F-C}$ (//) orbitals oriented across and along the main chain, with analogous features in the C 1s spectrum of PFSA, respectively. These peaks also appear in the C 1s and F 1s NEXAFS spectra of polytetrafluoroethylene (PTFE). PTFE samples prepared such that the molecules were aligned with polarized X-rays aided interpretation of the peaks (Castner, Lewis, Fischer, Ratner, & Gland, 1993; Ohta, Seki, Yokoyama, Morisada, & Edamatsu, 1990). The interpretation of the NEXAFS spectrum is generally understood through consideration of the

small molecules analogues (see gas phase bibliography (Hitchcock, 2018)) and using
computational approaches. For the interpretation of the S 2p and O 1s spectrum of PFSA related
to the sulfonated end group, the inner shell electron energy loss spectroscopy (ISEELS) spectra of
several gas phase molecules were acquired and used to help support a detailed interpretation of
the inner shell spectra of PFSA (Yan, Hayes, Melo, Goward, & Hitchcock, 2018).
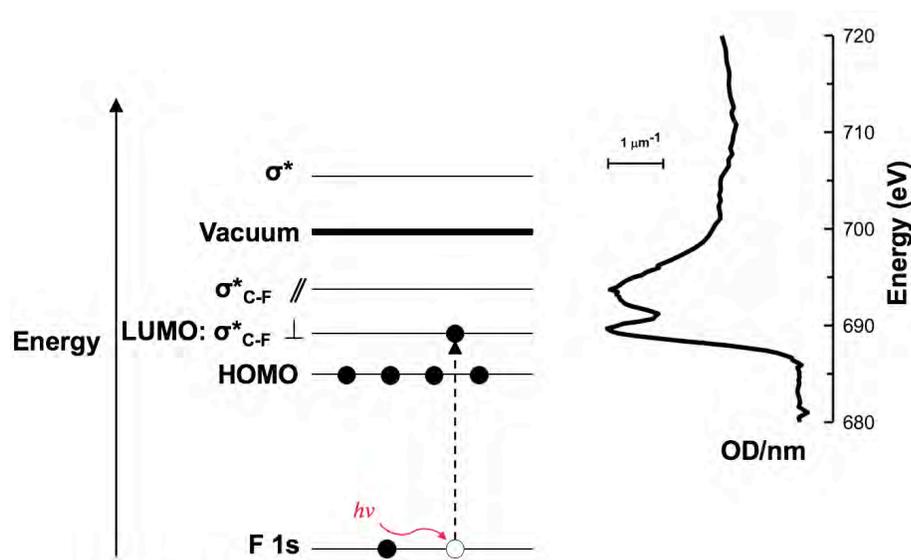
Figure 2.9 Energy diagram of the X-ray absorption and corresponding NEXAFS spectrum of
perfluorosulfonic acid (PFSA) at the F 1s edge.

2.4   Electron microscopy

2.4.1   Principles

A Transmission Electron Microscope (TEM) is an instrument in which an incident beam of
high energy electrons is transmitted through a thin sample. Due to the interaction of electrons
with matter, a variety of signals are generated. These signals can be captured by detectors,
cameras and spectrometers, leading to rich chemical and structural information. TEM has
allowed direct visualization of the atomic columns of a crystalline material, identification of

phases using diffraction methods, and elemental quantitation using several types of analytical microscopy. Typically, a modern TEM can be operated in two distinct modes: parallel (also called TEM) or raster scanning convergent beam (called Scanning Transmission Electron Microscope, STEM) (Williams & Carter, 2009, 2016).

The TEM can be divided into three systems: the illumination system, the objective lens/sample, and the image formation lens system. The illumination system uses condenser lenses to transfer electrons generated by an electron gun into a beam onto the sample. The electrons are emitted from the electron gun through thermionic emission (heating to high temperatures of a W filament or LaB_6 crystals) or field emission (usually tunneling of electron from a crystalline tungsten wire tip where a high voltage is applied) (Williams & Carter, 2009). The brightness (current density per lateral size, solid angle and kinetic energy of the source) of field emission guns (FEG) is much higher than that of thermionic guns (Williams & Carter, 2009). The image formation lens system consists of several lenses to magnify the image produced by the objective lens/sample section. Detectors, such as phosphor screens or cameras, are placed after the imaging lenses. Electron energy analyzers are often placed post-sample and used both for energy filtering (elastic only, or some energy band of inelastic electrons) and electron energy loss spectroscopy (EELS).

The signals are generated in the objective/sample holder system through the interaction of the incident electron beam and the sample. The signals can be divided into two classes depending on the energy transfer of the beam to the sample: elastic and inelastic scattering. Elastic scattering enables investigation of the crystalline nature of the sample using diffraction methods (such as selected area diffraction, large angle convergence beam electron diffraction). Inelastic scattering

is the basis for the EELS type of analytical electron microscopy, where spatial distributions of elements, their concentrations and their oxidation states can be mapped (Botton, 2007). When an incident electron of sufficient energy interacts with matter, the primary electron can transfer kinetic energy to an electron of the target, either valence or inner-shell. If the energy of the primary electron is higher than the ionization potential of an inner-shell electron, the inner shell electron can be ejected and the kinetic energy of the incident beam is decreased. The core hole will be filled by emission of an Auger electron or a characteristic X-ray, just as with X-ray absorption. In contrast to the resonant process of X-ray absorption, inelastic scattering is non-resonant and all possible states are excited with a particular probability.

2.4.2   TEM Instrumentation

The illumination system can be operated in a parallel beam (TEM) with post specimen image formation, or in a convergent beam, which can generate images by raster scanning the focused beam over the sample (STEM). A schematic of the parallel and convergent beam modes is shown in **Figure 2.10.** In reality, modern TEM microscope are comprised of several lens systems. In parallel mode, two condenser lenses (C1 and C2 in **Figure 2.10a**) are adjusted to provide a parallel beam incident on the sample. The condenser aperture is usually placed between the C2 and the objective lenses and limits the electron current that reaches the sample (Williams & Carter, 2009). The C1 lenses controls the size of the probe (also called spot size) and the current incident on the sample. A strong C1 lens results in a small probe and high current density. A weak C2 results in a large probe and low current density incident upon the sample. The C2 lenses can be adjusted to provide a convergent beam on the sample, as shown in **Figure 2.10b**. However, in order to see an image, the beam has to be scanned on the sample. The scanning coils

(not shown in **Figure 2.10b**) are usually placed between the two condenser lenses. Compared to X-ray microscopy, TXM is analogous to TEM and STXM is analogous to STEM. In TEM mode, images are acquired much faster than in STEM mode. Variable magnification in TEM is achieved by changing the strength of the imaging lenses placed after the sample, whereas in STEM the magnification depends on the probe size and the dimensions of the sample scanned (Williams & Carter, 2009).

After the imaging system, viewing screens and detectors facilitate the acquisition of the images. The viewing screen, which is coated with a phosphor that emits in a specific wavelength (generally 550 nm or green), is very useful for alignment of the microscope. Such screens are not used for image acquisition and are becoming obsolete in modern microscopes. For TEM images, charge coupled device (CCD) or direct electron detector cameras are the norm today. CCDs consist of several million capacitors that accumulate charge proportional to the intensity of the transmitted electron beam (after interaction with the sample) (Williams & Carter, 2009). Direct electron detectors are sensitive to each incoming electron such that each electron contributes to the image (Kuijper et al., 2015). Each electron creates electron-hole pairs through interaction with Si (Kuijper et al., 2015). Direct electron detectors have enabled ultra-low dose imaging in the biological sciences since less dose is necessary to acquire images with a good signal to noise ratio compared to traditional CCD cameras. For STEM images, retractable annular detectors are placed after the imaging system.
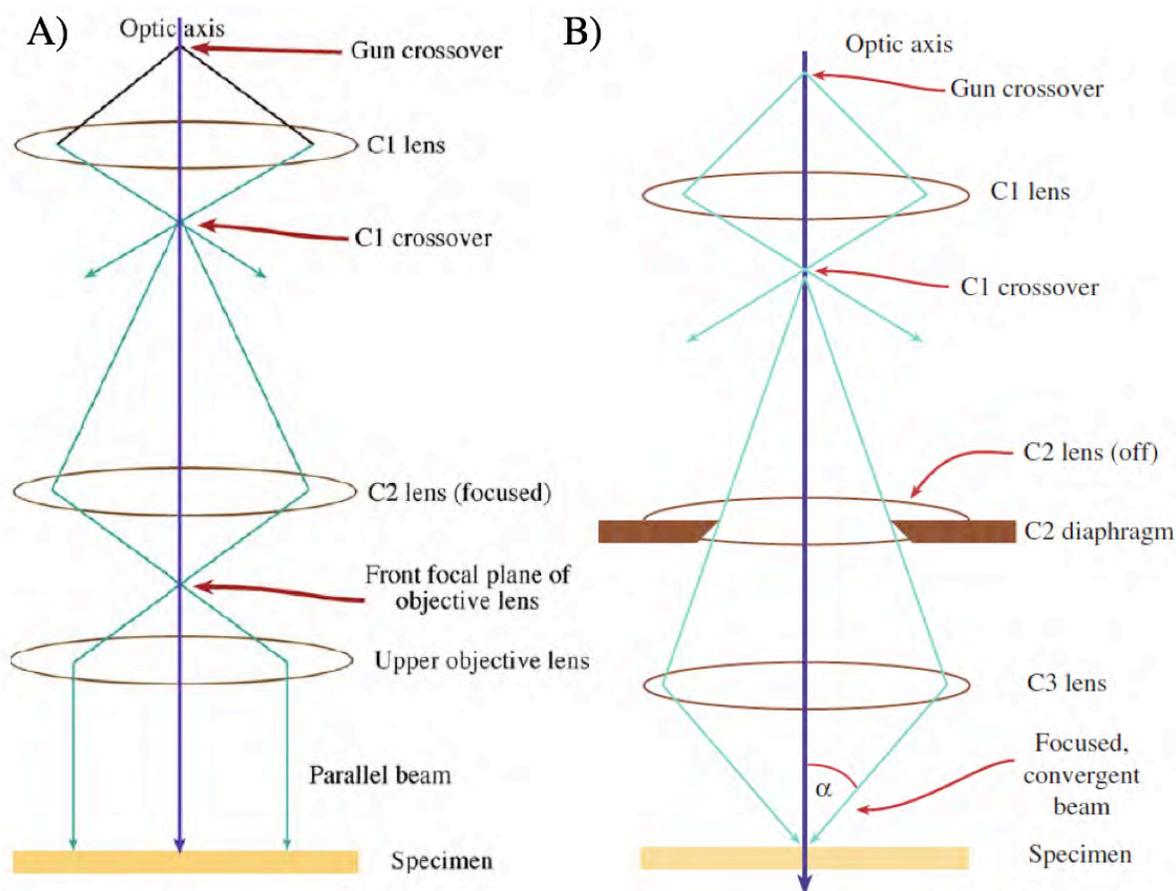
Figure 2.10 Schematic of a transmission electron microscope operating in (**A**) parallel and (**B**) convergent beam modes © *Springer Science Business Media from Williams & Carter 2009.*

There are several modes for imaging in the TEM and STEM. The most common is the bright field image that uses only the direct transmitted beam to form an image. Dark field images in both parallel and convergent beam modes are formed by selecting specific diffracted beams. Images can also be formed using amplitude contrast (mass-thickness and diffraction) or phase contrast (also called high resolution; more than one scattered beam makes up an image). For mass-thickness contrast, samples with thicker or denser areas will result in more interaction with the electron beam. For STEM image acquisition, different detectors are placed after the sample in

dedicated STEMS or after the imaging lenses in a TEM/STEM selecting different portions of the

scattered beam. Bright field images are formed using only the direct beam. Dark field images are

formed from the signal recorded by annular detectors that select the scattered beam. Z-contrast or

high angle annular dark field (HAADF) images, which are formed by using an annular dark field

detector that captures electrons scattered at high angles, are sensitive to the atomic number of the

elements.

2.4.3   Energy Dispersive X-ray spectroscopy (EDS)

Energy dispersive X-ray spectroscopy (EDS) consists of the detection of characteristic X-

rays emitted after the primary ionization of atoms due to the inelastic electron scattering. The

detector is placed as close as possible to the sample. The energy of the emitted photons varies

from a few hundred eV up to 40 keV and is specific to the energy levels involved in the XRF

processes (Botton, 2007). In order to relate XRF peak intensities to the concentrations of the

elements in the sample, several correction factors are involved including cross-sections,

fluorescence corrections, absorption in the sample and detector efficiency (Botton, 2007). In

addition to the low probability of X-ray emission for low atomic number elements and necessity

of high currents, the EDS detectors are generally rather inefficient due to a small solid collection

angle. Typical EDS detectors collect only~1% of the total emitted X-rays (Botton, 2007).

However, recent technical advancements have dramatically improved the efficiency of the XRF

detectors by increasing the detector solid angle. The ChemiSTEM Super-X^{TM} is a state-of-the-art

EDS detector with improved X-ray collection efficiency by Field Electron and Ion Company

(FEI) (Schlossmacher, Klenov, Freitag, von Harrach, & Steinbach, 2010). It has four windowless

silicon drift detectors (SDDs) symmetrically arranged about the sample which provides a solid

angle of 0.9 sr, as shown in **Figure 2.11** (Schlossmacher et al., 2010). In an SDD, the incoming

X-rays generate electron hole pairs, which are separated and collected as a pulsed current, where

each pulse is associated with a single X-ray. The number of electron hole pairs is proportional to

the X-ray energy, and thus the spectrum of fluorescence X-rays is measured with modest energy

resolution, typically ranging from ~70 eV at the C Kα line (270 eV) to ~130 eV at the Mn Ka

line (5.9 keV) (Williams & Carter, 2009). The windowless feature means that there is a higher

efficiency of collection of low energy X-rays, but at the risk of detector contamination (Botton,

2007). Due to the modest energy resolution of SDD detectors (Williams & Carter, 2009), EDS is

sensitive to different elements but not to systems with the same composition but different

electronic structure, like XAS and EELS are able to differentiate.
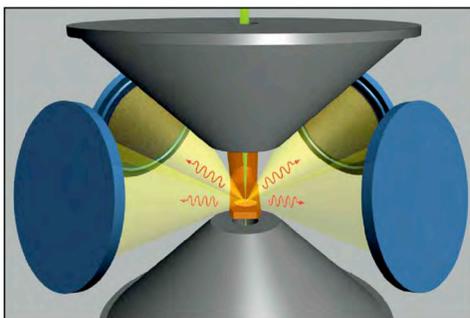
Figure 2.11 ChemiSTEM^{TM} schematic including the incident electron beam upon a sample with generation of X-rays. The Super-X^{TM} design includes the four SSD detectors symmetrically placed facing the sample (*Reprinted with permission John Wiley & Son Ltd. 2010 from Schlossmacher et al, 2010*).

2.5   Sample preparation methods

2.5.1   Ultramicrotomy

Ultramicrotomy is a method to prepare thin slices (sections) (to a nominal ~ 100 nm) of a sample for transmission microscopy, as depicted in **Figure 2.12**. The sample is usually embedded in an epoxy resin. The sample block is held and moved in a circular motion with a very slow advance. Sections are generated on the down stoke when the sample passes over the edge of a diamond knife. Usually the sections are deposited on a water bath and are then transferred on to TEM Cu grids or SiNx windows.
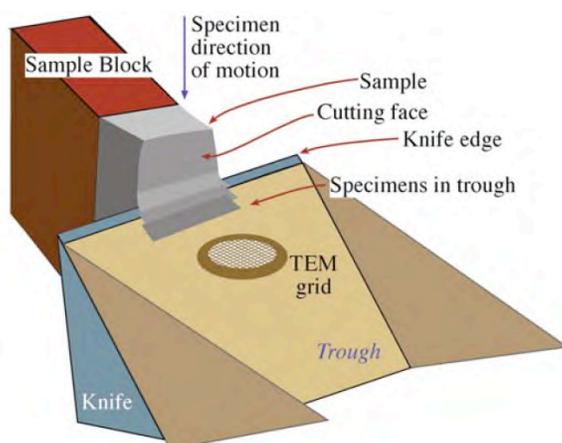
Figure 2.12 In ultramicrotomy, the polymer sample is embedded in a resin (sample block) which is consistently moved in the vertical direction towards the knife, resulting in thin slices in the trough (© *Springer Science Business Media from Williams & Carter 2009*).

2.5.2   Spin coating

Spin-coating consists of the formation of uniform thin films by spreading a solution on to a substrate as the substrate is rotated at high speed. The angular velocity of the rotating disk, concentration and viscosity of the solution all affect the uniformity and thickness of the film

(Norrman, Ghanbari-Siahkali, & Larsen, 2005). The rate of radial flow of the solution is determined by the interplay of the adhesion of the solution to the substrate and the centrifugal forces from the rotating disk (Norrman et al., 2005). As the solution spreads, the solvent evaporates. Most of the solution flies off the substrate leaving behind a thin solid film.

2.5.3   *Focused ion beam milling*

The focused ion beam (FIB) instrument is usually equipped with a scanning electron microscope, which is used to image during FIB milling. The FIB usually uses of a liquid metal ion source. The most commonly used ion is Ga^+ due to the low melting point of Ga (Giannuzzi & Stevie, 1999). The Ga^+ beam can be focused easily. A thin lamella is created by using the Ga^+ ion beam to remove unwanted parts of the sample. Radiation damage by the ion beam, and Ga implantation are frequently encountered (Giannuzzi & Stevie, 1999). The lamella is lifted out from the sample and deposited on a TEM grid typically using W as an adhesive between the lamella and the grid.

Chapter 3

Experimental procedures

This chapter describes thin film fabrication using spin coating. Solution composition and spin coating conditions are correlated with film thickness. The electron beam dose using the PMMA positive to negative crossover transition after development are described. Methods used to calibrate X-ray detector efficiency and a detailed description is given of the methods developed for optimization of dose evaluation and damage quantification using STXM. The methods used to interpret the results in terms of kinetic models are outlined.

3.1   Samples

Table 3.1 lists all of the samples, including PFSA and cathode catalyst layer samples and other polymers, used in this thesis. The sample preparation method used for each is indicated. The chemical structures of the fluoropolymers are shown in **Figure 3.1**. PFSA samples are characterized by their equivalent weight (EW), defined as "number of grams of dry material per mole of sulfonic acid groups when in acid form" (Mauritz & Moore, 2004). PFSA materials can be purchased in two forms: solid 'membranes' or liquid 'dispersions'.

PFSA is a commercially sourced Nafion^{TM} D521 (EW=1100, Ion Power Inc.) 5% alcohol-based dispersion. The solvent consists of 45±3 wt% water, 48±3 wt% 1-propanol, <4 wt% ethanol, <1 wt% mixed ethers. The samples were prepared by diluting the commercial dispersion to 2-4 wt% solutions using isopropanol (IPA) (99.5%, Caledon Laboratory Chemicals). After

dilution, the solutions were sonicated at room temperature (RT) for 5 mins. Polytetrafluoroethylene (PTFE) 60 wt% (25-43% of H_2O and 2-10% of Poly(oxy-1,2-ethanediyl, α-[3,5-dimethyl-1-(2-methylpropyl)hexyl]-ω]hydroxyl) was diluted to 2 wt% solutions with HPLC grade water and sonicated for 5 mins. The solutions were spin coated on cleaved mica using 1000 rpm/30 s. PTFE films were vacuum annealed at 190 °C for 2h to help form uniform films.

A small piece of Teflon®AF was cleaned with IPA and acetone and embedded in high molecular weight polystyrene (PS) for microtomy (Susac et al., 2011). Poly(methyl methacrylate) (PMMA) was dissolved in toluene (99.5%, Anachemia) to form 1.5-3 wt% solutions. The PMMA solution was ultrasonicated at 50 °C for 15 min to ensure complete dissolution (Evchuk, Musii, Makitra, & Pristanskii, 2005). The PMMA films were used in three Chapters of this thesis. In Chapter 4, different film thicknesses were prepared for correlating thicknesses measured by STXM and UV spectral reflectance (UV-SR). In Chapter 5, ~50 nm thick PMMA films were used for detector efficiency determination of the STXM microscopes (see **section 3.2.4.1**). In Chapter 6, 50 nm PMMA films were used to calibrate the electron dose (see **section 3.2.4.2**). After irradiation with X-rays (for STXM detector efficiency) and electrons (for dose correlation), the PMMA films were developed using 4-methyl-2-pentanone (MIBK, >98.5 wt% ACS reagent grade, Sigma-Aldrich) and IPA. For the STXM detector efficiency determination, the PMMA film on the SiNx window was developed by gentle stirring for 30 sec in a 3:1 MIBK: IPA mix followed by rinsing for 15 sec in pure IPA, at RT. This procedure was the same as previously described (Leontowich et al., 2012). For the electron dose calibration, the PMMA was developed

by gentle stirring for 3-5 sec in a 5:1 MIBK: IPA mix followed by immediate rinsing for 3-5 sec

in pure IPA, at RT.

The catalyst coated membrane (CCM) sample used in Chapter 8 (see **section 8.3.3**)

consisted of a commercial sample from Gore. The cathode layer of thickness ~13 um had Pt

loading of 0.4 mg/cm^2 on a low surface area graphitic carbon support. The layer was fabricated

by a Gore proprietary coating method on an 18 μm thick Gore-SELECT® ePTFE micro-

reinforced membrane.

Table 3.1 List of polymer and PEM-FC CCM samples used in this thesis and preparation method.

Sample	MW or EW (source)	Preparation method	Substrate	Comment
Nafion117	1100 (Sigma-Aldrich)	Embedded with TTE + microtomed	Formvar coated Cu grids	Chapter 5; *
Aquivion	870 (Solvay, Italy)	Embedded with TTE + microtomed/ Sucrose + cryo ultramicrotome	Formvar coated Cu grids	Chapter 5; *
Nafion®D521	1100 (Ion Power Inc.)	Diluted with IPA + spin coated	Cu grids and SiNx windows	Chapter 5 and 6
Liquion	1100 (Ion Power Inc.)	Diluted with IPA + spin coated	SiNx windows	-
PTFE 60 wt % dispersion	(Sigma Aldrich)	Diluted with H$_2$O + spin coated	SiNx windows	Chapter 5
Teflon®AF	Chemours, DuPont	Embedded with PS + microtomed	SiNx windows	Chapter 5
Poly(methy methacrylate)	120 kD (Sigma-Aldrich)	Diluted with Toluene + spin coated	SiNx windows, Si frames	Chapter 3, 4, 6
Polystyrene (PS)	300 kD (Polymer Source Inc.)	Diluted with Toluene + spin coated	SiNx windows, Si frames	Chapter 4
Decal (Aquivion®)	790 (AFCC)	Embedded with TTE + microtomed	Cu grids	Chapter 7
CCM (Gore)	Gore	Embedded with TTE + microtomed	Formvar coated Cu grids	Chapter 8

* films were washed in 3 wt% H$_2$O$_2$ for 1h at 90 ° C, then 1hr with deionized water, 1 hr with 0.5M H$_2$SO$_4$ solution, then deionized water until constant pH. Samples were dried in vacuum over at 80 ° C for 24 hrs (samples were pre-treated by PhD student Blossom Yan).

TTE is an amine epoxy resin, prepared by mixing trimethylolpropane triglycidyl ether and 4,4-methylenebis(2-methylcyclohexylamine) in a 1:1 weight ratio and cured at 50 °C overnight (Li & Stöver, 2010).
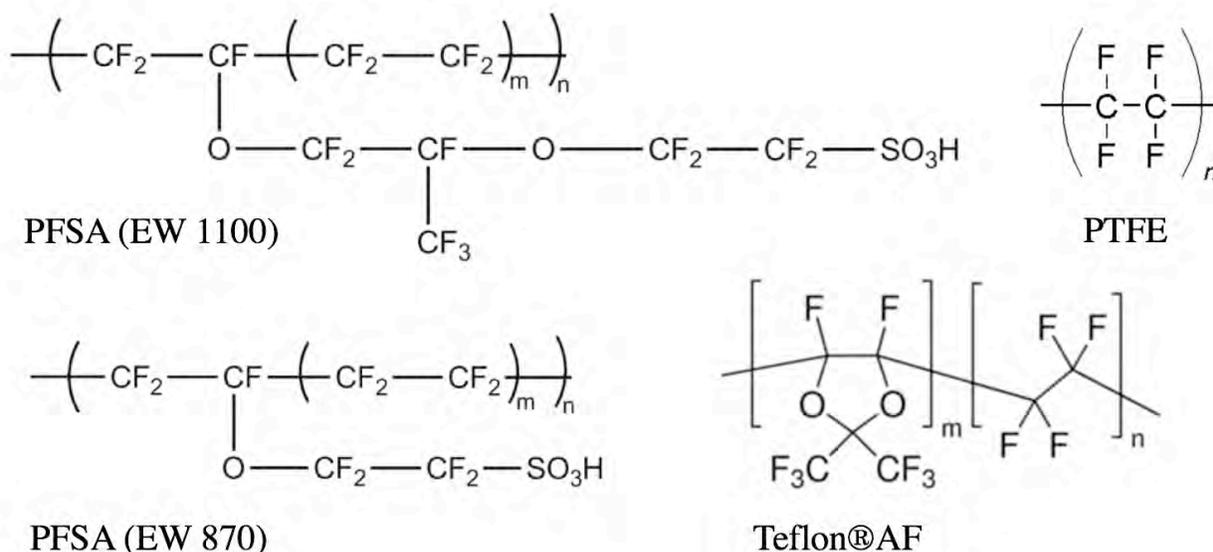
Figure 3.1 Molecular structure of several perfluorosulfonic acids (PFSA), polytetrafluoroethylene (PTFE) and Teflon®AF used in this thesis. The value of m for PFSA (EW 1100) is 6.5, and m for PFSA(EW 870) is 6 (Yan et al., 2018).

3.1.1 Examination of purity of solid and dispersed PFSA used in this thesis

The purity of each PFSA ionomer material was evaluated with STXM and Solid State Nuclear Magnetic Resonance (SSNMR). The Nafion117 and PFSA dispersions, both with EW of 1100, were compared using NEXAFS spectra at several edges in **Figure 3.2**. Both samples have nearly identical quantitative spectra, also called OD1 in OD/nm units (see **section 3.2.3.1** for derivation of the OD1 spectra). The calculated chemical structure for PFSA of EW1100 is $C_{20}F_{39}O_5SH$ (Mauritz & Moore, 2004). However, the elemental function of this chemical structure was not a good match for the materials (see **section 3.2.3.1**). The OD1 spectra are plotted with the elemental response of a deduced empirical chemical structure for PFSA: $C_{20}F_{39}O_8N_3S_5H$, with density of 2 g.cm^{-3}. These materials, including the Liquion^{TM} dispersions, were further studied with ^{13}C SSNMR spectroscopy, which detected residual solvents in all casted films (Yan et al.,

2018). At the C 1s NEXAFS spectrum, there is a notable difference for the peak at 289 eV, which was attributed to terminal -COOH groups due to the polymer manufacturing (Yan et al., 2018). Chemical shifts associated with the carbonyl groups were detected with ^{13}C SSNMR for the PFSA membrane and ionomer materials (Yan et al., 2018). The larger signal at 289 eV for the membrane compared to the spin coated material (**Figure 3.2a**) suggests that there are more terminal COOH in the membrane. These samples had different sample preparation. The Nafion117 was thoroughly washed: in 3 wt% H_2O_2 for 1h at 90 °C, 1hr with deionized water, 1 hr with 0.5M H_2SO_4 solution, then deionized water until constant pH was reached (Yan et al., 2018). The samples were dried in vacuum oven at 80 °C for 24 hrs and then microtomed (Yan et al., 2018). On the other hand, the PFSA dispersion (Dupont D521 5 wt % diluted to 3 wt % with IPA) was spun coat and was not washed or treated. Despite the drastically different preparation, the membrane and PFSA spin coated films have very similar O 1s spectra (**Figure 3.2b**).

The ideal sample for quantitative dose-damage measurements consists of large areas (at least 10 μm x 10 μm) of uniform thickness of a pure polymeric material. The uniformity of the thin film depends on the sample preparation method. Earlier spectroscopy and some dose-damage studies used ultramicrotomed membrane electrode assemblies (MEA) and ultramicrotomed membranes (Yan et al., 2018). However, it is extremely difficult to generate a film with 10 μm x 10 μm areas of uniform thickness or larger by ultramicrotome sectioning of a PFSA extruded membrane - see Fig. 1 of Yan et al. 2018. Therefore, PFSA films for dose-damage studies were prepared via spin-coating of diluted ionomer dispersions.
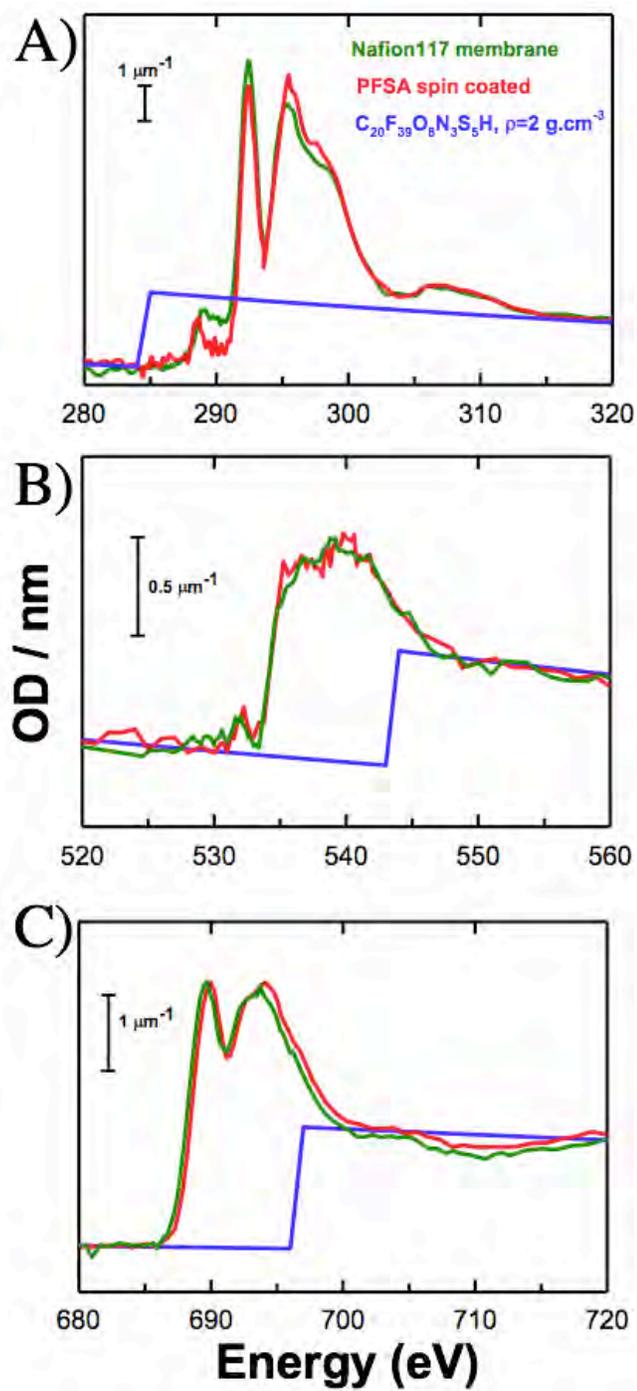
Figure 3.2 Quantitative STXM NEXAFS spectra at the (**A**) C 1s, (**B**) O 1s and (**C**) F 1s edges of a Nafion117 microtomed sample and PFSA spin coated dispersion.

3.1.2   Spin coating

PFSA, PS, PMMA and PTFE solutions were diluted and spin coated on mica. The mica was cut into ~1 cm^2 squares. Each square was only used once. The mica was cleaved by pressing it down on Scotch^{TM} tape. This step was repeated a few times until a clean mica sheet was fully detached from the tape. The diluted solutions were spin coated (6708D, Specialty Coating Systems) on the cleaved mica surface using different rotation speeds (rpm) in ambient temperature and pressure conditions. Using a clean blade, ~1 mm^2 squares were gently drawn on the film surface. Using tweezers, the mica was inserted at a 45° angle into the surface of distilled water to float the film squares (Leontowich, 2012). The water surface was first cleaned by passing lens paper over it. The films were then transferred from the water surface on to a SiNx windows or a bare Cu grid with the aid of an eyelash stick, working under a stereo optical microscope (Leica model EZ4W; 8-35x magnification). The eyelash stick was prepared by using candle wax to glue an eyelash on a thin wooden stick (2-3 mm diameter). The window or grid was pushed down perpendicular to the water surface and the eyelash was used to guide the films onto the substrate. Care was taken to position the film such that part of the substrate was uncovered, to act as I_0 for STXM measurements.

Several substrates were used in this thesis research as outlined in **Table 3.2**. Thin SiNx windows (100 μm frame and 50 nm SiNx) were used for some of the work in this thesis but these were very fragile and sometimes did not survive the trip from the sample preparation at McMaster to the STXM. They are recommended only for cases when the sample is encapsulated between two SiNx windows. Hydrophilic coatings on SiNx were also attempted to facilitate film transfer from the water but there was a risk of contamination. The hydrophilic coating likely

attracted particles from the air by electrostatic attraction. PMMA was deposited on formvar coated Cu grids as an alternative to the SiNx window for detector efficiency measurements. However, the grid has to be removed from the sample holder after STXM damage pattern generation for development, and it can easily bend (see **section 3.1.6** for details on how samples were attached to the holder). **Figure 3.3** shows how the underlying substrate plays a role in the polymeric film uniformity. Optical images of a PFSA spin coated film on a SiNx substrate (**Figure 3.3a**) are compared to that of a spun cast PFSA film supported on a Cu grid (**Figure 3.3b**). It is much easier to achieve large uniform areas of polymer films on the extremely flat SiNx substrates.

Table 3.2 Substrates used for thin film sample preparation for transmission microscopy.

Substrate (Source)	Specifications	Samples	Experiments
20 nm SiNx (SiMPore)	9 holes; 3 mm circle 200 μm frame thickness	PMMA	Correlation of electron dose with PMMA positive to negative cross-over; section 3.2.4.2
Cu grid (Electron Microscopy Sciences)	200 mesh finder grids	PMMA, PFSA	TEM damage - Chapter 6
70 nm SiNx (Norcada) – 1.5 x 1.5 mm	5 mm square 200 μm frame thickness	PFSA	STXM damage – Chapter 5
70 nm SiNx (Norcada) – 0.5 x 0.5 mm	5 mm square 200 μm frame thickness	PMMA	STXM detector efficiency – section 3.2.4.1
70 nm SiNx (Norcada) – 2 x 2 mm	5 mm square 200 μm frame thickness	PFSA, PMMA, PS	Thickness determination using STXM and UV-SR – Chapter 4
Cu grid	200 mesh grids	CL	STXM and STEM-EDS damage quantification – Chapter 8
2 nm Cr + 5 nm Au 70 nm SiNx (Norcada) – 1 x 1 mm	5 mm square 200 μm frame thickness	PFSA	STXM damage – Chapter 5
Si frames (Norcada)	5 mm square	PS, PMMA, PFSA	Correlate solution concentration and spin coating conditions and film thickness (see section 3.1.3)
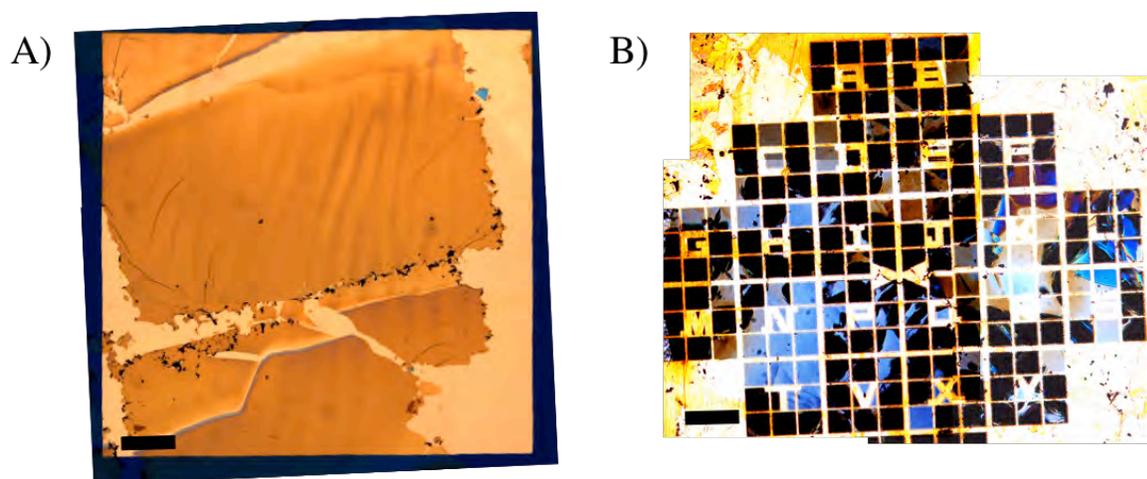
Figure 3.3 The polymer film uniformity depends on the substrate the film is deposited on. Optical microscopy images (5x objective, reflection mode) of PFSA spin-coated films deposited on a **(A)** SiNx substrate and **(B)** TEM Cu finder grid. The scale bar is 250 μm.

3.1.3   *Thickness of spin coated films*

UV spectral reflectance (UV-SR) can determine film thickness and refractive index values with a few mins of measurement time (see technique and method description in **section 4.2.2**). It is based on the interference of reflected light beam from the surface of the sample. The incident beam has wavelength in the UV and infrared regions (190-2200 nm) (Filmetrics, 2016). UV-SR thickness measurements were used to establish how the solution concentrations and rotation speeds used for spin-coating affected polymer film thickness. **Table 3.3** summarizes PMMA and PFSA film thicknesses and refractive indices determined by UV-SR for different solution concentrations and spin coating conditions. Between 5 to 10 measurements were taken for each sample by on several different areas across the 5 mm frames. With increasing solution concentration and lower rotational speeds, the thickness of the film increases. These results were used to determine the solution concentration and rotational speed that would produce a film with the desired thickness.

Table 3.3 UV-SR thickness and refractive index determination of PFSA and PMMA spin coated films (the indicated errors are the standard deviations taken from multiple measurements).

Sample	Rpm	[wt/wt %]	SiNx Refractive index	SiNx Thickness	Refractive index	Thickness (nm)
PFSA	2500	1	-	69 ± 0		34 ± 5
		2	-	-		68 ± 7
		3	-	-	1.3660 ± 0.0035	105 ± 37
		4	-	-	-	216 ± 20
	4500	1	2.2027 ± 0.0042	69 ± 0		32 ± 5
		2	2.2190 ± 0.0087	71 ± 1		54 ± 8
		3	2.2115 ± 0.0129	70 ± 1		86 ± 16
		4	2.2092 ± 0.0151	69 ± 1	1.3599 ± 0.0035	152 ± 26
PMMA	2500	1	-	-	-	41 ± 4
		2	-	-	-	60 ± 1
		3	-	-	1.4883 ± 0.0027	101 ± 33
		4	2.1898 ± 0.0035	71 ± 0	1.4720 ± 0.0050	173 ± 9
		5	2.1812 ± 0.0042	71 ± 0	1.4789 ± 0.0080	255 ± 17
	4500	1	-	-	-	34 ± 1
		1.5	2.2032 ± 0.0056	68 ± 1	-	46 ± 4
		2	2.1836 ± 0.0127	72 ± 1	-	58 ± 4
		3	2.1812 ± 0.0040	71 ± 0	1.4721 ± 0.0060	135 ± 20
		4	-	-	-	163 ± 6
		5	-	-	1.4789 ± 0.0080	241 ± 40

3.1.4   Microtomy

Samples that did not originate from dispersions were microtomed. This includes the membranes (Nafion117 and Aquivion87), Teflon®AF and all catalyst layer samples. The samples were embedded either with PS or with TTE epoxy. TTE is an amine epoxy resin, prepared by mixing trimethylolpropane triglycidyl ether and 4,4-methylenebis(2-methylcyclohexylamine) in a 1:1 weight ratio and curing at 50 °C overnight (Li & Stöver, 2010). Initially the TTE solution has

low viscosity and penetrates samples easily. In attempts to avoid penetrating catalyst layers and thus preserve the pore structure, delays prior to pushing the sample into the curing epoxy were explored without much success. Greater success was achieved by sandwiching the sample between two PS beads, previously softened by a brief exposure to toluene vapor. This 'sandwich' was then dried overnight at 60 ºC prior to microtomy. This approach was used for CL and Teflon®AF samples. The cathode catalyst layer on a decal (Teflon®AF substrate) used in Chapter 7 and the CCM used in Chapter 8 were embedded with TTE epoxy.

Using a clean blade, the bullets (embedded sample) were cut as close as possible to the polymer sample to ensure the face of the sample to be microtomed was approximately ~100-150 μm wide. This was done so that samples deposited on grids or windows had nearby areas for I_o (necessary for any STXM measurement). Due to mechanical limitations of the STXM microscope stages, it is not advised to acquire multi-region images that require the sample stage to move more than 100 μm. The sample was then ultramicrotomed to a nominal thickness of 100 nm with a diamond knife at room temperature (RT) with a Leica Ultracut UCT. The sections were transferred from a water surface to Cu/formvar, bare Cu grids or SiNx windows. All microtomed sections were prepared by Marcia West at the Faculty of Health Sciences at McMaster University.

Since dried membrane samples do not cut uniformly at room temperature (see **Figure 3.4a**), cryo microtomy was attempted on the Aquivion87 sample to improve uniformity. A sucrose solution was used to wet the sample and form an 'iced bullet', which was microtomed in cryo temperatures (-130 °C). While the cryo-cut sections (**Figure 3.4b**) are not wrinkled, they tended to be too thick.
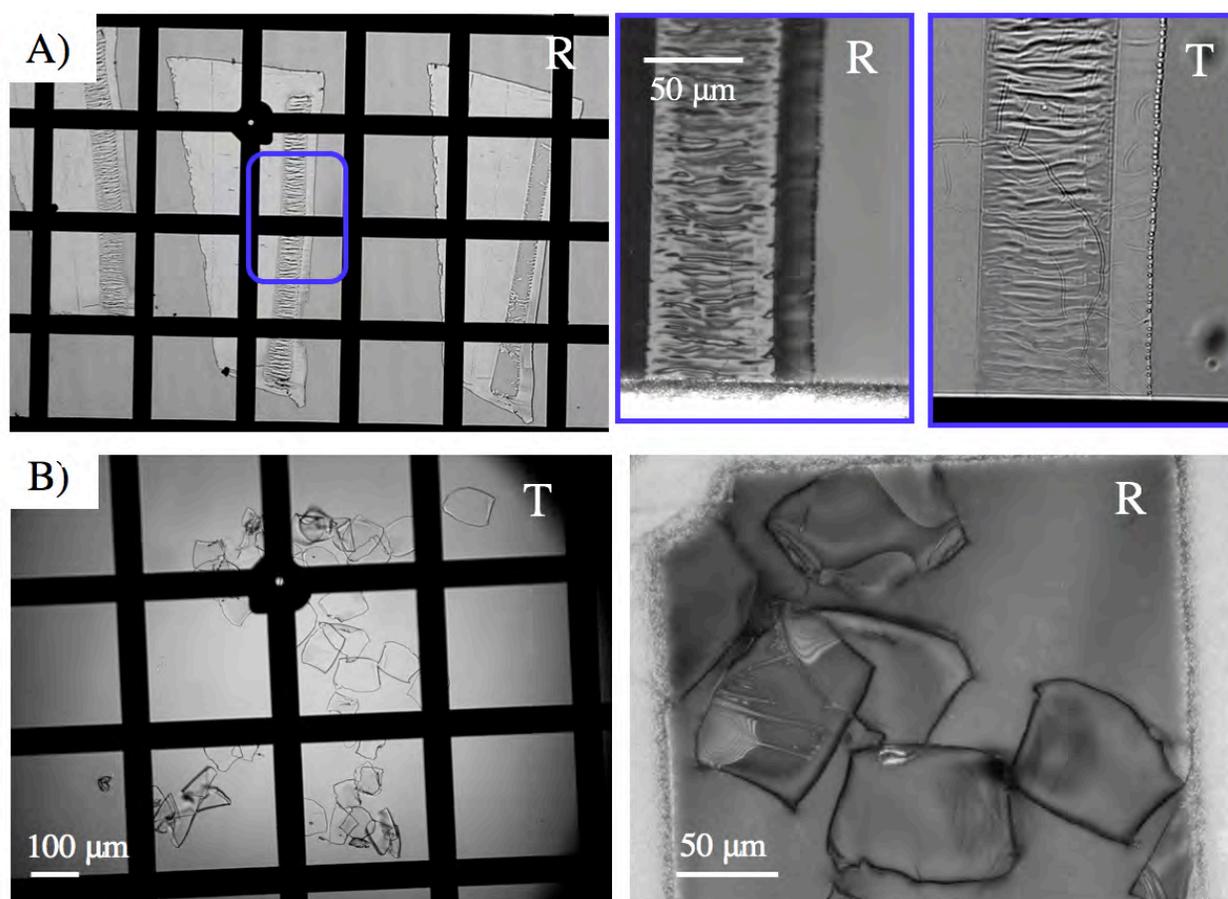
Figure 3.4 Optical images of **(A)** room and **(B)** cryo (-130 °C) temperature microtomed sections of Aquivion87, where R and T indicate reflection and transmission images.

3.1.5   Focused Ion Beam Milling

For the room temperature (RT) FIB milling (discussed in Chapter 8, **section 8.3.3**), a cross-section of the CCM sample was glued onto a 90° Al scanning electron microscope stub using double sided carbon tape. W metal was deposited on the top surface of the cathode layer using a Zeiss NVision40FIB coater. The Ga ion beam was operated at 30 KV using a 80 pA current with 10 kV, 40 pA polishing conditions. The cryo FIB sections were prepared by gluing the CCM on an Al stub with the cathode side upwards. The RT lamella was prepared by Julia Huang at the

Canadian Centre for Electron Microscopy, CCEM, at McMaster University. A FEI Helios Dual Beam FIB was used for milling with a Ga ion beam using currents between 24 pA - 21 nA and accelerating voltages of 16 and 30 kV using two steps. After the sections were thinned to ~5 μm and placed on a TEM grid, the sample was cooled to -180 °C and thinned to 300 nm and ~150 nm. The cryo-FIB sections for Chapter 7 were prepared by Ciprian Talpalaru at the 4D Lab at Simon Fraser University.

3.1.6   Sample mounting for STXM

Grid or SiNx samples are attached to standard trapezoidal Al plates by using: 1) double sided tape shown in **Figure 3.5a**; 2) epoxy glue (90 s or 5 min); or 3) by taping the grids or SiNx from the top **Figure 3.5b,c**. The Al sample support plates used at the 5.3.2.2 (ALS) and 10ID1 (CLS) beamlines usually contain 6 holes of 2.7 mm diameter. Recently rules for samples at ALS STXMs have been changed, preventing use of tape for mounting samples. Epoxy should be used instead. SiNx windows are best held to the Al plates using double sided tape or epoxy glue. However, if samples are required to be removed from the holder (i.e. developing PMMA samples for STXM detector efficiency determination) it is recommended to use option 3 (except at ALS). By gently levering a razor blade underneath the tape, the tape can be removed from the top surface of the SiNx window or grid without damage to the sample. If SiNx windows are taped to the sample holder (as shown in **Figure 3.5b**), one must ensure that the tape is properly fixed onto the sample and not sticking up. As the beam energy decreases, the focal length of the ZP decreases and samples are moved closer to the OSA. At the C 1s edge, samples are only ~ 250 μm away from the OSA. For samples placed between two SiNx windows, the thinner windows (100 instead of the 200 μm frames) should be used to reduce chances of touching the OSA.
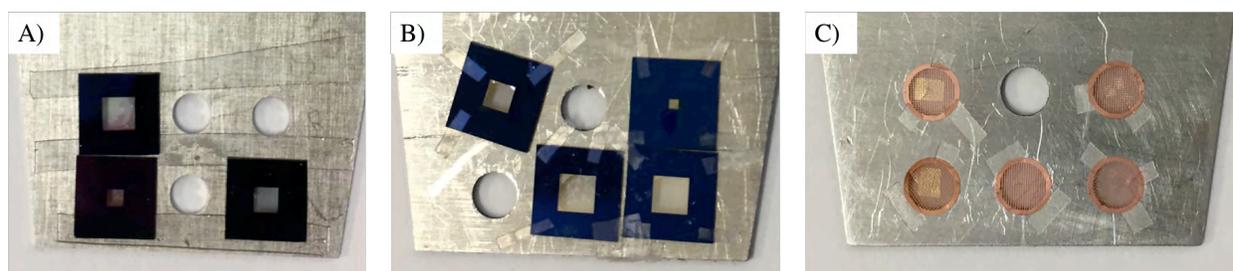
Figure 3.5 Photographs of samples mounted on Al plates for STXM analysis. SiNx windows are taped to the holder using **(A)** double sided tape and **(B)** single sided tape, similar to the Cu grids shown in **(C)**.

3.2   *Optimization of STXM & NEXAFS for dose-damage studies*

STXM data was acquired using the ambient STXM on the Canadian Light Source beamline 10ID1 (Kaznatcheev et al., 2007) and the polymer STXM on the Advanced Light Source beamline 5.3.2.2 (Warwick et al., 2002). Images and image sequences (also called stacks (Jacobsen et al., 2000)) were acquired at the C 1s, N1, O 1s, F 1s and S 2p edges. For further details please see the original interferometer STXM instrument paper (Kilcoyne et al., 2003) and reviews (Ade et al., 1995; Ade & Urquhart, 2002; A. P. Hitchcock, 2012).

3.2.1   *STXM operating procedures*

Once samples were mounted, the sample plate was loaded on to the 3-pin kinematic mount (Kilcoyne et al., 2003) in the STXM chamber. The chamber was then evacuated and backfilled with ~25 kPa He. For some experiments the STXM chamber was actively pumped and the measurements were done at a pressure of ~0.02 Pa (See Chapter 5, **section 5.3.1.5**). Higher order suppression filters were used for C 1s studies (Ti foil at CLS 10ID1 and N_2 gas at ALS 5.3.2.2). The C 1s energy scales were calibrated using the C 1s $\rightarrow$ 3s transition at 292.74 eV of CO_2 gas (Ma, Chen, Meigs, Randall, & Sette, 1991) or the C1s(C=O) $\rightarrow$ $\pi^*_{C=O}$ transition of

PMMA films at 288.45 eV (Wang et al., 2007). The O 1s energy scale was calibrated using

O1s(C=O) $\rightarrow$ $\pi^*_{C=O}$ transition of CO_2 gas at 535.4 eV (Ma et al., 1991). The F 1s energy scale

was calibrated using the F 1s $\rightarrow$ a_{1g} transition of SF_6 gas at 688.3 eV (Brion et al., 1982). At the

ALS bend magnet beamline, the light is horizontally linearly polarized. At the CLS 10ID1

beamline left circular polarized light was used. Studies with horizontal and linearly polarized

light were made occasionally. No dichroism was observed indicating samples were isotropic, and

most likely did not have any long-range order.

3.2.2   Generation of X-ray damage

There are many factors to consider when generating radiation damage with STXM. These

include sample, support, beam energy, chamber environment, size of exposed area, beam spot

size and shape (discussed in **section 2.2.3**), pixel spacing, and the method of generating the

damage pattern. In addition to sample uniformity, it is crucial that the incident beam is perfectly

focused on the sample since this affects the dose calculations. If a proper focus was not achieved,

the patterns were blurry and were not used to calculate damage-dose relationships. Optimal focus

is achieved by focusing on a high contrast feature, typically a dirt particle from the sample

preparation, which should be less than 10 μm away from the pattern area (Leontowich et al.,

2012). Areas near the edge of the film were preferred as this typically allows an I_o region

(through the substrate) to be included in post-damage analytical imaging.

In this work radiation damage was created using photon energies (E_D) in the C 1s (320

eV) or F 1s (710 eV) ionization continua. This choice was made so that absorption occurs at all

atoms of the given element and also because, in the continuum, the exact energy is not critical

(within 1 eV) whereas using photon energies at sharp peaks require an energy scale that is known and stable to within 0.1 eV.

The pattern generation (Pattern Gen) routine in *STXM_Control* (Tyliszczak & Hitchcock, 2000) was used to irradiate the sample for variable dwell times in a 3 x 3, 9-pad array of square pads, with each pad having 10 x 10 exposure points (Wang, 2008; Wang, Morin, et al., 2009; Leontowich et al., 2012). The pixel spacing, which is set by the (.xyt) pattern file or user (for imaging) independently from the beam diameter, is the distance between the center of two adjacent positions of the beam on the sample. The pixel spacing determines the total size of each pad. The beam defocus was adjusted to the same value as the pixel spacing so that the full area of the pad was illuminated without overlap. If the beam defocus is not set, then the pixel spacing is larger than the beam diameter and the pad would be under-illuminated. **Figure 3.6** compares the change in OD (measured with STXM) and thickness (measured with Atomic Force Microscopy, AFM) of two adjacent 9-pads damaged at E_D=320 eV in a PFSA sample. In **(a)** the beam was defocused and in **(b)** the beam was not defocused (beam diameter, S, is 30 nm and pixel spacing, PX, is 120 nm). The overall thinning of the material measured (see **Figure 3.6f**) by STXM and AFM was similar despite differences of doses up to 13% (due to different Io).

Three pixel spacings - 50, 60, 120 and 180 nm - were used to generate squares with widths of 2000, 600, 1200 and 1800 nm, respectively, in this thesis. **Table 3.4** lists the pad sizes/defocus used in this work. Larger pads were used to allow more accurate analysis by measuring stacks with more pixels and with defocused spots to minimize additional damage. The downside is that these pads take much longer to generate and a lower dose range was selected to

accommodate. The dose is proportional to the area of the beam spot and thus decreases by one

order of magnitude when the beam diameter increases by a factor of 3.
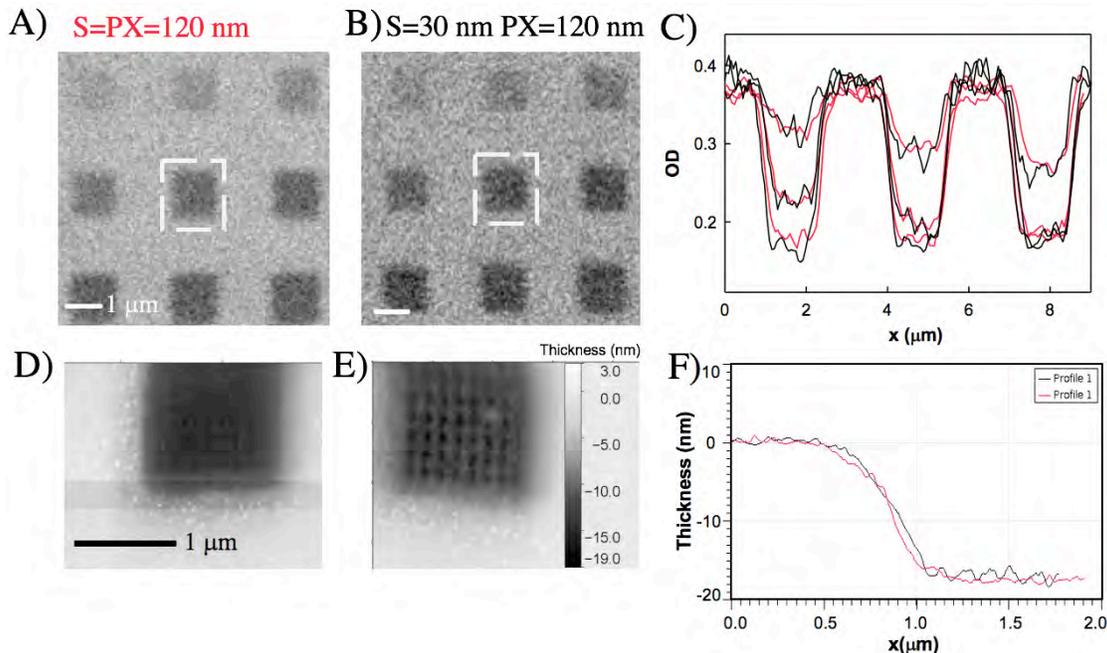
Figure 3.6 Adjacent 9-pad burns (damaged using E_D=320 eV soft X-rays) on a PFSA sample. Similar I_0 was used such that corresponding pads in both areas received a similar dose (with a difference of up to 13%). **(A)** and **(C)** are STXM images at 292.4 eV for 9-pad burns using 120 pixel spacing (PX), with defocus (S) set to 120 nm and with no defocus, respectively. **(C)** STXM image line profiles of each row in (a) and (b), where the black lines correspond to PX=S and red lines correspond to S=30 nm and PX=120 nm. **(D), (E)** and **(F)** are the AFM images and line profiles of the middle pad (indicated in (A) and (B)).

Table 3.4 Pixel spacings and defocus used for pattern generation in this work.

Pixel spacing/Defocus (nm)	Sample		
	PFSA	**PTFE/Teflon AF ®**	**Catalyst layer**
50	-	-	Qualitative spectral changes – see Chapter 7
60*	Single edge critical dose determination	Multi- edge critical dose determination	
120*	Multi-edge critical dose determination	Multi-edge stacks	
180	Multi-edge stacks	-	

*defocus setting is not as important for small defocus due to the large depth of focus/damage spread of PFSA

Defocusing can be achieved in several ways. Setting a specific defocus is only possible if best focus is first achieved. Once the A_0 was set to achieve a sharp focus, a specific spot size or beam diameter (S) can be achieved by changing the A_0 value by δA_0, which changes the ZP-z position by the same amount, thus defocusing the beam in a precise manner (see equation 2.11 in section 2.2.3). The Pattern Gen routine of *STXM_Control* does not provide the capability to adjust A_0 and thus the beam spot size. Therefore, the beam diameter was set (after ensuring the reference A_0 value was that of best focus) by adding the δA_0 value calculated. Since the ZP-z position (as defined by an A_0 value) tracks the photon energy automatically, after changing the A_0 value, the energy must be set to move the ZP the appropriate distance. The beam diameter and the pixel size were always set to the same value. The beam diameter can be verified with SEM (Leontowich, 2012) and AFM (Leontowich, Tyliszczak, & Hitchcock, 2011) images and also with STXM images (but with lower spatial resolution).

The 9-pad exposures are extremely useful to study dose-damage relationships as they cover a wide range of doses within a small area (between 5x5 and 15x15 μm^2), which facilitates spectral imaging and subsequent quantitative dose-damage analysis. 9-pad patterns with both linear and non-linear dwell time variation were used (see **Figure 3.7**). The non-linear patterns (**Figure 3.7a,b**) have dwell parameters which range from 0.025 to 1.0 ms which are then multiplied by a common factor to adjust the dose to the range of interest. The linear 9-pad pattern (**Figure 3.7c,d**) was used for detector efficiency determination.
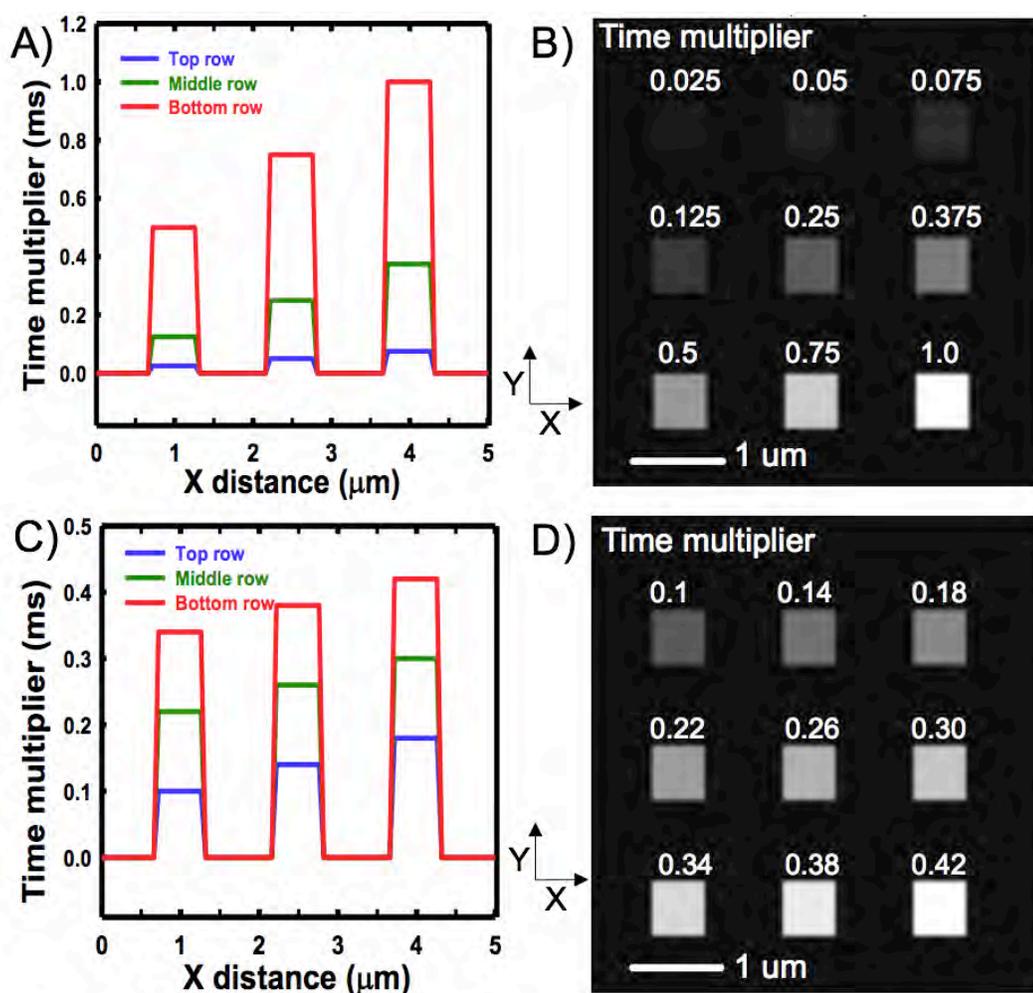
Figure 3.7 Non-linear (a,b) and linear (c,d) time multiplier used in the templates to generate damage. **(A)** shows a plot of the non-linear time multiplier in each pad as function of the X distance of the image shown in **(B)**. **(C)** shows a plot of the linear time multiplier in each pad as function of the X distance of the image shown in **(D)**.

3.2.3 Dose evaluation

3.2.3.1 Soft X-ray irradiation

The following data, which are required for dose determination, must be recorded during the STXM measurements: (i) a pre-damage image at the damage energy (E_D) to determine the OD and thus the sample thickness (if necessary, this can be used to normalize non-uniform

thicknesses in the region of the damage pad, which was done in several cases of membrane studies), (ii) incident flux through a hole (neither sample nor support present in the path), (iii) I_0 for spectroscopy (signal through the support, but not the PFSA film); and, (iv) after the damage one or more images, depending on the approach used for analysis (see **section 3.3.2**).

Dose is energy / mass, in units of Gy = 1 J/kg. The energy absorbed into a given volume of sample is related to the photon energy (E), the *OD(E)* of the material, and the length of time (t, in s) the X-rays hit the sample. The mass (m, in kg) of the material damaged is determined by the thickness of the sample (h, in nm), the incident beam area (S, in m^2), and the density of the sample (ρ, in kg.m^{-3}). The integrated dose derived from first principles, is:

$$D = \int_0^t \frac{F(t)E}{Km(t)} dt \qquad \text{Equation 3.1}$$

where K is the detector efficiency and F(t) is the instantaneous absorbed flux in MHz given by (Wang, Morin, et al., 2009):

$$F(t) = I_o - I = I_o (1\text{-e}^{-OD(E,t)}) \qquad \text{Equation 3.2}$$

where E is the photon energy, t, is time, I_o is the incident photon flux and OD is the optical density of the area at the time of exposure. The I_o is usually measured through a hole in the aluminum sample support plate or by moving the sample stage to x > 11000 μm. At the ALS and CLS during the period of these measurements, the detector became non-linear at flux levels above 10 MHz so the slits were always set so that I_o was less than 10 MHz. This is actually seen as 1 MHz on the chart mode of *STXM_Control* when the PMT/10 button is turned ON as was the case in this work. Note that early in my studies I was not aware of the x1 /10 button on the STXM_Control panel, and thus unintentionally reported critical doses for PFSA a factor of 10 too low (Melo, Botton, & Hitchcock, 2015).

Note that the total exposed area (i.e. total area of the pad) does not matter since the dose is calculated **per unit** mass or **per incident interaction mass** as defined by the beam diameter, sample thickness at the interaction area and the sample density. The irradiated mass depends on the volume and density of the material. Here an important assumption is made: the density is assumed to be constant despite the radiation damage. Electron irradiation of PTFE under several conditions (including a vacuum of 1.3×10^{-2} Pa) increases its crystallinity to some degree, which increases the density of the polymer (Fisher & Corelli, 1981). A value of 2 g/cm^3 was used for both PTFE (Gierke & Hsu, 1982; Rae & Dattelbaum, 2004) and Teflon®AF. The density of PFSA materials depend on the EW and history of material (including manufacturing conditions, sample storage and sample fabrication). In this work, a density of 2 g/cm^3 was always used (Takamatsu & Eisenberg, 1979; Zook & Leddy, 1996).

For this dose calculation, the incident area of the shape of the beam is considered to be a circle (Leontowich et al., 2011) although an annulus should be used for beam diameters larger than the calculated depth of focus, which depends on incident photon energy and the ZP properties, as discussed in Chapter 2. Equation 3.1 can be rewritten as:

$$D = \int_0^t \frac{I_o\left[1 - e^{-OD(E,t)}\right]E}{K \cdot \pi \cdot \left(\frac{S}{2}\right)^2 \cdot h \cdot \rho} dt \qquad \text{Equation 3.3}$$

The OD(E) spectrum of a pure material is directly proportional to the thickness of the material and the OD1(E) spectrum:

$$OD(E) = OD1(E)\, h \qquad \text{Equation 3.4}$$

The OD1 spectrum depends on the elemental composition (chemical formula) and density of the material (Hitchcock, 2012). The OD1 spectrum for a given edge of a compound can be generated by:

1) measuring the spectrum of the pure compound, *OD(E)*

2) calculating the SF-OD1(E) spectrum for the composition of the compound from tabulated mass absorption coefficients, μ (Henke, Gullikson, & Davis, 1993), and the material density.

3) dividing *OD(E)* by *SF-OD1(E)*. The ratio in the energy ranges below the onset of the edge (<10 eV of the onset), and far above the onset of the edge (>30 eV), give *h*, the thickness of the compound in the region measured (illustrated in **Figure 3.8a** for PFSA and two *SF-OD1(E)*).

4) Dividing *OD(E)*/*h* gives the OD1 spectrum of the compound, which is the spectral response for 1 nm of the compound at its standard density.

Given a chemical formula for the material, μ is the sum of the weighted atomic photoabsorption coefficients (Henke et al., 1993):

$$\mu = \frac{N_A}{M} \sum x_i \sigma_{ai}$$

Equation 3.5

where N_A is Avogadro's constant, M is the molecular weight of the material that contains x atoms of each element i, and σ_a is the mass absorption coefficient of x in element i. The σ_a values are experimentally determined and values are tabulated (Henke et al., 1993). The elemental mass absorption coefficient values are accurate in the pre-edge region (10 eV below the edge and lower) and at high energy in the post edge continuum region (>30 eV above the onset). Ideally, *OD(E)* spectra with long energy ranges should be used for OD1 conversion (20-30 eV pre-edge and extending up to 60 eV above the onset, sampled coarsely).

In some cases, the chemical formula may be not known or is not well-defined. In such cases, if multiple edges are measured, it is possible to estimate the composition from spectra of the same region measured at each edge of elements in the sample. In cases of spectral impurity, it is best to treat each edge separately. If not, all edges should be treated together. This requires multiple stacks from the exact same region (in order to facilitate appending stacks from different edges, all stack acquisition parameters should be the same, including the pixel spacing). The latter option was used in this work to estimate the composition of PFSA and heavily damaged PFSA. The procedure used consisted of:

1) appending stacks of each edge from the same region to construct a stack where each pixel contains multiple spectroscopic edges;

2) dividing the spectrum by an estimated elemental function and density of the material (SF-OD1)

3) adjust the elemental function until the ratio of the $OD(E)$ by SF-$OD1(E)$ at energy ranges below and far above the onset of the edge result in one consistent number (h), which is the sample thickness.

This is illustrated in **Figure 3.8a**, where the spectrum of a PFSA sample was divided by an elemental function SF-OD1$_{PFSA1100}$ considering the chemical formula of $C_{20}F_{39}O_5SH$ (green in **Figure 3.8a**) for PFSA with EW=1100 (Mauritz & Moore, 2004). The pre and post edge of the O 1s signal and pre edge of the F 1s for the ratio of the OD/ SF-OD1$_{PFSA1100}$ were above the threshold (dotted line) for the C 1s. This can be interpreted as the material having more oxygen or other lower atomic weight elements. Therefore, the chemical formula was adjusted until a similar threshold value was reached for all pre and post edges. A new chemical formula $C_{20}F_{39}O_8N_3SH$

was generated - called SF-OD1$_{PFSA}$. The ratio of the same PFSA OD spectrum to SF-OD1$_{PFSA}$ is in

red in **Figure 3.8a.** In this case, all pre and post edges align to a similar value of ~ 80 nm,

indicating that the generated elemental function was satisfactory (i.e. correct chemical formula).

The OD1 spectrum was derived by dividing the raw spectrum by the number 80. **Figure 3.8b,c,d**

illustrate the OD1 spectra at the C 1s, O 1s and F 1 of PFSA compared to the SF-OD1$_{PFSA1100}$ and

SF-OD1$_{PFSA}$. At the C1 s edge, there is very little difference between the OD1 spectrum and the

two SF (**Figure 3.8b**). At the F 1s edge, the pre-edge of the SF-OD1$_{PFSA1100}$ is lower than that for

the new SF (**Figure 3.8d**). A dramatic difference is seen at the O 1s edge (**Figure 3.8c**) – the SF-

OD1$_{PFSA1100}$ has a lower pre-edge and post edge compared to the new SF and the OD1 spectrum of

PFSA. If the SF-OD1 has a lower post-edge compared to the OD1 spectrum, this indicates that it

is underestimating the elemental content. A lower pre-edge can mean it is underestimating an

element with an absorption egde at lower energies. Since there is a good match at the C 1s edge,

this is indicative that there is an additional element in the material: nitrogen.

   As discussed in Yan et al. 2018, the NEXAFS C 1s and O 1s spectra of PFSA have

additional contributions of COOH groups, most likely due to terminal end groups from the

polymer synthesis. ^{13}C SSNMR also detected residual solvents in drop-casted PFSA materials

(Yan et.al., 2018). Therefore, the additional oxygen contribution to the PFSA can be due to the

COOH terminal groups due to the polymer fabrication process, and residual solvents.
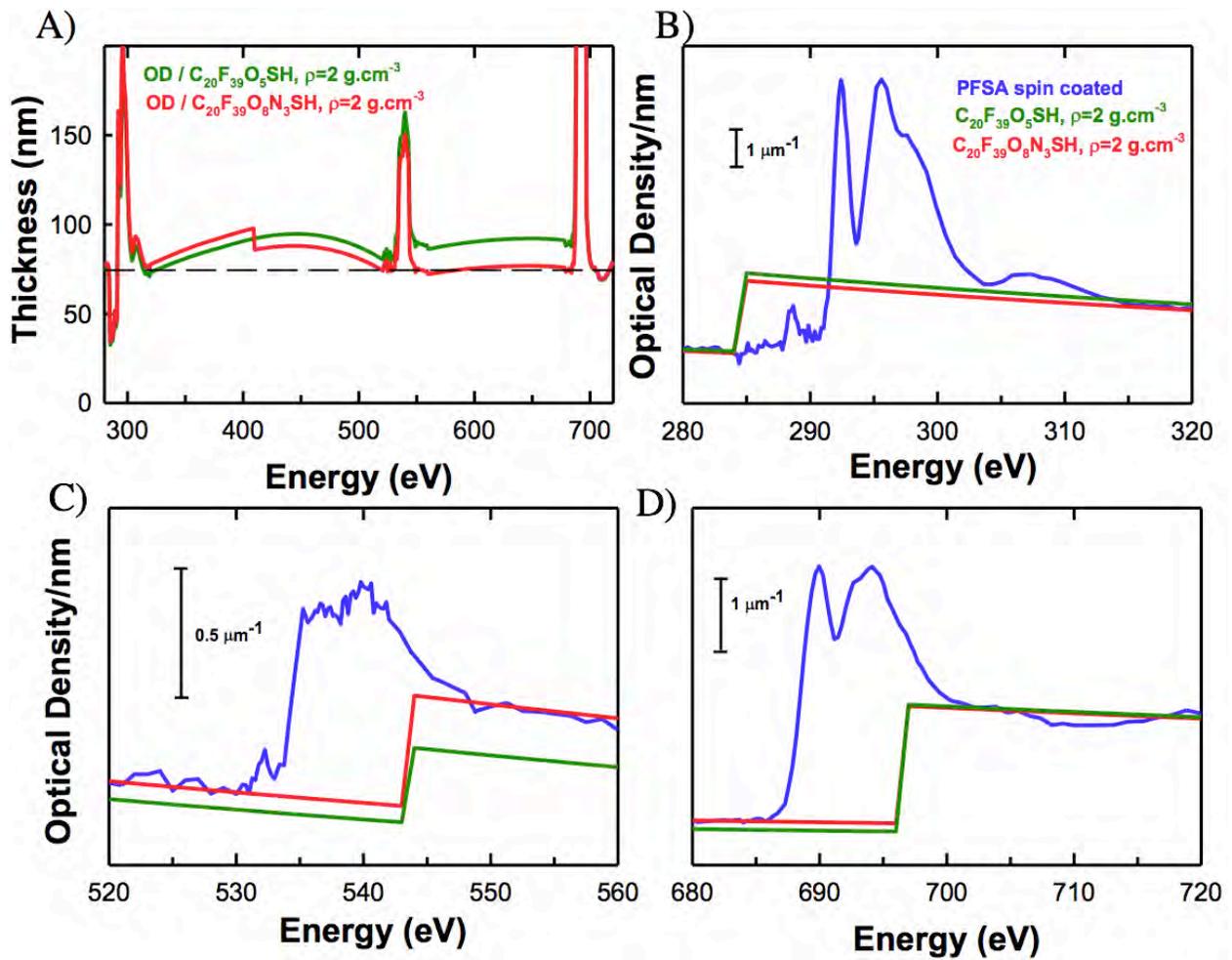
Figure 3.8 Generating the OD1 spectrum for PFSA consists of **(A)** dividing the OD spectrum by the elemental function. The OD spectrum should be divided by the thickness value the dashed line in (A) to generate the OD1 spectrum. To evaluate if the elemental function adequately describes the material, one should assess if there is a good match at the pre and post edge of the **(B)** C 1s, **(C)** O 1s and **(D)** F 1s.

The damage energies (E_D) used were 320 eV and 710 eV. Substituting **Equation 3.4** into **3.3**:

$$D = \frac{4E \cdot OD1 \cdot Io}{K \cdot \pi \cdot S^2 \cdot \rho} \int_0^t \frac{\left[1 - e^{-OD(E,t)}\right]}{OD(E,t)} dt \qquad \text{Equation 3.6}$$

or (including unit conversion factors):

$$D = \frac{4(E\ eV\cdot 1.6\cdot\frac{10^{-19}J}{eV})\cdot(\frac{OD1}{nm})\cdot(Io\cdot\frac{10^6}{s})}{K\ \pi\ (s\ nm)^2\rho\frac{g}{cm3}\cdot\frac{1\ kg}{1000\ g}\cdot\frac{1\ cm^3}{1E21\ nm^3}}\int_0^t \frac{1-e^{OD(E,t)}}{OD(E,t)}\,dt \qquad\text{Equation 3.7}$$

In principle, this expression must be integrated to determine the accumulated dose up to time t. This dose calculation differs from that previously used (Coffey et al., 2002; Leontowich et al., 2012; Wang, Morin, et al., 2009; Zhang et al., 1995) although it becomes the same if the OD in the numerator is integrated as an exponential function to account for the mass loss. However, in these previous papers, the OD in the denominator or the thickness change was not accounted for and resulted in underestimation of the dose. For some polymers, there is negligible thickness change with soft X-ray damage (Wang, 2008). In such cases **Equation 3.6** simplifies to:

$$D = \frac{4E\cdot OD1(E)\cdot I_0(1-e^{-OD(E)})\cdot t}{K\cdot\pi\cdot S^2\cdot\rho\cdot OD(E)} \qquad\text{Equation 3.8}$$

For samples that suffer a thickness decay due to the interaction with soft X-rays, h will change as a function of t. In such cases, the absorbed dose expression (**Equation 3.6)** requires a numerical integration between 0 and t to get D. This integration requires an explicit expression for how OD(E) changes as a function of time since h is determined from OD (**Equation 3.4**). Assuming first order kinetics (Coffey et al., 2002; Leontowich, 2013; Leontowich et al., 2012; Wang, Morin, et al., 2009; Zhang et al., 1995):

$$OD(E,t) = OD_\infty + ae^{-bt} \qquad\text{Equation 3.9}$$

where OD_∞, a and b are fitting parameters. A cumulative integration can be used to determine D up to time t. Substituting **Equation 3.9** into **Equation 3.6** gives the **Mass Loss Dose**, D_{ML}:

$$D_{ML} = \frac{4E \cdot OD1 \cdot Io}{K \cdot \pi \cdot s^2 \cdot \rho} \int_0^t \frac{\left[1 - e^{-(OD\infty + ae^{-bt})}\right]}{OD\infty + ae^{-bt}} dt \qquad \text{Equation 3.10}$$

The effect of using integration (**Equation 3.10**) relative to the non-integrated expression (**Equation 3.8**) was compared for samples where h varies as a function of the dose. 9 pad patterns were generated at 320 eV in PMMA and PFSA samples. The values used to calculate the dose are shown in **Table 3.5**. MATLAB calculations plotting the dose as a function of time are shown in **Figure 3.9** for both samples comparing the two methods to calculate dose and the method described in Wang, Morin, et al., 2009.

Table 3.5 Experimental values after 9-pad pattern generation damaged at 320 eV for calculation of dose using the integrated and non-integrated equations.

Parameter	PMMA	PFSA
OD	0.092	0.308
OD∞	0.06636	0.2028
a	0.02983	0.07056
b	7.487	2.843
Io (MHz)	6.8	4.2
h (nm)	32	100
s (nm)	120	60
ρ (g.cm^{-3})	1.18	2
E (eV)	320	320
K	0.25	0.30
Time (s)	0.25	0.25
OD1$_{320\ eV}$	0.0029	0.0027

Compared to the non-integrated expression (**Equation 3.8**), use of the explicit integral (**Equation 3.10**) changes the calculated dose by less than 5%. This is the case even in samples with very large changes in sample thickness, since, as the sample thins, the OD decreases and the numerator and denominator terms in **Equation 3.8** change at similar rates. However, this approximate cancellation is valid only for thin samples, where the OD(E_D) is less than unity.

Considering units, **Equation 3.8** can be written as:

$$D = \frac{6.4x10^5 \cdot E \cdot OD1(E) \cdot I_0 \left(1 - e^{OD(E)}\right) \cdot t}{K \cdot \pi \cdot s^2 \cdot \rho \cdot OD(E)}$$
                                                                                            Equation 3.11

where E is the incident energy (eV), Io is the incident photon flux through a hole (MHz), t is the exposure time (s), S is the spot size or beam diameter (nm), ρ is the sample density (g/cm^3), $OD1$ is in nm^{-1}, $OD(E)$ and K, the detector efficiency, are unitless. For each area exposed to X-rays, OD(E,0) was used, i.e. the value <u>before</u> damage at the exposure energy. Note that both OD1 and OD values are specific to each sample.
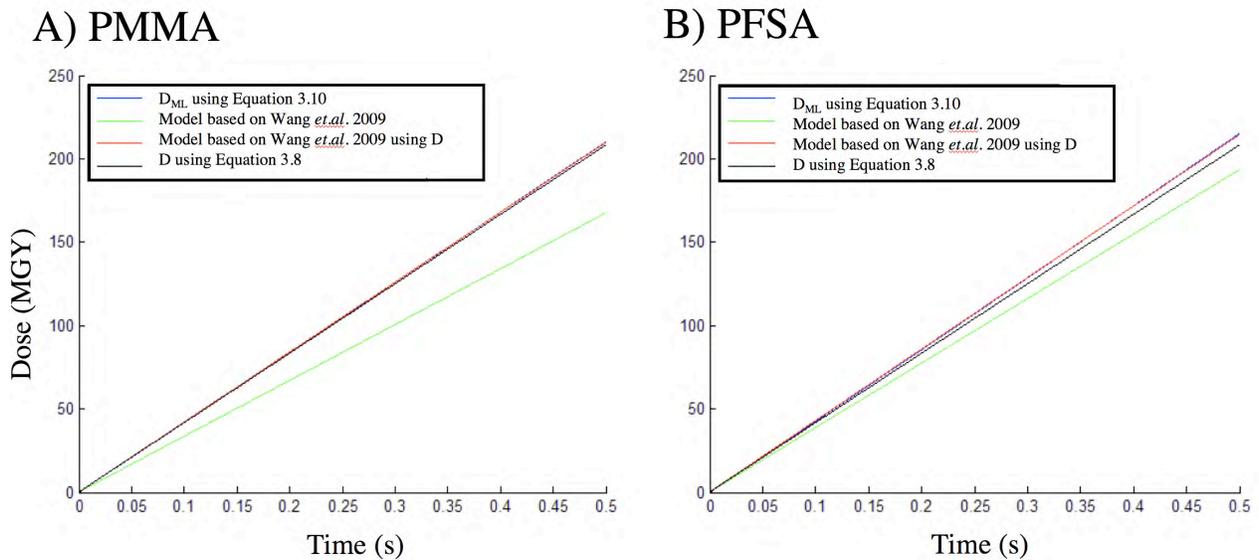
Figure 3.9 MATLAB simulations comparing dose as a function of time for **(A)** PMMA and **(B)** PFSA with values from Table 3.3. The dose was calculated using Equation 3.8, 3.10 and compared with the Wang *et.al*. 2009 method to evaluate the effect of using integration on the dose calculation.

3.2.4   PMMA development: calibration of the crossover transition

3.2.4.1   STXM Detector Efficiency

Since it is the largest source of uncertainty in determining the absorbed dose, the detector efficiency was determined regularly, ideally during each synchrotron beamtime in which STXM was used for quantitative damage versus dose studies. The efficiency of the phosphor-PMT detector was measured using the cross-over transition in PMMA lithography (Leontowich et al., 2012) using linear time templates (**Figure 3.7c,d**). The detector efficiency can be significantly different (higher or lower) when new detector coatings are applied (Kilcoyne et al., 2003). The efficiency is also sensitive to the PMT voltage and discriminator settings, which should be checked regularly to ensure the detector response is saturated. During the period of this thesis, the detector efficiency at 320 eV was 43 ± 14 % and 33 ± 14 % for the CLS and ALS microscopes, respectively (see **Figure 3.10).** The efficiency rises rapidly with photon energy to values at 710 eV of 83 ± 6 % and 77 ± 12 % for the CLS and ALS microscopes.
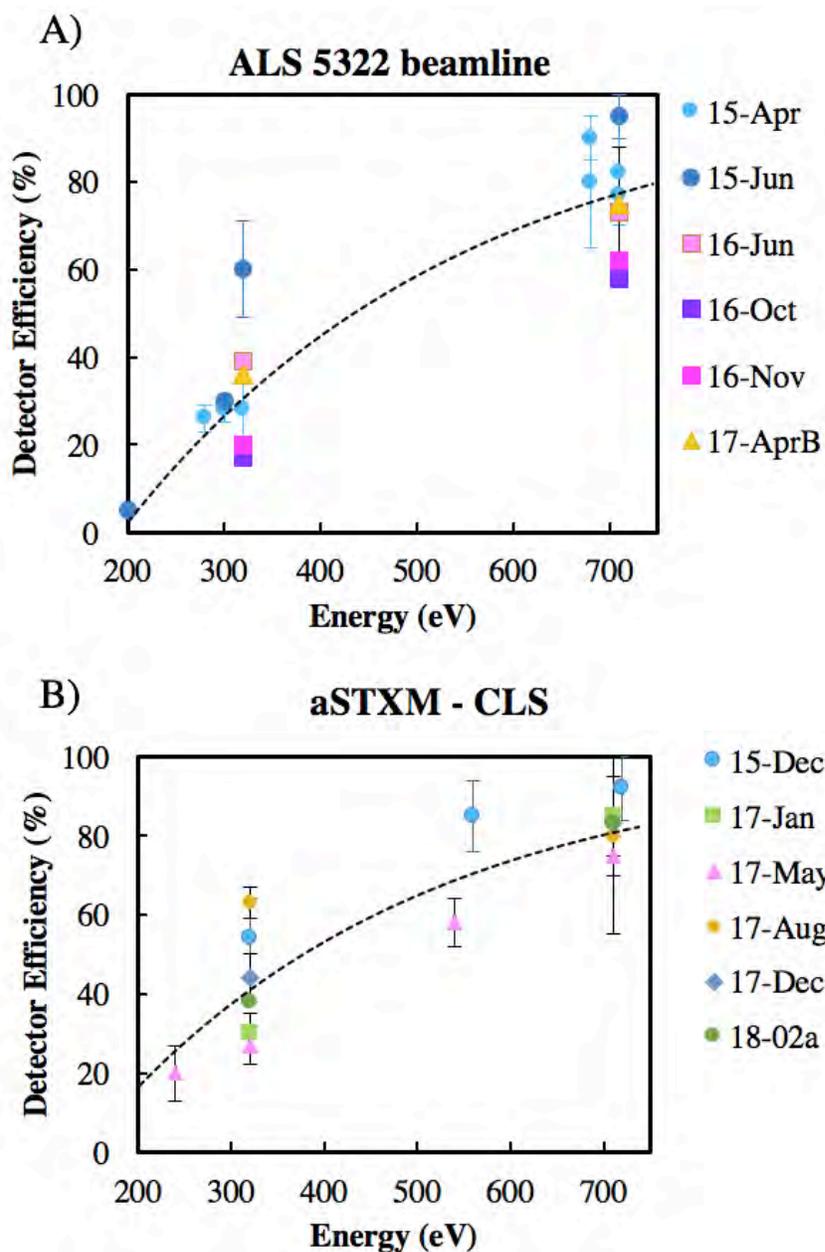
Figure 3.10 Detector efficiency of beamlines: **(A)** ALS 5.3.2.2. and **(B)** ambient STXM at CLS for all runs where quantitative data was taken during this thesis.

3.2.4.2   *Electrons: Dose calibration*

The electron irradiation of polymer thin films was done using the JEOL2010F TEM/STEM microscope operated at 200 kV at the CCEM, McMaster University. The electron irradiation and

EDS maps for the catalyst layer sample were acquired by a FEI Tecnai Osiris at the 4D Lab at Simon Fraser University. The dose was determined independently from the PMMA cross-over approach with the formula used by Rightor et al., 1997; Wang, Botton, et al., 2009:

$$D = \frac{i_0 \Delta E (\frac{h}{IMFP}) t}{V \rho} \; x \; 10^{18} \qquad \qquad \text{Equation 3.12}$$

where i_0 is the current of the incident electron beam (A), t is the exposure time (s), h is the thickness of the sample (nm), V is the volume ($V = \pi \cdot \frac{s^2}{2} \cdot h$, where s is the beam diameter incident on the sample in nm); ρ is the density (g.cm^{-3}), IMFP is the electron inelastic mean free path (assumed to be 100 nm (Akar, Gümüş, & Okumuşoğlu, 2006; Shinotsuka, Tanuma, Powell, & Penn, 2015) and ΔE is the average energy loss per inelastic scattering event, also known as stopping power (calculated as $\Delta E = 105$ and 70 eV for PFSA and PMMA (NIST Database - Berger et.al., 2005)). A recent publication showed that the values computed by the NIST database overestimates the ΔE by approximately 15% (Tahir & Sari, 2015). Therefore, the ΔE was multiplied by a factor of 0.85 to compensate the overestimation of the NIST database ($\Delta E = 89$ and 60 eV were used for PFSA and PMMA, respectively). The dose using Equation 3.12 is not directly proportional to fluence due to the functions related specifically to each material (i.e. ρ and ΔE). Although similar equations to determine the electron beam dose have been published (Egerton, Konstantinova and Zhu, 2015; Du and Jacobsen, 2018), we have noted that the dose is independent from the thickness due to the h/IMFP term (i.e. the thickness term in the denominator cancels out with the term in the numerator). We consider this equation to be a simplification and further theoretical considerations are needed.

The dose was determined for damaged series of the PMMA samples. Using **Equation 3.12**, the average of the dose before the positive to negative crossover was 101 ± 3 MGy and the average dose which first displays negative mode was 115 ± 7 MGy (excluding the outliers). This resulted in an average of 108 ± 9 MGy for the positive to negative crossover transition which is slightly higher than the literature value for these transformations using soft X-rays (90 ± 4 MGy) (Leontowich et al., 2012). The uncertainty is estimated from multiple measurements (total of 8 areas in multiple samples) and cases where there was a maximum of 20 MGy difference between two damaged areas where the crossover transition occurred. The positive mode means that the exposed regions are removed after development, while negative mode is when the radiation damaged material is insoluble to the development solution. Depending on the dose applied, PMMA can act as both a positive and negative resist (Zailer, Frost, Chabasseur-Molyneux, Ford, & Pepper, 1996). Therefore, **Equation 3.12** was used for determining the dose for electron irradiated PFSA samples.

Figure 3.11 shows an example of how the dose was calibrated using the positive to negative cross-over in PMMA. Optical images (reflection, 50x objective, reflection mode) of a damage series in PMMA deposited on a SiNx window are shown before (**Figure 3.11a)** and after development **(Figure 3.11b)**. Line profiles of the damage series in **Figure 3.11a** and **3.11b** are shown in **Figure 3.11c.** Areas that receive doses <50 MGy are not visible with optical microscopy either before or after development. Areas that received doses from 50 to 100 MGy are visible before development (dark contrast means the material was removed due to electron irradiation), but are barely visible after development. Areas that received doses higher than 150 MGy have a brighter contrast in **Figure 3.11b** (this means material is re-deposited) consistent

with a change to negative mode. This method was repeated in 10 areas in a total of 4 different

PMMA specimens made from the same solution. As shown in **Table 3.3,** the PMMA films spun

cast from 1.5 wt% solutions are ~50 nm thick (the thickness of these specific samples was not

measured before development). The uncertainty cited is the standard error of all measurements.

The dose corresponds to a fluence of 1295 ± 25 e$^-$/nm^2 (error is the standard deviation) on a 50

nm PMMA film since the thickness for these specific samples were not measured. Despite the

simplification of Equation 3.12 there is reasonable agreement between the calculated dose to the

PMMA cross-over lithographic transformation. Therefore, Equation 3.12 was used for

determining the dose for electron irradiated PFSA samples.
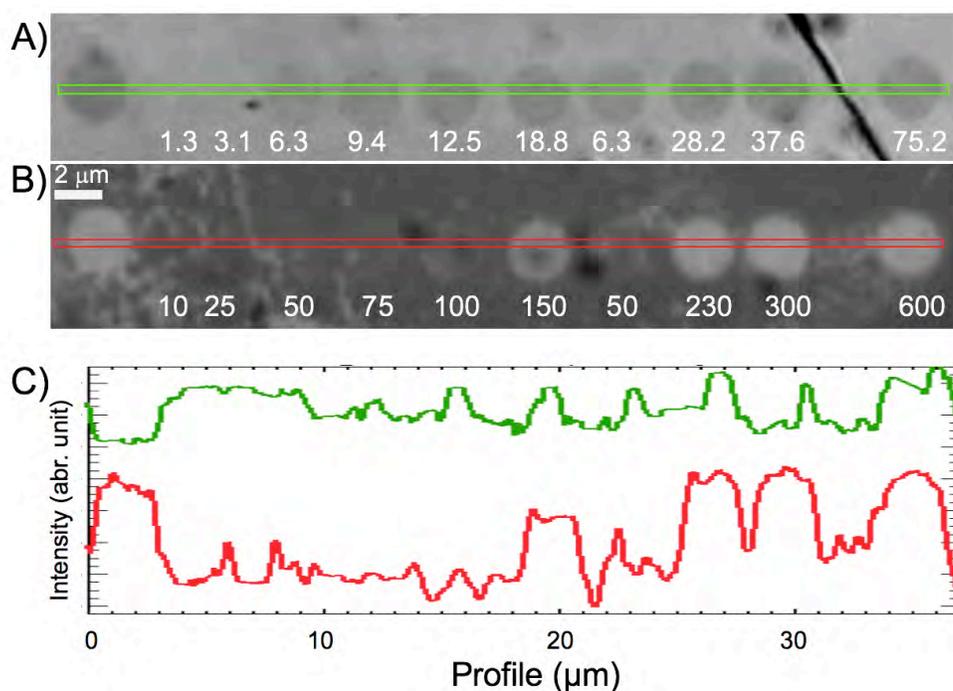
Figure 3.11 Optical microscope images of a 50 nm PMMA film damaged with 200 kV electrons
(A) before and **(B)** after development in RT. **(C)** Line profiles of the damage areas to calibrate the
dose using the crossover from positive to negative mode. Fluence (x10^2 e-/nm^2) and
corresponding dose (MGy) is shown for each damaged area in (A) and (B), respectively.

Freestanding PMMA films were also intentionally damaged in RT. However, the areas could not sustain more than 650 e⁻/nm², which corresponds to approximately 50 MGy, before completely burning a hole as seen during the TEM session. **Figure 3.12a** shows a damage series in freestanding PMMA before development, where all areas result in the formation of holes in the films. The freestanding films also did not survive development. One droplet of the development solution deposited on a grid held at 90° angle was sufficient to completely dissolve or destroy the film.

A PMMA film on SiNx mounted in the cryo-holder was damaged while cooled to -150 °C. An optical microscopy image of the cryo-damaged sample after development in RT is shown in **Figure 3.12b.** The PMMA under cryo conditions (-150 °C) could sustain more damage (up to 1200 MGy) with no signs of forming a hole. The crossover transition occurred between an exposure 1900 ± 250 and 3000 ± 400 e⁻/nm² which is double the exposure at RT. If all the factors converting exposure to dose are temperature independent, then this corresponds to an increase of the cross over dose from $\sim109 \pm 4$ MGy to 220 ± 20 MGy between RT and cryo temperature irradiation. A doubling of the cross over dose implies that at cryo temperatures the sample can absorb twice the energy to create the same damage as in RT. A doubling of the cross over fluence was also observed on 200 nm PMMA films deposited on a clean GaAs:Si surface and damaged using a scanning electron microscope (Gschrey et.al, 2014).
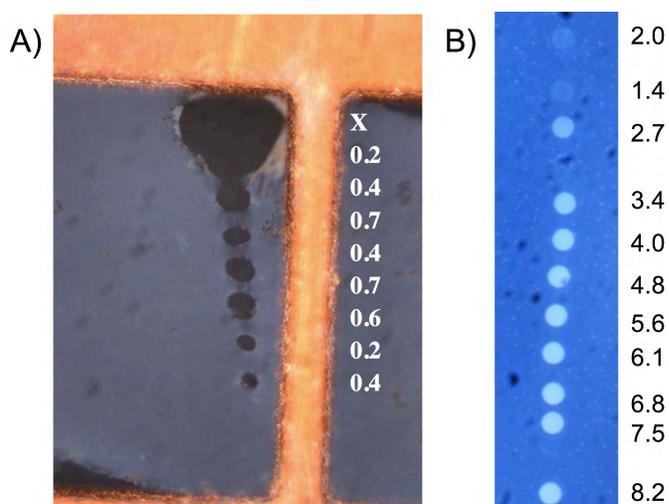
Figure 3.12 Optical microscopy images of PMMA films after damage by 200 kV electrons, where the film is **(A)** freestanding and damaged under RT and **(B)** deposited on a 20 nm SiNx substrate and damaged under cryo temperature (-150 °C). Image (B) is after development at RT. The electron fluence ($\times 10^3$ e$^-$/nm^2) is shown to the right of each damaged area.

3.2.5   *Measuring effects of damage*

Different core level spectral features change with radiation damage in different ways and at different rates. Thus, the rate of damage (the critical dose) and understanding of the underlying mechanistic steps will differ depending on which spectral feature or set of features is used to visualize and quantify the extent of damage. For example, in the F 1s spectrum of PFSA, the peaks at 690 and 694 eV, arising from F 1s $\rightarrow$ σ^*_{C-F} transitions (Yan et al., 2018) change very rapidly, as they are sensitive to the C-F bond reorganization as well as F mass loss (see **Chapter 5**).

In this work, the damage, created by either X-ray or electron radiation, was analyzed with STXM using low-damage conditions by decreasing the Io to ~2-4 MHz, defocusing the beam to 50-200 nm and using as few energy points as would still define the important spectral features.

3.3   Analyzing damage (Dose) data

3.3.1   Kinetic models

A framework for first principles calculations of absorbed dose during soft X-ray irradiation for soft materials that suffer mass loss was developed (Berejnov, Rubinstein, Melo, & Hitchcock, 2018). An integral expression was formulated which described the absorption of X-rays by a sample as a function of incident photon energy, time and mass changes. Asymptotic approximations and exact solutions were developed using both exponential decay (1st order kinetics) (**Equation 3.9**) and hyperbolic (2nd order kinetics) model functions for the dose(time). More complicated kinetic models, such as a bi-exponential or hyperbolic function to fit the damage vs. dose curves, did not improve the quality of the fitting (Berejnov et al., 2018). It was shown that STXM data for both PMMA and PFSA samples can be fit with similar precision to both exponential and hyperbolic models. It was concluded that STXM damage(dose) data is not sensitive to   kinetic order and therefore cannot be used to identify specific kinetics order (Berejnov et al., 2018). Therefore, first order kinetics was assumed in this work for simplification.

3.3.2   Data processing

For the 9-pad patterns, damage was evaluated by several different methods, including:

A) **high quality images** (30-60 nm spot & step size) recorded at energies where the contrast for damage is highest [E_A, OD_{EA}]. The measured images were converted to OD and the results for each of the 9 pads were extracted in order to measure how the OD changes as a function of dose. In some cases, images were also measured at a pre-edge energy [E_P, OD_{EP}].   The

difference of these two OD images, $OD_{EA} - OD_{EP}$, is specific to the chemical changes related to the transition at E_A. This is also called a <u>stack map</u>. For example, for PFSA, the fluorine loss can be measured by $OD_{710\,eV} - OD_{684\,eV}$, while the disruption of the local CF_2-CF_2 chains can be measured by $OD_{694\,eV} - OD_{684\,eV}$ or $OD_{690\,eV} - OD_{684\,eV}$. Extracting these OD or OD difference signals from each pad using the methods described below, allows quantitation of the specific chemical changes as a function of dose.

B) **image sequences** or stacks (Jacobsen et al., 2000) at C 1s, O 1s, F 1s for visualization of all chemical changes (i.e. formation and breakage of bonds). They were used to quantify damage by:

(1) stack analysis (Hitchcock, 2012) to generate **component maps (Cm)** of the undamaged and damaged material, in some cases with prior conversion of suitable reference spectra to OD1 scales.

(2) integration of each spectrum to evaluate elemental changes (mass loss or gain) by subtracting a background and then integrating each edge as a function of dose. However, stack measurements are time consuming (a stack takes between 20 mins and 1 hr for each edge) and can cause additional damage. The stack damage can be lowered significantly by minimizing the number of images, and by using a large spot and step size (>200 nm). Typically, large pads were burned when stacks were to be measured.

The signal at any single pad (either OD or component map) can be determined from:

i) an OD for each of the 9 pads by taking the average OD of the central 80 % of the pad area (Coffey et al., 2002; Leontowich et al., 2012) using a square selector. Masks can be used to guide the selection. The <OD> can then be normalized to the OD of the undamaged material

(Leontowich, 2013; Wang, Morin, et al., 2009). Normalization was done by dividing the OD by the OD(t=0).

ii) integration of the OD for each pad. For each row, a horizontal linescan profile, averaged over the height of the pad, is generated – OD(x). Three such profiles are generated, one for lines containing pads 1-3, another for pads 4-6 and the third for pads 7-9. The x-scales are then adjusted so the signal from all of the 9 pads can be combined into a single curve (see **Fig. 3.13c**) with 9 peaks. The spectrum is then inverted and shifted so the peaks are all positive and the OD decays with increasing x (which is $\propto$ dose). A background is then subtracted to compensate for thickness variations which makes the signal outside the peaks ~0. The signal is then integrated and each jump is measured to evaluated the damage. This method is useful to compensate for thickness variations over the 9-pad area but it was not used in this work since the spun cast films were quite uniform (see **Table 3.3**).

Typically, the OD changes exponentially as a function of dose, which is consistent with first order kinetics (**Equation 1.1**). In such cases, a critical dose was determined by one of two methods: 1) fitting the OD(dose) as a function of dose to **Equation 1.1**, or 2) graphically extrapolating (Wang, 2008; Wang, Morin, et al., 2009), or 3) experimentally determining the OD_∞ parameter (Leontowich, 2013). In each case, plotting $\ln(OD-OD_\infty)$ as a function of dose yields a straight line with a slope b where $b = a_c^{-1}$ (see **Figure 5.4)** In this work, the first option was used and the fit of OD(dose) to **Equation 1.1** was performed using Sigmaplot V.6 (Systat Software).

3.3.2.1   High quality single images and stack maps

Previously, soft X-ray damage has been evaluated at a single energy where the contrast for damage is highest [i.e. E_A = 288.4 eV for PMMA (Beetz & Jacobsen, 2003; Coffey et al., 2002;

Leontowich et al., 2012; Wang, Morin, et al., 2009), 284.8 eV for PET (Wang, Botton, et al.,

2009), and 286.4 eV for PAN (Leontowich, 2013)]. For PFSA, the rate of change of signal with

dose is greatest at 292.4 eV in the C 1s edge and 690.0 eV in the F 1s edge. The following

describes damage quantification of PFSA from the C 1s → σ^*_{C-F} ($\perp$) transition at 292.4 eV by

comparing the critical dose values obtained from a single image - $OD_{292.4\ eV}$ - see **Figure 3.13** -

with those from $OD_{292.4\ eV} - OD_{280\ eV}$ – see **Figure 3.14**) for the same dataset. The critical dose was

determined using methods (i) and (ii) for each data set and the resulting a_c values obtained by

fitting to an exponential fit using **Equation 1.1** are listed in **Table 3.5.**

Figure 3.13a shows the STXM OD image at 292.4 eV while **Figure 3.14a** shows the

$OD_{292.4\ eV} - OD_{280\ eV}$ stack map of the same area after a 9-pad damage was generated using 320 eV

incident photons. The dose at each pad is indicated in **Figure 3.13a**. **Figure 3.13b** and **Figure

3.14b** plot OD and ΔOD, derived using method (i), as a function of dose (MGy). The a_c is the

same for both (65 ± 15 MGy compared to 62 ± 15 MGy). Thus subtracting the pre C 1s edge

signal to compensate for the change in underlying signal due to fluorine loss does not change the

derived a_c for C 1s → σ^*_{C-F} transitions. <u>For all a_c determined in this thesis, the average OD taken

from the image at the energy of interest as a function of dose was fit to the function in **Eq. 1.1**</u>.

An alternative method to find the a_c consists of integrating the OD and the ΔOD as shown

in **Figure 3.13c** & **Figure 3.14c** using method (ii). The integrated OD and ΔOD values are shown

in **Figure 3.13d** & **Figure 3.14d,** respetively. The jumps in signal are plotted as a function of

dose in **Figure 3.13e** & **Figure 3.14e** and fit to an exponential growth function. The calculated a_c

(or b^{-1} in **Equation 3.13**) are listed in **Table 3.6**. Method ii results in different a_c values compared

to method i. The critical doses for both the single image at 292.4 eV compared to the subtracted

image at 292.4-280 eV were similar (103 compared to 113 MGy, respectively).
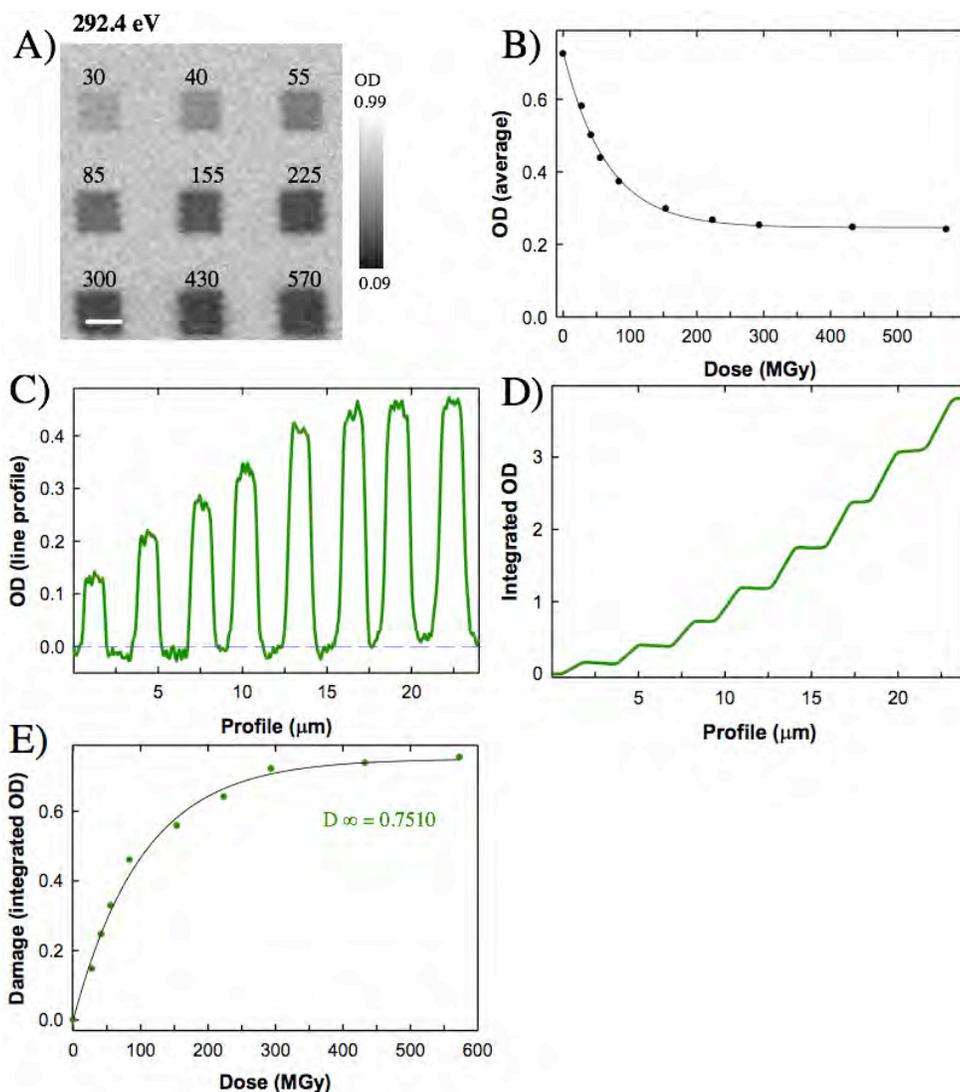
Figure 3.13 (A) STXM image at 292.4 eV for a PFSA sample damaged with 320 eV incident

photons. The scale bar is 1 μm and the doses (MGy) are indicated for each pad. **(B)** average OD

of each area as a function of dose; the curve is the fit to the exponential function, **(C)** OD line

profile inverted and set to zero, **(D)** integration of the OD line profile shown in (c) and **(E)**

damage values taken from the integration in (d) and plotted as a function of OD. An exponential

growth function was fitted to the data to determine a_c.
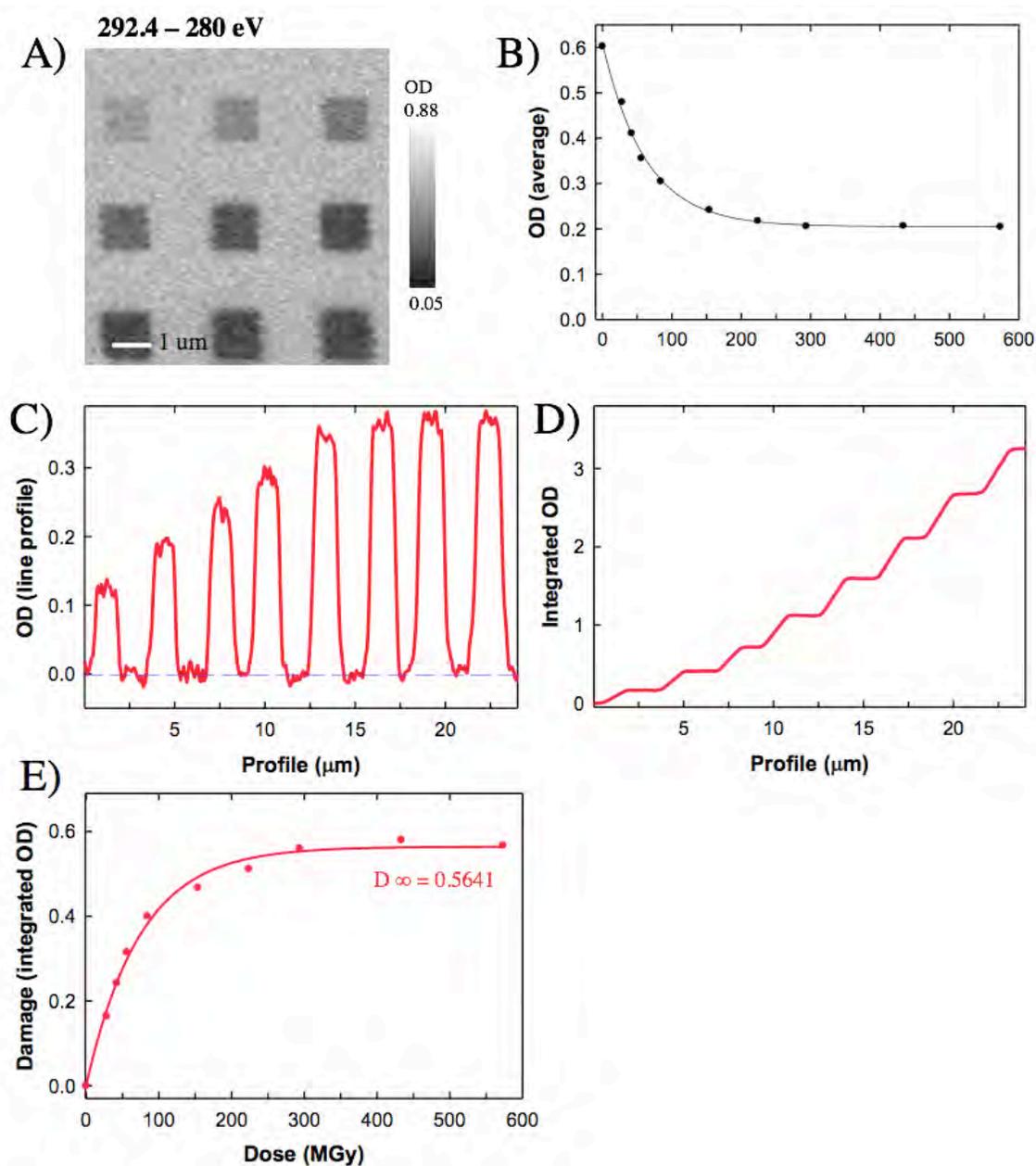
Figure 3.14 **(A)** STXM image at $OD_{292.4\ eV}$ - $OD_{280\ eV}$ for a PFSA sample damaged with 320 eV incident photons. The scale bar is 1 μm and the doses (MGy) are indicated for each pad. **(B)** average OD of each area as a function of dose; the curve is the fit to the exponential function, **(C)** OD line profile inverted and set to zero, **(D)** integration of the OD line profile shown in (c) and **(E)** damage values taken from the integration in (d) and plotted as a function of OD. An exponential growth function was fitted to the data to determine a_c.

Table 3.6 Critical dose evaluation: methods i(averaging OD) and ii (integration of OD) used on an image at a single energy vs a stack map.

Image	a_c (MGy)	
	OD av	OD integration
$OD_{292.4\ eV}$	65	103
$OD_{292.4\ eV} - OD_{280\ eV}$	62	75

The a_c determined using methods i and ii are different: 64 ± 2 MGy compared to 89 ± 20 MGy respectively. The difference is probably related to systematic errors related to each method. Although method (i) was used in this thesis, there may be some situations where method (ii) should be used (for example, when the film is non-uniform). **Table 3.7** lists the advantages and disadvantages for each method.

Table 3.7 Strengths and disadvantages to methods i(OD average of 80% of each pad) and ii (Integration of the OD).

OD average – method i		Integration – method ii	
Strengths	**Disadvantages**	**Strengths**	**Disadvantages**
Quantitative analysis is direct and done by fitting	Selection of area is done by eyeballing 80% of the pad	Compensates for sample non-uniformity	Requires eyeballing to evaluate jump at each pad
No data manipulation	Does not compensate for sample non-uniformity	Integrates entire damaged area	Background subtraction can be seen as data manipulation
Average pixels calculated for all pads	Actual damaged area may be different than area that was exposed	-	-

3.3.2.2   *Low resolution stacks for full spectral analysis*

Full stacks for complete C 1s, O 1s or F 1s spectra at each pad were only taken with the larger pads to allow defocused, low flux operation to minimize damage in the analysis (**Table 3.4**). The rate of decay of the entire chemical signature of a material (also called component loss) can be quantified by fitting the C 1s or F 1s stacks using singular value decomposition (SVD) (Koprinarov, Hitchcock, McCrory, & Childs, 2002) with suitable reference spectra for the

undamaged and damaged PFSA. If these spectra are placed on OD1 scales, then the thickness can be evaluated at each pixel of the dataset. However, the critical dose can be evaluated without this step. **Figure 3.15** is a worked example for PFSA damaged by 320 eV photons. Two internal reference spectra were generated (see **Figure 3.15a)** from an undamaged region and from the most damaged area (pad #9). Using SVD, the stacks were fit to these two internal spectra generating component maps (Cm) for the undamaged (**Figure 3.15b**) and damaged material (**Figure 3.15d**). These maps were then processed with method-i described in **section 3.3.2** (**Figure 3.15e)**. For both maps, a mask was used to ensure only the damaged pad areas were selected when taking the OD average. The masked maps are shown in **Figure 3.15c**. Masks are useful when the first pads (on the top row) have a low contrast due to small dose and thus negligible damage (**Figure 3.15e**).

After the damage is generated, the material in the pads becomes a mixture of undamaged and damaged PFSA. In this case, only one reference spectrum for the damaged material was used, assuming there is only one damage process. Thus, the intensity scale of the Cm of the damaged PFSA component runs between 0 and 1. The undamaged Cm varies from 1.0 in an un-exposed area to 0 for pad (#9) and vice-versa for the damaged Cm. The damage signal (relative amount of undamaged or damaged polymer) as a function of dose was then fit to the exponential model (**Equation 1.1**) to derive a critical dose. The a_c for the decay of the undamaged component using method i (**Figure 3.15b**) was 113±7 MGy (the errors indicated are due calculated from the error of the coefficient used to determine the critical dose). The a_c for damage of the ionomer component is higher than the values indicated in **Table 3.6** for the a_c for damage of the σ^*_{C-F}

transitions. Taking into account the errors from repeated measurements, **section 5.3.1.2** will show

that these values are within statistical significance.
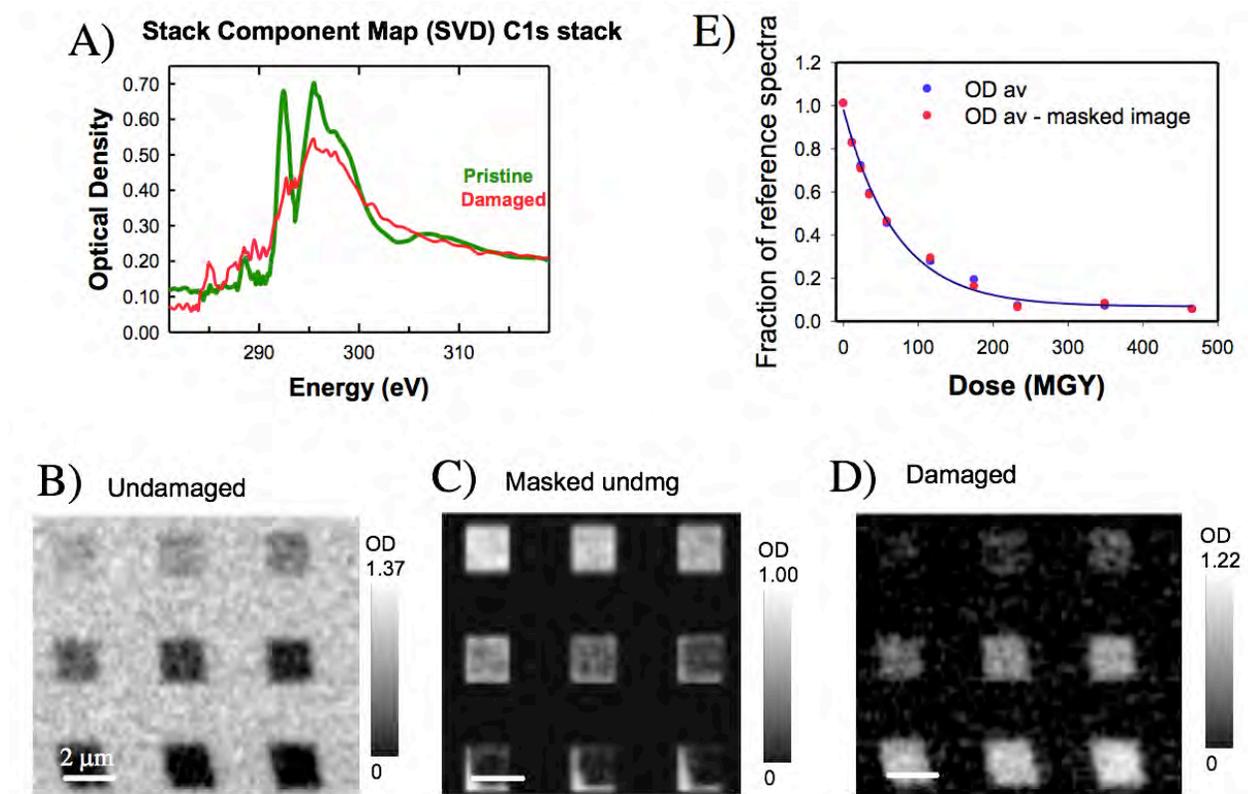
Figure 3.15 Component map analysis using SVD of a C1s stack of PFSA showing the **(A)** internal spectra **(B)** undamaged, **(C)** masked undamaged and **(D)** damaged component maps. Quantification of the undamaged component map was evaluated **(E)** using method-i.

3.3.2.3   *Elemental evaluation method*

The fitting approach uses all of the spectral information and can be used to derive

quantitative thickness information. In some cases, it is useful to evaluate elemental amount and

ignore the detailed spectral changes. In order to quantify changes in elemental amounts as a

function of dose, the spectrum of each pad was background subtracted using a linear fit to the

pre-edge region after converting the abscissa from energy to wavelength (pre- and post-continua

are significantly more linear when plotted in wavelength). The background subtraction separates the spectrum of a specific edge from the underlying contributions of other edges. The background subtracted spectra are then integrated over the full spectral range (280 - 320 eV for C 1s, 524 - 560 eV for O 1, 680 - 720 eV for F 1s). This was repeated for all damaged areas and an undamaged area. The damage data is then plotted as a function of dose and the critical dose was evaluated by applying the same exponential function (**Equation 1.1**).

For the area shown in **Figure 3.15**, the a_c for the oxygen and fluorine decay was 56±6 and 107±17 MGy, respectively. The a_c for fluorine decay is similar to the a_c reported in the previous section for the ionomer component damage.

3.4 Other chemical analysis and imaging methods

3.4.1 AFM

Two AFMs were used in this thesis. For visualization of the positive to negative cross-over of the developed PMMA, intermittent contact mode images were acquired in a Quesant Q-Scope 350 AFM instrument at McMaster University. Tap 150Al-G (force constant 5 N/m, 150 kHz) cantilever tips were used. Tapping mode images were acquired on an Agilent 55000 with a 90 x 90 μm sample stage by Isaac Martens (PhD student at the University of British Columbia). The SiNx tips were used as received (170 kHz AAC, Agilent).

3.4.2 Optical microscopy

After preparation, all samples were inspected with an optical microscope (Olympus model EX51, with camera QImaging Retiga EXi camera). Low and high magnification images (5x-100x objective) were used to identify areas for irradiation or STXM analysis. The optical microscope

was also used to identify the positive to negative cross-over of PMMA (Leontowich et al., 2012)

after electron irradiation and to check all electron damaged areas before STXM measurements.

Chapter 4

UV-SR versus STXM: comparison of thickness and damage

This paper presents a comparison of PFSA, PS, and PMMA polymer film thicknesses measured by UV spectral reflectance and X-ray absorption. It was found that PMMA and PS are damaged when irradiated by UV in air, whereas PFSA was not affected. The chemical damage was studied using STXM. An exposure limit for thickness determination of PS and PMMA by UV-SR was determined.

The idea of checking the accuracy of film thickness determination by STXM by comparing to the results of UV-SR was developed by Drs. Viatcheslav Berejnov, Darija Susac and Juergen Stumper, while I was an intern at AFCC. All samples used and all UV-SR and STXM measurements in this work were made by the author during a six-month internship at AFCC in 2016. The method for thickness determination using UV-SR of polymeric thin films was developed by the author under the supervision of Dr. Viatcheslav Berejnov. The UV-SR data was analyzed by the author of this thesis. The STXM data was analyzed by both the author and by Dr. Viatcheslav Berejnov. The paper was drafted by the author, and edited and revised by both Dr. Viatcheslav Berejnov and Dr. Adam Hitchcock. The paper is published: L.G.A. Melo, A. Hitchcock, D. Susac, J. Stumper, V. Berejnov: Effect of UV radiation damage in air on polymer film thickness, studied by soft X-ray spectromicroscopy. Physical Chemistry Chemical Physics, **2018**, 20, 16625 – 16640. doi: 10.1039/c7cp08621k. The supplementary info is available in **Appendix B**. Reproduced with permission from the Royal Society of Chemistry and PCCP Owner Societies.
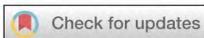
Check for updates

Effect of UV radiation damage in air on polymer film thickness, studied by soft X-ray spectromicroscopy†

Lis G. A. Melo, [iD] *[a] Adam P. Hitchcock, [iD] [a] Darija Susac,[b] Juergen Stumper[b] and Viatcheslav Berejnov[b]

The thicknesses of thin films of polystyrene (PS), poly(methyl methacrylate) (PMMA), and perfluorosulfonic acid (PFSA) were measured by Ultraviolet Spectral Reflectance (UV-SR) and Scanning Transmission X-ray Microscopy (STXM). At high doses, the UV irradiation in air used in the UV-SR method was found to modify the chemical structures of PS and PMMA (but not PFSA), leading to thinning of these polymer films. The chemical changes caused by UV/air radiation damage were characterized by STXM. When UV and X-ray radiation are applied using no-damage conditions, the film thicknesses measured with the two techniques differ by less than 15% for PS and PMMA and less than 5% for PFSA. This is an important result for verifying the quantitation capabilities of STXM. The chemical damage to PS and PMMA is explained by oxygen implantation from air with formation of ozone. The thickness depletion caused by UV/air radiation for PS and PMMA films is exponential with exposure time. Different rates of depletion are linked to surface or bulk driven photo-chemical product erosion. The initial rate of material erosion was found to be constant and non-specific to the studied polymers.

Introduction

Accurate measurements of the thickness of polymer thin films in the range of 20–500 nm with a few percent precision are important in many fields including lithography, organic electronics, fuel cells and Li-batteries. Depending on the application, the polymeric material could be either deposited on a flat substrate (*e.g.* for lithography and organic electronics) or distributed in a porous structure such as within the catalyst layer (CL) electrode in polymer electrolyte membrane fuel cells (PEM-FC). An important aspect of PEM-FC catalyst layer characterization is the determination of the amounts and spatial distributions of the major CL components – ionomer, carbon support and Pt catalyst. Scanning transmission soft X-ray microscopy (STXM) has been used to map the effective thickness of the perfluorosulfonic acid (PFSA) ionomer dispersed in CL.[1,2] The STXM thickness measurements are based on the analysis of component specific X-ray absorption.[3,4] The quantity of a particular component can be deduced from its effective thickness, the portion of a given volume that component occupies in the CL. If accurate measurements of the effective thickness can be made, then more precise structure–property–performance correlations can be achieved and used to improve manufacturing processes to optimize CL properties. The accuracy of STXM-based thickness determination has not been documented previously to our knowledge.

The thickness of chemically homogeneous and uniformly thick films can be measured with a variety of methods, including atomic force microscopy,[5,6] optical profilometry,[7,8] reflectometry,[9,10] ellipsometry[11–15] and Ultraviolet Spectral Reflectance[16–22] (UV-SR).‡ The optical methods are direct, provide absolute thicknesses, and give an average value over a sample area in the micron range. They are usually fast and very convenient for industrial application where it is often critical to monitor film thickness over large areas.

However, optical techniques are not suitable for the analysis of polymer thickness in porous systems. For that reason, the ability of STXM to measure the effective ionomer thickness across the CL is very unique. In the context of establishing a robust analytical method, it is important to evaluate the accuracy of the STXM effective thickness measurement. This can be done by comparing STXM derived thicknesses with results from another independent method applied to the same sample.

---

[a] Dept. Chemistry and Chemical Biology, McMaster University, Hamilton, ON L8S 4M1, Canada. E-mail: lismellow@gmail.com
[b] Automotive Fuel Cell Corporation Corp., 9000 Glenlyon Parkway, Burnaby, BC, V5J 5J8, Canada
† Electronic supplementary information (ESI) available: Supplementary figures and tables. See DOI: 10.1039/c7cp08621k

‡ While SR is often used as the acronym for spectral reflectance we choose to use UV-SR in this paper to avoid confusion with the common use in the X-ray microscopy community of SR for synchrotron radiation.

Phys. Chem. Chem. Phys., 2018, **20**, 16625–16640 | **16625**

105
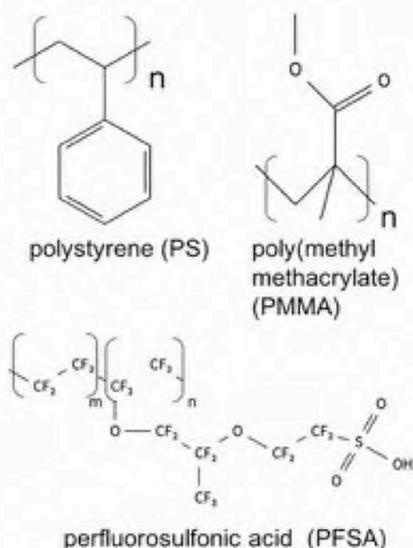
Scheme 1 Chemical structures of polystyrene (PS), polymethylmethacrylate (PMMA), perfluorosulfonic acid (PFSA), equivalent weight (EW) = 1100, where $m/n \sim 6$.

Therefore, the main objective of this study is to evaluate the accuracy of STXM thickness measurements by correlating STXM results with those obtained from UV-SR. For this work, spun-cast homogeneous thin films of three polymers were used: polystyrene (PS), poly(methyl methacrylate) (PMMA) and perfluorosulfonic acid (PFSA) (Scheme 1). A commercial UV-SR instrument, a Filmetrics model F40-UV,[23] which performs thin film thickness measurements based on the analysis of the interference response in a wide range of photon wavelengths from UV to infrared, was used in this work. By confirming the accuracy of STXM thickness determination for several different types of homogeneous thin films, the confidence in results measured from porous CL systems is increased. It was found that if the UV and X-ray measurements were performed under low dose conditions that do not result in chemical changes, then the thicknesses of films in the 30–200 nm range measured with both techniques differ by <10%. This is first direct, independent verification of the accuracy of STXM thickness determination. This is important since X-ray absorption derives thickness values based on mass and identity of the absorptive material, while UV-SR derives thickness from optical interference which is related to photon wavelength.

It is known that both the soft X-ray irradiation in He used in STXM and the UV irradiation in air used for UV-SR can induce chemical changes in polymer materials.[24–30] Therefore, thickness measurements acceptable for instrument cross-correlation must be conducted using optimized conditions which are known not to produce chemical alterations. In carrying out measurements to define low damage conditions, we found that PS and PMMA films

are extensively modified for UV/air exposure times >2 min. Moreover, if the exposure time increases to 5 min or more in the same area, which is the case when one is looking to increase the precision of the measurement or when creating thickness maps, both the film thickness and optical constants change, bringing into question the accuracy of UV-SR measurements. In order to understand these effects, we used near edge X-ray absorption fine structure (NEXAFS) spectroscopy in STXM to characterize the chemical changes to PS and PMMA films caused by UV/air irradiation. In contrast to PS and PMMA, the thickness of PFSA measured by UV-SR was constant over a large range of exposure times indicating PFSA is not damaged by UV/air irradiation. The chemical change of polymers measured by NEXAFS caused by UV/air radiation damage is explained by assuming oxygen implantation into the film from air with simultaneous formation of ozone in close proximity of the film/air interface. The mathematic model of thickness depletion due to UV/air radiation for PS and PMMA films is presented as an exponential behavior with the exposure time. The model outputs different rates of depletion depending on the type of polymer and is linked to either surface or bulk driven erosion of photo-chemical products. The initial rate of material erosion corresponding to small thickness depletion was found to be constant and similar for both PS and PMMA polymers.

Experimental methods

Sample preparation

Polystyrene (molecular weight (MW) = 344 kD) was obtained from Polymer Source Inc. PMMA (MW = 120 kD) was obtained from Sigma Aldrich. A PFSA alcohol-based dispersion with the commercial name of Dupont D521Nafion® was obtained from Ion Power. PS and PMMA were diluted with toluene (99.5%) obtained from Anachemia. For spin coating, the PFSA dispersion was further diluted with isopropyl alcohol (IPA) to between 1 and 3% (wt/wt) depending on the desired thickness. 0.5 to 1 g solutions of each polymer were prepared fresh for each use. Ultrasonication at 50 °C for 15 min was used to ensure the polymers were completely dissolved.[31]

The solutions were spin-coated on a cleaved mica substrate. A Specialty Coating Systems model 6708D spin coater was used. After spin-coating, the mica surface with the polymer film was cut into 1 mm² squares with a clean scalpel blade. The polymer film was then lifted off the substrate by immersing the sample into a distilled water bath. A floating piece of film was then transferred onto the top surface of a SiNx window. The SiNx windows, which were 75 nm thick with 2 × 2 mm membrane area in a 5 × 5 mm, 0.2 mm thick Si wafer frame, were obtained from Norcada Inc.

UV spectral reflectance (UV-SR)

The UV spectral reflectance method is based on the interference of incident light beams in the UV to IR regions (190–2200 nm) with part of those beams reflected from the air/material and material/substrate interfaces (see Fig. 1a).[23] The interference pattern depends on the light wavelength, λ, the film thickness,

16626 | *Phys. Chem. Chem. Phys.,* 2018, **20**, 16625–16640

This journal is © the Owner Societies 2018

106
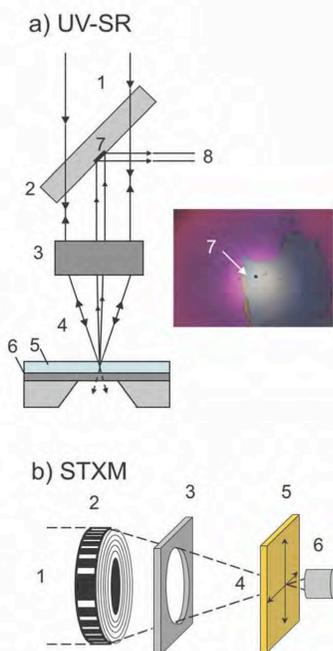
Fig. 1 (a) Schematic of UV spectral reflectance (UV-SR): 1 – incident beam, 2 – beam splitter, 3 – objective lenses, 4 – incident and sample reflected beams, 5 – thin film of PS on SiNx/Si, 6 – SiNx window substrate on a Si wafer, 7 – mirror (pin hole, also called the probe area), 8 – beam directed to spectrometer. Inset shows size of the signal acquisition area, mirror 7 compared to the total illuminated spot of ~500 µm diameter. (b) Schematic of scanning transmission X-ray microscopy (STXM): 1 – monochromated soft X-rays from the beamline, 2 – zone plate, 3 – order sorting aperture, 4 – first order diffracted soft X-ray beam, 5 – sample raster scanned in X and Y directions orthogonal to the beam, 6 – detector.

h, and the optical properties of the material and therefore its refractive index, n, which is also a function of the wavelength. The spectrum of the reflected light, $R(\lambda)$, contains interference fringes with a wavelength and thickness dependence which is described *qualitatively* by:

$$R(\lambda) = A + B\cos(4\pi \times h \times n(\lambda)/\lambda) \quad (1)$$

where A and B are complex functions incorporating the extinction coefficient, $k(\lambda)$, and the refractive index, $n(\lambda)$. Together k and n are called the "optical constants of the material" in this work.[23,32] The experimental $R(\lambda)$ spectrum is then fit to a theoretical model. In this study, all data in the interval of $250 < \lambda < 1000$ nm were fit using the "amorphous model", a proprietary model of Filmetrics.[23]

The polymer film mounted on the SiNx window covers the thin SiNx membrane in areas with and without the underlying Si frame. The part of the polymer film deposited on the window area (*i.e.* without underlying Si) was used for STXM and UV-SR correlation measurements. This allows measurements by both

instruments on areas of the polymer films which are at the same position within a few tens of microns (see Fig. S1 and S1, ESI†). UV-SR imaging experiments indicate the films were uniform to within 3% over these dimensions, with no evident structure on the few micron scale. The deposited polymer film on the SiNx membrane backed by a reflecting Si surface was used for those cases where only UV-SR measurements were made. The optical constants of the SiNx membrane were determined by UV-SR for each sample. The SiNx refractive indices measured at 630 nm were in the range of (2.168–2.219), depending on the window batch. These values differ from the range of 2.15–2.17 reported by Norcada,[33] as low stress silicon nitride thin membranes are non-stoichiometric silicon oxy-nitride.

Two methods of analysis of the UV-SR results were used: (i) based on measured optical constants, and (ii) based on assumption of applicability of previously measured optical constants. Method-i requires films thicker than 50 nm which can develop several interference fringes for the $R(\lambda)$ spectrum in order to accurately determine several parameters simultaneously. Method-ii has only a single parameter so that even a part of the interference fringe in the $R(\lambda)$ spectrum is enough to determine thickness. Upon UV/air exposure, radiation damage may change both the optical constants and film thickness. This effect is explored in a following section by comparing the thickness determined when the optical constants are assumed to be unchanged (method-ii) to that determined when optical constants were measured for each exposure (method-i).

UV-SR was measured using a Filmetrics model F-40UV, equipped with objective lenses, light source (model LS-DT2), spectrometer with a wavelength interval of $190 < \lambda < 1100$ nm§ and the StageBase-XY10-Auto motion stage. Fig. 1a describes the F-40UV instrument. The ~500 µm diameter optical probe directed normal to the sample film (5) is provided by two sources (1, 4), a deuterium lamp (UV) with output over $190 < \lambda < 400$ nm wavelengths, and a halogen white light lamp with output over $380 < \lambda < 2200$ nm. The polymer sample receives the polychromatic light through a fiber optic, which conducts the light from the two sources through the objective lens to the sample. The low wavelength cutoff of the fiber optic used is ~250 nm, which defines the lowest UV wavelength received by the sample and passed to the spectrometer. For imaging, a 15× UV compatible objective lens (3) was used, providing a field of view of ~500 µm diameter at the sample plane. The signal for $R(\lambda)$ measurements was taken from a much smaller area (7), 7×7 µm in the center of the field of view, with an optimally focused sample. The reflected light from this probe area is redirected into the spectrometer (8). For this model Filmetrics claims a refractive index accuracy of 0.2% for determining film thicknesses (5) in the range 4 nm to 10 µm.[23] Radiation intensity specifications for the light sources were not provided by Filmetrics. Background measurements without the sample were taken every 30 min and used over time intervals no longer than one hour. All measurements were done in a laboratory ambient

§ The Filmetrics model F40UV light sources provide radiation from $190 < \lambda < 2200$. However, the fibre optic used to transport the light has a low wavelength cut-off of 250 nm.

This journal is © the Owner Societies 2018

Phys. Chem. Chem. Phys., 2018, **20**, 16625–16640 | **16627**

107

environment with controlled temperature (T is 20 to 22 °C) and relative humidity (RH is 40 to 50%).

Scanning transmission X-ray microscopy (STXM)

STXM[34,35] is a synchrotron-based technique that forms images by raster scanning the sample through a focused, monochromatic X-ray beam, shown in Fig. 1b. Measurements were performed using the ambient STXM at the 10ID1 spectromicroscopy beam line[36] at the Canadian Light Source (CLS) and at the polymer STXM[37] on beamline 5.3.2.2[38] at the Advanced Light Source (ALS). The monochromated soft X-ray beam (1) illuminates a Fresnel zone plate (2) (provided by the Centre for X-ray Optics, Berkeley Lab) which focuses part of the X-rays to a spot size of ∼30 nm at the sample (5). The first order diffracted X-rays (4) are isolated from the unfocused X-rays by an order selected aperture (3) and the central stop of the zone plate. The sample is raster scanned in X and Y while the transmitted X-ray intensity is measured by a phosphor/photomultiplier detector (6), producing a transmission image.[3,34,37] The high chemical contrast in STXM images arises from material specific X-ray absorption at different photon energies.[39] The measured transmitted intensity at each pixel is converted to optical density, OD, using the Lambert–Beer law:

$$OD(E) = -\ln(I(E)/I_0(E)) \tag{2}$$

where $I(E)$ is the intensity transmitted through the sample and $I_0(E)$ is the intensity of the incident photon beam at photon energy E. If the material in the probe area is composed of multiple chemical species (components), the measured OD is a linear combination of absorption of all components:

$$OD(E) = \sum_i OD1(E)_i h_i \tag{3}$$

where $OD1(E)_i$ is the reference spectrum of component i obtained from experiment, and h_i is the effective thickness of component i. Reference spectra were obtained for each pure component which were set on an absolute $OD1(E)_i$ intensity scale of optical density per 1 nm thickness[34] by scaling the measured spectrum of the pure component outside of the near edge region to the spectrum of the component mass absorption coefficient $\mu_i(E)$.[40] See ESI,† S2 for further details on this procedure.

The STXM data was analyzed using aXis2000 software.[41] Image sequences or stacks[42] were recorded at specific edges (C 1s, O 1s, F 1s). In order to minimize the radiation damage from soft X-ray exposure (which is known to occur at quite low doses for PMMA[25,27] and PFSA[43]), all stacks were measured under negligible X-ray damage conditions, with exit slit sizes set to limit the incident photon intensity to <5 MHz, the X-ray beam defocused to a diameter of 500–700 nm, a pixel spacing of the same size as the defocused spot size, and a dwell time of 1 ms per pixel. The signal from areas between 900–2000 µm² was measured in several regions in all three materials (PS, PMMA and PFSA). In order to verify that these conditions did not cause X-ray damage, after the stack was completed an image was recorded over an area larger than the area of the stack, at the photon energy of highest X-ray damage contrast

(285.2 eV for PS, 288.4 eV for PMMA and 292.4 eV for PFSA). There was no change in the OD values between the stack areas and adjacent non-irradiated areas for any of the materials studied. This means that the conditions used did not cause any radiation damage detectable by STXM, so STXM can be used to detect spectral changes in the UV-SR exposed sample areas without itself making any chemical modifications to the polymer film.

The accuracy of the STXM thickness determination was improved by measuring the same area at several edges *i.e.* C 1s for all 3 polymers, O 1s for PMMA and F 1s for PFSA. The stacks were appended and aligned together. I_0 was recorded for each Y line of pixels of the image and used to convert the transmitted intensity to optical density. The $OD(E)$ spectrum was averaged over the entire available probe area, excluding defects irrelevant to the single layer of the polymer film *i.e.* dust particles, folds, and the edge of the film. The $OD(E)$ spectrum was then divided by the $OD1(E)$ reference spectrum for that particular polymer to get an effective thickness $h = OD(E)/OD1(E)$, hereafter just labeled thickness. Based on repetitive measurements at the combined edges (three regions in a thick sample and three regions in a thin sample of each material), there were 6 sets of thickness values for PS (280 data points/edge) and PMMA (264 data points/edge) and 4 sets for PFSA (380 data points/edge). This numerical data was further analyzed using Excel to find the average, standard deviation and standard error for the thicknesses of each material.

Characterizing material sensitivity to UV exposure

The Filmetrics F40-UV instrument focuses the light to a spot of ∼500 µm diameter on the sample. However, the UV-SR spectrometer only reads the reflected signal from ∼50 µm² (see Fig. 1a, label 7) thus providing only one thickness data point while STXM measures ∼30 spots of 0.5–0.7 µm each. To determine whether the UV-SR thickness results were affected by possible UV radiation damage occurring during measurements, the thickness of each sample was measured at two characteristic time intervals: (i) short – sufficient for the measurement to produce adequate signal-to-noise ratio, and (ii) long – sufficient to observe material changes. The short intervals (up to 2 min total exposure) were used for quantitative measurements to compare to STXM results on the same area. The long exposures were performed by continuously exposing the same area for up to 30 min or 60 min at a fixed irradiation rate (unknown for UV-SR, but always constant) and then performing the UV-SR thickness measurement which takes ∼5 s at specific time points during that long exposure. If the material is not affected by the UV/air irradiation, then one can assume the thickness and optical constants should not change. In the case of radiation damage, these values are expected to change systematically with exposure time. A similar method using different regions for each dose is well established for STXM,[25,44] but this type of systematic exposure dependence has not been applied previously to UV-SR to the best of our knowledge.

The UV-SR conditions for providing minimal radiation damage were: UV-lamp warm-up time ∼15 min; total measurement

16628 | *Phys. Chem. Chem. Phys.*, 2018, **20**, 16625–16640

This journal is © the Owner Societies 2018

time <30 to 40 s including finding the region of interest, focusing, and taking repetitive reflectivity measurements if needed. The maximum time interval available for thickness measurements before the UV radiation damage is detectable was estimated from plots of the thickness *versus* exposure time and extrapolated to zero exposure time to obtain the non-damaged thickness. For PMMA and PS the no-damage interval is <2 min. When comparing polymer film thicknesses determined by UV-SR and STXM, the same area of the film on a SiNx window was measured by UV-SR in <2 min, and by STXM using no-damage conditions.

Repeat measurements were made in order to characterize the measurement uncertainty and find the standard error and standard deviation for each technique. For UV-SR, this was done for two instances: (i) in a pristine area of the sample not previously exposed to any radiation, and (ii) for regions of the sample previously exposed to UV light (*e.g.* the 30 min exposure under the UV-SR light source), after STXM analysis. In each case, the UV-SR measurements were repeated in the same area for each material for up to a total of 13 measurements involving ~60–100 s of UV exposure time (see Table 1 for details of the replicate measurements).

Results

UV-SR: effect of UV exposure on film thickness

Upper limit of UV exposure time for reliable thickness measurements. Fig. 2 plots the thicknesses of PS, PMMA and PFSA spun cast films and a SiNx film on a Si wafer, measured by UV-SR as a function of the time the same spot was exposed to UV/air. The thicknesses reported in Fig. 2 were evaluated using the same optical constants (method-ii) for all exposure times. The initial thicknesses of the PMMA, PFSA, PS and SiNx thin films, determined by UV-SR with low UV exposure conditions, were 33, 52, 41 and 67 nm, respectively. The different material sensitivity to the UV/air irradiation is apparent: PMMA and PS suffer extensive thickness reduction as the exposure time increases, while PFSA and the SiNx substrate are unaffected by the UV exposure. For PMMA and PS an exposure of 2.0 min
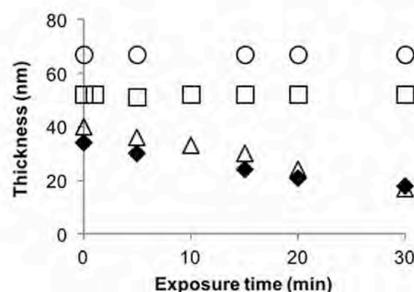
Fig. 2 Absolute thickness (nm) of thin films of silicon nitride (SiNx); and PS, PMMA and PFSA thin films on a SiNx window, measured by UV-SR at 0, 5, 10, 15, 20, and 30 min exposure time in air. □ = PFSA on SiNx; ♦ = PMMA on SiNx; △ = PS on SiNx; O = SiNx.

and 1.5 min causes a thickness change of 1 nm which is 3% and 2.5% of the film thickness, respectively. These results set an upper bound of exposure times for obtaining meaningful thicknesses for the original PMMA and PS films when using Filmetrics UV-SR in a laboratory environment. The thicknesses of SiNx and PFSA are constant over 30 min UV exposure, within the measurement uncertainty (±1 nm).

Sensitivity of Filmetrics fitting procedure to extent of UV/air exposure. The Filmetrics instrument determines film thickness from a fit of a specific optical model to the $R(\lambda)$ spectrum. The quality of the fit depends on how many interference fringes are developed by the measured area of a particular film. We expect that UV radiation damage changes both the thickness (as documented in Fig. 2) and the optical constants. Below we show how this affects the fitting procedure and thus the derived results.

In order to test the sensitivity of the Filmetrics fitting to changes caused by the UV exposure, UV-SR measurements were made for two different initial thicknesses of PMMA: 92 and 49 nm (results presented in Fig. 3) and for PS: 110 and 49 nm (results presented in Fig. 4). The same method and exposure conditions were used to measure all four samples. The polymer films were deposited on a SiNx film on top of the 0.2 mm Si wafer frame. To test the sensitivity of the fitting procedure for

Table 1 UV-SR thickness as a function of total UV-SR measurement time for multiple areas of PS and PMMA thin films on SiNx to calculate the standard deviation

Sample[a]		PS					PMMA				
		[]^b wt%	Total time[c] (s)	#[f]	Thickness (nm)	Std dev	[]^b wt%	Total time[c] (s)	#[f]	Thickness (nm)	Std dev
Pristine	I	2	65	7	122.6	0.5	3^e	75	9	96.4	0.8
	II	1	90	12	43.5	0.2	3^e	55	5	73.7	0.8
	III	—	—	—	—	—	1.5	85	11	47.7	0.7
Damaged[d]	I	2	85	11	79.6	0.6	3^e	85	11	39.7	0.8
	II	1	90	12	35.3	0.4	3^e	85	11	27.4	1.0
	III	—	—	—	—	—	1.5	75	9	24.5	1.2

^{a} Samples I, II and III are distinct samples, made with different solution concentrations, except for the replicate PMMA 3% samples – see footnote (e). ^{b} Concentration of spin coat sample (wt% in toluene). ^{c} The exposure time for generating the damage is not counted towards the exposure time for determining the reproducibility of the measurements. ^{d} Damaged areas were exposed to the UV-SR for 30 to 60 min, depending on initial thickness. ^{e} Samples I and II are separate samples made from the same solution. ^{f} Number of measurements taken for the same area to get the thickness average and standard deviation.
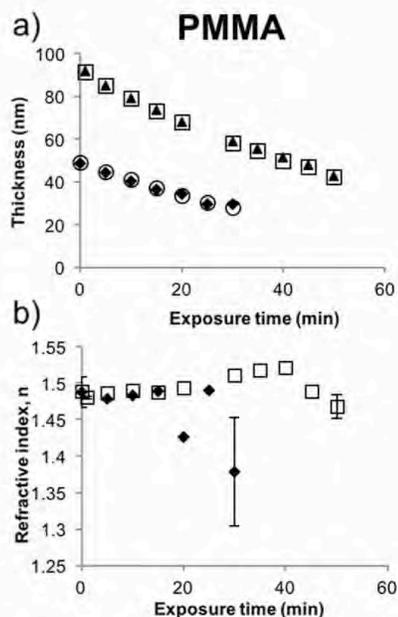
Fig. 3 Effect of UV/air exposure time (min) on PMMA: (a) thickness (nm) and (b) refractive index values, determined by UV-SR for two samples of PMMA on a SiNx window (on the Si frame) with initial thicknesses of 49 nm and 91 nm. $\bigcirc$ = thin(t) and $\blacktriangle$ = thick(t) are values where only the thickness was determined using method-ii with $k = 0$ and fixed refractive index of 1.482 ± 0.001 at $\lambda = 632.8$ nm. $\blacklozenge$ = thin(t,n,k) and $\square$ = thick(t,n,k) are values where both thickness and optical constants were determined using method-i. Note that the larger error bar at the 30 min exposure is because the thickness has decreased to values where the signal is weak and the error for the refractive index is much larger.
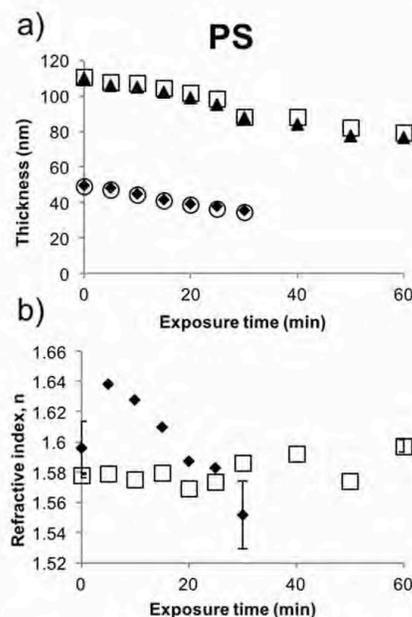
Fig. 4 Effect of UV/air exposure time (min) on PS: (a) thickness (nm) and (b) refractive index values, determined by UV-SR for two samples of PS on SiNx window (on the Si frame) with initial thickness of 49 nm and 110 nm. $\bigcirc$ = thin(t) and $\blacktriangle$ = thick(t) are values where only the thickness was determined using method-ii with $k = 0$ and fixed refractive index value of 1.587 ± 0.001 at $\lambda = 632.8$ nm. $\blacklozenge$ = thin(t,n,k) and $\square$ = thick(t,n,k) are values where both thickness and optical constants were determined using method-i. Note that the larger error bar at the 30 min exposure is because the thickness has decreased to values where the signal is weak and the error for the refractive index is much larger.

each sample, the thickness was determined by both method-i (simultaneously fitting the thickness and the optical constants), and method-ii (using optical constants measured for the non-damaged thick sample). The refractive indices for the non-damaged films at $\lambda = 632.8$ nm were 1.482 ± 0.001 for PMMA and 1.587 ± 0.001 for PS, respectively. These values agree with those reported elsewhere.[45]

The UV-SR thickness (determined using both method-i and method-ii) and the refractive index for PMMA (PS) are plotted *versus* the exposure time in Fig. 3a (Fig. 4a) and Fig. 3b (Fig. 4b), respectively. Error bars for the refractive indices are shown for the first (<1 min exposure) and the last (30 min exposure) measurement. After 30 min of exposure the quality of the fit of the $R(\lambda)$ spectrum for the thin PS and PMMA samples decreases and the standard error of the refractive index increases from 0.001 for samples thicker than 50 nm to 0.01 for samples thinner than 50 nm. The measured $R(\lambda)$ spectra for PMMA and PS, which are presented in ESI,† S3, Fig. S2 and S3, change significantly over the 30 min exposure time.

For PMMA, the UV-SR thickness values (Fig. 3a) do not depend on whether method-i or method-ii is used, down to a

sample thickness of 25 nm. For PS (Fig. 4a) the two methods produce thicknesses differing by ~3% for the thick sample. Thicknesses derived using method-ii are systematically lower than those from method-i. PMMA has a rate of thickness decay of 0.97 ± 0.03 and 0.66 ± 0.05 nm min^{-1}, for the thick and thin samples respectively. The rate of thickness decay for the thick PS sample is 0.56 ± 0.04 nm min^{-1}, and 0.48 ± 0.02 nm min^{-1} for the thin PS sample. Thus, relative to PS, PMMA is damaged with lower UV/air exposure. Fig. 3b and 4b show the evolution of the refractive indices with exposure time, as measured using method-i. The refractive index of the PMMA and PS thin films changes by ~0.1. The error of the refractive index is higher for the thinner samples for both materials. Since the thicknesses derived using method-i and method-ii for the same initial thickness and exposure time are nearly identical (plotted in Fig. 3a and 4a), we conclude that the derived thicknesses are not sensitive to the refractive index changes of ~0.1 that result from 30 min of UV/air exposure of PS and PMMA.

UV-SR: substrate effect on UV damage of PMMA

From the perspective of the material properties of a polymer film, the derived thickness should not depend on the substrate

16630 | *Phys. Chem. Chem. Phys.*, 2018, **20**, 16625–16640

This journal is © the Owner Societies 2018
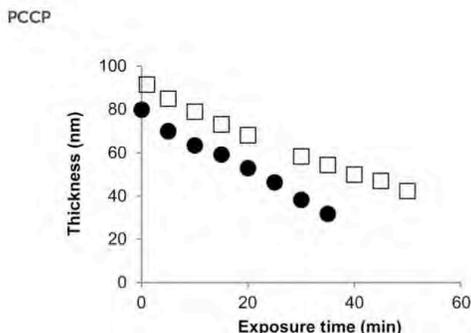
Fig. 5 Influence of substrate on the PMMA thickness dependence of the UV/air exposure, determined using method i. □ = PMMA on 75 nm SiNx on a Si frame, ● = PMMA on a Si wafer with native oxide.

on which the film is deposited. However, if the thin film material partially absorbs radiation then the substrate may affect the degree of absorption because it affects the fraction of light that is reflected from the thin film/substrate interface.[32] Since radiation damage of polymers occurs due to absorption,[28-30] the type of substrate can affect the degree of damage. PMMA was used for this test since it is more sensitive than PS to UV/air damage. Fig. 5 compares the UV-SR thickness as a function of the exposure time measured by method-i, for two substrates: PMMA on SiNx on an oxidized Si wafer and PMMA on an oxidized Si wafer only. The refractive index values determined in these measurements are presented in ESI,† S3 and Fig. S4. Two PMMA samples were used: one film, 91 nm thick before UV damage, was deposited on a 75 nm-SiNx layer on SiO$_2$ and another film, 80 nm thick before UV damage, was deposited on a clean Si wafer with native oxide. The raw $R(\lambda)$ spectra are shown in ESI,† S3, Fig. S2a and c for PMMA on SiNx on SiO$_2$, and for the bare Si wafer, respectively. According to Fig. 5, the thickness of the PMMA film on the Si wafer changes more rapidly than that for the PMMA film on SiNx. These results show that the substrate indeed affects the damage rate of UV-sensitive polymers. In particular, using PMMA on the SiO$_2$ substrate increases the thickness depletion rate by a factor of 2 (slope of Fig. 5), relative to PMMA deposited on SiNx on a SiO$_2$-on-Si substrate.

STXM: characterization of chemical changes from UV-damage

All of the spectral changes observed in the UV-SR exposed areas are associated with radiation damage caused by UV/air exposure. The regions of the PS, PMMA and PFSA films UV/air exposed to generate the data presented in Fig. 2 were subsequently analyzed by STXM (see Fig. 6–8). A transmission electron microscopy (TEM) Cu grid was placed on top of each polymer film before the UV-SR measurements to shield parts of the sample and produce adjacent sites of exposed and non-exposed sample regions. The TEM grid was removed before the STXM experiments to give access to the non-exposed areas, which were taken as the non-damaged standards for spectroscopic measurements.

For each of Fig. 6–8, image a is an optical image (reflection mode taken with a 15× magnification objective lenses) recorded using the UV-SR microscope with the TEM Cu grid

on top of the film; image b is an optical image without the TEM Cu grid, (reflection mode taken with a 50× magnification objective lenses) of the same area after UV-SR measurements; and image c is a STXM image, without the TEM Cu grid, at a photon energy very sensitive to radiation damage. For both PS (Fig. 6b) and PMMA (Fig. 7b), there is a visible discoloration after 30 min UV light exposure and the exposed areas are easily seen in the STXM image. In contrast, PFSA (Fig. 8b) does not show any discoloration after 30 min exposure and the STXM image has uniform signal over the whole UV/SR irradiated area. Table 2 summarizes the thickness of the damaged areas determined by UV-SR after 30 min exposure and by STXM.

STXM: chemical changes of PS films from UV/air damage. The C 1s and O 1s spectra of PS samples UV irradiated in air for 30 min exposure are presented in Fig. 6d and e, while those for 5 min exposure are presented in ESI,† S4 (Fig. S5d and e).
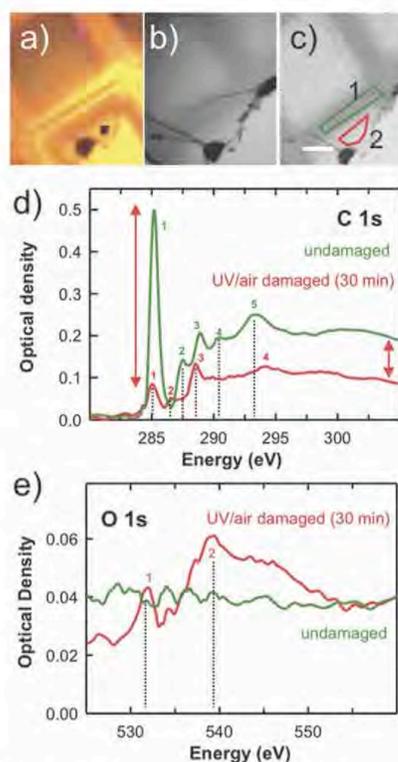
Fig. 6 Optical and STXM characterization of a PS thin film after 30 min of exposure to UV-SR illumination. (a) Visible light image (15×) recorded at the beginning of the measurement. A TEM Cu grid was used as a mask to expose only certain areas and leave others unexposed. (b) Visible light image (50×) of the same area after the UV-SR measurements (the TEM Cu grid has been removed). (c) STXM transmission image at 285.2 eV of the same area. Scale bar is 20 μm. (d) C 1s spectra of the undamaged (green) and strongly damaged (red) areas, indicated in (c). (e) O 1s spectra of the undamaged (green) and damaged (red) areas indicated in (c).

This journal is © the Owner Societies 2018

Phys. Chem. Chem. Phys., 2018, 20, 16625–16640 | 16631
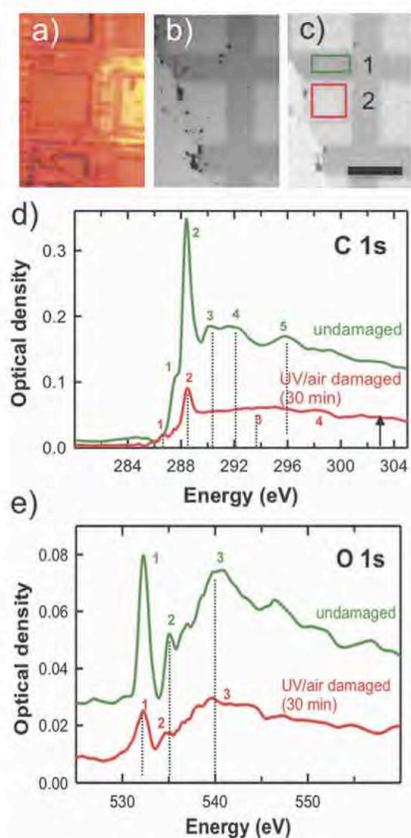
Fig. 7 Characterization of a PMMA thin film after 30 min of exposure to UV-SR illumination. (a) Visible light image (15×) recorded during the measurements. A TEM Cu grid was used as a mask to expose only certain areas and leave others unexposed. (b) Visible light image (50×) of the same area after the UV-SR measurements (TEM grid has been removed). (c) STXM transmission image at 288.4 eV of the same area. Scale bar is 50 μm. (d) C 1s spectra of the damaged (red) and undamaged (green) areas measured at the locations indicated in (c). (e) O 1s spectrum of the damaged (red) and undamaged (green) areas indicated in (c).

Fig. 8 Characterization of a PFSA thin film after 30 min exposure to UV-SR illumination. (a) Visible light image (15×) recorded during the measurements. A TEM Cu grid was used as a mask to expose only certain areas and leave others unexposed. (b) Visible light image (50×) of the same area after the UV-SR measurements (TEM grid has been removed). (c) STXM transmission image at 690 eV of the same area. Scale bar is 20 μm. The area in the red rectangle is where the PFSA film was UV illuminated while the green rectangle was un-exposed as it was under the TEM grid. (d) STXM C 1s spectrum of the un-exposed (green) and exposed (red) areas (see c). (e) STXM F 1s spectrum of the un-exposed (green) and exposed (red) areas (see c).

Energies and spectral assignments are summarized in Table S1 (ESI,† S4). PS consists of phenyl functional groups attached to an aliphatic main chain (see Scheme 1). The chemical formula of PS is $(C_8H_8)_n$, with monomer molecular mass $M_r = 104$ g mol^{-1} and a gravimetric density of 1.04×10^3 kg m^{-3}. After the 5 min exposure (Fig. S5d, ESI†), there is a small reduction in the intensity of the C 1s → $1\pi^*_{C=C}$ transition at 285.2 eV (peak 1) while a much larger reduction is observed upon 30 min exposure (Fig. 6d), indicating extensive damage to the phenyl groups. It is also possible that new C=C bonds are formed in the main chain, which would generate signal at 285 eV and partly compensate for phenyl group damage.[25] The C 1s → $2\pi^*$ transition present at 287.5 eV[46] (peak 2) in undamaged PS (Fig. 6d) is nearly absent

after 30 min UV/air exposure (Fig. 6d), consistent with extensive degradation of the phenyl groups. Also, in the 30 min exposed PS, there is reduced intensity and a shift to higher energy of the peaks at 294 (peak 5 in undamaged → peak 4 in damaged spectrum) and 301 eV which are C 1s(ring) → $\sigma^*_{C=C}$ transitions characteristic of 6-membered unsaturated rings.[46] A new peak appears at 286.6 eV (peak 2 in the damaged spectrum) after 30 min exposure, which corresponds to C 1s(C=O) → $\pi^*_{C=O}$ transitions, indicating that C=O bonds are formed. C 1s (C=O) → $\pi^*_{C=O}$ transitions occur between 286–290 eV for other polymers that have C=O functional groups attached to a chain which also

16632 | *Phys. Chem. Chem. Phys.*, 2018, **20**, 16625–16640

This journal is © the Owner Societies 2018

Table 2 Thickness (nm) of spin coated films of PS, PMMA and PFSA thin films determined by UV-SR and STXM after 30 min exposure (from Fig. 2 and 6–8)

Material	Thickness (nm)		Ratio UV-SR/ STXM	% difference[d]
	UV-SR ±0.2	STXM		
PS	40.2	35 ± 1[c]	1.15 ± 0.03	12.9 ± 0.4
30 min UV PS[a]	17.5	26.3 ± 0.6	0.67 ± 0.02	−50.3 ± 1.3
PMMA	34.3	30.9 ± 0.6[c]	1.11 ± 0.02	9.9 ± 0.2
30 min UV PMMA[b]	18.2	12.8 ± 0.4	1.42 ± 0.05	29.7 ± 1.0
PFSA	52.0	51.9 ± 0.5[c]	1.00 ± 0.01	0.19 ± 0.00
30 min UV PFSA	51.9	51.3 ± 0.6	1.01 ± 0.01	1.16 ± 0.01

[a] Based on derived chemical formula of $C_8O_4H_8$ for 30 min UV/air damaged PS. [b] Utilized derived chemical formula of $C_5O_4H_8$ for PMMA. [c] STXM thickness determined in adjacent area. [d] Percentage calculated by as $(1 - STXM/UV\text{-}SR) \times 100$.

has pendant phenyl groups.[47] Clearly a new chemical species has been formed after 30 min UV/air exposure. In particular, although initially there was very little or no oxygen (Fig. 6e and Fig. S5e, ESI†), an O 1s signal appears even after only 5 min of exposure (Fig. S5e, ESI†), and the O 1s signal increases dramatically with further UV-SR exposure in air. After 30 min, a well-developed O 1s spectrum exists which is dominated by a peak at 531.6 eV (Fig. 6e, peak 1). That peak is the O 1s $(C=O) \to \pi^*_{C=O}$ counterpart to the C 1s $\to \pi^*_{C=O}$ transition at 286.6 eV (Fig. 6d, peak 2 damaged curve).[48]

The mass loss can be assessed qualitatively from the change in the C 1s continuum intensity. In order to use STXM to determine the thickness of the UV-SR damaged areas a new $OD1(E)$ spectrum was constructed by changing the net-chemical formula to incorporate oxygen (Fig. S6, ESI†). The net-chemical formula accounts for all chemical species absorbing light in the beam cross-section. Initially, there is only PS in the UV-SR irradiated area, but after UV/air damage there is residual PS and the damage product(s). The O-species can be distributed over the film volume or concentrated at the air/film interface. For the 30 min exposed area, the O/C ratio was 0.5, while for undamaged PS the O/C ratio is 0. The changed elemental composition was determined from a simultaneous consideration of the C 1s and O 1s continuum jumps (Fig. S6, ESI†). The appended spectrum was least square fit to match its pre- and post-edge signal to that of the spectrum of a component mass absorption coefficient $\mu_i(E)$ calculated for the net-chemical formula $C_xO_yH_z$. The numbers of C and O atoms ($x_q = x$, y in ESI,† S2) were chosen to minimize the cumulative residual of the least square fit to the pre- and post-edge regions. The net-chemical formula of UV/air damaged PS was found to be $(C_8O_4H_8)_n$. Using this chemical formula, the C 1s and O 1s $OD1(E)$ reference spectra of UV-damaged PS were obtained from the 30 min exposed sample. Based on this $OD1(E)$ and assuming no change in density, the thickness of the UV damaged area was calculated to be 23 nm, compared to 35 nm of the adjacent pristine (non-damaged) PS (see Table 2), indicating the film thickness decreased by 34% after 30 min UV/air exposure. Note that the intensity of the 285.15 eV $\pi^*_{C=C}$ peak decreases to ∼20% of the original intensity after 30 min UV/air exposure whereas about 50% of the carbon remains based

on the C 1s continuum intensity at 328 eV (see arrows in Fig. 6d). These results indicate drastic bond re-configuration.

STXM: chemical changes of PMMA films from UV/air damage. The C 1s and O 1s spectra of PMMA samples UV/air irradiated for 30 min are presented in Fig. 7d and e while those for 5 min exposure are presented in ESI,† S4 (Fig. S7d and e, ESI†). Energies and spectral assignments are summarized in Table S2 (ESI,† S4). PMMA has a methyl ester functional group and a methyl group attached to the same carbon of an aliphatic main chain (see Scheme 1). The chemical formula of PMMA is $(C_5O_2H_8)_n$, with a molecular mass $M_r = 100$ g mol^{-1}, and a gravimetric density of 1.18×10^3 kg m^{-3}. The main peak at 288.45 eV is the C 1s$(C=O) \to \pi^*_{O-C=O}$ ester transition (peak 2).[27,47] Its intensity is slightly reduced after 5 min (Fig. S7d, ESI†) and significantly reduced after 30 min UV exposure (Fig. 7d), indicating the ester side chains are removed, probably with production of CO_2, some of which escapes the sample. The C 1s(C–H) $\to \sigma^*_{C-H}$ transition, seen as the small shoulder at 287.6 eV (peak 1 in undamaged spectrum),[47] also decreases in intensity with UV/air exposure. The C 1s(C–C) $\to \sigma^*_{C-C}$ is a broad feature centered around 291.9 eV[47] (peak 4 in undamaged spectrum) that is no longer visible after 30 min exposure (Fig. 7d). A small peak appears at 286.7 eV (peak 1 in damaged spectrum) which could be related to formation of aldehydic C=O bonds. Changes are also observed in the O 1s spectrum (Fig. 7e). The O 1s$(C=O) \to \pi^*_{O-C=O}$ peak at 532.3 eV (peak 1), and the O 1s$(OCH_3) \to \pi^*_{O-C=O}$ peak[48] at 535.2 eV (peak 2) both decrease (Fig. 7e), consistent with loss of the ester group.[49,50]

After 30 min exposure the C 1s continuum intensity of PMMA decreased by >50% when compared to the adjacent undamaged area, which indicates extensive mass loss and a >50% decrease in thickness. Quantitative thickness analysis with STXM (Table 2) shows that the undamaged PMMA film is 31 nm thick while the damaged PMMA is 11 nm thick (assuming the damaged and un-damaged material have the same density). The new net-chemical formula for the 30 min UV/air radiation damaged area is $C_5O_4H_8$, obtained by the same method used to analyze the composition of the damaged PS, presented above. Fig. S8 (ESI†) presents the simultaneous analysis of the C 1s and O 1s spectra of undamaged and 30 min UV/air damaged PMMA. For the damaged area the O/C elemental ratio was found to be 0.8, while for the non-damaged PMMA area O/C was 0.4. The C 1s and O 1s spectra (Fig. 7e and Fig. S8, ESI†) of the damaged area indicate extensive loss of the ester C=O bonds but the net-chemical formula of $C_5O_4H_8$ indicates an increased O/C ratio (note that both C and O amounts decrease with UV damage). This can be explained by a more rapid loss of C than O. Based on STXM analysis with the estimated formula for the UV damaged PMMA, there is a 65% reduction in thickness in the UV damaged area, relative to the adjacent un-damaged area. This is consistent with results from UV-SR which determined a 50% decrease in thickness (Fig. 3a).

STXM: UV/air does not damage PFSA films. The C 1s and F 1s spectra of the unexposed and the 30 min UV/air exposed areas of PFSA are presented in Fig. 8d and e. Energies and spectral assignments are summarized in Table S3 in ESI,† S4.

This journal is © the Owner Societies 2018

Phys. Chem. Chem. Phys., 2018, **20**, 16625–16640 | **16633**

The PFSA used in this study has a long side chain, an equivalent weight (EW) of 1100, and a chemical formula of $S_1C_{20}O_5F_{39}H$ with $M_r = 1094$ g mol^{-1}, and a gravimetric density of 2.00×10^3 kg m^{-3}. PFSA consists of a polytetrafluoroethylene (PTFE) backbone with perfluorinated, sulfonate-terminated side chains containing CF, CF_2, CF_3, ether (–O–) and sulfonic acid groups (see Scheme 1). The interpretation of the C 1s and F 1s spectra of PFSA[51] are similar to those of polytetrafluoroethylene (PTFE) and polyvinyldifluoride (PVDF).[52] The strongest C 1s peaks at 292.4 eV and 295.5 eV (peaks 2 and 3 in the C 1s edge) and F 1s peaks at 689.9 eV and 693.9 eV (peaks 1 and 2 in the F 1s edge) are due to 1s → σ*$_{C-F\perp}$ and 1s → σ*$_{C-F\parallel}$ transitions respectively, where the indicated orientation of the upper level is relative to the main polymer chain direction.[51] These transitions are particularly sensitive to ionizing radiation, undergoing damage and mass loss/thickness decrease.[43]

Surprisingly, a 30 min UV/air exposure had no effect on thickness (Table 2), optical response (Fig. S9, ESI†), or the C 1s or F 1s spectra of PFSA (Fig. 8). After UV exposure, there is no change to the C 1s and F 1s spectra when compared to adjacent undamaged areas, consistent with the same thickness of the two regions within the experimental error (51 and 52 nm, respectively, determined from STXM – see Table 2). The raw UV-SR data for exposures of PFSA up to 30 min is shown in Fig. S9 (ESI†). The spectra for all exposure times up to 30 min are identical, consistent with the thickness not changing with UV-SR exposure time. We speculate that the lack of damage when PFSA is UV/air irradiated is the result of negligible UV absorption by PFSA in the 250–400 nm range.[53] In principle, PFSA does absorb UV light in the 200–250 nm range[53] which the UV lamp in the Filmetrics UV-40 unit supplies, but it does not reach the sample due to the ~250 nm low wavelength cutoff of the fiber optic transport system.

Correlating UV-SR and STXM thickness measurements

Thickness measurements were performed on freshly prepared spin coated samples of PS, PMMA and PFSA of at least two different thicknesses. Several areas in each sample (with only underlying SiNx) were either first measured with UV-SR and then STXM, or vice versa. A single UV-SR thickness measurement took no longer than 5 s total exposure for all operations. UV-SR measurements were taken from 1–3 adjacent points. STXM was recorded from areas of ~40 μm × 40 μm, which included the same area where the low-dose UV-SR data was measured (see Fig. S1, ESI†). A defocused beam spot (>0.5 μm) and no-damage conditions were used. The thicknesses determined by UV-SR and STXM for each sample are plotted against each other in Fig. 9 with numerical values listed in Table 3. Linear correlation analysis of this data is presented in ESI,† S5 (Fig. S10 and Table S4). For all film thicknesses, there is an excellent linear correlation of the sample thickness determined by the two methods ($R^2 = 0.997$, 1.00, 1.00 for PS, PMMA, PFSA respectively). However, the UV-SR thickness values for samples thicker than 100 nm are systematically higher than the STXM determined values (see Fig. 9). The average difference of thicknesses for all 3 materials determined by the two techniques is 10%. For PFSA, the average difference of thicknesses
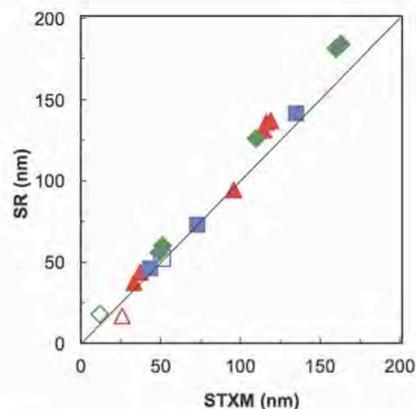
Fig. 9 Plot of thickness of PS, PMMA, and PFSA thin films (both undamaged and UV/air damaged) determined by UV-SR versus those derived from STXM. Table 3 lists numerical values. Thicknesses of the UV/air exposed areas are from Fig. 2 are the damaged areas. These values were determined by UV-SR before and after exposure, and by STXM from adjacent non-damaged and the UV/air damaged areas. All closed symbols represent undamaged materials, while open symbols represent the UV/air 30 min exposed areas. Undamaged: ▲ = PS, ◆ = PMMA, and ■ = PFSA. UV/air 30 min exposed: △ = PS, ◇ = PMMA, □ = PFSA.

is only 2.8% (which is within 1 standard deviation), while for PS and PMMA the average difference is 11% and 13%, respectively, which is approximately 2 standard deviations. If STXM measurements were done before UV-SR, or vice versa, the results were the same.

Thicknesses determined by STXM and UV-SR for the 30 min UV/air damaged samples of PS, PMMA and PFSA in Fig. 6–8 are also plotted in Fig. 9 and listed in Table 3. The difference between STXM and UV-SR thickness values for UV/air damaged PS (53%) and PMMA (33%) is much larger than for the minimal exposure measurements. These differences may be related to density changes in the modified material and uncertainty of the new chemical composition. When plotted against the minimal exposure measurements, the correlated thicknesses of the UV damaged areas are consistent with the general trend of a linear relationship between all of the UV-SR and STXM measurements.

Discussion

Film thickness determination and evolution with UV/air exposure time

When measured under negligible damage conditions, the film thicknesses measured by UV-SR and STXM differ by less than 15% for PS and PMMA and less than 5% for PFSA. The differences between the two methods are not large. In particular, less than 5% systematic difference for PFSA justifies the use of STXM to measure the effective thickness of PFSA ionomer in dispersed CL electrodes for fuel cell applications and supports the use of STXM as a method for quantitative mapping of ionomer distributions in CLs.[1,2] When radiation damage from UV is significant, film

16634 | Phys. Chem. Chem. Phys., 2018, 20, 16625–16640

This journal is © the Owner Societies 2018

Table 3 Thickness (nm) of spin coated films of PS, PMMA and PFSA thin films determined by UV-SR and STXM using optimized, low-damage conditions

Material[a,b,c]	Thickness (nm)		Ratio	% difference[d]
	UV-SR $\pm$ 0.2	STXM $\pm$ 0.5	UV-SR/STXM	
PS 1% A	43.7	37.2	1.17 $\pm$ 0.02	14.9 $\pm$ 0.2
PS 1% B	37.6	33.5	1.12 $\pm$ 0.02	10.9 $\pm$ 0.2
PS 2%*	94.6	95.5	0.99 $\pm$ 0.01	−1.00 $\pm$ 0.01
PS 2.6% A*	131	114.7	1.14 $\pm$ 0.01	12.4 $\pm$ 0.1
PS 2.6% B*	137	118.8	1.15 $\pm$ 0.01	13.3 $\pm$ 0.1
PS 2.6% C*	136	116.3	1.17 $\pm$ 0.01	14.5 $\pm$ 0.1
PMMA 2% A	59.9	51.1	1.17 $\pm$ 0.01	14.7 $\pm$ 0.2
PMMA 2% B	56.1	48.9	1.15 $\pm$ 0.01	12.8 $\pm$ 0.1
PMMA 3%*	126	110	1.15 $\pm$ 0.01	12.7 $\pm$ 0.1
PMMA 4% A	184	163	1.129 $\pm$ 0.004	11.40 $\pm$ 0.04
PMMA 4% B	181	160	1.131 $\pm$ 0.004	11.60 $\pm$ 0.04
PFSA 4%	141	135	1.044 $\pm$ 0.004	4.30 $\pm$ 0.02
PFSA 2% A	72.6	73.2	0.99 $\pm$ 0.01	−0.80 $\pm$ 0.01
PFSA 2% B	45.9	43.6	1.05 $\pm$ 0.01	5.0 $\pm$ 0.1

[a] Percentage is weight % of the toluene (PS, PMMA) or IPA (PFSA) solution used for spin coating the sample. [b] * indicates STXM measurements were performed first and then UV-SR. [c] A, B, C indicate different regions of the same sample. [d] Percentage calculated as $(1 - \text{STXM/UV-SR}) \times 100$.

Fig. 10 Plot of thicknesses determined by UV-SR using method-i and ii as a function of UV/air exposure using reduced co-ordinates. See text for details. All closed symbols represent PS, and open symbols represent PMMA. Initial thickness determined by UV-SR: $\bigcirc$ = method-ii PS 110 nm (Fig. 4), $\bigcirc$ = method-ii PS 40 nm (Fig. 2), $\blacklozenge$ = method-i PS 49 nm (Fig. 4), $\blacklozenge$ = method-i PS 110 nm (Fig. 4), $\bigcirc$ = method-ii PMMA 34 nm (Fig. 2), $\square$ = method-ii PMMA 92 nm (Fig. 3), $\bullet$ = method-i PMMA 91 nm (Fig. 3), $\triangle$ = method-ii PMMA 49 nm (Fig. 3), $\blacktriangle$ = method-i PMMA 49 nm (Fig. 3), $\blacksquare$ = method-i PMMA (Fig. 5).

thickness is reduced and the chemical structure is modified. UV/air and soft X-ray/He (STXM) irradiation affect the sample differently due to the different environmental conditions, and possibly different nature of the applied radiation. All STXM measurements were made in a He atmosphere at ~ 0.2 atm. It is well known that high doses of soft X-ray cause extensive damage to PMMA[25–27,54] and PFSA.[43] In contrast, PS requires much larger X-ray doses ($>10\times$ higher than that for PMMA) for detectible radiation damage.[25] The Filmetrics UV-SR instrument does not provide a means to exclude air from the intersection of the light beam and the sample and so all UV-SR measurements were made in air at 1 atmosphere pressure.

Exposing a polymer film to UV radiation in air induces photochemical reactions in the bulk of the material and at the air/film interface. The change in PS and PMMA sample thickness with UV/air exposure (Fig. 3–5 and Fig. S10, ESI† which combines all the above) can be described by a thickness depletion rate R:

$$\mathrm{d}h(t)/\mathrm{d}t = R, \text{ where } R < 0 \qquad (4)$$

Assuming the rate is proportional to thickness, $R = -h(t)b$, where b is a constant independent on time. The differential eqn (4) has the following solution:

$$h(t) = h_0 e^{-bt}, \text{ were } h_0 = h(t = 0) \qquad (5)$$

where $h(t)$ is the time dependent film thickness, t is time and b is reciprocal time $\tau = 1/b$, where τ has a meaning of a characteristic time of the decay. The experimental data presented in Fig. 1 and 3–5 for both PS and PMMA are plotted in Fig. 10 with new dimensionless coordinates $X = tb$ and $Y = \ln(h(t)/h_0)$, where the coefficients h_0 and b were found for each given data set by applying a least square fit with respect to the solution (5), see ESI,† S6 and the Table S5. The points for PS and PMMA

materials collapse along one line with insignificant spread, indicating that dynamic eqn (4) describes the mechanism of the thickness decay and its solution (5) is indeed a reasonable approximation of the thickness evolution measured experimentally. Note, this spread does not reflect measurement uncertainties, which are smaller than the size of each symbol.

Our experiments show that b is between ~ 0.006 and ~ 0.03, i.e. it is a small parameter, $b \ll 1$, and thus, the solution (5) can be simplified to the linear form (see ESI,† Section 6.II):

$$h(t) \approx h_0(1 - bt) = h_0 - at \qquad (6)$$

where parameter $a = h_0 b = h_0/\tau$ is a characteristic rate of the thickness decay. Solution (6) is convenient for analysis the mechanics of the material release from the polymer film due to chemical damage.

Whatever chemical reactions occur upon UV/air irradiation, the damage products must escape through the air/film interface in order to change the film thickness. Those mobile species are most likely of low molecular weight. Two possibilities are considered: (a) the reaction products are released at the air/film interface and all damage processes happen in a thin δ layer near the film surface; (b) the radiation damage products are generated through the bulk of the whole film, migrate to the air/film interface, and then leave the film. Case (a) is limited by the product release rate and is constant for any film thickness. Case (b) is limited by the diffusion of the product(s) through the film and depends on the film thickness.

Thorough testing of both models requires mathematical modeling of the chemical reactions on a microscopic level and is not the target for this paper. However, both mechanisms have been explored as a means to describe the experimentally

This journal is © the Owner Societies 2018

Phys. Chem. Chem. Phys., 2018, **20**, 16625–16640 | **16635**
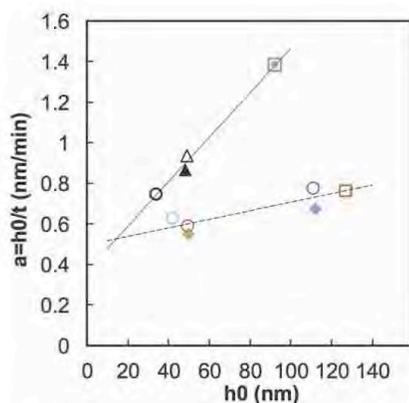
Fig. 11 Rate of reduction of thickness as a function of the initial film thickness for PMMA and PS samples. See text and ESI,† Section 6 for further details. The following samples are on SiNx on SiO₂ frame: ○ = method-ii PS 110 nm (Fig. 4), ◌ = method-ii PS 40 nm (Fig. 2), ◆ = method-i PS 49 nm (Fig. 4), ◆ = method-i PS 110 nm (Fig. 4), ○ = method-ii PMMA 34 nm (Fig. 2), □ = method-ii PMMA 92 nm (Fig. 3), ● = method-i PMMA 91 nm (Fig. 3), Δ = method-ii PMMA 49 nm (Fig. 3), ▲= method-i PMMA 49 nm (Fig. 3), ■ = method-i PMMA (Fig. 5).

observed characteristic thickness decay rate a in terms of an initial thickness of the film h_0 and characteristic decay time τ (or $1/b$). The results of this analysis are presented in ESI,† S6, in particular Table S5. Fig. 11 plots a *versus* the initial film thickness h_0 for all PS and PMMA data. Despite having a similar thickness evolution with exposure time $h(t)$ (as shown in Fig. 10), the thickness decay rate a for PS and PMMA depends on the initial film thickness. The decay rate constant for PS films is much less dependent on initial thickness and thus may be limited mostly by surface product release, model (a). The higher dependence on initial film thickness in the case of PMMA suggests there is a larger contribution of bulk diffusion, consistent with model (b). A similar behavior has been observed for PMMA etched with laser.[55] It is important to note, that the decay rate a is inversely proportional to the characteristic time τ (compare Fig. 11 and Fig. S13, ESI†), *i.e.* the thickest PMMA sample has a shorter characteristic thickness decay time than PS.

When extrapolating the PS and PMMA data in Fig. 11 and (ESI† S6, Fig. S13) to $h_0 = 0$, the initial polymer thickness decay rate a and the characteristic time τ are not zero and both parameters do not depend on the material, within the accuracy of our measurements and the validity of the approximations. The parameters $a^* = a(h_0 = 0)$ and $\tau^* = \tau(h_0 = 0)$ could be related to the processes occurring at the surface of the film and the release of the chemical products of the UV damage from the film surface since it depends on the products – not on the initial materials. Thus, it is non-specific and it must have some non-zero value of the rate of the material release. Below we estimate the material removal flux q^* corresponding to this non-specific product release from the film surface. The number

of molecules removed is $N = qSt$, where S is the surface area from which N molecules are removed over time t. Also $N = m/M_r$, where m is the removed mass, $m = \rho V$ and M_r is the molecular mass of the removed molecules. The removal flux q is simplified to:

$$q = (\rho/M_r) \times (h/t) \quad \text{or} \quad q^* = a^*\rho/M_r \qquad (7)$$

This approach disregards the complexity of the photo-chemical reactions involved and the identity of the low molecular weight damage products. Eqn (7) is defined for the removed mass for all products of damaged PS and PMMA. For the sake of estimation, we assume: $\rho \sim 1$ g cm^{-3} and $M_r \sim 100$ g mol^{-1}, $\rho/M_r \sim 0.2$ molecule nm^{-3}. As estimated from Fig. 11, $a^* \sim 0.4$ nm min^{-1} is the non-specific flux of molecule removal from the film surface, which corresponds to a rate of $q^* \sim 1.3 \times 10^{-3}$ molecule s^{-1} nm^{-2} or 1 molecule leaving from each 1 nm^{+2} of the film surface every ~ 750 s. For comparison, the highest flux plotted in Fig. 11 corresponds to a removal rate of $\sim 4.7 \times 10^{-3}$ molecule s^{-1} nm^{-2} or 1 molecule nm^{+2} every ~ 210 s. The above material removal is quite slow and it requires many seconds to remove a single molecule even for the highest observed removal rate. This correlates with the observation that PS and PMMA develop macroscopically noticeable damage only when they are left under the exposure of the sun for many months or years.

The fact that the polymer film has a limiting thickness decay rate a^* which is non-specific (or nearly non-specific) with respect to polymer material/chemistry is not expected from eqn (7) and can't be predicted from the solution (8). Indeed, the effect of UV/air irradiation is material specific. We attribute the non-specific nature of the limiting thickness decay rate (here and after thickness depletion rate) to a common rate of impingement at the film surface of molecules sufficiently energetic to desorb the low molecular weight UV damage products. Following ref. 56, we estimate the impingement rate of any type of molecule at 1 atmosphere pressure as $\sim 10^9$–10^{10} molecule s^{-1} nm^{-2}. Comparing this with $\sim 10^{-3}$ molecule s^{-1} nm^{-2} removed molecules from the surface we conclude that only a small fraction of the damage products have enough kinetic energy to leave the surface.

Chemistry of UV/air radiation damage

UV photons must be absorbed in order to cause chemical changes. The probability of absorption will in turn depend on the photon energy. The subsequent generation of low molecular weight damage products or radicals[30] will depend on both the net absorption and a complex set of secondary reactions, probably involving electrons, ions and radicals. In order to remove material and thus result in thickness reduction, the damage products must have sufficient kinetic energy to reach and escape from the polymer surface. One effective energy source for material removal could be collisions of energetic gas molecules with the polymer surface. In that case, the molecular mass of the damage product could be a limiting factor: if it is high, or if the radiation-modified species is still attached to the polymer backbone, then thickness erosion will not occur.

The energy range of the light used in UV-SR that is most likely to damage polymers is from 250 nm (4.95 eV) to 400 nm

16636 | *Phys. Chem. Chem. Phys.*, 2018, **20**, 16625–16640

This journal is © the Owner Societies 2018

(3.10 eV). Transitions $\pi \to \pi^*$ and $n \to \pi^*$ associated with specific C=C or C=O bonds occur in this region.[57] Exciting the C=C bonds in PS by using UV-SR in air yields a completely different chemical transformation compared to using 285.1 eV soft X-rays, which corresponds to the C 1s $\to \pi^*_{C=C}$ absorption as shown in Wang et al., 2009.[25] Soft X-ray excitation induces only a small reduction of the C 1s $\to \pi^*_{C=C}$ intensity and does not lead to mass loss.[25] In contrast, UV excitation in air causes noticeable changes of both the π^* peak and continuum intensities (see Fig. 6d). The combination of oxygen from air with UV irradiation causes significant damage to the PS, with a high rate of C=C bond dissociation, a reduced C 1s continuum intensity due to mass loss, and clear proof of the formation of C=O bonds (peaks at 288.5 and 539 eV – see Fig. 6b and e). This discrepancy is due to the presence of oxygen in UV-SR which significantly modifies radiation damage of PS, changing both the extent of mass loss and the nature of the chemical changes. A similar effect of oxygen on soft X-ray damage has been noted by Coffey et al.[26]

Here we note some remarkable alignments among results of (i) our UV/air measurements and (ii) UV-O plasma treated PS, where the changes were studied by NEXAFS.[58] In the latter work, ozone generated in the plasma significantly accelerates PS radiation damage. The $\pi^*_{C=C}$ signals are reduced, and $\pi^*_{C=O}$ signals are generated.[58] Therefore, we assume that UV/air exposure in the Filmetrics instrument produces ozone in close proximity to the polymer/air interface.

On the other hand, soft X-rays in vacuum rapidly damage PMMA causing destruction of the C 1s $\to \pi^*_{C=O}$ bonds, thickness decay (net loss of material), and formation of C 1s $\to \pi^*_{C=C}$ bonds.[25,26] Air or active oxygen species such as ozone are not needed to cause soft X-ray radiation damage to PMMA since oxygen radicals can be generated from the oxygen in PMMA. UV/air irradiation of PMMA also causes substantial damage, which is probably due to an ozonolysis mechanism. Comparing the NEXAFS spectra of the undamaged and UV/air damaged PMMA (Fig. 7) to those reported by Wang et al.[25] using soft X-rays at 300 eV, the C 1s $\to \pi^*_{C=O}$ peak at 288.45 eV is still present in soft X-ray damaged PMMA despite severe mass loss. The shapes of the C 1s and O 1s spectra of damaged and undamaged PMMA (Fig. S7, ESI†) are surprisingly similar, differing mainly in the oxygen composition: $C_5O_{1.3}H_8$ for non-damaged PMMA and $C_5O_{2.5}H_8$ for damaged PMMA. Therefore, oxygen incorporation into damaged PMMA is occurring, probably in a way similar to that of UV/air irradiated PS.

The thickness depletion rates for UV/air irradiated PS and PMMA measured by UV-SR and the major NEXAFS spectral peaks are shown in Fig. 12. For PS, the thickness depletion rate (as measured by UV-SR) is similar to the rate of C=C bond scission, which we define as a ratio of the OD at 285.1 eV (C=C) divided by the OD at 320 eV, represented by the dashed line in Fig. 12a, producing a damage product rich in oxygen (dash-dotted line). The phenyl ring destruction by UV/air exposure corresponds to a process rate-limited by molecule removal at a fixed rate through the surface. For PMMA, the reduction in the $\pi^*_{C=O}$ peak intensity occurs at approximately the same rate as thickness depletion (Fig. 12b). There is a small difference between the
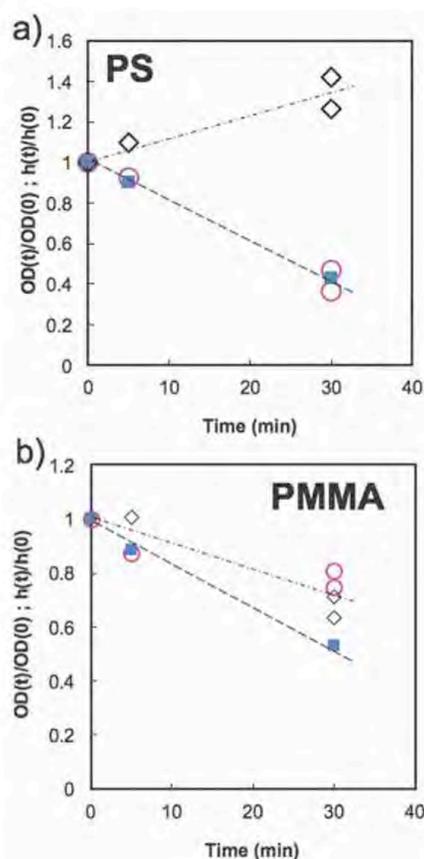
Fig. 12 Thickness measured by UV-SR and NEXAFS spectral feature evolution with time due to UV damage for (a) PS and (b) PMMA. For (a) ○ is the OD at 285.1 eV (C=C) and for (b) the same symbol represents the OD at 288.4 eV (C=O). Both are divided by the OD at 320 eV (total carbon content) of the UV damaged area normalized to the undamaged PS. ◇ is the OD at 538.9 eV divided by the OD at 569 eV (total oxygen content) of the UV damaged area normalized to the undamaged polymer. ■ is the UV-SR thickness for the damaged area normalized to the undamaged polymer. All dashed and dash-dotted lines are qualitative trends for the UV-SR thickness and STXM NEXAFS signals, respectively.

thickness depletion rate measured by UV-SR and the rate of reduction of the $\pi^*_{C=O}$ peak intensity in PMMA. This difference can be due to additional structural changes (i.e. scissions of C–O and C–C bonds) and diffusion of the radical species that generate damaged products throughout the bulk of the PMMA film.

Summary

Two methods of thickness measurements, one based on X-ray absorption, the other based on UV-IR optical interference, were compared. Thicknesses of polymer thin films of PS, PMMA and

This journal is © the Owner Societies 2018

Phys. Chem. Chem. Phys., 2018, 20, 16625–16640 | 16637

PFSA, prepared by spin-coating, were determined using soft X-ray spectromicroscopy (STXM) and the ultraviolet spectral reflectance (UV-SR) methods. It was shown that there is a limit to the allowable UV exposure in air for meaningful results. While it is easy to make single point measurements within the allowable UV exposure, this is not the case for typical mapping applications of the instrument in which many measurements are made at an array of points all within the same UV-illuminated area (500 μm diameter). Since the UV-illuminated area is much larger than the size of the analysis spot (7 μm diameter), a complete map the size of the illuminated area takes 30 minutes or longer, by which time the UV-radiation damage discussed in the paper will have occurred.

When working below the exposure time limit, the chemistry of polymer material is not altered and the average difference between the film thicknesses measured by STXM and UV-SR is below 15% for 30–185 nm thick PS and PMMA films, and <5% for PFSA films. The observation that polymer film thicknesses derived by UV/SR and STXM are similar is obtained for the first time, providing strong experimental validation of the use of STXM for quantitative determination of ionomer in the cathode layers of PEM-FC.

When long UV/air exposure times were used, the initial chemistry of PS and PMMA films was significantly changed while PFSA films were not affected. Using an exponential depletion model, the rates of PS film depletion could be explained by surface/air interface release of photo-chemical radiation damage products. The higher depletion rates for PMMA suggests a larger contribution of bulk diffusion of the photo-chemical radiation damage products. The depletion rate, a^*, for small thicknesses was found to be similar for both PS and PMMA polymers. A combination of the NEXAFS spectroscopic analysis with the model of thickness depletion and with the results reported in the literature[25,58] suggest that the chemical changes induced by UV/air radiation for PS and PMMA are due to incorporating oxygen from air into the polymer material facilitated by UV generated ozone. We speculate that this effect triggers photo-chemical reactions that significantly damage PS and PMMA. For thickness measurements of polymers sensitive to ozone and oxygen radicals using ultraviolet spectral reflectance (UV-SR) methods, we recommend to blanket the beam-sample area with an inert gas, or to construct a vacuum enclosure.

Conflicts of interest

The authors declare no competing financial interests.

Acknowledgements

References

1 D. Susac, V. Berejnov, J. Stumper and A. P. Hitchcock, STXM Characterization of PEM Fuel Cell Catalyst Layers, *ECS Trans.*, 2012, **50**(2), 405–413.

2 D. Susac, V. Berejnov, A. P. Hitchcock and J. Stumper, STXM Study of the Ionomer Distribution in the PEM Fuel Cell Catalyst Layers, *ECS Trans.*, 2011, **41**, 629–635.

3 H. Ade and A. P. Hitchcock, NEXAFS Microscopy and Resonant Scattering: Composition and Orientation Probed in Real and Reciprocal Space, *Polym. J.*, 2008, **49**(3), 643–675.

4 I. N. Koprinarov, A. P. Hitchcock, C. T. McCrory and R. F. Childs, Quantitative Mapping of Structured Polymeric Systems Using Singular Value Decomposition Analysis of Soft X-Ray Images, *J. Phys. Chem. B*, 2002, **106**(21), 5358–5364.

5 C. Ton-That, A. G. Shard and R. H. Bradley, Thickness of Spin-Cast Polymer Thin Films Determined by Angle-Resolved XPS and AFM Tip-Scratch Methods, *Langmuir*, 2000, **16**(5), 2281–2284.

6 R. F. M. Lobo, M. A. Pereira-da-Silva, M. Raposo, R. M. Faria, O. N. Oliveira, M. A. Pereira-da-Silva and R. M. Faria, Thickness Measurements of Ultra-Thin Multilayer Polymer Films By Atomic Force Microscopy, *Nanotechnology*, 2000, **10**, 389–393.

7 E. Tekin, E. Holder, V. Marin, B. J. De Gans and U. S. Schubert, Ink-Jet Printing of Luminescent Ruthenium- and Iridium-Containing Polymers for Applications in Light-Emitting Devices, *Macromol. Rapid Commun.*, 2005, **26**(4), 293–297.

8 Y. Fainman, E. Lenz and J. Shamir, Optical Profilometer: A New Method for High Sensitivity and Wide Dynamic Range, *Appl. Opt.*, 1982, **21**(17), 3200–3208.

9 M. Foster, M. Stamm and G. Reiter, X-Ray Reflectometer for Study of Polymer Thin Films and Interfaces, *Vacuum*, 1990, **41**(4–6), 1441–1444.

10 E. Chason and T. M. Mayer, Thin Film and Surface Characterization by Specular X-Ray Reflectivity, *Crit. Rev. Solid State Mater. Sci.*, 1997, **22**, 1–67.

11 K. Vedam, Spectroscopic Ellipsometry: A Historical Overview, *Thin Solid Films*, 1998, **313–314**, 1–9.

12 S. Kohli, C. D. Rithner, P. K. Dorhout, A. M. Dummer and C. S. Menoni, Comparison of Nanometer-Thick Films by x-Ray Reflectivity and Spectroscopic Ellipsometry, *Rev. Sci. Instrum.*, 2005, **76**(2), 10–15.

13 D. E. Aspnes, Spectroscopic Ellipsometry—A Perspective, *J. Vac. Sci. Technol., A*, 2013, **31**(5), 058502.

16638 | *Phys. Chem. Chem. Phys.*, 2018, **20**, 16625–16640

This journal is © the Owner Societies 2018

118

14 E. A. Irene, *A Brief History and State of the Art of Ellipsometry. In Ellipsometry at the Nanoscale*, Springer Berlin Heidelberg, Berlin, Heidelberg, 2013, pp. 1–30.

15 D. Cattelan, C. Eypert, M. Kloul, M. Gaillet, J.-P. Gaston, R. Seitz, A. Shagaleeva and M. Stchakovsky, *Thin Film Applications in Research and Industry Characterized by Spectroscopic Ellipsometry. In Ellipsometry at the Nanoscale*, Springer Berlin Heidelberg, Berlin, Heidelberg, 2013, pp. 629–667.

16 C. M. Stafford, C. Harrison, K. L. Beers, A. Karim, E. J. Amis, M. R. VanLandingham, H. C. Kim, W. Volksen, R. D. Miller and E. E. Simonyi, A Buckling-Based Metrology for Measuring the Elastic Moduli of Polymeric Thin Films, *Nat. Mater.*, 2004, **3**(8), 545–550.

17 M. W. Meyer, V. H. T. Nguyen and E. A. Smith, Scanning Angle Raman Spectroscopy Measurements of Thin Polymer Films for Thickness and Composition Analyses, *Vib. Spectrosc.*, 2013, **65**, 94–100.

18 Y. Berdichevsky, J. Khandurina, A. Guttman and Y. H. Lo, UV/Ozone Modification of Poly(Dimethylsiloxane) Microfluidic Channels, *Sens. Actuators, B*, 2004, **97**(2–3), 402–408.

19 H. Lu, W. Chen and T. P. Russell, Relaxation of Thin Films of Polystyrene Floating on Ionic Liquid Surface, *Macromolecules*, 2009, **42**(22), 9111–9117.

20 L. J. Crawford and N. R. Edmonds, Calculation of Film Thickness for Dip Coated Antireflective Films, *Thin Solid Films*, 2006, **515**, 907–910.

21 A. Zanutta, F. Villa, C. Bertarelli and A. Bianco, Refractive Index Modulation in Polymer Film Doped with Diazo Meldrum's Acid, *Opt. Mater.*, 2016, **58**, 158–163.

22 A. Vital, M. Vayer, T. Tillocher, R. Dussart, M. Boufnichel and C. Sinturel, Morphology Control in Thin Films of PS:PLA Homopolymer Blends by Dip-Coating Deposition, *Appl. Surf. Sci.*, 2017, **393**, 127–133.

23 Filmetrics Inc., Taking the Mystery out of Thin-Film Measurement, 2016.

24 J. Wang, G. A. Botton, M. M. West and A. P. Hitchcock, Quantitative Evaluation of Radiation Damage to Polyethylene Terephthalate by Soft X-Rays and High-Energy Electrons, *J. Phys. Chem. B*, 2009, **113**(7), 1869–1876.

25 J. Wang, C. Morin, L. Li, A. P. Hitchcock, A. Scholl and A. Doran, Radiation Damage in Soft X-Ray Microscopy, *J. Electron Spectrosc. Relat. Phenom.*, 2009, **170**(1–3), 25–36.

26 T. Coffey, S. G. Urquhart and H. Ade, Characterization of the Effects of Soft X-Ray Irradiation on Polymers, *J. Electron Spectrosc. Relat. Phenom.*, 2002, **122**(1), 65–78.

27 T. Beetz and C. Jacobsen, Soft X-Ray Radiation-Damage Studies in PMMA Using a Cryo-STXM, *J. Synchrotron Radiat.*, 2003, **10**(3), 280–283.

28 A. R. Shultz, Degradation of Polymethyl Methacrylate By Ultraviolet Light, *J. Phys. Chem.*, 1961, **65**(6), 967–972.

29 A. Torikai, M. Ohno and K. Fueki, Photodegradation of Poly(Methyl Methacrylate) by Monochromatic Light: Quantum Yield, Effect of Wavelengths, and Light Intensity, *J. Appl. Polym. Sci.*, 1990, **41**(5–6), 1023–1032.

30 E. Yousif and R. Haddad, Photodegradation and Photostabilization of Polymers, Especially Polystyrene: Review, *Springerplus*, 2013, **2**(1), 398.

31 I. Y. Evchuk, R. I. Musii, R. G. Makitra and R. E. Pristanskii, Solubility of Polymethyl Methacrylate in Organic Solvents, *Russ. J. Appl. Chem.*, 2005, **78**(10), 1576–1580.

32 O. S. Heavens, *Optical Properties in Thin Solid Films*, Dover Publications, Inc., New York, NY, 1991.

33 Norcada, X-ray Microscopy Windows Specification Sheet http://www.norcada.com/wp-content/uploads/2013/10/Xray-Window-Specsheet.pdf.

34 A. P. Hitchcock, Soft X-Ray Imaging and Spectromicroscopy, in *Handbook on Nanoscopy*, ed. G. Van Tendeloo, V. D. Dyck and S. J. Pennycook, Wiley-VCH Verlag GmbH & Co. KGaA, 2012, vol. II, pp. 745–791.

35 H. Ade, A. P. Smith, S. Cameron, R. Cieslinski, G. Mitchell, B. Hsiao and E. Rightor, X-Ray Microscopy in Polymer Science: Prospects of a 'New' Imaging Technique, *Polymer*, 1995, **36**(9), 1843–1848.

36 K. V. Kaznatcheev, C. Karunakaran, U. D. Lanke, S. G. Urquhart, M. Obst and A. P. Hitchcock, Soft X-Ray Spectromicroscopy Beamline at the CLS: Commissioning Results, *Nucl. Instrum. Methods Phys. Res., Sect. A*, 2007, **582**(1), 96–99.

37 A. L. D. Kilcoyne, T. Tyliszczak, W. F. Steele, S. Fakra, P. Hitchcock, K. Franck, E. Anderson, B. Harteneck, E. G. Rightor, G. E. Mitchell, A. P. Hitchcock, L. Yang, T. Warwick and H. Ade, Interferometer-Controlled Scanning Transmission X-Ray Microscopes at the Advanced Light Source, *J. Synchrotron Radiat.*, 2003, **10**, 125–136.

38 T. Warwick, K. Franck, J. B. Kortright, G. Meigs, M. Moronne, S. Myneni, E. Rotenberg, S. Seal, W. F. Steele, H. Ade, A. Garcia, S. Cerasari, J. Denlinger, S. Hayakawa, A. P. Hitchcock, T. Tyliszczak, J. Kikuma, E. G. Rightor, H.-J. Shin and B. P. Tonner, A Scanning Transmission X-Ray Microscope for Materials Science Spectromicroscopy at the Advanced Light Source, *Rev. Sci. Instrum.*, 1998, **69**(8), 2964.

39 J. Stöhr, *NEXAFS Spectroscopy*, 1992, vol. 25.

40 B. L. L. Henke, E. M. M. Gullikson and J. C. C. Davis, X-Ray Interactions: Photoabsorption, Scattering, Transmission, and Reflection at E = 50-30,000 EV, Z = 1-92, *At. Data Nucl. Data Tables*, 1993, **54**(2), 181–342.

41 Hitchcock AXis, AXis 2000 is written in Interactive Data Language (IDL). It Is Available Free for Non-Commercial Use from http://Unicorn.Mcmaster.ca/AXis2000.Html, 2016.

42 C. Jacobsen, S. Wirick, G. Flynn and C. Zimba, Soft X-Ray Spectroscopy from Image Sequences with Sub-100 Nm Spatial Resolution, *J. Microsc.*, 2000, **197**(Pt2), 173–184.

43 L. G. D. A. Melo, G. A. Botton and A. P. Hitchcock, Quantification of the Critical Dose for Radiation Damage to Perfluorosulfonic Acid Membranes Using Soft X-Ray Microscopy, *Microsc. Microanal.*, 2015, **21**(1220), 2443–2444.

44 A. Leontowich, *Tunable Focused X-Rays for Patterning and Lithography*, PhD thesis, McMaster University, 2012.

45 A. V. Leontyev, V. I. Kovalev, A. V. Khomich, F. F. Komarov, V. V. Grigoryev and A. S. Kamishan, PMMA and Polystyrene Films Modification under Ion Implantation Studied by Spectroscopic Ellipsometry, *SPIE*, 2003, **5401**(X), 129–135.

This journal is © the Owner Societies 2018

Phys. Chem. Chem. Phys., 2018, **20**, 16625–16640 | **16639**

119

46 J. A. Horsley, J. Stöhr, A. P. Hitchcock, D. C. Newbury, A. L. Johnson and F. Sette, Resonances in the K Shell Excitation Spectra of Benzene and Pyridine: Gas Phase, Solid, and Chemisorbed States, *J. Chem. Phys.*, 1985, **83**(12), 6099.

47 O. Dhez, H. Ade and S. G. Urquhart, Calibrated NEXAFS Spectra of Some Common Polymers, *J. Electron Spectrosc. Relat. Phenom.*, 2003, **128**(1), 85–96.

48 S. G. Urquhart and H. Ade, Trends in the Carbonyl Core (C 1s, O 1s) → Pi*C═O Transition in the near-Edge X-Ray Absorption Fine Structure Spectra of Organic Molecules, *J. Phys. Chem. B*, 2002, **106**(34), 8531–8538.

49 C. Wochnowski, M. A. S. Eldin and S. Metev, UV-Laser-Assisted Degradation of Poly(Methyl Methacrylate), *Polym. Degrad. Stab.*, 2005, **89**(2), 252–264.

50 J. O. Choi, Degradation of Poly(Methylmethacrylate) by Deep Ultraviolet, X-Ray, Electron Beam, and Proton Beam Irradiations, *J. Vac. Sci. Technol., B: Microelectron. Nanometer Struct.--Process., Meas., Phenom.*, 1988, **6**(6), 2286.

51 Z. B. Yan, R. Hayes, L. G. A. Melo, G. R. Goward and A. P. Hitchcock, X-Ray Absorption and Solid-State NMR Spectroscopy of Fluorinated Proton Conducting Polymers, *J. Phys. Chem. C*, 2018, **122**(6), 3233–3244.

52 T. Ohta, K. Seki, T. Yokoyama, I. Morisada and K. Edamatsu, Polarized XANES Studies of Oriented Polyethylene and FIuorinated PolyethyIenes, *Phys. Scr.*, 1990, **41**(4), 150–153.

53 S. H. De Almeida and Y. Kawano, Ultraviolet-Visible Spectra Membrane of Nafion, *Eur. Polym. J.*, 1997, **33**(8), 1307–1311.

54 A. F. G. Leontowich, A. P. Hitchcock, T. Tyliszczak, M. Weigand, J. Wang and C. Karunakaran, Accurate Dosimetry in Scanning Transmission X-Ray Microscopes via the Cross-Linking Thresh-old Dose of Poly(Methyl Methacrylate), *J. Synchrotron Radiat.*, 2012, **19**, 976–987.

55 N. Bityurin, S. Muraviov, A. Alexandrov and A. Malyshev, UV Laser Modifications and Etching of Polymer Films (PMMA) below the Ablation Threshold, *Appl. Surf. Sci.*, 1997, **109**(110), 270–274.

56 *Surface Analysis: The Principal Techniques*, ed. J. C. Vickerman and I. Gilmore, Wiley, 2009.

57 T. L. Cottrell, *The Strengths of Chemical Bonds, Prop. atoms, radicals, Bond*, 2nd edn, 1966, vol. 372(84), pp. 41–53.

58 R. J. Klein, D. A. Fischer and J. L. Lenhart, Systematic Oxidation of Polystyrene by Ultraviolet-Ozone, Characterized by near-Edge X-Ray Absorption Fine Structure and Contact Angle, *Langmuir*, 2008, **24**(15), 8187–8197.

120

Chapter 5

Soft X-ray damage to PFSA and other fluoropolymers

This chapter reports a quantitative study of the chemical and physical changes when spun cast fluoropolymers (PFSA, PTFE and Teflon®AF) are irradiated with controlled doses of monochromatic soft X-rays. STXM was used for generating and analyzing the radiation damage. Structural changes and possible mechanisms are described. Assuming first order kinetics, critical doses for various damage processes are reported. The critical doses were used to identify minimal dose STXM analysis procedures for quantitative mapping of the ionomer in PEMFC cathode catalyst layers.

5.1 Introduction

Chapter 1 introduced the concept of PEM-FC and the importance of the characterization and quantitation of the PFSA in the cathode catalyst layer. Radiation damage to PFSA during analytical microscopies based on ionizing radiation severely limits the analytical information. The objective of the research described in this chapter was to characterize the physical and chemical changes and quantify the radiation damage of PFSA by soft X-rays using STXM. The findings of this chapter have assisted several other projects (see Chapter 8) where STXM was used to quantify the PFSA in the cathode.

In this study, STXM-NEXAFS was used to determine how PFSA changes when it is irradiated with monochromatic X-rays at 320 and 710 eV. Quantitative dose-damage

measurements of PFSA, polytetrafluoroethylene (PTFE) and an amorphous fluoropolymer Teflon^TM AF are reported. Questions of interest include:

i) Assuming first order kinetics model, what is the critical dose (a_c) for various damage processes, including fluorine loss, ether group loss, sulfonate loss, and main chain crosslinking?

ii) Does the a_c for any given process depend on the environment of the sample?

iii) Does the a_c for any given process depend on the analytical method used to measure it?

iv) Does the a_c for any given process depend on the photon energy used to create the damage?

v) For the dominant damage process (fluorine mass loss) does the a_c change as a function of extent of damage?

The critical dose results and comparison of rates of fluorine loss for the three fluoropolymers studied are presented in **Section 5.3. Section 5.4** discusses the mechanisms for chemical damage to PFSA and PTFE. Different parts of the PFSA damage at different rates: fluorine loss dominates, along with loss of sulfonate and ether bonds. There is also formation of new unsaturated C=C bonds, C-O bonds and C=O bonds.

5.2   *Experimental procedures*

PFSA and PTFE dispersions were used in this work. Both dispersions were diluted using isopropanol, IPA, and H_2O (high performance liquid chromatography, HPLC, grade) and spin coated, as described in **section 3.1**. Teflon®AF was microtomed. All samples were deposited on SiNx windows or Cu grids (without a substrate film). **Table 5.1** summarizes the details of the samples used in this chapter, as well as damage patterning conditions and the analytical measurements used for spectroscopy and dose-damage studies. **Table 5.2** summarizes the chemical changes observed and how they were evaluated.

Table 5.1 Samples, properties and data sets for measuring dose-damage properties of PFSA, PTFE and TeflonAF.

set	sample	code	run	Det eff.	Thickness nm	Damage-E_D eV	analysis	Comment
	PFSA Ionomer							
A	Dup 2%	LM130	aSTXM Aug17	C1s (63±4%)	45	320	**S,** C, O, F stacks	Figure 5.1, 5.2, 5.5, 5.8
B	Dup 4%	LM058b	aSTXM Dec17	C1s (44±6%)	170	320	C, O, F stacks	Fig 5.3, 5.4, 5.6, 5.8; Table 5.3
C	Dup 3%	LM163	aSTXM Feb18	C1s (38±5%) F1s (83±3%)	88	320, 710	C, O, F stacks C, O, F images	Table 5.3, Fig. 5.6, 5.8 *active vacuum at E_D 320 eV, Fig 5.7
D	Dup 4%	LM030c	aSTXM Mar16	C1s (54±10%)	210	320	**S,** C, F stacks	Table 5.4
	PTFE							
E	2%	LM147	aSTXM Mar18	C1s (38±5%)	155	320	C, O, F stacks	Table 5.3, 5.4; Fig 5.9-5.12
	Teflon-AF							
F	-	-	aSTXM Mar18	C1s (38±5%)	225	320	C, O, F stacks	Table 5.3, 5.4; Fig 5.9-5.12

Table 5.2 Changes to fluorinated polymers observed by STXM.

Type of change	Visualized at	Quantified by (*)
CF_2-CF_2 amorphization	292.4, 690 eV	OD
Ether loss	540 eV	$OD_{540\ eV}$
Sulfonate loss	540, S 2p	S 2p
C=C creation	285.1 eV	$OD_{285.1\ eV} - OD_{280\ eV}$
C=O creation	286.4, 531.8 eV	-
Carboxylate loss/change	532.2 eV	-
Elemental mass loss	C, F, O 1s edges	integration
Oxidation due to residual O_2 in tank	O 1s edge	integration
Carbon build-up	C 1s edge	Integration
Component loss	C 1s or F 1s edges	Stack analysis(#)

(*) Methods described in **section 3.3.2**
(#) Using internal reference spectrum as described in **section 3.3.2.2**

The CLS ambient STXM (10ID1) (Kaznatcheev et al., 2007) and the polymer STXM (Kilcoyne et al., 2003) at ALS 5.3.2.2 (Warwick et al., 2002) were used for irradiation and subsequent analytical spectromicroscopy. The chemical changes were evaluated using a variety of STXM methods, as explained in **Section 3.3.2**.

5.3   Results

5.3.1   PFSA dose-damage

5.3.1.1 Spectral changes caused by X-ray damage

Figure 5.1a is a STXM OD image at 320 eV of a ~45 nm PFSA thin film before pattern generation at E_D = 320 eV (**Sample set A – see Table 5.1**). There are some 'dirt' particles which are useful for focusing. The dashed square shows the area where a 9-pad damage pattern was burned at 320 eV. **Figure 5.1b** shows the STXM OD image measured at E_A = 292.4 eV after a non-linear 9-pad pattern generation. **Figure 5.1c** presents a histogram of thickness of the undamaged area in **Figure 5.1b**. The $OD_{292.4 \text{ eV}}$ of the pads decreases as the dose increases. The green rectangle in **Figure 5.1b** is a nearly undamaged area (dose ~0.6 MGy, from navigation and pre- and post-damage imaging). The blue outlined pad is a low damage area (20 MGy) while the red outlined pad is the most heavily damaged area (400 MGy).
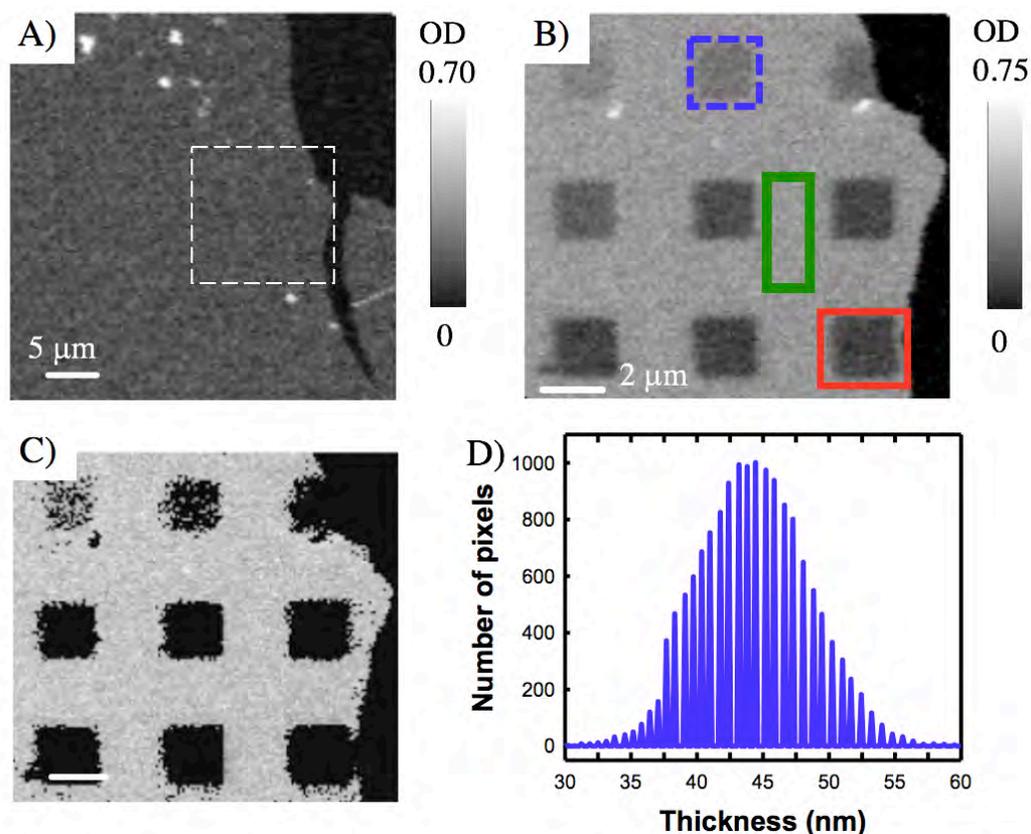
Figure 5.1 (A) STXM OD image at 320 eV over a large area of spun cast PFSA sample set A, measured before damage. **(B)** STXM OD image at E_A = 292.4 eV of a 9-pad pattern burned at E_D = 320 eV in a He environment, into the area indicated as a square in (a). The green rectangle, blue and red squares indicate regions of undamaged, low and heavily damaged areas of the PFSA for which spectra are plotted in Figure 5.2. The calculated absorbed doses are 10, 20, 30, 50, 100, 150, 200, 300 and 400 MGy, for pads 1 through 9. **(C)** same figure as in (b) masked so only undamaged area is shown **(D)** histogram of image (c) showing that the thickness of the spin coated area is 44 ± 4 nm. (CLS aSTXM)

The C 1s, F 1s, O 1s and S 2p spectra from these three regions are presented in **Figure 5.2(a-d)**. The changes in the C 1s spectrum (**Figure 5.2a**) are quite dramatic. With increasing dose the signal below the C 1s onset decreases significantly, since that region is dominated by F 1s valence ionization which decreases due to F mass loss. The peaks at 292.4 and 295.4 eV are

the C 1s (CF$_2$) $\rightarrow$ σ^*_{C-F} ($\perp$) and C 1s $\rightarrow$ σ^*_{C-F} (//) transitions, where the upper level orbital is oriented perpendicular and parallel to the main chain, respectively (Castner et al., 1993; Ziegler et al., 1994; Yan et al., 2018). The shoulder at 298.7 eV arises from C 1s (CF$_2$) $\rightarrow$ σ^*_{C-C} ($\perp$) transitions. All three of these features reduce in intensity and eventually disappear with increasing dose. They are replaced with a broad peak centered at 295 eV, which also exhibits shoulders at 292 eV and 304 eV. The broad feature at 307 eV, due to C 1s (CF$_2$) $\rightarrow$ $\sigma^*_{(C-C)}$ transitions, also disappears in heavily damaged PFSA. In addition, new peaks appear at 285.2 eV which is the C 1s $\rightarrow$ $\pi^*_{C=C}$ transition from C=C formation in the main or side chain, and at 287 eV, which is the C 1s $\rightarrow$ $\pi^*_{C=O}$ transition indicating formation of C=O bonds (Urquhart & Ade, 2002).

Radiation damage by E$_D$ = 320 eV X-rays also causes dramatic changes in the F 1s spectrum (**Figure 5.2b**). At 684 eV, below the onset of F 1s excitation, there is little change in OD. The OD in the pre-F 1s region arises from both C 1s ionization and fluorine valence ionization with also some contribution from O 1s ionization. The amount of carbon changes very little (see the elemental analysis below), but there is extensive fluorine mass loss, which is very apparent from the reduction and merging/disappearance of the two peaks as well as by the reduction in the F 1s continuum intensity. The peaks at 690 and 694 eV are the F 1s $\rightarrow$ σ^*_{F-C} ($\perp$) and F 1s $\rightarrow$ σ^*_{F-C} (//) transitions (Castner et al., 1993; Yan et al., 2018; Ziegler et al., 1994). The changes in the C 1s and F 1s NEXAFS spectra indicates the local structure of the CF$_2$ sites is changed in a way consistent with CF$_2$-CF$_2$ amorphization, since there is no longer any differentiation of σ^*_{F-C} ($\perp$) and σ^*_{F-C} (//) states at both the C 1s and F 1s edges. In addition, there is fluorine loss (F-loss, for short).
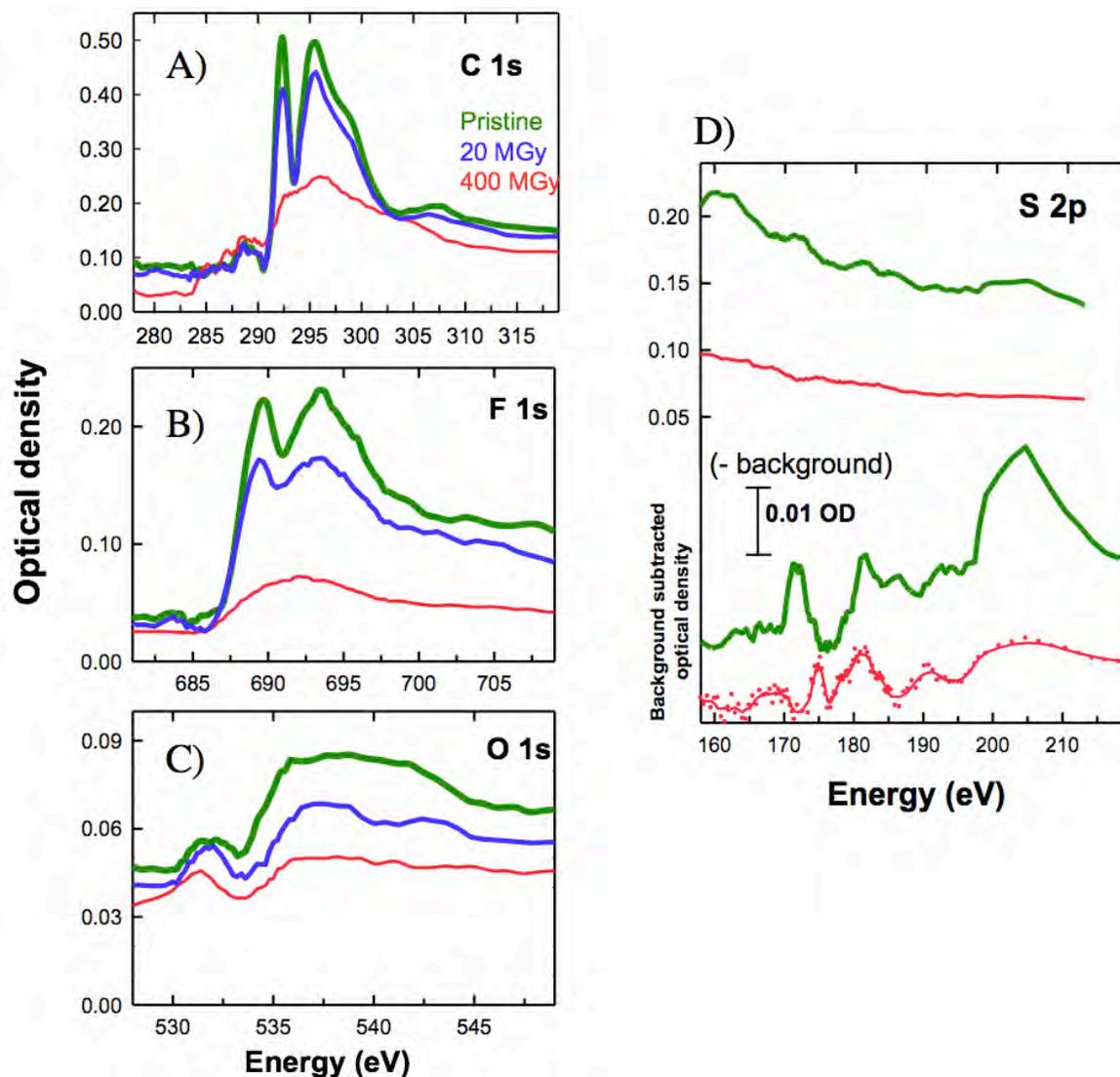
Figure 5.2 (A) C 1s, **(B)** F 1s **(C)** O 1s and **(D)** S 2p X-ray absorption spectra of PFSA for the same area as shown in **Figure 5.1** (sample set A) of undamaged (green), low (blue; 20 MGy) and heavily damaged (red; 400 MGy) areas PFSA, measured using STXM after damage with 320 eV photons. For the S 2p spectra, background subtracted spectra are also plotted. (CLS aSTXM)

At the O 1s edge (**Figure 5.2c**), the relatively sharp peak at 532 eV in undamaged PFSA, which has been assigned to O 1s → $\pi^*_{C=O}$ bonds associated with terminal carboxyl groups (Yan et

al. 2018), shifts by ~0.5 eV to lower energy as the damage increases. This is consistent with generation of C=O bonds in the bulk of the material, which are likely aldehydic or ketonic, since these transitions occur at lower energy than the $\pi^*_{C=O}$ transitions in carboxyl groups (Ishii & Hitchcook, 1988; Urquhart & Ade, 2002). The very broad peak at ~538 eV is attributed to the overlap of O 1s $\rightarrow \sigma^*_{C-O}$ transitions at the terminal carboxyl groups, O 1s $\rightarrow \sigma^*_{C-O}$ transitions at the ether bond, and O 1s $\rightarrow \sigma^*_{S-O}$ transitions at the sulfonate group (Yan et al. 2018). This broad peak significantly decreases, possibly due to carboxyl group, ether and/or sulfonate loss. However, there is considerable evidence for oxygen containing impurities in this sample (solvent, residual reagent used to sulfonate the side chain, and the terminal carboxyl groups) (see **section 3.1.1**). Damage to those components or to the side chains could equally well explain the change in shape and reduction in the O 1s continuum intensity. It is clear that the changes in O 1s are not only due to ether and sulfonate loss so caution is needed in interpreting O 1s data. The sample thinning through F-loss is seen as a decrease in the underlying continuum below the O 1s signal, which has large contributions from F 1s valence ionization.

The S 2p, and (less uniquely) the O 1s signals sense changes to the sulfonate group. The S 2p spectrum (**Figure 5.2d**) is challenging to measure due to the low amount of S in the sample (<3 wt%), the low flux in the S 2p photon energy region at both the ALS and CLS STXM beamlines, and the fact that the S 2p spectrum is superimposed on a large background of valence ionization of the other elements. Heavily damaged PFSA has a significantly lower signal in the S 2p region. The decrease in the underlying continuum is mostly due to F-loss, while the decrease in the S 2p signal is associated with loss of the sulfonate groups. A 3 section, first order spline curve fit to, and extrapolated from, the pre-S edge signal, was subtracted from the spectrum to

derive the background-subtracted S 2p spectrum shown in **Figure 5.2d**. Comparison of the pre- and post-damage background subtracted spectra indicates there are some changes in the spectral shape. The rise at 190 eV and the broad, strong peak at 205 eV is the Cl 2p edge. This is most likely from residual chlorosulfonating acid ($ClHO_3S$) used to introduce the sulfonate group on to the end of the side chain of PFSA (Fuller & Dobulis, 2015).

The same C 1s and F 1s spectral changes are observed when a much thicker (~170 nm) PFSA spin coated film is damaged using 320 eV photons (**Sample set B**, **Figure 5.3**). The changes to the O 1s spectrum (**Figure 5.3e)** are seen more clearly due to higher absorption in the thicker sample. The O 1s $\rightarrow \pi^*_{C=O}$ peak, initially at 532 eV, lowers by approximately 0.5 eV (**Figure 5.3c**), as observed in the thin PFSA sample. There is also a significant intensity reduction and spectral shape change of the broad peak (537 – 543 eV). At the S 2p edge, despite higher OD due to increased sample thickness, it is still necessary to subtract the underlying valence ionization signal to properly visualize the S 2p signal (**Figure 5.3b)**. The broad peaks at 172 and 182 eV, related to S-C and SO_3 bonds, respectively (Yan et al. 2018), disappear with damage indicating that the sulfonate group likely is lost in an intact form with little transformation to the –SO_3X group.

The damaged area exposed to a dose of 20 MGy shows decay of the C-F related transitions in both the C 1s and F 1s spectra in both **samples A** and **B** (see blue curves in **Figure 5.2** and **Figure 5.3**). At the O 1s edge, there is some decay of the continuum signals with an increase of the intensity of the 532 eV peak, likely due to formation of aldehydic or ketonic C=O groups (Ishii & Hitchcook, 1988).
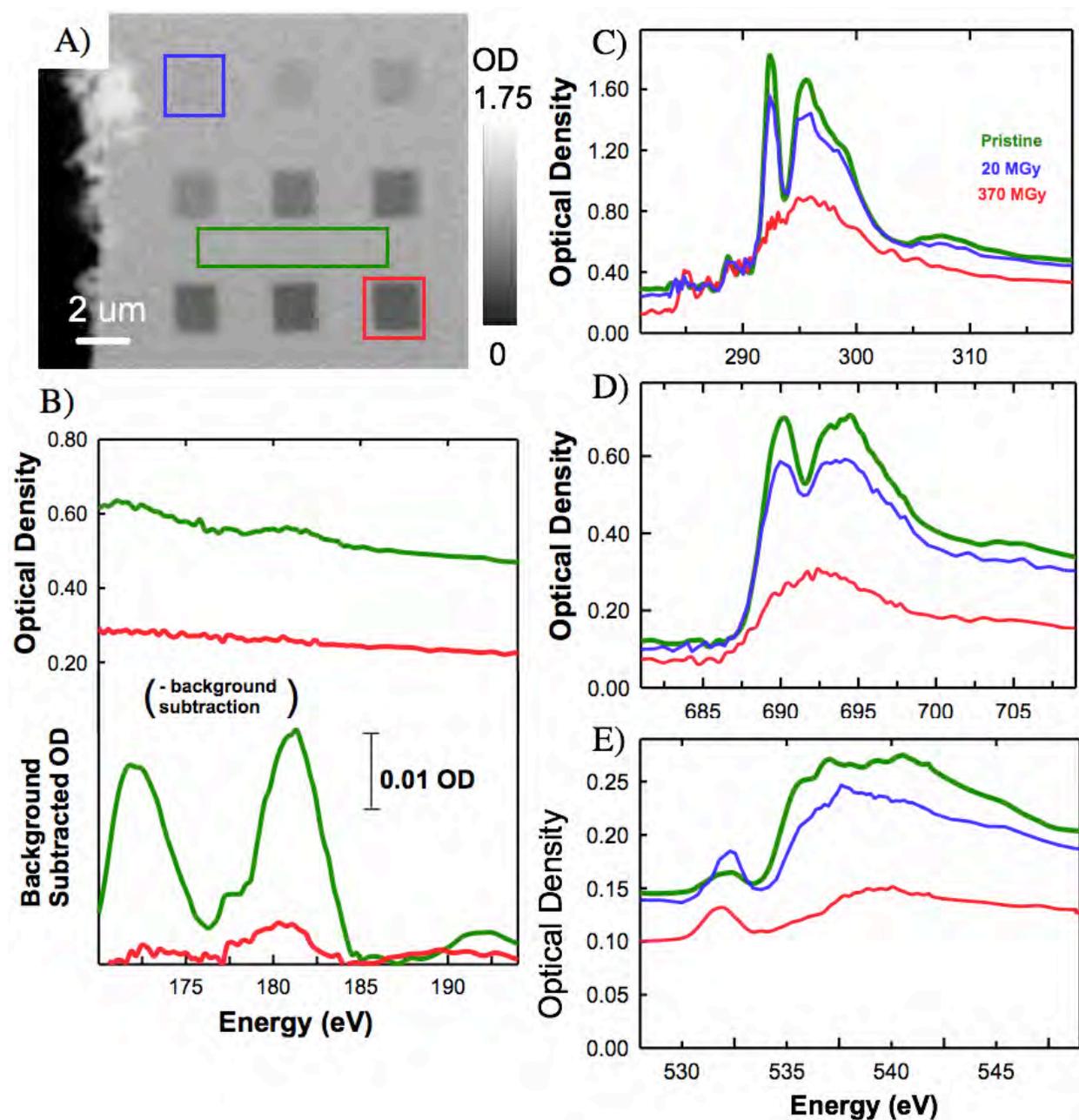
Figure 5.3 Dose-damage results for PFSA (sample set B) using STXM after exposure to 320 eV photons. (**A**) STXM optical density (OD) image at 292.4 eV with 9 square pads at damage E_D = 320 eV. (**B**) S2p, (**C**) C 1s, (**D**) F 1s and (**E**) O 1s X-ray absorption spectra of PFSA of undamaged (green), low (blue; 20 MGy) and heavily damaged (red; 370 MGy) areas, measured using STXM. For the S 2p spectra, background subtracted spectra are also plotted. (CLS aSTXM)

5.3.1.2   Quantitative analysis: determination of critical dose, a_c

The spectral changes that occur when PFSA (**sample set B**, **Table 5.1**) is damaged by soft X-rays were analysed quantitatively using the methodologies presented in **section 3.3.2**. **Table 5.2** summarizes the various chemical changes caused by soft X-ray irradiation of PFSA which could be tracked using STXM. Not all changes can be quantified with STXM, such as the formation of the C=O bonds [visualized at $OD_{286.4\ eV}$ or $OD_{531.8\ eV}$] due to the small signal to background ratio and a periodic (moiré) noise at 286.4 eV at the 10ID1 beamline in the CLS.

Figure 5.4a plots four different damage signals of each pad ($OD_{285.1\ eV}$ - $OD_{280\ eV}$, and OD at 292.4, 540 and 690 eV) as a function of dose for **sample set B** (spectra presented in **Figure 5.3**) damaged with 320 eV photons. Elemental mass changes (carbon, oxygen and fluorine) with dose evaluated using $OD(E_A)$-$OD(E_P)$ where E_A is a continuum energy, E_P is a pre-edge energy are plotted in **Figure 5.4c.** The analysis where the entire edge signal is integrated, is presented in **Figure 5.4e.** Each dataset was fit to an exponential decay function (**Equation 1.1**). The data is also plotted as $\ln(OD\text{-}OD_\infty)$ as a function of dose, where OD_∞ is determined by fitting, in **Figure 5.4b,d,f** for the $OD_{292.4\ eV}$, $OD_{690\ eV}$ and $OD_{710\ eV}$ – $OD_{680\ eV}$ signals along with the associated OD_∞ value **(sample set B, Table 5.1).** For each of these three datasets, the linear fit has $R^2 > 0.97$. The good linear relationship implies first order kinetics is a reasonable assumption.
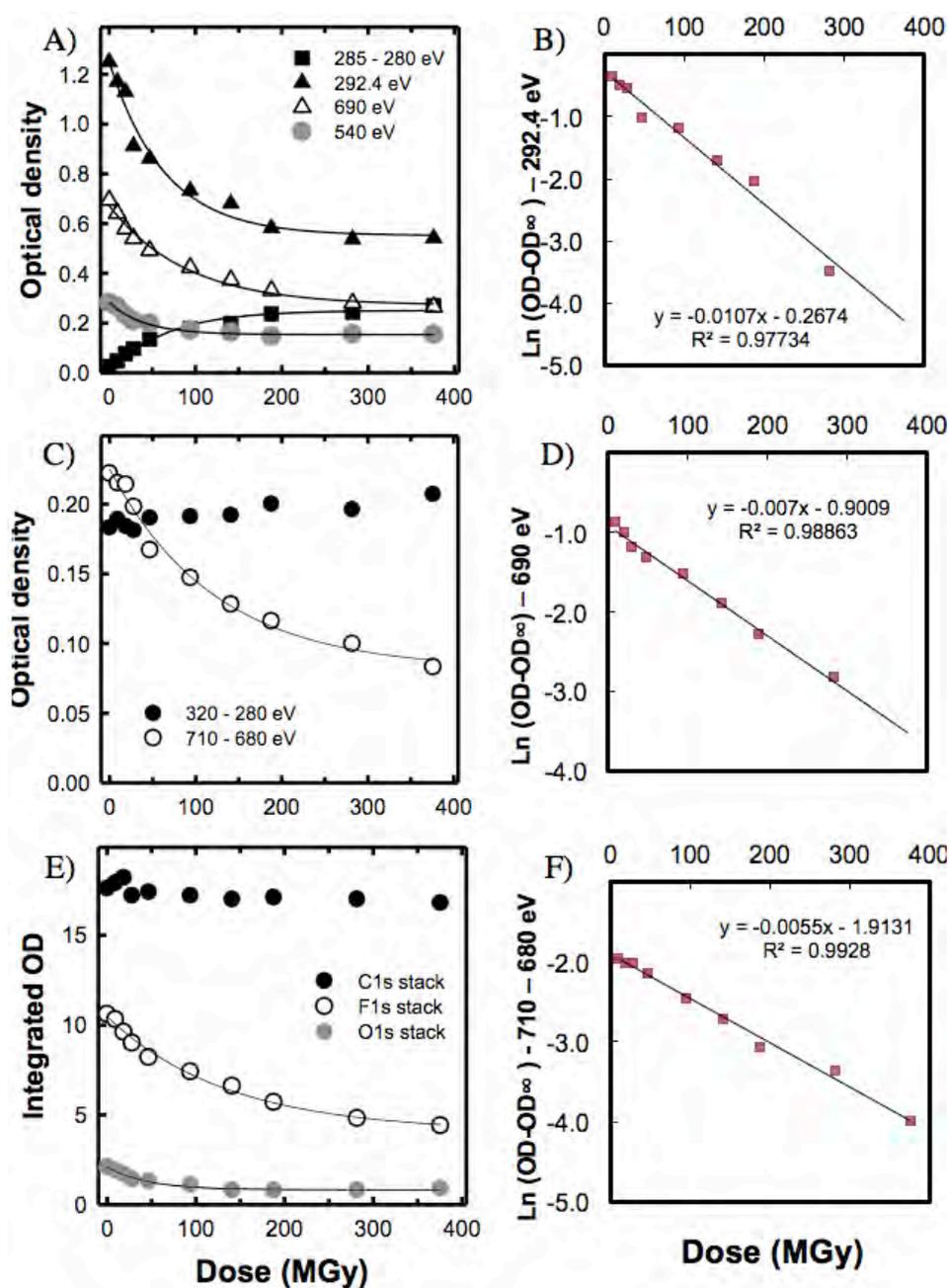
Figure 5.4 (A) Damage with 320 eV photons as a function of absorbed dose at 285 – 280, 292.4, 540 and 690 eV for PFSA (sample set B) with raw OD. The solid lines are fits to exponential function, **(B)** linearized plot of $OD_{292.4\ eV}$. **(C)** Change in net C 1s [$OD_{320\ eV}$ - $OD_{280\ eV}$] and F 1s [$OD_{710\ eV}$ - $OD_{684\ eV}$] continuum signals, **(D)** linearized plot of $OD_{690\ eV}$, **(E)** Elemental loss, from integration of the full spectra, **(F)** linearized plot of [$OD_{710\ eV}$ - $OD_{680\ eV}$]. (CLS aSTXM)

The signal at 292.4 eV and 690 eV reduces significantly with increasing dose. When all the PFSA measurements are examined together (see **Table 5.3**) the average a_c over many areas and samples, using the same dosing and analysis approaches, are 86±22 MGy at 292.4 eV and 109±23 MGy at 690 eV. I conclude that the a_c measured at these two energies is the same within statistics, as expected since the 292.4 and 690 eV transitions reflect the same processes, namely amorphization or re-organization of the local CF_2-CF_2 structure.

In order to quantify the rate for creation of the peak at 285.1 eV ($\pi^*_{C=C}$ due to C=C bond formation from intra or interchain reduction), $OD_{285.1\ eV}$ – $OD_{280\ eV}$ should be used because the signal at 285.1 eV is very low and does not change (see **Figure 5.3a**). The C=C creation is masked by the decrease of the pre C 1s signal due to F mass loss and so the pre-edge should be subtracted from the 285.1 eV for proper quantitation. a_c for C=C creation was determined to be 65 MGy (see **Figure 5.4a**).

Table 5.3 Critical dose (MGy) for fluoropolymers (PFSA, PTFE and Teflon®AF) at several E_a at the C 1s, O 1s and F 1s edges exposed to soft X-rays in a He environment.

Material		# of measurements and critical dose (MGy) at E_a(eV)*					
	E_d	#	292.4	#	540	#	690
PFSA DupontD521[a]	320	1	127	1	47	1	117
PFSA DupontD521	320	10	68 ± 10	5	39 ± 8	8	101 ± 15
PFSA DupontD521	710	3	94 ± 5	3	66 ± 9	3	118 ± 19
Membrane Nafion117	320	4	133 ± 17	-	-	-	-
Membrane Aquivion	320	5	91 ± 5	-	-	-	-
AVERAGE			86 ± 22				109 ± 23
PTFE	320	3	257 ± 36	-	-	3	256 ± 6
Teflon®AF	320	3	219 ± 23	-	-	3	177 ± 9

*standard deviations noted are from replicate measurements
[a]Sample first received 60 MGy and then a 9-pad was burned on top – see **section 5.4.4**

Changes in the C 1s continuum signal can be related to changes in the amount of carbon. The $OD_{320\ eV}$(dose) curve should be isolated from the mass loss of other elements. The $OD_{320\ eV} -$ $OD_{280\ eV}$ (shown in **Figure 5.4c)** and analysis of the full C 1s stack **(Figure 5.4e)** was used to evaluate carbon loss. In addition, the carbon spectrum can be affected by a build-up of amorphous carbon due to X-ray cracking of hydrocarbons at the sample surface (Grubb, 1974; Leontowich & Hitchcock, 2012). The $OD_{320\ eV} - OD_{280\ eV}$ increases slightly with increasing dose while the integrated OD from the C1s stack (**Figure 5.4e)** shows that the carbon content does not change. For **sample set A** (see **Figure 5.5**) the integrated OD decreases slightly up to 150 MGy, and then increases. There are likely two processes happening, carbon decay and carbon contamination. The latter becomes evident at higher doses. The trade-off of carbon mass loss and carbon gain from deposition depends on the microscope and when the sample was run. Therefore, I consider the change in the elemental amount of carbon to be unreliable as a measure of carbon mass loss under the STXM chamber conditions during which these measurements were made. It is possible that repeating them in the new UHV-STXM at CLS, which has a much lower carbon contamination and thus carbon deposition, will allow determination if carbon is lost at a rate consistent with CF_2, CF_3 or CF_4loss – i.e. ½, 1/3 or ¼ that of F-loss.
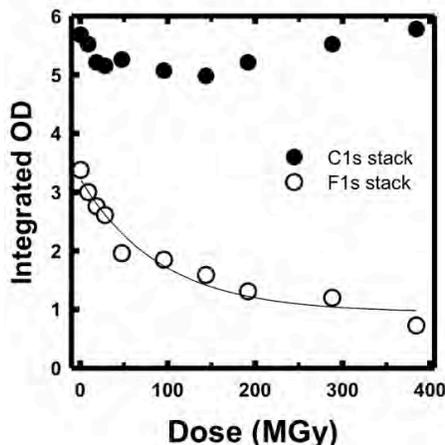
Figure 5.5 Integrated OD of the C 1s and F 1s stacks for damaged areas in sample set A as a function of dose.

For the corresponding F 1s analysis, both $OD_{710\ eV} - OD_{680\ eV}$ and fluorine amount from F 1s background subtracted integration show a similar exponential decay of the fluorine content with dose (see **Figure. 5.4c** and **Figure 5.4e**). When all the PFSA measurements are examined together, the average a_c from $OD_{710\ eV} - OD_{680\ eV}$ is 109±12 MGy while that for F-loss from the full F 1s signal is 136±19 MGy. Those values are not statistically different, and are comparable to a_c of 109±23 MGy for CF_2-CF_2 amorphization evaluated from OD_{690eV}(dose).

Given the low contrast in the OD_{Ea}-OD_{Ep} signal, it is preferable to use the evaluation of elemental F-loss from integrating the background subtracted F 1s spectra (**Figure 5.4e**). The derived a_c for loss of oxygen was much smaller than that for F-loss. For O 1s, the a_c from integrating the stack OD was 45 ± 8 MGy, while a_c for $OD_{540\ eV}$ was 41 ± 8 MGy.

This type of analysis was repeated for many data sets measured at both the ALS 5322 and CLS 10D10 beamlines for a variety of PFSA materials. The average results are presented in **Table 5.3**. The critical dose for PFSA damaged in He with 320 eV incident photons and measured

at E_A = 292.4 eV is **86 ± 22 MGy**, while that at 690 eV is equal to **109 ± 23 MGy**. The value

measured at 540 eV is **39 ± 8 MGy**, which needs to be treated with caution, given the evidence

for the presence of non-PFSA oxygen components. Typically, there is 15-20% measurement

precision for a_c determination. This is dominated by uncertainties in the detector efficiency. In

addition there are possible systematic errors related to possible leakage when the chamber is

backfilled with He, leading to the presence of O_2 in the STXM tank, which is known to modify

damage processes (Coffey et al., 2002).

In order to determine if there are different processes at low (<20 MGy) compared to

higher doses (>80 MGy), 9-pad patterns were burned at 320 eV in a He environment in a thick

PFSA spin coated film (170 nm, **sample set-B**). The changes in amounts of C, O and F from

integrating all of the C 1s, O 1s and F 1s signals were quantified and are plotted in **Figure 5.6**.

The initial rate of oxygen depletion is significantly higher than that for F mass loss. The oxygen

loss stops after approximately 140 MGy. Changes to the carbon content are minimal. This does

not necessarily indicate that the PFSA damage is strictly a function of oxygen and fluorine mass

loss since carbon contamination is also likely happening, and the elevated rate of O loss at lower

dose may be from an impurity such as radiation induced loss of solvent.
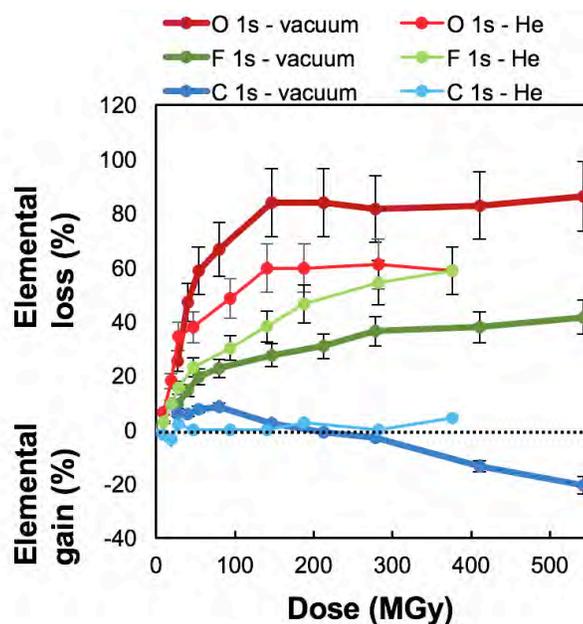
Figure 5.6 Elemental loss for radiation damaged PFSA in a He environment compared to active vacuum of oxygen (red) and fluorine (green) as a function of dose (MGy) of sample set B and C. The change in amount of carbon (blue) is also indicated. The elemental loss was normalized to the amount of undamaged material. (CLS aSTXM)

The O 1s and F 1s curves in **Figure 5.6** were fit to an exponential growth function to determine the a_c; the results are listed in **Table 5.4.** The a_c for elemental oxygen and fluorine mass loss is 45 ± 15 MGy and 136 ± 14 MGy, respectively. These values agree with the a_c values for single energy damage analysis at 540 and 690 eV reported in **Table 5.3.**

Table 5.4 Elemental loss (%) due to radiation damage of the fluoropolymers PFSA, PTFE and

TeflonAF exposed to high doses of 320 eV soft X-rays.

Material		PFSA	PFSA	PFSA	PFSA	PTFE	TeflonAF
Data set		A	B	C[(a)]	D	E	F
Dose (MGy)		360	380	540	260	520	420
Formula[(b)]		C18F9O5SH	C18F16O4SH	C18F16	-	CF5	C6F6O
Elemental loss (%) [(c)]	S 2p	-	-	-	35 (10)	-	-
	C 1s	9 (5)	5 (5)	-21(7)	8 (6)	0	10 (6)
	O 1s	50 (10)	60 (12)	86 (16)	-	-	-
	F 1s	88 (20)	59 (11)	42 (9)	27 (7)	75 (15)	60 (12)
Critical dose (MGy)[(d)]	O 1s	-	45 (15)	66 (18)	-	-	-
	F 1s	-	136 (14)	116 (18)	-	256 (15)	237 (31)

(a) value for sample C is for damage done at 320 eV under active vacuum. All others were done
      with 1/6th atm He.
(b) estimated from elemental loss for the damaged polymer
(c) errors were estimated
(d) errors given are the fitting error for the b coefficient used to determine a_c

5.3.1.3 *Effect of damage energy (320 vs 710 eV)*

Figure 5.7 compares the critical dose of PFSA for each of the processes for which dose-

damage is plotted in **Figure 5.4**, with samples at a variety of conditions that will be discussed in

subsequent sections. Results from damage to PFSA (**sample set C**) using 710 eV photons (E_D =

710 eV) in a He environment are presented in **Figure 5.7** and **Table 5.3**. The a_c values at E_D =

710 eV for analysis energies (E_A) of 292. 4, 540 and 690 eV are: 94 ± 5, 66 ± 9 and 120 ± 20

MGy respectively.

When the damage was generated at 710 eV the a_c values from elemental (integration) and

component analysis (Cm, stack analysis) (**Figure 5.7b)** are similar to the a_c values evaluated in

the same way after damaging PFSA at 320 eV. Note that the elemental integration quantifies the

amount of fluorine while the component fit analysis is also sensitive to the chemical changes in

the PFSA spectrum. Since the a_c values from the two methods of analysis are similar (119 ± 9

MGy), F-loss and re-organization occur at a similar rate.
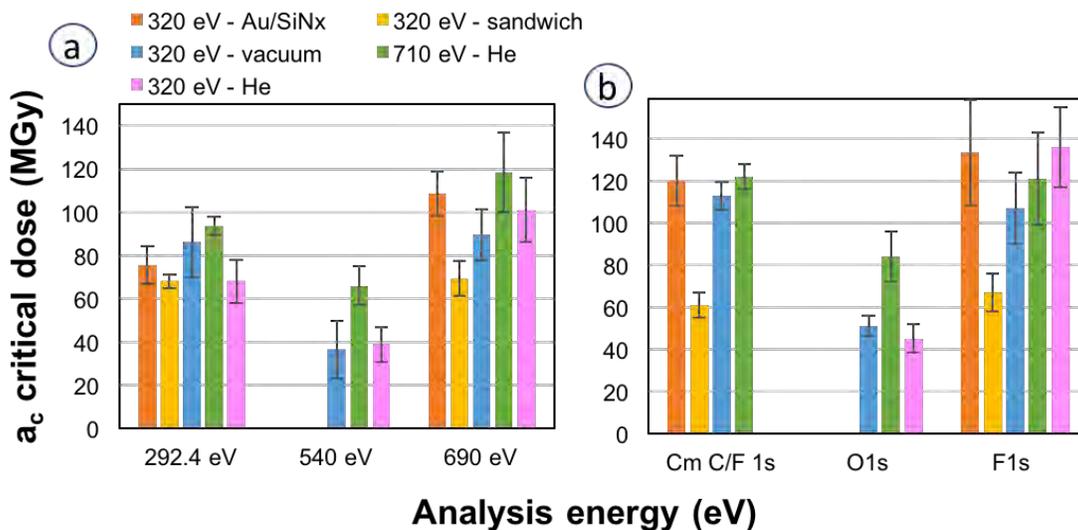
Figure 5.7 Influence of damage energy (320 and 710 eV), environment and substrate (conductivity) on the critical doses for PFSA damage analyzed **(a)** at 292.4 and 690 eV and **(b)** by comparing the component loss at the C 1s and elemental loss of oxygen and fluorine. Vacuum environment is compared to He. Influence of conductive substrate is also shown. (CLS aSTXM & 5.3.2.2 ALS)

5.3.1.4 *Environmental effects on soft X-ray damage to PFSA*

5.3.1.4.1 Effect of residual O_2

Under normal operating conditions, the STXM sample chamber is pumped to ~15 Pa and then backfilled with pure He to a pressure of 15 kPa. **Sample set C** was exposed to 320 eV photons while the STXM tank was actively pumped to a vacuum of 0.02 Pa (3x10^{-4} mbar) using a turbo pump. If small amounts of residual O_2 are present, it can affect the radiation damage

mechanisms and kinetics, since O_2 significantly changes the chemistry and rate of X-ray damage to polymers (Coffey et al., 2002).

The presence of residual solvents can also be affected by active pumping. C 1s solvent related signals have been detected in ^{13}C SSNMR spectra from the same solid material as composes the PFSA films (the films were drop cast and not spin coated) (Yan et al., 2018). Although all films were prepared using the same methodology, the samples were not fabricated or stored in clean room conditions with controlled ambient temperature and humidity. Thus, residual solvent may be present in the films, which might then be removed during active pumping but retained in the regular sample chamber conditions. To test this hypothesis, **Figure 5.8** compares several quantitative OD1 spectra of the PFSA film i) dried in a vacuum annealer at 80 ^{o}C for 30 mins, ii) not dried and in the STXM chamber with active vacuum compared to iii) the typical condition (He). **Figure 5.8a,b,c** shows the C 1s, O 1s and F 1s NEXAFS spectra of the vacuum annealed sample compared to **sample set A** – typical conditions. **Figure 5.8d,e,f** compares quantitative OD1 C 1s, O 1s and F 1s NEXAFS spectra of **sample set A** and **B** (both were done in He environment) to **sample set C** (this sample was measured in two separate runs, both under active vacuum). If there are residual solvents present in the spin coated PFSA films, these would potentially affect the O 1s spectrum. However, the <u>oxygen spectral shape and intensity are very similar</u> for the dried and not dried samples or between the PFSA samples in the active vacuum compared to the rough vacuum and He environment. Therefore, drying the PFSA sample at 80 ^{O}C for 30 mins or using active vacuum during STXM measurements does not affect the content of residual solvents. The solvents were detected with SSNMR on the drop cast films (not spin coated) vacuum annealed at 80 °C for 4 hrs (Yan et.al., 2018). Either the spin coated films are

solvent-free or STXM is not sensitive to residual solvents at the level they are present. Drying the

PFSA films at higher temperature and for approximately 24 hours results in chemical changes.
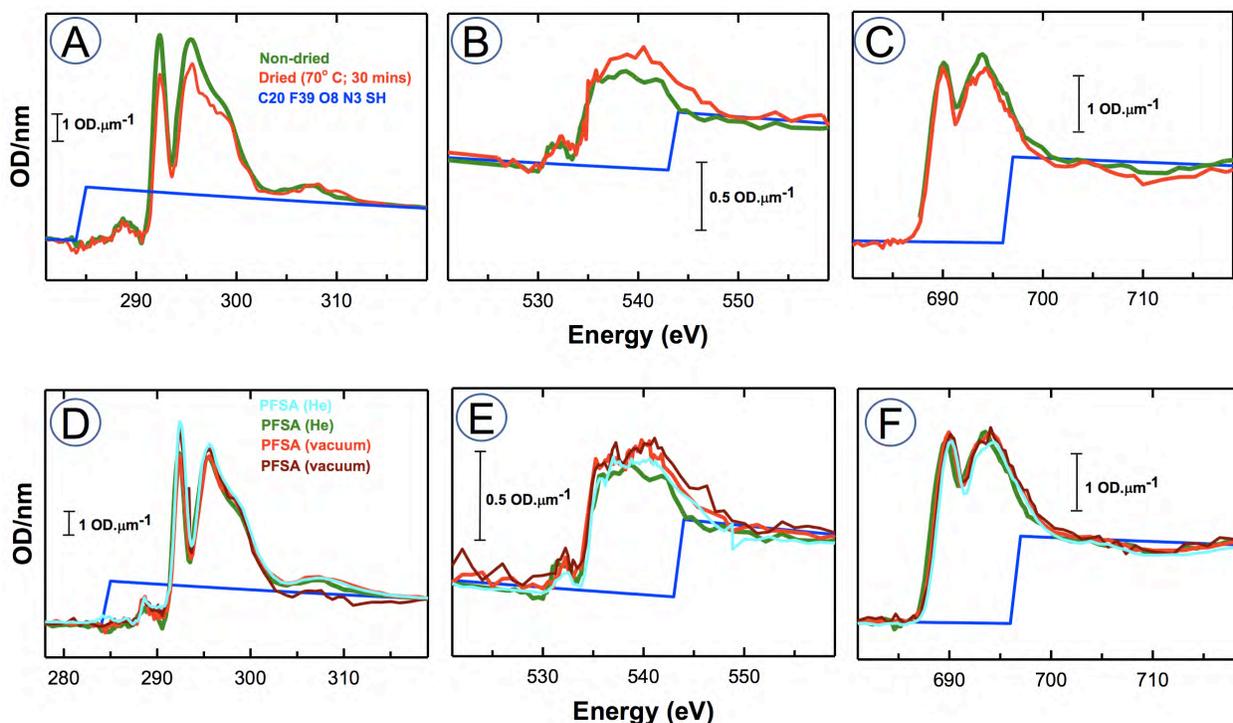
Figure 5.8 Comparison of quantitative OD1 STXM spectra at the C 1s, O 1s and F 1s to verify

presence of residual solvents in PFSA films that were i) dried in a vacuum annealer at 70 °C for

30 mins, red curve, compared to non-dried PFSA film (green curve, Sample set A) in **(A), (B)** and

(C) and ii) in active vacuum in the STXM chamber (two red curves depict the same sample

measured in two separate CLS runs - Sample set C) compared to the typical He environment

(green - Sample set A and light blue - Sample set B curves) in **(D), (E),** and **(F).** The blue curve in

all figures is the theoretical reference spectrum generated for all samples using a chemical

formula of $C_{20}F_{39}O_8N_3SH$.

When the STXM tank was actively pumped (turbo pump), a similar extent of oxygen

depletion was observed when the sample was damaged to a dose of 540 MGy (80±15% versus

60±15% at 380 MGy) but higher carbon contamination was observed (**Figure 5.6**). The elemental

loss analysis showed that oxygen and fluorine are lost at nearly the same rate as in the He environment (**Figure 5.7b**). The critical doses with and without active vacuum are indistinguishable - 89 ± 12 MGy versus 101 ± 15 MGy as measured using (E_D=320 eV, E_A=690 eV). The (E_D=320 eV, E_A=292.4 eV) critical dose was 86 ± 16 MGy when the tank was actively pumped, similar to that of 68 ± 10 MGy observed when the tank was backfilled with He. Therefore, the residual O_2 present during measurements under He (pressure of 20 Pa) did not affect the X-ray radiation damage chemistry of PFSA.

5.3.1.4.2   Effect of substrate conductivity

In order to test whether the substrate conductivity influences the rate or mechanisms of soft X-ray damage to PFSA, the SiNx substrate was coated with 2 nm of Cr (for adhesion) and then 5 nm of Au. The Au coating increases conductivity, which can minimize charge accumulation. For a 50 nm PFSA film, there was no significant changes in the spectra or the rate of damage of PFSA (see **Figure 5.7**), indicating that the substrate conductivity does not influence the damage. However, when the film was sandwiched between two layers of this substrate, the critical dose at E_D=320 eV, E_A = 690 eV was 69 ± 8 MGy identical to that of 68 ± 3 MGy measured at 292.4 eV. In the sandwich sample, the critical dose for PFSA component loss was 61 ± 6 MGy and the fluorine elemental loss was 67 ± 9 MGy, nearly half of the a_c value when damage was done in a He or active vacuum environment.

5.3.2   PTFE and Teflon®AF damage spectroscopy and critical dose results

The 9-pad damage creation and subsequent analysis was also performed on two related fluoropolymers, PTFE (**Sample set E**) and Teflon®AF (**Sample set F**) using E_D = 320 eV, E_A=

292.4, 690 eV, with the samples in He. C 1s, O 1s and F 1s spectra from undamaged and heavily

damaged regions (~750 MGy) for each material are presented in **Figure 5.9**. The C 1s, F 1s, and,

to a lesser extent, O 1s spectra of undamaged PTFE, Teflon®AF and PFSA (**Figure 5.2**) are very

similar, despite PTFE being oxygen-free, while Teflon®AF and PFSA both contain oxygen (**see**

Figure 3.1) and have ether bonds. Interestingly, the C 1s spectrum of Teflon®AF does not

contain a peak at 289 eV (**Figure 5.9d**) or significant oxygen signal (**Figure 5.9e**), which is

consistent with the attribution made in the recent PFSA spectroscopy study (Yan et al. 2018) that

the 289 eV peak in PFSA is associated with chain termination carboxylate groups that are present

but not indicated in the usual chemical descriptions of PFSA.

For both PTFE and Teflon®AF the signals at 285.2, 286.5 and 288 eV which appear upon

radiation damage indicate formation of new C=C and C=O bonds related to C1s$\rightarrow\pi^*_{C=C}$ (C-C)

and C1s$\rightarrow\pi^*_{C=O}$ (C=O) transitions (Dhez, Ade, & Urquhart, 2003). The formation of C=C bonds

has been observed in many polymers including PMMA (Wang, Morin, et al., 2009) and nylon

(Coffey et al., 2002) where the loss of H on 2 adjacent carbons leads to C=C bond formation. In a

similar fashion, loss of F• on 2 adjacent carbons appears to lead to C=C bond formation.

The O1s spectra of damaged Teflon®AF (**Figure 5.9e**) and PTFE (**Figure 5.9b**) are

remarkably similar to that of PFSA (**Figure 5.2c**), consistent with significant radiation catalyzed

oxidation in each case. The oxygen content increases with increasing dose for both

fluoropolymers. Therefore, residual oxygen in the sample chamber plays a role in the damage of

PTFE and Teflon®AF fluoropolymers.
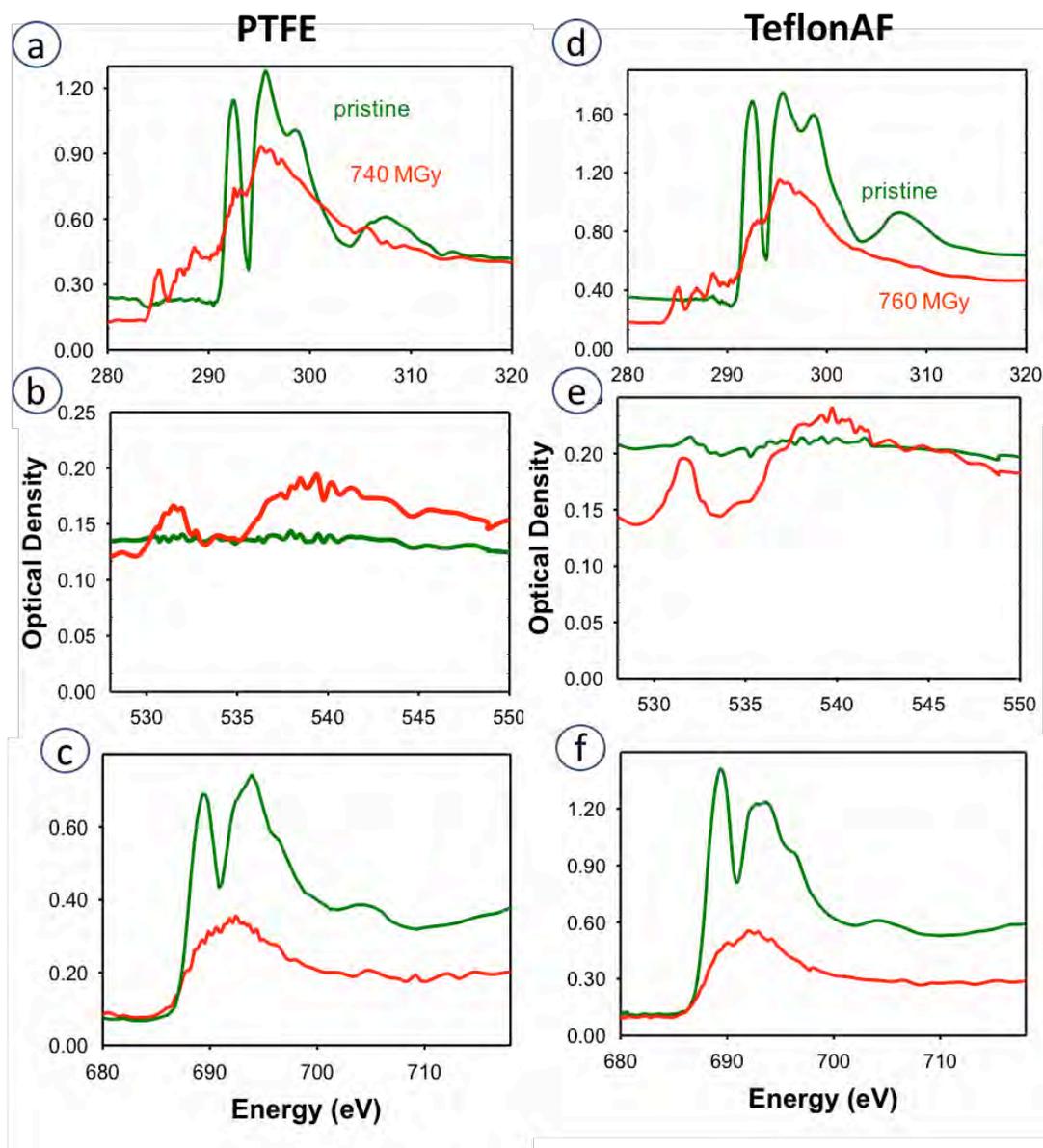
Figure 5.9 Spectral changes to PTFE (sample set E) and Teflon®AF (sample set F) caused by X-ray exposure at E_D= 320 eV. **(a), (b), (c)** and **(d), (e)** and **(f)** show C 1s, O 1s and F 1s spectra of the undamaged and damaged (doses of ~750 MGy) regions for PTFE and Teflon®AF, respectively. (CLS aSTXM)

The sample chamber environment was identical as both samples were run on the same support plate and on the same day. Pristine and damaged PTFE have similar carbon continuum intensities while there is a significant decrease of the carbon continuum for damaged, compared to pristine Teflon®AF. This indicates significant carbon build-up for PTFE. The C 1s and O 1s pre-edge decay, related to fluorine depletion, is visible for both damaged materials. There was also significant oxidation in the case of both damaged PTFE and damaged Teflon®AF (oxygen post-edge increases). These measurements were repeated in several separate runs and the results were very similar.

Heavily damaged PFSA, PTFE and Teflon®AF have similar F 1s spectra in which the characteristic two-peak structure is replaced with a single peak at ~693 eV. After large doses (> 500 MGy for PTFE and Teflon®AF and >200 MGy for PFSA), the F 1s spectra, and thus the fluorine environment, are very similar in all three fluoropolymers.

Figure 5.10 plots the change in $OD_{292.4 \text{ eV}}$ and $OD_{690 \text{ eV}}$ (C-F amorphization) for PTFE and Teflon®AF as a function of dose. Compared to PFSA where the OD decay for the 292.4 and 690 eV peaks saturates around 150 MGy (**Figure 5.3**), the OD decay for PTFE and Teflon®AF declines more slowly, with saturation only occurring around 1000 MGy. **Figure 5.11** presents the results for elemental C and F loss. By a dose of 300 MGy, ~40% of the fluorine is lost for both fluoropolymers. The fluorine depletion curves for PTFE and Teflon®AF are the same within statistical precision, and do not saturate even with doses of 1000 MGy. Initially a small extent of C loss is detected but then the rate of carbon deposition becomes larger, eventually resulting in a net carbon build-up, similar to that noted for PTFE (see **Figure 5.9a**). The results presented in **Figure 5.11** were all measured with the sample in a He environment with some residual O_2.
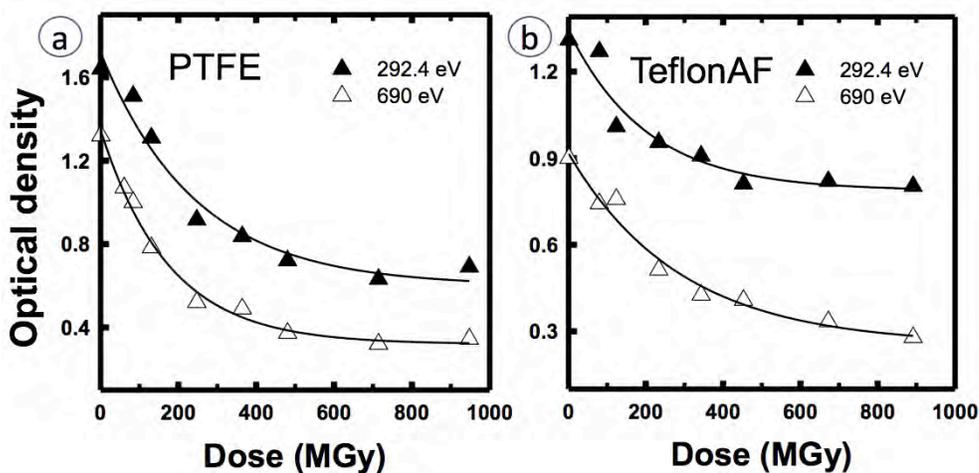
Figure 5.10 Dose-damage curves for C-F amoprhization of **(a)** PTFE and **(b)** Teflon®AF, as measured at 292.4 and 690 eV. The solid lines are fits to a single exponential decay.
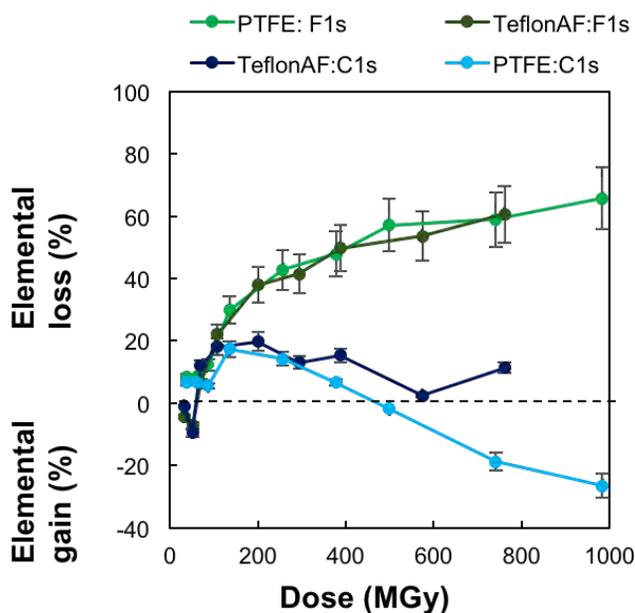
Figure 5.11 Elemental loss of fluorine (green) and carbon (blue) for radiation damaged PTFE and Teflon®AF as a function of dose (MGy), determined using method-i. The elemental loss was normalized to the amount of undamaged material.

Figure 5.12 compares the critical doses for C-F amorphization (E_A = 292.4 and 690 eV) and C and F loss of PFSA, PTFE and Teflon®AF. The numerical values can be found in **Tables 5.3** and **5.4**. PFSA is significantly more radiation sensitive than PTFE and Teflon®AF. Teflon®AF has slightly lower critical doses than PTFE for all damage processes. **Fig. 5.12** also compares the rate of carbon and fluorine loss for the three fluorocarbon species. The rate of change of the PTFE or Teflon®AF component is 2x faster than for PFSA. This indicates that the structure and morphology of the PFSA, the oxygen content and its side-chains affect the damage mechanism since the PFSA backbone is similar to PTFE.
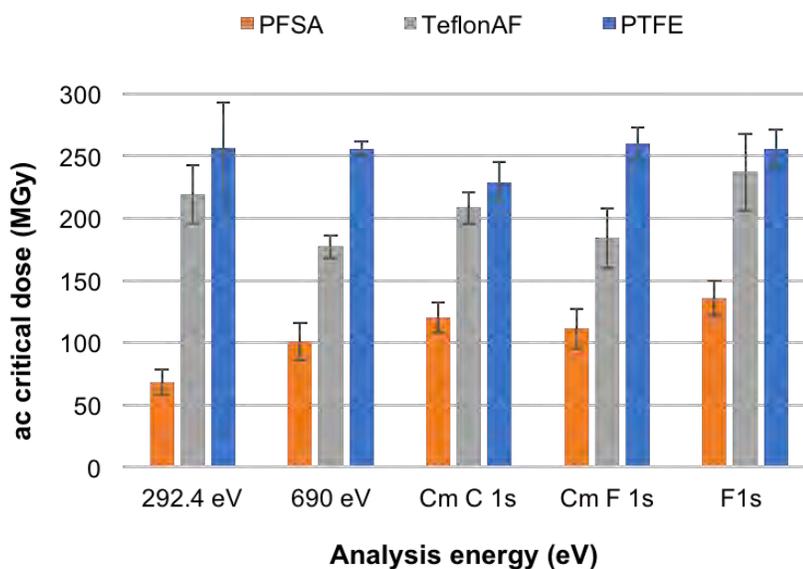
Figure 5.12 Comparison of the critical doses for PFSA, PTFE and Teflon®AF damage damaged at 320 eV and analyzed at 292.4 and 690 eV. The fluorine loss was quantified by integrating background subtracted spectra from the F 1s stack. The component loss (Cm) at both the C 1s and F 1s edges are also compared.

5.4   Discussion

5.4.1   Summary of key observations in this chapter

There are multiple processes happening simultaneously and several methods using STXM were used to quantify both elemental and spectroscopic signals (methods A and B as discussed in section 3.3.2). Formation of new C=C and C=O bonds in soft X-ray damaged PFSA was detected by observation of growth of peaks at 285 eV, 287 eV and 532 eV. For PFSA, the results indicate that the side-chains and oxygen decay at a faster rate compared to the fluorine loss or CF_2-CF_2 amorphization due to the smaller critical dose of the 540 eV peak and O 1s elemental loss. However, given that there are oxygen impurities, I cannot determine if, and if so, how much faster the side-chains are falling off relative to the fluorine and C-F bonds. Sulfur depletion was also detected but was not quantified. The fluorine loss and CF_2-CF_2 amorphization occur at similar rates (both methods A and B agree with each other). However, it was not possible to determine if these processes occur serially (presumably with amorphization prior to F-loss) or in parallel (see **section 5.4.4** for discussion of alternate kinetic models). Although the measurements in this work indicate that carbon loss is negligible, there may still be carbon loss masked by a compensating carbon contamination build-up as the dose increases.

The nature of the chemical changes in X-ray damaged PFSA or the damage rate for each process did not depend on whether the damage photon energy (E_D) was 320 to 710 eV. This is consistent with previous results on soft X-ray damage to PMMA and polystyrene where it was concluded that chemical changes and damage rate did not depend on whether the irradiation was done at the C 1s pre-edge (280 eV) or in the continuum (300 eV) (Leontowich et al., 2016).

For PFSA, there is oxygen loss, which could be interpreted as occurring from ether group, sulfonate, terminal carboxylates or residual solvent. The loss stops at the relatively low dose of ~150 MGy, perhaps due to yet another process, namely solvent loss. Alternatively, there could be simultaneous O-loss from damage and O-gain from oxidation, as was observed for PTFE and Teflon®AF. For both PTFE and Teflon®AF, which do not have (much) O to begin with, residual O_2 in the chamber results in a growth of oxygen signal with dose. More experiments are needed to confirm the extent that the vacuum conditions and O_2 content affect radiation damage of the fluoropolymers (including the sandwiched sample).

The error in the critical dose quantitation varied between 10-25% throughout this thesis. The detector efficiency is one of the major sources of error and is why a linear template (**Fig. 3.7**) was used to minimize the random error. Other systematic errors include but are not limited to: quantification of the damage signal (convolution of the spectral features at a specific edge), cleaner sample preparation and storage in a laboratory with a strict and controlled environment, standardize sample environment conditions (including further exploration of the sample sandwich between two SiNx windows).

5.4.2   *PFSA: side chain removal*

Although preferential side-chain removal was expected from literature (Paul, Giorgi, & Karan, 2013; Schulze et al., 1999), my results neither support nor refute that interpretation. The excess oxygen content quantified with STXM preclude me from concluding that the side chains are damaged faster. Most of the sulfur is depleted in X-ray damaged PFSA, as seen clearly in the S 2p spectra, which indicates sulfonate removal. However, quantitation of the S 2p spectra is not trivial due to the low signal-to-noise ratio.

The faster damage rate of PFSA relative to that for PTFE can be due to the side-chains. They could be the preferred damage site since the main-chains of PFSA and PTFE are similar. However, dry PFSA supposedly has pores 2-5 nm wide due to the hydrophilic and hydrophobic channels (Kusoglu & Weber, 2017; Mauritz & Moore, 2004). It is also possible that these channels facilitate the migration of the damage products out from the film.

5.4.3   *Fluoropolymer radiation chemistry*

The chemical changes that X-ray damage cause to each fluoropolymer are very similar, as measured at the C 1s and F 1s edges. I hypothesize that the apparent zero net loss of carbon is due to an equilibrium between the carbon loss and carbon deposited due to cracked hydrocarbons in the sample chamber. This could be proved by repeating the experiment in a UHV STXM microscope.

The changes to the CF_2 local environment are very similar for all three fluoropolymers. As the dose increases, the peaks related to $\sigma^*(C\text{-}F)$ bonds in both the C 1s and F 1s spectra reduce in intensity and transform into a single, broad peak. At this point the remaining CF_2 units are in a disordered state, as a result of structural amorphization. The depletion of fluorine and the changes to the two $\sigma^*(C\text{-}F)$ peaks occurs much faster for PFSA than for PTFE or TeflonAF.

The story is quite different at the O 1s edge. Comparison between the oxygen spectra of the damaged fluoropolymers suggests that the end product of X-ray damage to all 3 species has similar oxygen environment. The oxygen content increases when PTFE and Teflon®AF are damaged indicating that all three species likely are subject to X-ray catalyzed oxidization associated with the presence of residual O_2 in the STXM tank.

5.4.4 Alternate kinetic models

If the spectral changes caused by soft X-ray irradiation is a single process that follows an exponential decay, the rate of decay of the sample will be the same regardless of the range of selected datapoints i.e. the first datapoint can be at dose 0 MGy or at 100 MGy, the rate of decay will be the same. The OD as a function of dose for E_D=320 eV and E_A=292.4 eV was fit to an exponential decay as shown in **Figure 5.13**. The dataset was then fit to an exponential function but selecting different dose ranges. The fitting results (**Table 5.5**) show that the critical dose increases when the range of doses starts at 93 MGy rather than 0 MGy. This is evidence that a single exponential fit may not be the best model for modeling PFSA decay as measured with STXM.
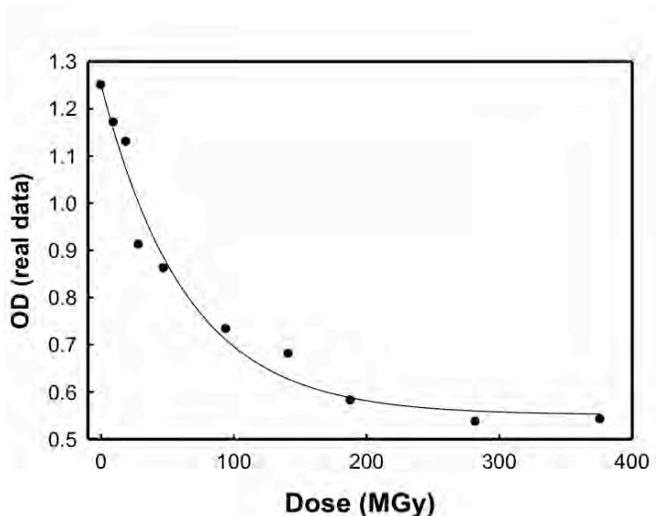
Figure 5.13 Average OD for a PFSA dose damage dataset as a function of dose with the exponential fit curve superimposed.

Table 5.5 shows the fitting parameters for the dataset shown in **Figure 5.13** considering different data ranges.

Dose range (MGy)	Exponential fitting parameters				
	Standard error	R^2	y_0	a	1/b or a_c (MGy)
0-376	0.048	0.975	0.551	0.70	65
93-376	0.027	0.953	0.519	0.61	95

Initially, a bi-exponential model was suggested since in previous work where PFSA in cathode samples were used (Melo et al., 2017; Wu et al., 2018) two separate damage mechanisms seemed apparent: the first process at lower doses (up to ~100 MGy) consisting of fast damage and significant fluorine loss with consequent rearrangement of the remaining fluorine atoms, and a second slower process (above ~100 MGy) where the remaining, fluorine-depleted material loses fluorine at a much lower rate, and there were no significant additional spectral changes.

Figure 5.14 shows the F 1s spectra of a pristine area of PFSA (green); an adjacent area of 5 x 5 μm that was damaged to 60 MGy (blue), and pad#9 (red), of a 9-pad pattern burned on top of the area damaged to 60 MGy using E_D=320 eV. Two processes can be visualized in this figure. However, the a_c values determined from this specific burn (see **Table 5.3**) at E_D=320 eV, E_A=292.4 eV are 127 MGy and E_A=690 eV is 117 MGy. Although a bi-exponential model did not improve the fit to any of the data, including **Figure 5.14**, the single exponential decay may still be an oversimplification of the damage mechanism for PFSA. For sake of comparison with literature damage rates to other polymers, a single exponential decay analysis was used in this work.
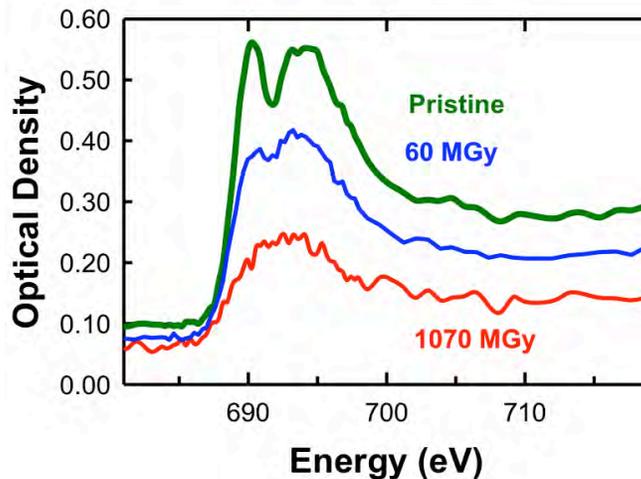
Figure 5.14 F 1s spectrum of Sample set B in an area initially damaged with 60 MGy at 320 eV and then a 9-pad template was burned on the same area to evaluate the bi-exponential decay model (the critical doses using exponential fit are shown in Table 5.3; the bi-exponential model does not improve the fitting quality).

5.4.5 *Comparison to literature results*

A decrease in fluorine signal at the surface of Nafion® (EW=1100 and thickness of 175 μm) has been observed by X-ray photoelectron spectroscopy (XPS) damaged by X-rays (300 W tube in Mg mode, hour long experiment, no dose quantitation) (Schulze et al., 1999). The same work indicated a faster depletion of oxygen and sulfur compared to fluorine, which led the authors to conclude that the rate of cleavage of the side-chains is faster than the rate of damage and F-loss to the main chain (Schulze et al., 1999). The authors attributed the changed spectrum to main-chain disintegration since fluorine depletion was also observed in PTFE damaged with X-rays (Schulze, Bolwin, Gülzow, & Schnurnberger, 1995). Preferential cleavage of the side-chains in ultra-thin PFSA films was also concluded in another XPS study, which saw a much faster decay of the S2p and sulfonic oxygen compared to the F1s signal (Paul et al., 2013). The

formation of new C=C and C=O bonds in soft X-ray damaged PFSA has been detected with infrared (IR) spectroscopy, in a study of PFSA damaged up to a dose of 1.3 MGy using 40 kV X-rays (Almeida & Kawano, 1998). Scissions of the sulfonic acid end group and damage to ether bonds were detected with Raman spectroscopy in the same study (Almeida & Kawano, 1998). C=C formation in X-ray damaged PTFE has only been detected when radiation damage occurred in an inert atmosphere, while formation of carbonyl difluoride occurs for damage in air or oxygen (Lunkwitz, Lappan, & Scheler, 2004).

PTFE is known to oxidize when damaged in the presence of air or weak vacuum (Zhong, Li Yu, Jiazhen Sun, & Y. Zhang, 1993). XPS quantification of the O/C ratio of PTFE damaged using a ^{60}Co source showed that a similar vacuum as considered typical in this work (20 Pa) results in approximately half of the oxygen content compared to when damage was done in air (Zhong et al., 1993). The presence of molecular O_2 has been shown to result in more severe chemical changes and mass loss of carbon rich polymers (Coffey et al., 2002). The molecular weight of PTFE decreases more when irradiated with the same fluence of an electron beam in the presence of dry oxygen (ultrahigh purity) compared to irradiation in vacuum (~ 0.01 Pa) (Fisher & Corelli, 1981). In order to decrease the rate of oxidation, the partial pressure of O_2 during STXM damage measurements should be much lower.

5.4.6 *Relationship to electrochemical damage to PFSA in PEM-FC devices*

Understanding the mechanisms of damage caused by ionizing radiation may also shed light on PEM-FC electrochemical degradation mechanisms which are typically studied by accelerated electrochemical testing. An increase of carbon in a graphitic state has been observed for both X-ray damaged (this work) and electrochemical stressed PFSA, as well as fluorine decay

(Schulze et al., 1999). Fluorine depletion and increase of graphitic carbon was seen by XPS in PFSA degraded by electrochemically stressing MEAs (Schulze et al., 1999). Side chain disintegration was observed by NMR in PFSA membranes tested by the Felton reaction chemical stress, which mimics fuel cell degradation conditions (Ghassemzadeh, Kreuer, Maier, & Müller, 2010). In-situ hard X-ray studies of PEM-FC cells lead to a rapid loss of performance the PEM-FC (Roth, Eller, & Buchi, 2012). The X-ray exposure resulted in a decrease of the equivalent weight of PFSA membranes and formation of carboxylic end groups seen with Fourier Transform InfraRed (FTIR) (Roth et al., 2012) .

5.4.7   *Recommendations with respect to optimization of STXM as a tool for accurate mapping of ionomer in PEM-FC electrodes*

Recommendations to be used in future studies of PFSA radiation damage:

- Cleaner chamber environment (use of ultra high vacuum or a clean high vacuum, with an O_2 getter)

- Quantitative doses should be measured which requires measuring the detector efficiency for the microscope in use.

Recommendations to be used in future studies for accurate (minimal damage) studies of PFSA quantitation in fuel cells materials:

- Cryo temperatures are likely to reduce the damage, at least the F-loss.

- As a convenience, a dose measuring tool should be embedded in the microscope software such that the user inputs the detector efficiency and characteristics of the sample (thickness, density and the OD). The software would then calculate the expected dose before initiating

the measurement and the user can evaluate if a lower dose should be used or if a higher dose can be used according to the critical dose of the material.

- It is recommended that quantitative measurements for PFSA should use less than 20 MGy which is ~20 % of the critical dose. For 100 nm films, 20 MGy corresponds to approximately 10 images at maximum spatial resolution (30 nm) or 80 images with 80 nm spatial resolution using 3 MHz incident beam with 1 ms dwell time. Therefore, 20 MGy allows for only a few 2- or 4- energy stack maps at maximum spatial resolution or 1 stack (~80 energies) with lower spatial resolution (~80 nm). These conditions are similar to what had been identified by empirical procedures guided by post-measurement damage checks (Susac et al., 2011, 2012).

5.5   *Summary*

The critical doses for radiation damage to perfluorosulfonic acid, polytetrafluoroethylene and Teflon®AF by 320 eV and 710 eV soft X-rays was evaluated using direct write patterning at several photon energies in a STXM. Damage was evaluated at energies of characteristic S 2p, C 1s, O 1s and F 1s spectral features: through SVD analysis of full stacks; and by evaluation of elemental changes by integration of the full edge signal. For pathways of damage for PFSA (CF_2-CF_2 amorphization and fluorine loss), the critical dose for damage measured at different energies and different edges is rather similar. This work was unable to confirm the preferential side-chain removal previously claimed in the literature. The damage chemistry of PFSA is rather sensitive to the sample chamber environment. Future quantitative dose-damage studies of PFSA should be done in a STXM with much better vacuum. I have found that PFSA is 2-3 times more sensitive to

X-ray damage than PTFE or Teflon®AF. Recommended dose limits and procedures to acquire

spectra with minimal modification of PFSA were given.

Chapter 6

STXM evaluation of electron beam damage to PFSA

This chapter compares chemical changes and radiation damage rates for room and cryo temperature electron irradiation of PFSA thin films measured using STXM-NEXAFS. The damage rates were compared to those for soft X-ray irradiation of the same material (Chapter 5). The effect of temperature and choice of substrate were evaluated for the electron irradiated PFSA samples. The dose-limited TEM spatial resolution was calculated for PFSA.

6.1   Introduction

Understanding the structure of, and mapping the hydrophilic and hydrophobic channels in hydrated PFSA can help model the transport of protons and water in the membrane, as well as in the cathode during ORR reactions. X-ray scattering techniques have given considerable insight into the nanoscale morphology of PFSA (Kusoglu & Weber, 2017). However, several different models can explain the scattering data equally well, leading to ambiguity. Direct visualization of the nanostructure of dry and hydrated PFSA with sub-nm spatial resolution has been attempted several times using transmission electron microscopy (TEM) (Allen et al., 2015; Peron et al., 2010; C. Wang et al., 2013). However, a major concern for electron microscopy when applied to radiation sensitive soft materials such as PFSA is that radiation damage limits the achievable spatial resolution (Egerton, 2012; Egerton, Lazar, & Libera, 2012) and can result in damage artifacts such as mass loss and phase separation (Yakovlev et al., 2013). Recently, Yakovlev et al.

2013 claimed that "*morphologies that have been observed (in the literature) are, in many cases, artifacts caused by (radiation) damage*."

This chapter reports STXM characterization of damage chemistry and measurement of quantitative rates for radiation damage to PFSA by high energy electron irradiation. As described in **section 3.2.4.2**, the electron beam dose was determined by exposing PMMA under controlled conditions, developing the films, and calibrating the dose with the positive to negative lithography cross-over. This method was previously developed for determination of detector efficiency of X-ray microscopes (Leontowich et al., 2012). Then, spun cast PFSA films were damaged in a 200 kV electron microscope using transmission mode and ultra-low dose imaging irradiation conditions. Ultra-low 'dose' imaging is considered as 8 e-/Å or 800 e-/nm^2 (for complete tilt series acquisition) (Migunov et al., 2015) and 5 e-/Å or 500 e-/nm^2 (for atomic resolution imaging of biological materials) (Rodriguez, Eisenberg, & Gonen, 2017) using direct electron detectors. The effect of sample temperature on the damage kinetics was studied by electron beam irradiation with the sample both at ambient temperature (~25 °C) and at -170 °C using a cryo-sample mount. Damage rates when the sample was mounted on Cu grids (without any substrate film) and SiNx substrates were compared. In all cases the electron beam damaged films were examined by STXM in order to quantify the chemical changes due to electron beam irradiation.

6.2   *Experimental Methods*

Prior to electron beam exposure, optical microscopy images were recorded of all samples using 5x to 20x objective lenses in both transmission and reflection modes. Areas of interest were

identified beforehand to avoid unnecessary damage from navigation in the TEM. All electron beam exposure was done using full field transmission mode in a TEM microscope (JEOL model 2010F with a field emission electron gun) operated at 200 kV. A Gatan, model 4-950-90 cryo-holder used.

Several specimens of PFSA and PMMA materials were damaged in multiple areas using low current densities in the microscope in transmission mode. First, the orientation of the grid/window and the areas of interest were identified using low magnification (50-200x). When changing magnification, there is potential confusion from rotation of the image which results in additional exposure. This was minimized by working at the edge of a Cu grid square or beside the frame of the SiNx window.

Table 6.1 summarizes all electron irradiation conditions used in this Chapter. In JEOL microscopes, the spot size knob changes the strength of the condenser lenses. Higher spot sizes decrease the condenser electron lenses strength (and hence number of incident electrons). The irradiation was done using the highest spot size and a condenser aperture of 20 μm to minimize the flux of incident electrons on the sample.

Table 6.1 Parameters used for irradiation of films using transmission mode in a JEOL-2010F.

Sample	Temperature	Condenser aperture	Spot Size	Magnifi-cation	Real current (pA)	Exposure time (s)	Electron Fluence (e-/nm^2)
PMMA	Room	20 μm	5	15,000	50-60	2-120	125-8000
PMMA	Cryo	20 μm	4	15,000	120-150	5-70	700-12000
PFSA	Cryo	20 μm	5	20,000	53-55	2-60	200-6300
PFSA	Room	20 μm	5	20,000	54	2-16	200-1800
PFSA	Room/SiNx	20 μm	5	20,000-40,000	50-56	2-180	200-50000

Damage spots were made using 15x to 40,000x magnifications and illuminating only the 2 cm diameter fluorescent screen, which measures current. See the schematic shown in **Figure 6.1**. In JEOL microscopes, the exposure area on the sample is not linearly proportional to the magnification, M. The area of the exposed regions (A_s) was calculated as the area of a circle according to:

$$A_s = \pi \cdot \left(\frac{r}{M \cdot 10^7} \cdot 2\right)^2$$

Equation 6.1

where r is the radius of the small fluorescent screen (1 cm), M is the microscope magnification used during damage, and A_s is given in [nm^2]. These areas agree with the areas observed in the post-damage STXM images. The current density reported by the microscope was low by x10, as verified with current measurement using a Faraday cup. Exposure times varied from 2 seconds to 2 minutes by manually clicking a button that inserts and removes the shutter. Two seconds is the lowest practical time due to the time required for opening and closing the shutter. The conditions used in this work were similar to those used for ultra-low dose measurements (Migunov et al., 2015; Rodriguez et al., 2017).

After the TEM session was completed, the samples were taken to an optical microscope to view the damaged regions using reflection mode and 50-100x objective lens. The PFSA samples were taken to STXM microscopes for detailed analysis. All samples used in this work are listed in **Table 6.2.**
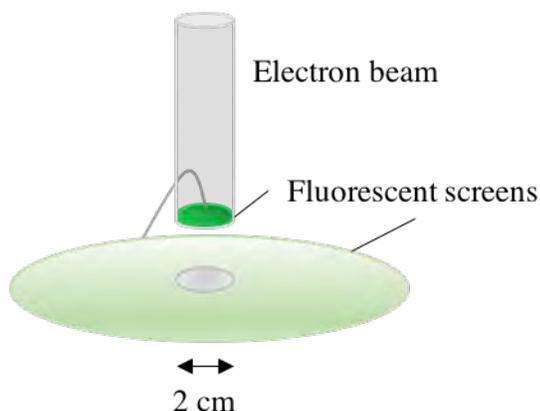
Figure 6.1 Schematic of the two fluorescent screens in a JEOL-2010F microscope. The electron beam (transmission mode) was set to only illuminate the small 2 cm diameter screen.

Table 6.2 Data summary for TEM damage and STXM analysis.

Set	Sample	Thickness (nm)	Substrate	Analysis	Comment
B	PFSA 2%	70-110	None	C, O, F stacks	Fig. 6.2-6.9; cryo TEM damage
C	PFSA 2%	70-110	70 nm SiNx	C, O, F stacks	Fig. 6.3; electron damage free
D	PFSA 2%	45-60	None	C, F images	Fig. 6.7, 6.9; RT* TEM damage
E	PFSA 2%	95-110	100 nm SiNx	C, F images	Fig. 6.7; RT* TEM damage
F	PFSA 2%	50-80	100 nm SiNx + 5 nm Pt	C, F images	Fig. 6.7; RT* TEM damage
G	PFSA 3%	80-100	70 nm SiNx	C, O, F images	Fig. 6.9; RT* STXM damage at 320 eV, He environment
H	PFSA 4%	120	none	C, O, F images	Fig. 6.9; RT* STXM damage at 320 eV, He environment
I	PFSA 4%	160-230	none	C, O, F images	Fig. 6.9; Cryo TEM damage

*RT = Room temperature

6.3   Results

6.3.1   NEXAFS spectra of undamaged PFSA versus electron damaged PFSA at cryo temperature

An area of a ~100 nm thick PFSA film (**Sample set B**) was damaged using 200 kV electrons with the sample cooled to -170 °C. **Figure 6.2** shows post-damage images using optical microscopy and STXM. **Figure 6.2 a** is a low magnification reflection mode optical image where the Cu grid (bronze color) is visible through the overlaid PFSA film. A higher magnification image of the region in the white square is shown in **Figure 6.2b**. The incident electron fluence ($x10^3$ e⁻/nm²) is shown for each damaged region. All damaged regions are clearly visible in the optical microscopy image (**Figure 6.2b**). The same damage area was studied using STXM - an OD image at 690 eV is shown in **Figure 6.2c** with indicated electron doses. As the dose increases, the OD in each damaged area decreases, indicating that both mass loss and chemical change are caused by the incident electron beam.

One can argue that PFSA will always be damaged in TEM due to an inevitable dose from low magnification navigation. **Figure 6.3** compares the quantitative OD1 spectra at the C 1s, F 1s and O 1s edge of 'pristine' PFSA, where 'pristine' designates an area not intentionally dosed. The 'X-ray pristine' sample (**set C**) was never examined by TEM. The 'cryo TEM pristine' sample (**set B**) was examined using cryo temperature in the TEM. All spectra were measured in STXM under very low damage conditions (less than 5 MGy). The elemental response spectrum for PFSA EW 1100 is shown in blue in **Figure 6.3**. The C 1s and F 1s spectra for the X-ray and Cryo-TEM pristine samples are nearly identical, while the O 1s signal is slightly more intense for the Cryo-TEM sample.
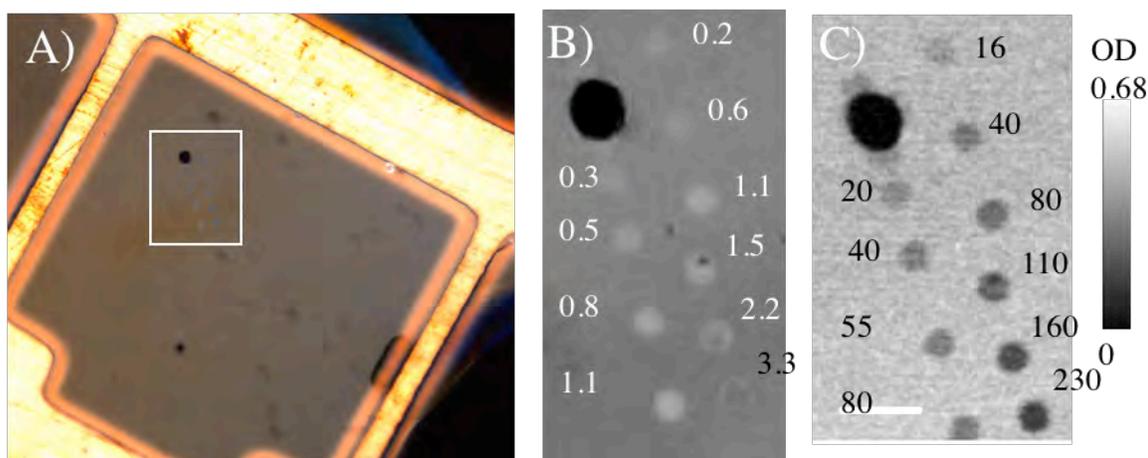
Figure 6.2 Images of PFSA film of 110 nm thickness (sample set B) after damage with 200 kV electrons using **(A)** optical microscopy at (5x magnification; reflection mode) showing the film on a Cu TEM grid **(B)** 50x magnification optical microscopy reflection image of the squared area in (a) with indicated fluences (x10^3 e$^-$/nm^2). **(F)** a STXM OD image recorded at 690 eV of the same area with indicated electron beam doses (MGy). Scale bar is 5 μm.

The C 1s and F 1s spectra of the PFSA are dominated by peaks at 292.4, 296, 690 and 694 eV related to the C1s and F 1s → σ*$_{C-F}$ transitions (Yan et al., 2018). The O 1s signal is dominated by a broad feature between 535-545 eV related to transitions O 1s → σ*$_{C-O}$ and O 1s → σ*$_{S-O}$ (Urquhart, Hitchcock, Priester, & Rightor, 1995; Yan et al., 2018). There is a small peak at 532 eV, which has been attributed to O 1s → π*$_{C=O}$ transitions at carboxylic/carboxylate groups terminating the PFSA chains (Yan et al., 2018).

The C 1s, O 1s and F 1s NEXAFS spectra of a few areas from **Figure 6.2** are shown in **Figure 6.4**: the most damaged region (i.e. 230 MGy), the 'pristine area' previously discussed, and the area dosed with 20 MGy. The exposure of PFSA to electrons resulted in extensive chemical changes. At the C 1s edge (**Figure 6.4a**), there is significant reduction in the intensity of the 292.4 eV peak after 230 MGy and it appears that the C 1s spectrum of the damaged material

converts to a shape with a single C 1s $\rightarrow$ σ^*_{C-F} transition centered at 296 eV. The broad feature at 308 eV, related to the C 1s $\rightarrow$ σ^*_{C-C}, is also significantly changed after 230 MGy incident electrons. New peaks, probably related to C 1s $\rightarrow$ $\pi^*_{C=C}$ and C 1s $\rightarrow$ $\pi^*_{C=O}$ transitions (Urquhart & Ade, 2002) are visible at 285.1 and 286.8 eV. The significant decay of the pre-edge of the C 1s spectra, which is dominated by the fluorine valence ionization continuum, indicates fluorine mass loss. The significant post-edge decay suggests both fluorine and carbon loss. At the O 1s edge (**Figure 6.4b**), there is an extensive decay in intensity over the full spectrum, including the pre-O1s edge. There is no evidence for oxygen mass loss since the pre-edge signal and post-edge O 1s signals change by similar amounts. Changes to the F 1s edge (**Figure 6.4c**) are similar to that occurring at the C 1s edge. By a dose of 230 MGy the peak at 690 eV is nearly disappeared. The decrease at the F 1s post-edge indicates fluorine mass loss. These observations are very similar to those of soft X-ray damaged PFSA – see Chapter 5 - with the main differences occurring at the F 1s pre-edge. Due to the ultra-high vacuum (10^{-5} Pa) in electron microscopes compared to the STXM chamber (~20 Pa) carbon contamination was probably minimized and carbon deposition is not visible, whereas it is observed in STXM damaged fluoropolymers (see Chapter 5). The low dose electron irradiation at 20 MGy results in some damage. This dose corresponds to an incident areal flux of 300 e-/nm^2 on a 110 nm film and was enough to cause visible chemical changes and elemental fluorine mass loss to the PFSA.
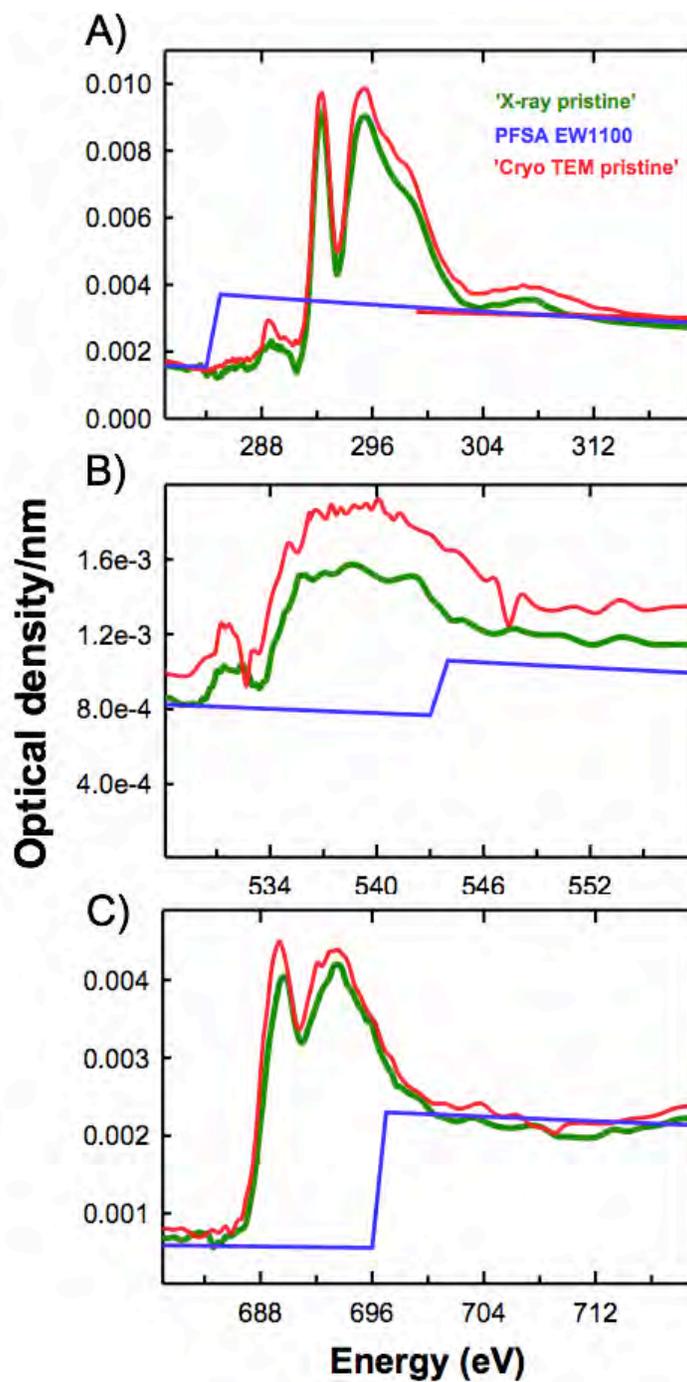
Figure 6.3 Comparison of quantitative STXM NEXAFS spectra at the **(A)** C 1s **(B)** O 1s and **(C)** F 1s edges of i) a PFSA film not intentionally exposed using cryo electron microscopy (red; sample set B), ii) a PFSA film not intentionally exposed to soft X-rays (green; sample set C) and ii) the spectrum for PFSA with density = 2 g/cm^3 and $C_{20}F_{39}O_5SH$ (blue).
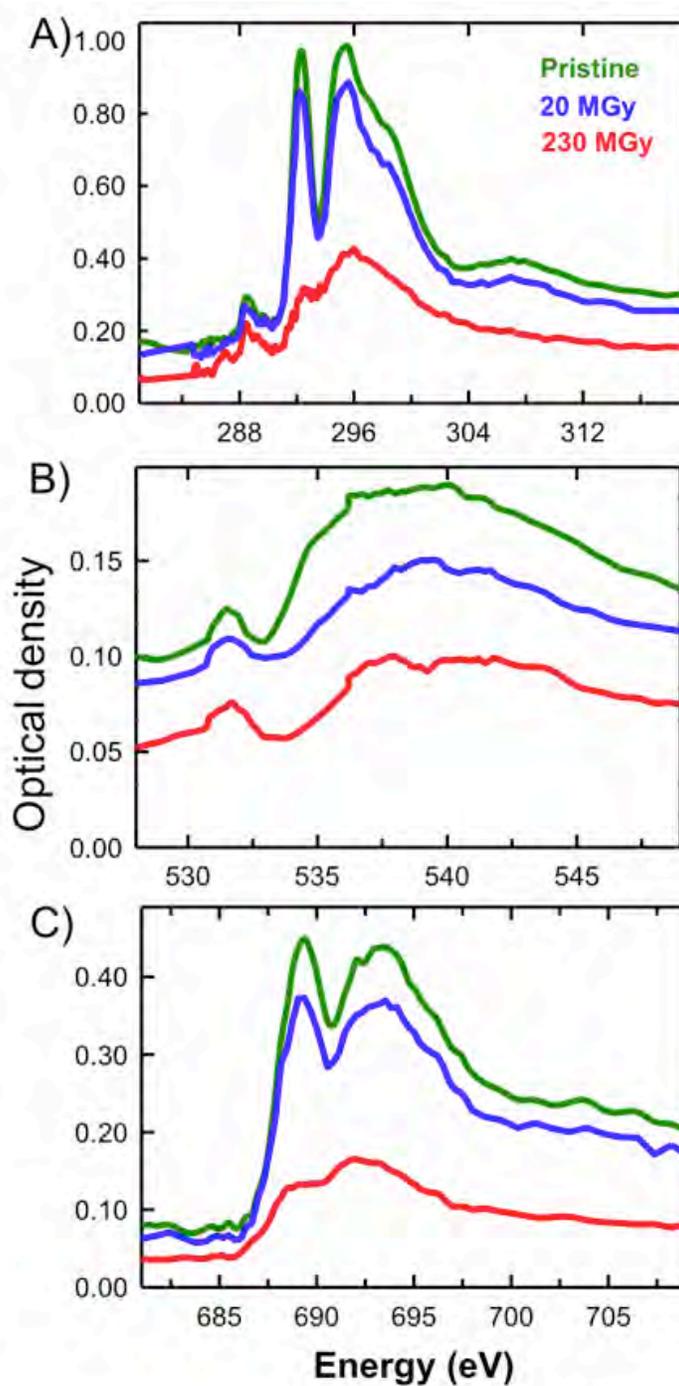
Figure 6.4 STXM NEXAFS spectra of a PFSA film (sample set B) of the **(A)** C 1s **(B)** O 1s and **(C)** F 1s edges of a pristine area (green), lowest dose of 20 MGy (blue) and damaged by a dose of 230 MGy (red) of 200 kV electrons in a TEM.

6.3.2 Quantitative analysis of electron damaged PFSA

The elemental changes caused by electron irradiation were evaluated quantitatively using the methods described in Chapter 3 – **section 3.3.2.** The decay was modeled using an exponential function which assumes the damage follows first order kinetics (Beetz & Jacobsen, 2003; Coffey et al., 2002; Leontowich et al., 2012; Wang, Morin, et al., 2009). The fit curves along with the derived elemental amounts are plotted in **Figure 6.5.** At 20 MGy, the oxygen content decays by 32 ± 8 %. After this dose, no further oxygen loss is observed. The a_c for the oxygen loss was 15 ± 3 MGy, where the error is from the fitting procedure. This value is lower than the value of 45 ± 6 MGy observed for X-ray damaged PFSA (see Chapter 5). Note that the 'cryo-TEM pristine' sample has slightly more oxygen compared to the 'X-ray pristine' sample as noted in **Figure 6.3**. It is possible that after the sample was warmed to RT and transferred to the STXM microscope oxygenated contaminants were adsorbed on the sample surface. The low critical dose for oxygen can also be related to the presence of non-PFSA oxygenated species on the sample surface and residual solvents in the bulk. The a_c for the fluorine loss for the cryo-TEM damaged PFSA was 97 ± 17 MGy, which is similar to that of X-ray damaged PFSA in active vacuum (2×10^{-2} Pa) (107 ± 17 MGy) and He environment (136 ± 19 MGy) (discussed in Chapter 5). Although there is also significant carbon loss, it was not possible to fit the integrated background subtracted C 1s data to the exponential model. The results indicate carbon loss has a linear rather than exponential dose dependence indicating zero-order kinetics.
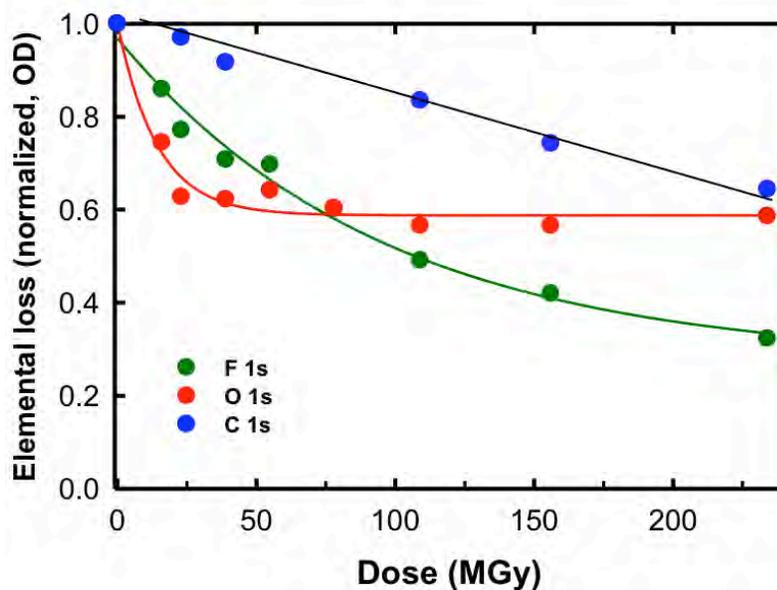
Figure 6.5 STXM quantitative analysis of the elemental changes (F 1s, C 1s and O 1s) for PFSA sample set B under cryo conditions from the same damage area shown in Figure 6.3 and Figure 6.4.

In order to understand the spectroscopic changes in terms of damage mechanisms, it is useful to examine how the intensities of specific transitions change as a function of increasing dose. **Figure 6.6a** presents STXM images of the same sample but different areas as that depicted in **Figure 6.2** (**sample set B**). After electron irradiation, STXM OD images were measured at specific energies. In each case, **Figure 6.6a** presents differential STXM images (peak minus pre-edge) to compensate for mass loss. Images related to the C-F bonds (690 and 292.4 eV) have the highest contrast. The images related to the formation of new bonds: C=C (285.1 eV) and C=O (287 eV) have low contrast and are quite noisy due to the weak signal (**Figure 6.4a**). The C 1s continuum image $OD_{320 \text{ eV}} - OD_{280 \text{ eV}}$ shows that carbon mass loss is insignificant except for the highly dosed areas. **Figure 6.6b** plots the optical density for each of the damage circles in the images in **Figure 6.6a** as a function of electron dose. This shows how the formation of C=O

bonds, amorphization of C-F bonds, and elemental mass loss change as a function of electron dose.

Table 6.3 compares the critical dose for all the transitions shown in **Figure 6.6b**. The a_c for the C 1s $\rightarrow \sigma^*_{C-F}$ and F 1s $\rightarrow \sigma^*_{C-F}$ transitions, 117 ± 13 and 113 ± 13 MGy respectively, are identical. The a_c for fluorine mass loss (F-loss) (101 ± 28 MGy) from electron irradiation of PFSA at cryo conditions is the same as the decay of the σ^*_{C-F} transitions (113 ± 13 MGy). This is in agreement with the result shown in **Figure 6.5** which was a different area damaged and evaluated with a full F 1s stack. I conclude that C-F bond breakage and fluorine mass loss occur at the same rate for the cryo-TEM damaged sample. On the other hand, the a_c for carbon mass loss evaluated using (OD_{320} − $OD_{280 \text{ eV}}$) is significantly larger than the F-loss at 245 ± 13 MGy using the exponential decay. The amorphization of the C-F bonds leads to fluorine loss at the same rate and carbon loss at a much slower rate.
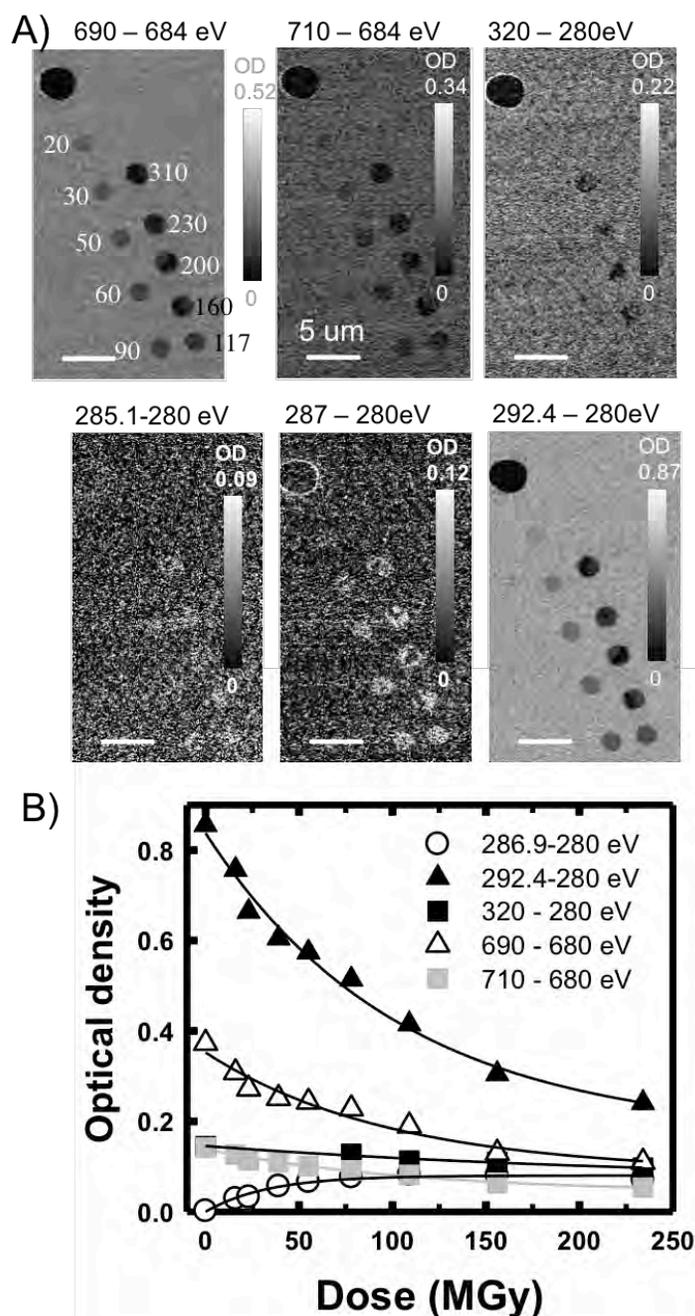
Figure 6.6 STXM **(a)** images and **(b)** OD decay as a function of dose at several transitions (subtracted by the respective pre-edge signals) for the F 1s and C 1s edges for PFSA damaged under cryo conditions (Sample set B; different area from Figure 6.2). The dose for each area is shown in (a) The exponential fit is also plotted and quantitative results are shown in Table 6.3.

Table 6.3 Critical dose (MGy) for different damage processes in a freestanding PFSA film damaged by electron beam irradiation in a TEM in cryo conditions (Sample set B).

Transition	Energy (eV)	a_c (MGy)
C1s $\rightarrow \pi^*_{C=O}$	287 - 280	32 ± 3
C1s $\rightarrow \sigma^*_{C-F}$	292.4 - 280	117 ± 13
Elemental C	320 - 280	245 ± 13
Elemental O	O 1s spectra *	15 ± 3
F1s $\rightarrow \sigma^*_{C-F}$	690 – 680	113 ± 13
Elemental F	710 - 680	101 ± 28
Elemental F	F 1s spectra*	97 ± 17

*Background subtracted integrated spectra

6.3.3 Effect of temperature and support on electron damage to PFSA films

Figure 6.7 plots TEM-induced damage to freestanding cryo-cooled and ambient PFSA films as a function of dose for **(a)** CF_2-CF_2 amorphization ($OD_{690\ eV}$ - $OD_{680\ eV}$) and **(b)** fluorine mass loss ($OD_{710\ eV}$ - $OD_{680\ eV}$) (**Sample set D**). In each case the OD (or ΔOD) was divided by the OD (or ΔOD) for the undamaged material to compensate for thickness differences. The freestanding PFSA film ruptures after approximately 100 MGy when damaged at RT. At -150 °C the film can sustain much more damage and does not rupture until doses exceed 450 MGy. The rate of decay of CF_2-CF_2 amorphization and fluorine mass loss are similar with average values of 45 ± 10 MGy and 113 ± 13 MGy for the RT and cryo temperature damaged PFSA, respectively. This slower decay rate was also observed in cryo-TEM damaged PFSA films by quantifying the EELS elemental content (Yakovlev et al., 2013).
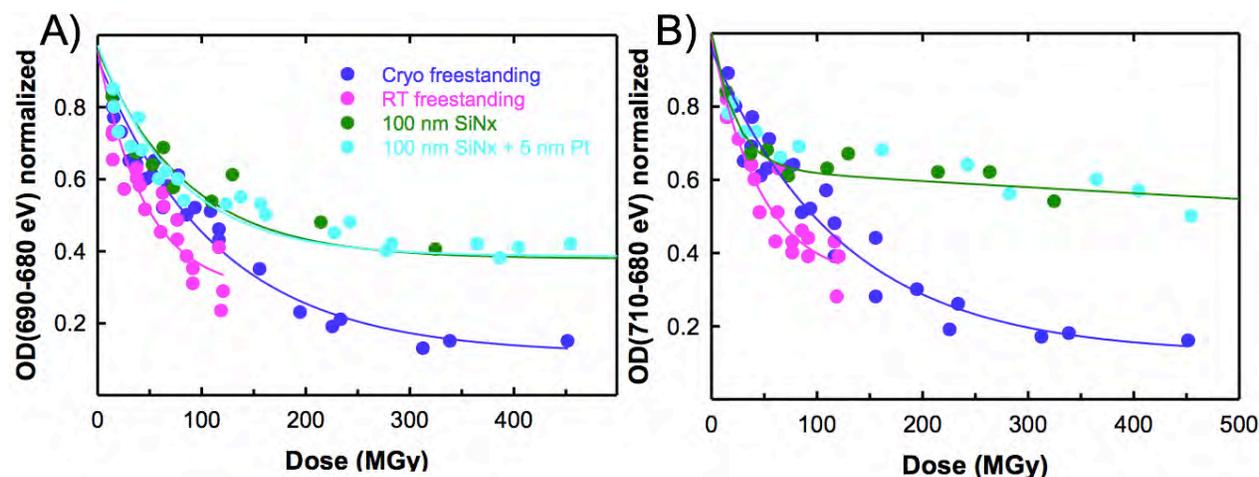
Figure 6.7 Quantitative analysis of the decay of the OD at **(A)** 690 eV (F 1s → σ*$_{C-F}$ transition) subtracted by the pre-edge signal at 680 eV and **(B)** OD$_{710\ eV}$ − OD$_{680\ eV}$ for freestanding PFSA damaged with electrons at room and cryo temperature and for PFSA films on SiNx substrates.

Figure 6.7 also compares the effect of RT-TEM damage of the freestanding PFSA compared to the film deposited on a 100 nm SiNx substrate (**Sample set E, Table 6.2**) and 5 nm sputtered Pt on a 100 nm SiNx substrate (**Sample set F, Table 6.2**). The Pt was sputtered on a SiNx window to assess the role of conductivity of the substrate. There was no significant effect on the PFSA damage chemistry or rate. It is possible that the sputtering process did not completely cover the surface and did not form a uniform layer capable of properly conducting the electrons. Using a 100 nm SiNx substrate changes the rate of damage of the C-F bonds and the fluorine elemental mass loss compared to the freestanding film. At high doses (>400 MGy), the normalized OD$_\infty$ of (690-680 eV) is ~0.4, which means that 40% of the remaining OD signal does not result in further decay. This is quite different for the freestanding film, where the normalized OD$_\infty$ is extrapolated to 0.20 (but in reality the film ruptures at ~100 MGy). For the fluorine loss (as shown in **Figure 6.7b**), the substrate affects the rate of decay and does not

follow an exponential decay, indicating that the damage mechanism is different. The normalized

OD_∞ at 710-680 eV is much higher than for the freestanding film: approximately 0.6 compared to

0.2, respectively, which indicates that the substrate either affects the primary ionization or

prevents the diffusion of the damaged products, generated through the secondary processes, from

the film surfaces to the sample chamber.

The a_c measured for $OD_{690\ eV} - OD_{680\ eV}$ for samples B, D, E and F are summarized in

Figure 6.8. The a_c values for CF_2-CF_2 amorphization, as measured at the F 1s edge, for PFSA on

SiNx and Pt-coated-SiNx are 87±17 and 76±9 MGy, respectively. This is roughly double that of

the freestanding film. Electron beam damage to a cryo-temperature, freestanding film yields the

highest critical dose for CF_2-CF_2 amorphization, indicating that the cryo temperature <u>helps slow

down the damage process</u>.
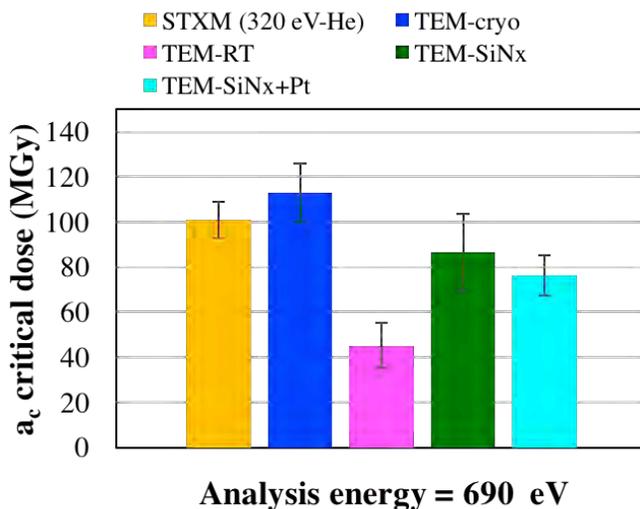
Figure 6.8 Quantitative analysis of the decay of the OD at 690 eV (F 1s → σ^*_{C-F} transition)
subtracted by the pre-edge signal at 680 eV for freestanding PFSA damaged with electrons
at room and cryo temperature and for PFSA films on SiNx substrates.

6.3.4   Quantitative comparison of electron and X-ray damaged PFSA

Figure 6.9 compares damage measured at $OD_{690\ eV} - OD_{680\ eV}$ as a function of dose for

PFSA films damaged by cryo and RT TEM to that for RT X-ray irradiation at 320 eV. PFSA film

on SiNx substrate and freestanding (**Sample set G** and **H**, respectively, shown in **Table 6.2**) were

damaged by 320 eV photons. As previously discussed (see Chapter 5), the substrate does not have

an effect on PFSA damaged by photons. The rate of damage to PFSA by photons is similar to that

for freestanding PFSA films damaged by electrons at cryo temperature (**Figure 6.8**). The

normalized OD_∞ between 0.3 and 0.18, respectively, is similar for both cases. As shown in

Figure 6.9, the normalized response at 690-680 eV between 0-100 MGy is similar for all

processes (cryo-TEM, RT-TEM, 320 eV X-rays), but deviates at doses higher than 100 MGy. It is

possible that after 100 MGy dose of electron irradiation, sample charging plays a bigger role in

the damage process, generating more secondary electrons and resulting in more damage.
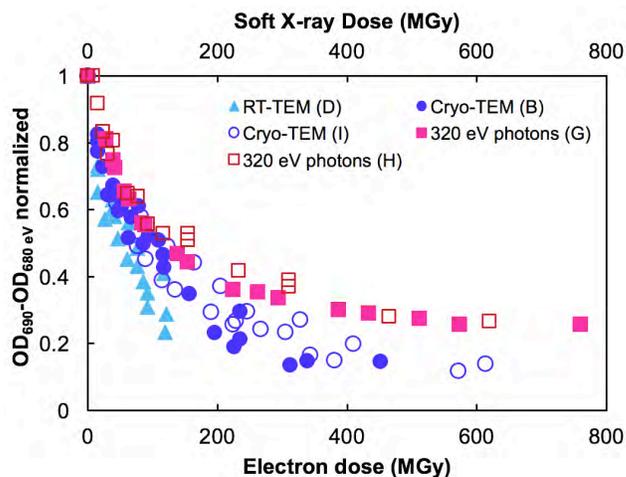
Figure 6.9 Analysis of the $OD_{690\ eV} - OD_{680\ eV}$ decay (F 1s $\rightarrow$ σ^*_{C-F} transition) for PFSA freestan-
ding and on SiNx substrate damaged with electrons at RT, freestanding at cryo temperature, and
damaged with X-rays at RT. For each data set, the sample set is indicated (see **Table 6.2**).

6.4   *Discussion*

6.4.1   *Electron versus X-ray damage to PFSA*

6.4.1.1   *NEXAFS chemical changes*

A comparison of the spectra of PFSA dosed with 20 MGy of 320 eV soft X-rays (**Figure 5.2 & 5.3**) and that dosed with 200 keV electrons (**Figure 6.4**) show that the chemical changes are very similar. In both cases, by 20 MGy the damage is apparent and should be the upper limit when studying a specific area. In the TEM, 20 MGy corresponds to a fluence of only 0.004 C/cm^2 or 2.5 e$^-$/ Å for a 100 nm film. This fluence is lower than that currently used for **near-atomic resolution** imaging of biological materials (Rodriguez et al., 2017).

The similarity of the chemical changes from electron and X-ray irradiation indicates that the damage process is caused mostly by secondary electrons generated after the initial ionization, as previously noted (Wang, Botton, et al., 2009). Secondary electrons generated by both types of radiation result in further ionization generating free electrons, ions and radicals, leading to a cascade of damage reactions. There were some differences for the heavily dosed areas, with the most noticeable differences occurring at the F 1s pre-edge and C 1s spectrum. Due to the much lower pressure in the sample chamber and the cold finger present in the TEM microscope to avoid contamination, it is apparent that there is more organic contamination when the sample is damaged in the STXM. This was evident when the carbon mass loss was compared – there was no evident carbon mass loss for the STXM damaged PFSA, while the carbon mass loss was calculated to be ~2.5 times slower than that for fluorine mass loss for the electron damaged PFSA.

6.4.1.2 Mechanistic discussion

Oxygen was lost with minimal electron irradiation. Several factors might explain this. First, there is evidence for more oxygen present in the sample than is expected from the published structure of PFSA (see **section 3.2.3.1** and **Figure 3.8**). This could be from chain termination carboxylates or from residual solvent in the spun cast samples. The latter could be lost with very low electron doses. Since one cannot differentiate the loss of the different oxygen species, it is not possible to conclude if the side-chain is in fact lost at a faster rate compared to the amorphization of the C-F bonds.

With increasing dose, amorphization of the C-F bonds and fluorine loss occur at the same rate. The scission of the C-F bonds and subsequent chemistry probably results in the formation of volatile products such as CF_4 due to a recombination of the $F\cdot$ with $CF_3\cdot$ radicals, and not F_2 (Forsythe & Hill, 2000). Due to the slower carbon loss compared to fluorine loss, our data seems consistent with formation of CF_3 or CF_4 molecules.

Electron beam irradiation of a co-polymer of PTFE with ether bonds (i.e. polytetrafluoroethylene-co-perfluoropropyl vinyl ether with ether bonds, PFA) in vacuum resulted in formation of COF and COOH groups detected with infrared spectroscopy (Lappan, Geißler, Scheler, & Lunkwitz, 2003). The formation of C=O bonds (see **Figure 6.4**) is consistent with formation of C=O(F) and COOH groups.

6.4.2 Effect of environment (T, substrate)

Radiolysis is the predominant form of damage for organic materials irradiated with 10-300 keV electron beams (Egerton, 2012). Although knock-on displacements (due to energy transfer in nominally elastic scattering) occur in organic materials, they are relatively weak and

have cross-sections that are orders of magnitude smaller than for ionization (Egerton et al., 2012). The carbon knock-on displacement can be avoided by using lower kV, but the knock-on cross-section is orders of magnitude smaller than radiolysis (Egerton, 2012).

Cooling samples to cryo temperatures when using electron or X-ray irradiation is known to reduce the rate of damage to radiation sensitive material (Beetz & Jacobsen, 2003; Egerton, 2013; Warkentin et al., 2013). For X-ray irradiation at cryo temperature of PMMA, the authors quantified a similar critical dose for damage of the C=O bond loss, but drastically different damage rates for the elemental oxygen mass loss (Beetz & Jacobsen, 2003). For PFSA damaged in the TEM in cryo conditions, it was observed that the mass loss slows down with EELS (Yakovlev & Libera, 2006; Yakovlev et al., 2013). However, the structural damage during cryo temperature electron irradiation depends largely on the material (Lamvik, 1991). Electron irradiation damage quantification in the TEM is usually limited to elemental mass loss using EELS (Egerton, 1982, 2013; Yakovlev & Libera, 2006; Yakovlev et al., 2013).

The reduced damage rate at cryo temperature is probably because the frozen material traps the volatile damage products. This is apparently only a temporary measure since there is evidence that the bond breaking and reorganization continues at cryo temperatures (Beetz & Jacobsen 2003), and the full effect of the damage, in particular mass loss, is observed after warming the sample to room temperature. This was observed for both X-ray (Beetz & Jacobsen 2003) and electron damaged organic materials (Egerton 1980). **The work presented in this chapter shows that electron irradiation of a sample at cryo temperature and warming up the sample to RT reduces the damage in PMMA and PFSA by half when compared to RT irradiation.** Therefore, the trapping of the volatile products and limiting the diffusion of damaged species

including low molecular weight fragments at cryo temperature affects the damage (Knapek & Dubochet, 1980). In the case that the damaged products were only trapped at cryo temperature, the rate of damage would be similar for the sample damaged at cryo then warmed to RT and for the sample damaged in RT. This is a very interesting observation worth following up as prior cryo TEM work (Egerton, 2013) has assumed the damage rate to be partially temperature independent.

Besides the generation of secondary electrons, other issues that arise during electron irradiation include sample charging and thermal effects (Egerton et al., 2012). Note that the thermal effect is minor in TEM mode (Egerton, 2013). Sample charging, which arises due to secondary electron emission when inelastic scattering occurs near the sample surface (Egerton, 2013), can be minimized by using lower beam currents (Egerton, 2012). Sample charging was minimized in this work by using low beam currents (50 pA) in the JEOL2010F microscope. Combining charging with thermal effects can soften and result in tearing of the sample (Egerton, 2012). The tearing of samples was observed throughout this Chapter and is clearly shown in **Figure 3.12a** for PMMA samples. However, the tearing was not observed for films deposited on SiNx substrate, which were observed to be slower to damage (i.e. have larger critical doses) than freestanding films. The underlying substrate seems to minimize sample charging and affects the damage rate of PFSA during electron irradiation. Similar effects have been observed when insulating samples were coated with conductive materials (Egerton, 2013). Using a continuous carbon substrate while irradiating PFSA with electrons has been shown to slow the elemental removal rate of fluorine and oxygen but at the cost of increased contamination (Yakovlev et al., 2013).

For X-ray irradiation, there was no observable relationship between the substrate and damage rate. I conclude that sample charging is minimal for X-ray compared to electron irradiation.

6.4.3   Can TEM be used for direct visualization of the morphology of PFSA ?

The **dose-limited resolution** (δ) for bright-field imaging in TEM has been estimated as 5 nm for signal to noise ratios (SNR) of 5 (which may be an over-stringent requirement) and considering the a_c as 0.01 C/cm^2 for amorphous aliphatic organic materials such as PMMA (Egerton, 2013; Egerton et al., 2012):

$$\delta = (SNR)(DQE)^{-0.5}C^{-1}\left(\frac{F \cdot a_c}{e}\right)^{-0.5} \qquad \text{Equation 6.2}$$

where DQE is the detector quantum efficiency (estimated as 0.2 for charge integrating cameras), $C = 0.1$ is the contrast between different resolution elements, F ~0.8 is the efficiency of the signal-collection system and e is 1.6×10^{-19} C. In order to image near-pristine PFSA with bright-field TEM, the recommended dose should not exceed 20 MGy, which corresponds to a fluence of ~ 0.004 C/cm^2 for 100 nm films. The dose-limited resolution calculated for PFSA using the parameters above is **8 nm**. This value decreases to 3.5 nm if a DQE of 1 is used (consistent with state-of-the-art direct electron counting detectors). Note that this estimation is valid for the sample in cryo temperature warmed up to room temperature.

This estimate indicates that only detectors with DQE of 1 may allow direct visualization of the sub-5 nm hydrophyllic and hydrophobic channels in PFSA without resulting in damage while using cryo temperatures. In addition, such studies should be performed using a substrate which also protects the film from sample charging related damage. At higher doses, radiation damage clearly changes the PFSA material and the resulting image is therefore not that of pristine

PFSA. Yakovlev (Yakovlev et al., 2013) concluded in their work that truly meaningful TEM imaging of PFSA materials is not possible since images with high enough signal to noise ratio require an exposure that causes changes to the morphology and results in elemental changes as seen with EELS. The results presented in this work directly corroborate Yakovlev's work.

6.5   Summary

I have shown that, when imaging PFSA in the TEM, it is crucial that cryo-temperatures are used since it slows the rate of decay of the film by more than a factor of 2. Electron irradiation in cryo temperatures followed by warm up to RT **doubles the positive to negative cross-over dose for PMMA** and the critical dose for damage of the σ^*_{C-F} related transitions for PFSA relative to RT irradiation. The chemical changes to PFSA due to electron and soft X-ray irradiation are similar, and the critical doses for the same damage process are similar. This indicates that the damage process for both types of radiation are dominated by damage caused by secondary electrons. The differences between the measured critical doses for electrons and X-rays can be related to uncertainties in the electron dose determination and the fact that different vacuum conditions were used. Depositing the polymeric film on a substrate affects the damage rate for both PMMA and PFSA. This indicates that sample charging plays a role in electron irradiation of soft materials.

The dose limited resolution for bright field TEM imaging of PFSA was calculated as 8 nm (or δ = 3.5 nm considering DQE of 1), which under low-dose cryo-TEM conditions would deliver a dose of 20 MGy (~0.004 C/cm^2 for 100 nm film) on a PFSA film, about 25% of the critical dose.

Chapter 7

Quantitative Mapping of Ionomer in Catalyst Layers by Electron and X-ray Spectromicroscopy

This paper compares the damage to the PFSA ionomer in the cathode using F Kα STEM-EDS and F 1s NEXAFS in STXM. The chemical changes caused by electron and X-ray irradiation were quantified using STXM.

The experiment design was developed by the author, Dr. Jasna Jankovic, Dr. Viatscheslav Berejnov and Dr. Darija Susac during the author's internship at AFCC in 2016. The STEM-EDS measurements were acquired by Dr. Jasna Jankovic and the author at Simon Fraser University. The electron damaged areas were measured with STXM by Dr. Viatcheslav Berejnov. The pattern generation template for STXM irradiation was developed by the author. The STXM damage measurements and all analysis were done by the author and Dr. Viatcheslav Berejenov. The paper was prepared by the author under the guidance of Dr. Adam Hitchcock and Dr. Viatcheslav Berejenov. The paper was revised by all authors. The paper was published ©The Electrochemical Society, 2017: L.G.A. Melo, A. Hitchcock, J. Jankovic, J. Stumper, D. Susac, V. Berejnov: Quantitative Mapping of Ionomer in Catalyst Layers by Electron and X-ray Spectromicroscopy. ECS Transactions, **2017**, v80(8) p275-282. doi: 10.1149/08008.0275ecst

Quantitative Mapping of Ionomer in Catalyst Layers
by Electron and X-Ray Spectromicroscopy

L.G.A. Melo,[a] A.P. Hitchcock,[a] J. Jankovic,[b] J. Stumper,[b] D. Susac[b] and V. Berejnov[b]

[a] Chemistry & Chemical Biology, McMaster University, Hamilton, ON L8S4L8, Canada
[b] Automotive Fuel Cell Cooperation Corp., 9000 Glenlyon Parkway, Burnaby, BC
Canada

Quantitative mapping of ionomer in polymer-electrolyte membrane fuel cell (PEM-FC) cathodes, and associated radiation damage was studied by electron and X-ray microscopies. Mapping and damage quantification was performed by F K-α fluorescence mapping using a high-performance energy dispersive spectroscopy (EDS) detector in a scanning transmission electron microscope (STEM-EDS), and by F 1s X-ray absorption spectromicroscopy in a scanning transmission X-ray microscope (STXM). STXM was used to quantitatively analyze both STEM-EDS and STXM damage. The results show that STXM can provide ionomer maps with satisfactory quality and negligible radiation damage while STEM-EDS mapping causes significant fluorine loss. Radiation damage transforms PFSA into a disordered, fluorine depleted material.

Introduction

Limited durability and high costs are the major impediments for cheap mass production of Polymer Electrolyte Membrane Fuel Cell (PEM-FC) for automotive applications. One of the mitigating strategies for maximizing the efficiency and minimizing the cost of the fuel cell stacks is nanoscale structural optimization of the support, active catalyst and ionomer components of the catalyst layer. Successful nano-engineering of catalyst layer structure depends on accurate component quantification and high spatial resolution mapping. Optimizing the spatial distribution of the ionomer in the catalyst layer is of particular importance, as it maximizes access of protons and oxygen to the catalyst and facilitates exhaust of produced water, which will improve performance, durability and enable further reduction of Pt loading.

The commonly used ionomer, perfluorosulfonic acid (PFSA), consists of a hydrophobic polytetrafluoroethylene backbone with perfluoronated ether side chains terminated with sulfonate groups responsible for proton conduction. The biggest challenge in imaging and/or quantifying PFSA with a variety of techniques is radiation damage (1–5). The damage results in material transformation i.e. the signal attributed to PFSA *before* measurement is coming from a different material *after* some time of measurement. These changes occur at the same time as the probe beam generates the analytical signal. Given the ongoing radiation damage, one must ask: can the observed signal be attributed to PFSA? and, to what extent do the measured maps represent the original PFSA distribution and amounts?

Scanning Transmission X-ray Microscopy (STXM) uses absorption of X-rays rather than scattering of electrons to perform analytical imaging. STXM can accurately speciate and quantify different chemical components within a cathode layer (6). This approach has been used to study a variety of PEM-FC materials (7–9). It is especially useful in quantitative mapping of ionomer in catalyst layers (10). In addition, STXM has also been used to quantify soft X-ray damage in a variety of polymeric materials (11–13). One of its biggest advantages over higher spatial resolution transmission electron microscopy (TEM) techniques coupled with core level electron energy loss (EELS) spectroscopy (14,15) or energy dispersive X-ray spectroscopy (EDS) is that, when evaluated in terms of analytically useful information per unit damage, STXM causes much less damage to soft materials than TEM.

This study compares measured fluorine maps, and associated radiation damage from different levels of electron and soft X-ray exposures of PFSA in a real dispersive cathode electrode sample. The electron exposure was done using a scanning TEM equipped with a high-performance Energy Dispersive X-ray Spectroscopy (STEM-EDS) detector. The soft X-ray exposure was done with STXM. The areas exposed to electrons and X-rays were analyzed with STXM to quantify fluorine loss and spectrally characterize the structural changes that occur.

Experimental

A decal sample of a dispersive catalyst layer containing high surface area carbon, Pt and PFSA ionomer (Aquivion® with 790EW) was embedded with TTE epoxy. The sections were microtomed with a Leica Ultracut UCT to a nominal thickness of 100 nm at room temperature using a diamond knife. The sections were floated on to a water surface and transferred to TEM grids (Cu, without support film).

The electron beam irradiation was performed at room temperature using a FEI Tecnai Osiris STEM operated at 200 kV, with gun lens 3, spot size 3, and 1.92 nA current. Four FEI Super-X silicon drift detectors (SDD) were used for Energy Dispersive X-ray Spectroscopy (EDS) measurements. The exposure time of the electron beam at each point of a map was controlled by the EDS software and ranged from 2 μs to 5 ms. This enabled accurate determination of the acquisition time of EDS maps. The maps were acquired at 7000x magnification, with 200 x 800 pixels, and a pixel size of 14 nm. The electron irradiation covered an area of approximately 12-15 μm^2 of the sample and consisted of two methods: i) series of adjacent areas with increasing exposure times (single map), and ii) series of increasing times on the same area (multi-map). TEM navigation and STEM-EDS mapping conditions used in this work are listed in Table I.

For each technique, the area of interest was located using minimal exposure (transmission mode was used in the electron microscope, condition e-A Table I). For STXM the navigation conditions (1 ms dwell, 100 nm defocused beam, conditions p-A Table II) produce no detectible chemical damage. On the other hand, TEM navigation results in minor structural damage to PFSA which can be measured by STXM (see Figure 5a, spectrum 1). This damage is not quantifiable with STEM-EDS since the counts/pixel are below the noise level. For the quantitative aspects of this study, the exposure from navigation imaging was considered to have zero damage and was not included in the calculated exposure (particle/nm^2).

Table I. TEM and STEM-EDS measurement conditions used in this study.

Code	Description	e⁻/nm²	F loss* (%)	Dwell time/pixel (us)	pixel size (nm)
e-A	TEM navigation	1.2	~1	3000	-
e-ND	STEM -EDS(no damage)	1.2×10^2	~4	2	14
e-B	STEM-EDS, Area B *	6.1×10^2	19	10	14
e-C	STEM-EDS, Area C *	3.1×10^4	83	500	14

* from Fig. 4

Table II. STXM measurement conditions used in this study.

Code	Description	ph/nm²	F loss* (%)	Total dwell time (ms)	Io (MHz)	Beam size (nm)
p-A	Navigation (no-damage)	~1	0	1	2.5	100
p-B	F stack map (2 E, low resolution)	5	0	4	2.5	50
p-C	F stack map (2 E, high resolution)	47	~5	4	10	30
p-D	full F 1s stack (70 energies)	10	0	70	2.1	125

* from fig. 4

The soft X-ray irradiation was performed with the sample at room temperature using the ambient STXM on beamline 10ID1 at the Canadian Light Source (CLS) (16) and the polymer STXM on beamline 5.3.2.2 at the Advanced Light Source (ALS) (17). Radiation damaged areas were created by raster scanning a 50 nm diameter beam of 710 eV X-rays over a 4 μm² area with 50 nm pixel spacing, for exposure times ranging from 12.5 to 600 ms. Table II summarizes the STXM measurement conditions used in this study.

Fluorine loss after both electron and X-ray irradiation was evaluated by both STEM-EDS and STXM. Fluorine loss was estimated by STEM-EDS (no damage condition, e-ND in Table I) from the change of F/Pt net count ratio, since the sample is not experiencing Pt loss (5). The STXM technique and methods used to evaluate fuel cell samples have been described previously (10,17,18). Fluorine quantitation was performed using fluorine stack maps – the difference of optical density (OD) images at 694 eV (peak F 1s absorption by PFSA) and 680 eV (F 1s pre-edge) (10). The fluorine signal in the areas damaged by electrons or soft X-rays were analyzed with STXM using method p-B (low resolution F stack map) which does not generate detectable damage (see table II). For soft X-ray irradiation, fluorine maps were acquired before high dose exposure using method p-B. This allowed accurate determination of the fluorine loss relative to the initial value in the same area, thereby correcting for spatial variation in the initial amounts of ionomer. For any given sample there are local areas where the amount of ionomer averaged over ~2 μm² varies by up to 10%. For the electron irradiated sample the original amount of ionomer in the exposed area was estimated by STXM from the average fluorine value in an adjacent area which had not been intentionally exposed to the electron beam (see the above discussion related to TEM navigation exposure).

Results & Discussion

In order to evaluate electron beam irradiation damage during STEM-EDS mapping, a series of maps in adjacent areas were acquired with EDS using exposure times from 3.1×10^3 to 3.1×10^5 e⁻/nm². These areas were then measured with STXM using method p-B. Figure 1 presents F Kα STEM-EDS maps with electron exposures differing by x100,
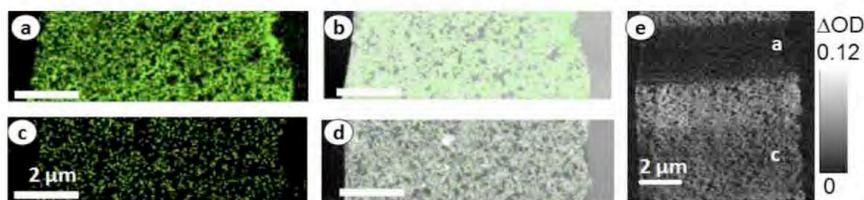
Figure 1 (a) and (c) are F Kα STEM-EDS single maps of the ionomer in the cathode using 3.1×10^5 and 3.1×10^3 electrons/nm^2, respectively. Each EDS map is approximately 15 μm^2. (b) and (d) are these F Kα maps overlaid on high angle angular dark field (HAADF) images of the same areas. (e) is the STXM F 1s map ($OD_{694} - OD_{684}$) of the same areas after the STEM-EDS exposure. Areas where STEM-EDS maps were taken are labeled (a) and (c).

along with subsequent imaging with STXM. At an exposure of 3.1×10^3 electrons/nm^2 (e$^-$/nm^2), the F Kα map shows very little detail (Fig. 1c, d). Higher exposures, such as 3.1×10^5 e$^-$/nm^2, are needed to provide an analytically useful map (Fig. 1a, b). The subsequent STXM fluorine mapping of the same areas (Fig. 1e) shows that even the low STEM-EDS exposure (Fig. 1c) causes noticeable ionomer depletion (Fig. 1e, area c), while the high exposure (Fig.1a) has caused extensive fluorine loss (Fig. 1e, area a).

The extent of fluorine loss due to electron beam exposure was evaluated both from the EDS data (F Kα signal, normalized to Pt Lα signal) and from post-EDS STXM stack maps ($OD_{694} - OD_{684}$). Fluorine counts/pixel below 0.11 were indistinguishable from the background. Figure 2 plots the loss of F Kα signal determined by EDS (i.e. during the electron beam exposure) against the loss of fluorine evaluated by STXM from the same area after the electron beam exposure. STEM-EDS estimates the fluorine signal loss to be 2- 3 times less than that estimated by STXM. We attribute this difference to the fact that STXM was measured after the EDS measurements were complete, whereas the EDS fluorine loss evaluation was based on the signal measured during electron beam exposure, with the fluorine only partially lost. The EDS signal is continually changing as the exposure
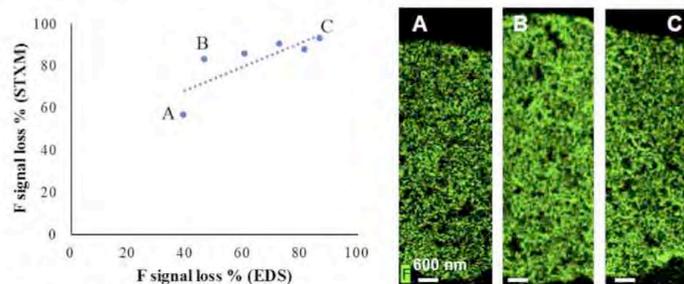
Figure 2 Comparison of the fluorine signal loss during STEM-EDS map acquisition with that measured by STXM stack maps (method p-B) of the same area. Blue dotted line is a linear fit. Each axis is normalized to amount of PFSA in adjacent undamaged areas. A, B, C are STEM-EDS F Kα maps at the labeled exposures. C corresponds to the same area as in Fig. 1A.
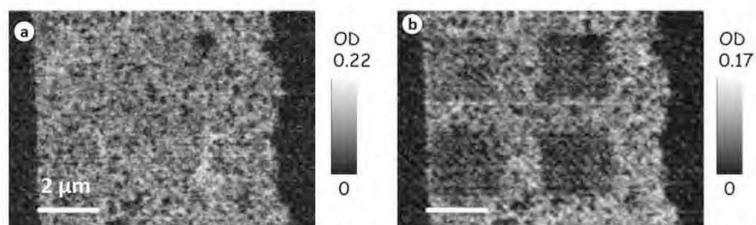
Figure 3 STXM fluorine maps of the same area recorded using method p-B, (a) before and (b) after controlled STXM exposure at 710 eV. Each area is 4 μm^2 with exposures of 1.0×10^3, 2.1×10^3, 3.1×10^3, 4.2×10^3 ph/nm^2 from left to right, top to bottom.

occurs. The signal to noise ratio improves with the exposure, but for the F Kα signal this also results in fluorine loss.

In order to compare fluorine loss caused by the electron exposure in STEM-EDS with the loss caused by X-ray exposure in STXM, a STXM experiment with varying X-ray exposure was performed. Four (2 μm x 2 μm) pads were X-ray damaged at 710 eV using 4 different exposures from 1.0×10^3 to 4.2×10^3 photons/nm^2 (ph/nm^2) on a separate grid of
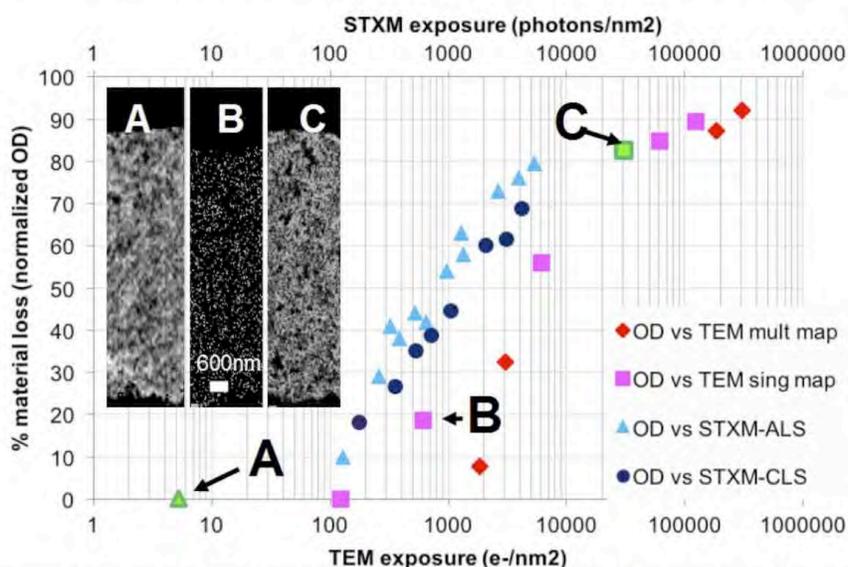
Figure 4 Fluorine loss as a function of X-ray exposure in STXM (upper x-axis: blue, navy blue symbols) and electron exposure in STEM-EDS (lower x-axis: red, pink symbols), measured by STXM, method p-B. Point A: STXM F-map (good image quality, insignificant F loss, exposure of 5 ph/nm^2). Point B: STEM-EDS F map (low image quality, low F loss, exposure 6.1×10^2 e$^-$/nm^2). Point C: STEM-EDS F-map (good image quality, high F loss, exposure of 3.1×10^4 e$^-$/nm^2). All images come from adjacent areas in the same catalyst layer sample. A and C are typical STXM and STEM-EDS exposure conditions.
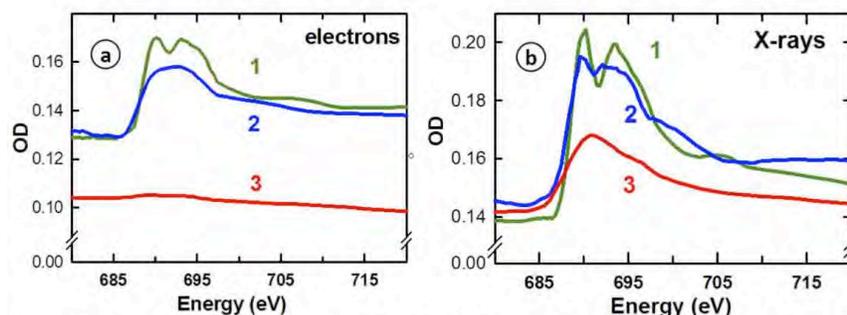
Figure 5 F 1s X-ray absorption spectra of (a) electron and (b) X-ray damaged PEM-FC cathode (see Figure 4) derived from full F 1s stacks (see table 1 for conditions). The spectrum labeled 1 in each figure is from PFSA after navigational exposure in electron and X-ray microscopy, respectively. Spectrum 2 is exposed with (a) 3.6×10^3 e$^-$/nm^2 (poor image quality, 30% F loss, low exposure) and (b) 1.0×10^3 ph/nm^2 (good image quality, 45% F loss, moderate exposure). Spectrum 3 is PFSA exposed with (a) 3.1×10^5 e$^-$/nm^2 (good image quality, 80% F loss, high exposure) and (b) 5.3×10^3 ph/nm^2 (good image quality, 50% F loss, high exposure).

the same sample material. Figure 3 shows fluorine maps ($OD_{694} - OD_{684}$) measured before and after the X-ray beam exposure. The squares visible in Fig. 3b are due to the X-ray beam damage. Figs. 1 and 3 show that increasing the exposure of either X-rays or electrons causes increased depletion of ionomer in the catalyst layer, the extent of which depends on the exposure and thus the radiation dose (dose = absorbed energy per unit mass of the exposed material). Note that exposure is used rather than dose because: i) all regions of the sample have similar thickness; and ii) exposure in ph/nm^2 can be compared to exposure in e$^-$/nm^2 which is easily computed in STEM-EDS measurements.

STXM at very low exposure (5 ph/nm^2, method p-B) was used to quantify the fluorine present in all areas damaged with electron and x-ray beams. The extent of fluorine signal loss is plotted in Figure 4 as a function of electron and X-ray exposures. Each point in Fig. 4 is a fluorine map. The major difference between STXM and STEM-EDS is that the former produces high quality image maps at very low exposure, modest spatial resolution, and negligible F-loss (Fig. 4, map A) while high quality EDS maps at room temperature with sufficient counts for proper visualization need at least ~3×10^5 e-/nm^2 (Fig. 4, map C). Analytical EDS maps can be measured with lower exposure which causes less fluorine loss. However, they are not analytically useful (Fig. 4, map B). By the time adequate image quality is achieved, the fluorine loss is >80%. The higher spatial resolution of the EDS maps is of course an important factor.

These results show that STXM provides useful quantitative ionomer mapping with significantly lower radiation damage as compared to STEM-EDS. This is in agreement with previous electron beam, X-ray beam comparative radiation damage studies on polyethylene-terephthalate (PET), a much more X-ray damage resistant polymer, done with TEM-EELS [14,15].

Full STXM F 1s stacks were recorded using method p-D (see table 2) to measure F 1s spectra in order to better understand the chemical changes caused by the incident radiation.

Figure 5 presents F 1s spectra of areas exposed to electrons (Fig. 5a) and to X-rays (Fig. 5b). The major peaks at 690 and 694 eV are F 1s $\rightarrow$ $\sigma^*_{(C-F,\,perpendicular)}$ and F 1s $\rightarrow$ $\sigma^*_{(C-F,\,parallel)}$ transitions, which are also present in PTFE (19). The electron beam exposure due to sample navigation (Fig. 5, curves 1) causes very little change to the PFSA spectra. With similar soft X-ray (1.0×10^3 ph/nm^2) and electron (3.6×10^3 e^-/nm^2) exposures (Fig. 5, curves 2), the peaks at 690 and 694 eV broaden and decrease in intensity. At higher exposures (Fig. 5, curves 3) the double peak structure disappears and is replaced with a single broad peak that gets broader and less intense as the exposure further increases. At the same exposure level, the spectral changes caused by electron beams are much larger than those caused by soft X-rays. In each case, the original PFSA ionomer is being transformed into a disordered material with extensively depleted fluorine levels. Discussion of possible damage mechanisms and structure of the damaged material is postponed to a future paper.

Damage studies such as this work help determine imaging conditions for minimal damage to soft materials. Using low dose conditions and short exposures, it is possible to use STXM to measure high quality maps of ionomer in PEM-FC cathode at 30 nm spatial resolution with negligible radiation damage. On the other hand, room temperature STEM-EDS quantitative mapping provides satisfactory image quality with higher spatial resolution (14 nm or smaller), but results in significant fluorine loss and PFSA structural damage. If one had a method to compensate for the quantitative errors caused by electron beam damage and could show that the remaining fluorinated material has the same spatial distribution as the original PFSA, the ability of room temperature STEM-EDS to provide reliable quantitative measurements of ionomer content and distribution in fuel cell catalyst layers with high spatial resolution would significantly increase. Operating STEM-EDS at different beam voltages and with cryogenically cooled samples should also be explored [5].

Acknowledgments

References

1. S. Yakovlev, K.H. Downing, *Phys. Chem. Chem. Phys.* **15** 1052 (2012).
2. S. Yakovlev, N.P. Balsara, K.H. Downing, *Membranes* **3** 424 (2013).
3. M. Schulze, M. Lorenz, N. Wagner, E. Guelzow, *J. Anal. Chem.* **365** 106 (1999).
4. S.H. Almeida, Y. Kawano, *Polym. Degrad. Stab.* **62** 291 (1998).
5. D.A. Cullen, R. Koestner, R.S. Kukreja, Z.Y. Liu, S. Minko, O. Trotsenko, et al., *J. Electrochem. Soc.* **161** F1111 (2014).
6. D. Susac, V. Berejnov, A.P. Hitchcock, J. Stumper, *ECS Trans.* **50**(2) 405 (2012).
7. V. Lee, D. Susac, S. Kundu, V. Berejnov, R.T. Atanasoski, A.P. Hitchcock, et al., *ECS Trans* **58**(1) 473 (2013).
8. A.P. Hitchcock, V. Berejnov, V. Lee, M. West, V. Colbow, M. Dutta, et al., *J. Power Sources* **266** 66 (2014).
9. V. Berejnov, D. Susac, J. Stumper, A.P. Hitchcock, *ECS Trans.* **50**(2) 361 (2013).
10. D. Susac, V. Berejnov, A.P. Hitchcock, J. Stumper, *ECS Trans.* **41**(1) 629 (2011).

11. J. Wang, C. Morin, L. Li, A.P.A. Hitchcock, A. Scholl, A. Doran, *J. Electron Spectros. Relat. Phenomena* **170** 25 (2009).
12. G. Tzvetkov, A. Späth, R.H. Fink, *Radiat. Phys. Chem.* **103** 84 (2014).
13. T. Beetz, C. Jacobsen, *J. Synchrotron Radiat.* **10** 280 (2003).
14. E.G. Rightor, A.P. Hitchcock, H. Ade, R.D. Leapman, S.G. Urquhart, A.P. Smith, et al., *J. Phys. Chem. B.* **101** 1950 (1997).
15. J. Wang, G.A. Botton, M.M. West, A.P. Hitchcock, *J. Phys. Chem. B*. **113** 1869 (2009).
16. K.V. Kaznatcheev, C. Karunakaran, U.D. Lanke, S.G. Urquhart, M. Obst, A. P. Hitchcock, *Nucl. Instruments Methods Phys. Res. A.* **582** 96 (2007).
17. T. Warwick, H. Ade, D. Kilcoyne, M. Kritscher, T. Tylisczcak, S. Fakra, et al., *J. Synchrotron Radiat*. **9** 254 (2002).
18. A.P. Hitchcock, in *Handb. Nanoscopy Vol.II*, G. Van Tendeloo, V.D. Dyck, S.J. Pennycook, Editors, p.745, Wiley (2012).
19. T. Ohta, K. Seki, T. Yokoyama, I. Morisada, K. Edamatsu, *Phys. Scipta*. **41** 150 (1990).

Chapter 8

Summary and Outlook

This chapter provides a summary of this thesis, followed by an outline of the major original contributions. Additional contributions, not included in previous chapters, are also described briefly. The thesis concludes with suggestions for future work for characterization of radiation damage by ionization radiation, particularly as applied to perfluorosulfonic acid.

8.1   Summary

This thesis developed and optimized quantitative STXM-NEXAFS methods for studies of radiation induced damage to polymeric films, with a focus on PFSA materials. The chemical damage to PFSA thin films and PFSA ionomer in PEMFC cathodes due to UV, soft X-ray and high energy electron irradiation was characterized and quantified using STXM.

(**Chapter 4**) To assess the accuracy of determination of the thickness of ionomer in PEMFC cathodes by X-ray absorption in STXM, thickness measurements on PS, PMMA and PFSA thin films were compared to values derived using UV spectral reflectance. I demonstrated that the thickness values reported by the two techniques agree within 10%. Extrapolating the results to PFSA-in-cathode samples, STXM should provide maps of the absolute ionomer thicknesses with a 10% uncertainty from systematic errors. I found that UV exposure in air for up to 60 mins in the Filmetrics instrument did not modify PFSA. On the other hand, I found that both PS and PMMA suffered thickness decay and chemical change with increasing exposure to

UV in air. I established a maximum exposure time for reliable UV spectral reflectance measurements for PS and PMMA. The exponential decay of the thickness combined with the NEXAFS chemical changes suggested that oxygen from the air was incorporated into the UV damaged PS and PMMA films. The depletion rate for PS was explained by release of the photo-damaged products from the film surface. The higher depletion rate for PMMA indicated a larger contribution from diffusion of the damaged products from the bulk.

(**Chapter 5**) Radiation damage to PFSA, PTFE and Teflon®AF was generated by soft X-rays in STXM using direct write patterning at the C 1s and F 1s continua energies, and then characterized with STXM. The damage was quantified at energies of characteristic S 2p, C 1s, O 1s and F 1s spectral features, as well as by evaluation of elemental changes by integration of the full edge signal. For similar pathways of damage to PFSA (ether/sulfonate compared to CF_2-CF_2 amorphization and fluorine loss), analysed assuming a first order kinetics model, the critical dose for damage measured at different energies and different edges was similar. The preferential side-chain removal previously claimed in literature based on XPS analysis (Paul et al., 2013; Schulze et al., 1999) was not confirmed in this study. PFSA was 2-3x more sensitive to X-ray damage than PTFE or Teflon®AF. Recommended dose limits and procedures to acquire spectra with minimal modification of PFSA were given.

(**Chapter 6**) PFSA thin films were irradiated in a TEM microscope using 200 kV at room and cryo temperatures using ultra-low dose conditions. The damage was analyzed using STXM at room temperature by quantifying the spectral features related to the σ^*_{C-F} transitions and the elemental content by edge integration. It was observed that the spectral changes due to electron irradiation are qualitatively similar to those observed with soft X-ray irradiation. This suggests

that the damage mechanism for both ionizing sources is dominated by the damage generated by secondary electrons. It was observed that the rate of damage to the σ^*_{C-F} peaks and the fluorine loss by electron irradiation depends on the sample temperature (RT vs cryo conditions) and whether or not a substrate was used for the sample. Since there was no substrate effect observed for soft X-ray irradiation, it was suggested that electron irradiation results in sample charging, which affects the rate of damage but does not result in additional spectral changes. A dose-limited resolution of ~5 nm for TEM imaging of PFSA was estimated.

(**Chapter 7**) The PFSA ionomer in PEM-FC catalyst layer samples was quantified using the F Kα signal in STEM-EDS and F 1s$\rightarrow \sigma^*_{C-F}$ transitions in STXM. First, STEM-EDS maps were acquired using different electron irradiation fluences. A minimal electron exposure to ensure that the F Kα signal was above noise was observed. Quantification of the fluorine loss during STEM-EDS and post-damage analysis with STXM-NEXAFS showed that STEM-EDS underestimates fluorine loss compared to STXM-NEXAFS. It was noted that extensive exposure to photon and electron irradiation results in similar chemical damage as noted for PFSA films. It was shown that STXM quantitation using a few images results in negligible damage to the PFSA while STEM-EDS provides higher spatial resolution fluorine maps but only at the expense of significant damage to the PFSA.

8.2 *Original contributions reported in this thesis*

Based on the experimental procedures, results and discussion of each chapter, the original contributions described in this thesis include:

- Developing a method for thickness correlation measurements using UV spectral reflectance and STXM of polymer thin films and applying it to evaluate accuracy of STXM. As the sample environment plays a role in the chemical changes due to radiation damage, it was shown that there is an exposure time limit for UV-SR measurements for PMMA and PS. PFSA is not modified by UV/air exposure under the same conditions.

- Developing and optimizing methods for quantitative analysis of radiation damage to polymer thin films using soft X-ray spectromicroscopy.

- Determining critical doses for various modes of damage to PFSA and PTFE, providing insight into the damage mechanisms.

- Evaluating the critical dose for damage to PFSA thin film irradiated with high energy electrons, thereby estimating the dose-limited resolution for TEM imaging of the nanomorphology of PFSA.

- Comparing extent of fluorine loss to PFSA in a cathode catalyst layer sample during analytical mapping by STXM-NEXAFS and STEM-EDS and using these results to compare relative utility of the two techniques for quantitative mapping.

8.3   Additional contributions not included in this thesis

I took part in a number of other research studies during my PhD which are not described in detail in this thesis.

8.3.1   First principles dose calculation of soft X-ray irradiation

I provided experimental data and helped develop some of the ideas in the paper. The mathematical calculations were done by Drs. Viatcheslav Berejnov and Boris Rubinstein. The

first draft of the manuscript was written by Dr. Viatcheslav Berejnov. Dr. Adam Hitchcock

provided feedback on the manuscript (Berejnov, V., Rubinstein, B., <u>Melo, L. G. A</u>. & Hitchcock, A.

P. (2018) J. Synchrotron Rad. 25, 833-847: https://doi.org/10.1107/S1600577518002655).

Historically, the calculation of the absorbed dose of incident soft X-rays by a sample was calculated using a simple expression (X. Zhang et al., 1995), similar to **Equation 3.8**. The absorbed energy was calculated based on the dwell time, incident photon flux and energy and the fraction of X-rays absorbed by the sample. The absorbed energy was divided by the mass as evaluated from the volume of the irradiated area and the density of the material. The calculation of the dose was further developed by J. Wang (Wang, Morin, et al., 2009) for cases where samples lose a considerable amount of mass as a function of dose. The fraction of the absorbed X-rays was calculated as a function of the OD (see **Equation 3.2**). The absorption or OD ($E_A = E_D = C$ 1s continuum) changes as a function of the dose for samples that lose mass. Therefore, an integrated expression of the optical density based on the exponential decay as a function of time was formulated and used instead (Wang, Morin, et al., 2009):

$$S_{OD} = \frac{\int_0^t (y_0 + ce^{-bt})dt}{t} = \frac{y_0 t + (c/b)\,(1 - e^{-bt})}{t}$$

Equation 8.1

Dr. Viatcheslav Berejnov noted that although the OD in the numerator of **Equation 3.8** was taking into account the mass loss, the change in thickness was not taken into account. The thickness can be calculated from **Equation 3.4**. The integrated expression in **Equation 8.1** was averaging the OD from a time = 0 to a time = t as calculated by integrating the function using an exponential decay from time 0 to *t*. However, in order to calculate the dose, it was not clear why the OD was integrated and not the entire dose expression. In this thesis, I showed in **Figure 3.9**

that calculating the dose using the method developed by J. Wang underestimated the dose. Some details of this work were given in **section 3.3.1**.

8.3.2   4D soft X-ray imaging – room temperature tomography of catalyst layer components with minimal damage

This study is a key part of the PhD thesis of Juan Wu. I assisted her with dose calculations and helped revise the manuscript (Wu, J., <u>Melo, L. G. A</u>., Zhu, X., West, M., Berejnov, V., Susac, D., Stumper, J., & Hitchcock, A. P. Journal of Power Sources, 2018, 381, 72-83).

The objective of this paper was to develop methods to perform STXM spectro-tomography on a PEM-FC catalyst layer at the C 1s and F 1s edges to quantify the ionomer and carbon support, with an acceptable level of radiation damage. The carbon support and the PFSA ionomer were quantified using 2-energy stack maps from the C 1s $\rightarrow \pi^*_{C=C}$ transitions of the graphitic carbon support and the F 1s $\rightarrow \sigma^*_{C-F}$ transitions of the ionomer. The dose was calculated for each STXM measurement. A 3-set protocol was developed to monitor not only the spectral and quantitative changes (as described in this thesis, Chapter 3) but also changes to the 3D morphology caused by radiation damage. After identification of the initially excessive damage, reduction in flux (20 $\rightarrow$ 2 MHz), number of tilt angles (14), and a slight defocus (30 $\rightarrow$ 50 nm) was found to dramatically reduce the extent of damage. This was the first time 3D distributions of the ionomer and carbon support were measured with minimal radiation damage. These results were free of chemical modifications due to staining techniques or sample preparation techniques, which are a major concern for electron tomography. It was shown that with increasing dose the 3D volume of the ionomer does not change in a fixed amount or in proportion to the amount

present in a voxel. This indicates that a simple extrapolation of the 3D distribution of damaged

PFSA ionomer does not render the original 3D volume before damage.

8.3.3   Damage to PFSA in a PEMFC cathode by RT-FIB and cryo-FIB milling

*I developed the idea and experimental design for this project under the supervision of Dr.
Berejnov and Dr. Susac during my internship at AFCC. Dr. Talpalaru prepared the cryo-FIB
lamella and Dr. Jankovic did the electron tomography measurements. Dr. Bejerenov and I did the
STXM measurements and analysis together. I wrote the first version of the paper. Dr. Berejnov
and Dr. Hitchcock revised the manuscript (*Melo, L. G. A*., Hitchcock, A. P., Talpalaru, C.,
Jankovic, J., Susac, D., Stumper, J., & Berejnov, V. manuscript in preparation. To be submitted to
Journal of Power Sources).*

As discussed in **Section 2.5.3**, FIB is an alternative method to ultramicrotomy for preparing

samples for electron and X-ray microscopy. It is particularly useful for preparing thin lamellas

from specific areas of a sample. FIB tomography has been used to quantify the 3D distribution of

the porous framework of the catalyst layer (Ziegler, Thiele, & Zengerle, 2011; Zils et al., 2010).

The objective of this work was to quantify the chemical changes to PFSA and the carbon support

due to FIB milling at cryo temperatures, compared to room temperature FIB milling and room

temperature ultramicrotomy. The FIB preparation was described in **section 3.1.5**.

The same CCM PEM-FC sample was prepared with two different techniques:

ultramicrotomy and FIB. The sections were milled using a Ga ion beam in a FIB at both room

temperature (RT) and -180 °C. The final polishing conditions varied: at RT, one section was

prepared using a low voltage (10 kV); at cryo temperature four sections were prepared, one thin

(~150 nm) and one thick (~300 nm) with Ga^+ kinetic energies of 16 and 30 kV. The lamellae were

then analyzed with STXM-NEXAFS to quantify the chemical changes to the PFSA and the carbon support due to cryo-FIB milling. The results were compared to those from a microtomed section of the same sample. **Figure 8.1** shows STXM background subtracted and normalized F 1s spectra of all sections. Under all of the conditions tested, FIB milling resulted in fluorine mass loss and CF_2-CF_2 amorphization of the PFSA ionomer. It was found that the cryo-temperature during milling helps preserve the ionomer structure, relative to room temperature FIB. However, the PFSA material still damages significantly. Both chemical changes and thickness loss to the PFSA were determined.
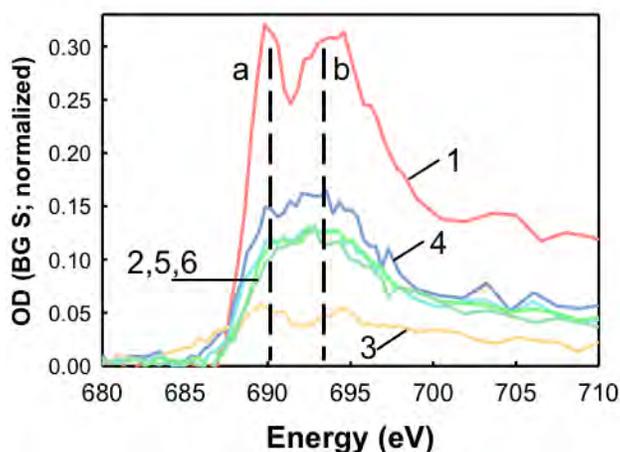
Figure 8.1 Background subtracted STXM F 1s spectra normalized to the total amounts of carbon content of each area ($OD_{320\ eV} - OD_{280\ eV}$) of the cathode region of a catalyst coated membrane sample prepared by (1) room temperature (RT) ultramicrotomy, (2) cryo-FIB 30 kV '150 nm section' (3) RT-FIB from a previous publication (Melo et al., 2016), (4) cryo-FIB 16 kV '150 nm section' (5) cryo-FIB 16 kV '300 nm section' and (6) cryo-FIB 30 kV '300 nm section'.

8.3.4   Understanding the X-ray damage in PFSA using correlative microscopy

The experimental design for this project was developed within the CaRPE-FC network by myself and Isaac Martens, a PhD student co-supervised by Profs. David Wilkinson and Dan

Bizzotto (UBC). Although I suggested to run AFM on the same areas, the AFM and FTIR data were acquired and analyzed by I. Martens. I prepared the samples, designed and performed the STXM damage and carried out all STXM data analysis under the supervision of Dr. Adam Hitchcock. The first draft of the manuscript was written by Isaac Martens. Dr. Adam Hitchcock provided feedback on the manuscript (*Martens, I., *Melo, L. G. A., Wilkinson, D., Bizzotto, D., & Hitchcock, A. P. (manuscript in preparation) to be submitted to J. Phys. Chem. C (*co-first authors).

An extension of the work in **Chapter 5** was developed in this project. Soft X-rays were used to irradiate the PFSA thin films and post-damage analysis was carried out by STXM-NEXAFS, Fourier Transform InfraRed (FTIR) and AFM. The three microscopy techniques were used to complement each other to take advantage of the strengths of each. NEXAFS and FTIR served to give insight into the chemical changes. AFM and STXM were used to visualize the morphological changes to the PFSA. FTIR and AFM provided additional insight into the damage process of PFSA.

Spin-coated PFSA thin film samples were exposed to soft X-rays in a STXM. Areas of at least 16 x 16 μm were irradiated with 320 eV photons with different doses. After the irradiation, STXM analysis were performed on each area. The large areas were necessary for post-damage analysis using a FTIR microscope. AFM and STXM images detected the annular shape of the incident beam due to a large defocus used (500 nm), as discussed in **section 2.2.3**.

FTIR detected extensive damage to the ether bonds in PFSA even for low dose soft X-ray irradiation. The oxygen depletion observed by STXM was less than that found by FTIR, probably due to the overlapping peaks related to similar functional groups in the NEXAFS O 1s spectrum.

Quantitation of the fluorine loss and amorphization of the CF_2-CF_2 chains using both techniques gave similar results. It was shown that for a dose of only 5 MGy, approximately 40% of the ether bonds were lost (FTIR) while 10% of the fluorine lost and CF_2-CF_2 signals modified (as measured by STXM and FTIR).

Ablated ejected material redeposited on the surface of the film was observed with AFM. The particle sizes were such that they should be observable by STXM, but they were not. The thickness changes in both low and high dose areas were determined with AFM.

8.4 Future work

8.4.1 Quantifying radiation damage in a wet, hydrated PFSA sample

It is possible to encapsulate an aqueous solution between two SiNx windows and perform spectromicroscopy studies in STXM. One of the main goals in PEM-FC research is 3D visualization of all components, including the water, inside a working fuel cell. It is known that radiation damage rates increase and the chemical changes are modified when a sample is in contact with water (Fukushima, Katoh, & Fukami, 1982). Radiolysis of water has been studied for decades. Upon exposure to ionizing radiation, radiolysis products H_2O^+, e^-, H^+, OH^- are created which react to form H^+, OH^-, H_3O^+, H_2 that diffuse and react with other products, often in chain reactions (Hamill, 1969; Nagaishi & Kumagai, 2011; Samuel & Magee, 1953). These damage products may react with the undamaged PFSA and affect radiation damage chemistry and rates. It is expected that the rate of soft x-ray damage to wet PFSA will be increased relative to that of dry PFSA, but there are no published quantitative studies to my knowledge.

The preparation of wet PFSA samples is challenging since hydration of PFSA films is strongly dependent on the sample preparation method (Zawodzinski et al., 1993), as well as the chemical environment, time and temperature of the hydration process (Gruger, Régis, Schmatko, & Colomban, 2001). In a preliminary study of a wet cell PFSA dispersion (20% Nafion® EW1100 in n-propanol and water), I observed some changes to the spectra of damaged wey-PFSA compared to the spectra of damaged dry-PFSA films (see **Figure 8.2**). The peak at 531 eV in dry PFSA materials is not observed for 80 MGy wet PFSA. The changes at the F 1s edge due to damage is similar in wet and dry PFSA (see **Chapter 5**). The O 1s and C 1s spectra for the undamaged material is different compared to those of the dry PFSA. More studies are required to quantify the dose in the case of a wet sample. *How to accurately determine the thickness of the fluid layer in a wet sample? Should the I$_0$ be acquired in a separate wet cell with only the solvents? In this case, an internal I$_0$ was used in an area where it appeared there was no material. Could the n-propanol also play a role in the damage?*
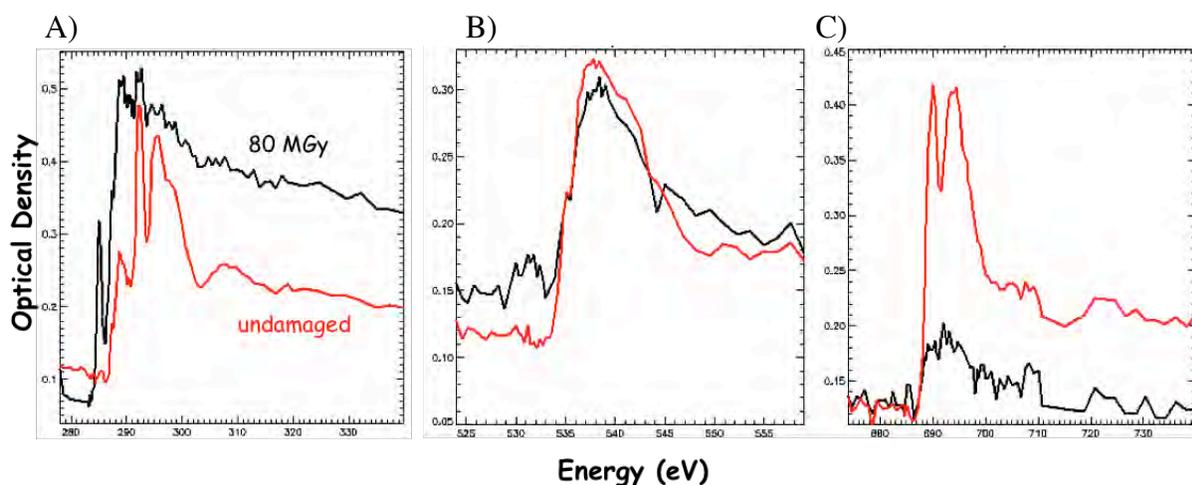
Figure 8.2 STXM NEXAFS spectra at the **(A)** C 1s, **(B)** O 1s and **(C)** F 1s edges of undamaged PFSA dispersion (red) and damaged to 80 MGy with 320 eV photons (black) of a wet cell sample.

8.4.2   UHV & mass spec during X-ray irradiation of PFSA

Most existing STXM chambers are constructed with low vacuum technologies and mechanical stages designed for air operation with large amounts of oil lubrication (Hitchcock, 2012). The volatile organic compounds migrate to the sample and result in carbon contamination when an intense fine focused X-ray beam is incident on the sample (Hitchcock, 2012). Quantitation of the C 1s spectra of PFSA irradiated in the STXM (vacuum at 20 Pa) (**Figures 5.2 & 5.3**) and TEM in UHV (10^{-5} Pa) (**Figure 6.4**) show that carbon contamination exists during STXM damage measurements. Since low doses are recommended for quantitation characterization of PFSA in the cathode, carbon contamination should not be problematic. However, as was discussed in Chapter 5, contamination is a problem for quantitation of elemental changes due to radiation damage. For future work involving damage studies, the O_2 in the sample chamber should be always be quantified. This can be done in the STXM by increasing the path

202

length and measuring the O 1s edge after pumping, after backfill with He and then 1 hour after the backfill. Therefore, true UHV vacuum systems with low carbon contamination levels should be developed and used for future radiation damage studies. The vacuum technology of the recently commissioned cryo-STXM at the CLS is near-UHV - a chamber pressure of $2x10^{-9}$ torr is readily achieved. If a mass spectrometer is coupled to the cryo-STXM, mass spectra could be acquired during soft X-ray irradiation, possibly detecting the votalile components. It is expected that the combination of UHV and mass spectroscopy measurements during X-ray irradiation, coupled with NEXAFS spectra, will give additional insights into the damage mechanisms of these fluoropolymers. This can be achieved by quantifying the elemental changes and correlating them to the mass spectra of the detected fragments. A similar work was done with PTFE and PVDF but the authors did not quantify the irradiation dose (Okudaira, Yamane, & Ito, 2002). The time of flight mass spectrometry detected F^+, CF^+ and CF_3^+ fragments for PTFE irradiated with soft X-rays in a synchrotron beamline. F^+ was not observed in Teflon®AF irradiated in a UHV ($2x10^{-7}$ Pa) XPS chamber (Popovici, Sacher, & Meunier, 1998). Instead, the main fragments detected with mass spectroscopy were CF^+, CF_2^+, CF_3^+ and $C_2F_3O^+$ (Popovici et al., 1998).

8.4.3   *Radiation damage characterization during cryo temperature irradiation*

In Chapter 6, I showed that electron irradiation of a PFSA film at cryo temperature changes the rate of damage compared to room temperature irradiation. However, the chemical analysis was done after the sample was warmed up to room temperature. *If the measurements were done while the sample was still at cryo temperature, would the same chemical changes be observed?* Cryogenic operation has been shown to affect the rate of mass loss since it prevents damaged products from leaving the sample surface for both electron (Egerton, 2011) and X-ray irradiation

(Beetz & Jacobsen, 2003). For damage of PMMA in cryo conditions, STXM did not detect differences in the rate of decay of the main C 1s → $\pi^*_{C=O}$ spectral feature (Beetz & Jacobsen, 2003). It has been suggested that formation of gas in the sample instead of bond scission is responsible for damage observable in samples X-ray irradiated at cryogenic temperatures (Meents, Gutmann, Wagner, & Schulze-Briese, 2010). *Are the chemical changes and rates of bond cleavage during X-ray damage for samples irradiated at cryogenic temperature the same as room temperature?*

Since similar chemical changes to PFSA were observed with both photon and electron irradiation, both STXM and EELS could be used to quantify the rate of bond cleavage during irradiation while maintaining the sample at cryo temperature for the post-damage analysis. The CLS in collaboration with groups of beam team members, including Profs. S. Urquhart and A. Hitchcock, has finished commissioning a new STXM microscope that can operate in ultra-high vacuum. It features a variable temperature sample holder that permits measurements at temperatures from -180 °C to +200 °C (Leontowich et al., 2018). Direct-write 9-pad patterns could be prepared on PFSA using 710 eV photons at cryo temperature and the changes to the F1s → σ^*_{C-F} transitions could be measured while maintaining the sample at cryo temperature. *Does cryo conditions really reduce bond breaking in addition to mass loss, as my results comparing TEM damage of PFSA under cryo and RT suggest? What is the upper temperature at which the damage processes and rates become similar to that observed at RT ?*

EELS is an alternative spectroscopic technique to STXM that, in principle, can be used to analyze the chemical changes caused by radiation damage. In practice this has not been possible, even for polyethylene terephthalate (PET), a polymer that is much less sensitive to radiation than

PFSA (Wang, Botton, et al., 2009). Further studies are needed to quantify the dose for minimal damage EELS spectral acquisition of PFSA samples. Recent development of direct electron detectors has improved the quantum efficiency and promises efficient spectroscopy analysis with low doses (Hart et al., 2017). Damage to PFSA during electron irradiation in cryo temperatures has been studied with EELS in the past. However, in both cases only the elemental content was quantified (Cullen et al., 2014; Yakovlev et al., 2013). Yakovlev showed a decrease of elemental content (carbon, oxygen and fluorine) using EELS in PFSA during electron irradiation in both room and cryo temperature (Yakovlev et al., 2013) without however, assessing the chemical changes to the CF_2-CF_2 or ether bonds. *Using new direct electron counting* detectors, *is it possible to acquire EELS spectra of PFSA similar to that acquired by STXM-NEXAFS? Does cryo temperature reduce the bond breaking to PFSA as my results suggest?*

References

Ade, H. (1998). *NEXAFS and X-Ray Linear Dichroism Microscopy and Applications to Polymer Science*. In: Thieme, J., Schmahl G., Rudolph D., Umbach E. (eds) X-Ray Microscopy and Spectromicroscopy. Springer, Berlin, Heidelberg.

Ade, H. (1998). X-ray Spectromicroscopy. In J. A. R. Samson & D. L. Ederer (Eds.), *Experimental Methods in the Physical Sciences 32* (p. 225). Academic Press.

Ade, H., & Hitchcock, A. P. (2008). NEXAFS microscopy and resonant scattering: Composition and orientation probed in real and reciprocal space. *Polymer*, *49*(3), 643–675.

Ade, H., Smith, A. P., Cameron, S., Cieslinski, R., Mitchell, G., Hsiao, B., & Rightor, E. (1995). X-ray microscopy in polymer science: prospects of a 'new' imaging technique. *Polymer*, *36*(9), 1843–1848.

Ade, H., & Urquhart, S. (2002). NEXAFS spectroscopy and microscopy of natural and synthetic polymers. *Adv. Ser. Phys. Chem.*, *12A*, Chemical Applications of Synchrotron Radiation, Pt. 1, 285–355.

Ade, H., Zhang, X., Cameron, S., Costello, C., Kirz, J., & Williams, S. (1992). Chemical contrast in X-ray microscopy and spatially resolved XANES spectroscopy of organic specimens. *Science*, *258*(5084), 972–975.

Akar, A., Gümüş, H., & Okumuşoğlu, N. T. (2006). Electron inelastic mean free path formula and CSDA-range calculation in biological compounds for low and intermediate energies. *Applied Radiation and Isotopes*, *64*(5), 543–550.

Allen, F. I., Comolli, L. R., Kusoglu, A., Modestino, M. A., Minor, A. M., & Weber, A. Z. (2015). Morphology of Hydrated As-Cast Nafion Revealed through Cryo Electron Tomography. *ACS Macro Letters*, *4*(1), 1–5.

Almeida, S. H., & Kawano, Y. (1998). Effects of X-ray radiation on Nafion membrane. *Polymer Degradation and Stability*, *62*(2), 291–297.

Anderson, D. W. (1984). *Absorption of ionizing radiation*. Baltimore USA: University Park

Press.

Andrady, A. L. (2007). *Ultraviolet radiation and polymers*. *Physical Properties of Polymers Handbook*. Springer Science + Business Media, LLC

Aquilanti, G., Vaccari, L., Plaisier, J. R., & Goldoni, A. (2015). Instrumentation at Synchrotron Radiation Beamlines. In *Synchrotron Radiation* (pp. 65–104). Berlin, Heidelberg: Springer Berlin Heidelberg.

Attix, F. H. (1986). *Introduction to Radiological Physics and Radiation Dosimetry*. New York, NY: Wiley.

Attwood, D. (1999). *Soft X-rays and Extreme Ultraviolet Radiation*. Cambridge: Cambridge University Press.

Balerna, A., & Mobilio, S. (2015). Introduction to Synchrotron Radiation. In *Synchrotron Radiation* (pp. 3–28). Berlin, Heidelberg: Springer Berlin Heidelberg.

Barbir, F. (2005). *PEM Fuel Cells : Theory and Practice* (1st editio). Academic Press.

Bassim, N. D., De Gregorio, B. T., Kilcoyne, A. L. D., Scott, K., Chou, T., Wirick, S., … Stroud, R. M. (2012). Minimizing damage during FIB sample preparation of soft materials. *Journal of Microscopy*, *245*(3), 288–301.

Beetz, T., & Jacobsen, C. (2003). Soft X-ray radiation-damage studies in PMMA using a cryo-STXM. *Journal of Synchrotron Radiation*, *10*(3), 280–283.

Berejnov, V., Martin, Z., West, M., Kundu, S., Bessarabov, D., Stumper, J., … Hitchcock, A. P. (2012). Probing platinum degradation in polymer electrolyte membrane fuel cells by synchrotron X-ray microscopy. *Physical Chemistry Chemical Physics : PCCP*, *14*(14), 4835–43.

Berejnov, V., Rubinstein, B., Melo, L. G. A., & Hitchcock, A. P. (2018). First-principles X-ray absorption dose calculation for time-dependent mass and optical density. *Journal of Synchrotron Radiation*, *25*(3), 833–847.

Berejnov, V., Susac, D., Stumper, J., & Hitchcock, A. P. (2013). 3D Chemical Mapping of PEM

Fuel Cell Cathodes by Scanning Transmission Soft X-ray SpectroTomography. *ECS Transactions*, *50*(2), 361–368.

Berger, M.J., Coursey, J.S., Zucker, M.A., and Chang, J. (2005), *ESTAR, PSTAR, and ASTAR: Computer Programs for Calculating Stopping-Power and Range Tables for Electrons, Protons, and Helium Ions*(version 1.2.3). [Online] Available: http://physics.nist.gov/Star [*2018, May 2*]. National Institute of Standards and Technology, Gaithersburg, MD

Bernard, S., Benzerara, K., Beyssac, O., Brown, G. E., Stamm, L. G., & Duringer, P. (2009). Ultrastructural and chemical study of modern and fossil sporoderms by Scanning Transmission X-ray Microscopy (STXM). *Review of Palaeobotany and Palynology*, *156*(1–2), 248–261.

Biello, D. (2016). Electric Cars are not necessarily clean. *Scientific American*.

Botton, G. (2007). Analytical Electron Microscopy. In P. W. Hawkes & J. C. H. Spence (Eds.), *Science of Microscopy* (pp. 273–405). Springer New York.

Braun, A., Kubatova, A., Wirick, S., & Mun, S. B. (2009). Radiation damage from EELS and NEXAFS in diesel soot and diesel soot extracts. *Journal of Electron Spectroscopy and Related Phenomena*, *170*(1–3), 42–48.

Brion, C. E., Daviel, S., Sodhi, R., Hitchcock, A. P., Wolfe, H. C., & Crasemann, B. (1982). Recent Advances in Inner-Shell Excitation of Free Molecules by Electron Energy Loss Spectroscopy. In *AIP Conference Proceedings* (pp. 429–446). AIP.

Bryant, P. J., & Johnsen, K. (1993). *The Principles of Circular Accelerators and Storage Rings*. Cambridge: Cambridge University Press.

Campanari, S., Manzolini, G., & Garcia de la Iglesia, F. (2009). Energy analysis of electric vehicles using batteries or fuel cells through well-to-wheel driving cycle simulations. *Journal of Power Sources*, *186*(2), 464–477.

Carlsson, G. A. (1981). Absorbed dose equations. On the derivation of a general absorbed dose equation and equations valid for different kinds of radiation equilibrium. *Radiat. Res.*, *85*,

219–237.

Carrette, L., Friedrich, K., & Stimming, U. (2001). Fuel cells–fundamentals and applications. *Fuel Cells*, (1), 5–39.

Castner, D. G., Lewis, K. B., Fischer, D. A., Ratner, B. D., & Gland, J. L. (1993). Determination of Surface Structure and Orientation of Polymerized Tetrafluoroethylene Films by Near-Edge X-ray Absorption Fine Structure, X-ray Photoelectron Spectroscopy, and Static Secondary Ion Mass Spectrometry. *Langmuir*, *9*(2), 537–542.

Cetinbas, F. C., Ahluwalia, R. K., Kariuki, N., De Andrade, V., Fongalland, D., Smith, L., … Myers, D. J. (2017). Hybrid approach combining multiple characterization techniques and simulations for microstructural analysis of proton exchange membrane fuel cell electrodes. *Journal of Power Sources*, *344*, 62–73.

Chu, M. W., Liou, S. C., Chang, C. P., Choa, F. S., & Chen, C. H. (2010). Emergent chemical mapping at atomic-column resolution by energy-dispersive X-ray spectroscopy in an aberration-corrected electron microscope. *Physical Review Letters*, *104*(19), 1–4.

Cody, G. D., Brandes, J., Jacobsen, C., & Wirick, S. (2009). Soft X-ray induced chemical modification of polysaccharides in vascular plant cell walls. *Journal of Electron Spectroscopy and Related Phenomena*, *170*(1–3), 57–64.

Coffey, T., Urquhart, S. . G., & Ade, H. (2002). Characterization of the effects of soft X-ray irradiation on polymers. *Journal of Electron Spectroscopy and Related Phenomena*, *122*(1), 65–78.

Cullen, D. A., Koestner, R., Kukreja, R. S., Liu, Z. Y., Minko, S., Trotsenko, O., … More, K. L. (2014). Imaging and Microanalysis of Thin Ionomer Layers by Scanning Transmission Electron Microscopy. *Journal of the Electrochemical Society*, *161*(10), F1111–F1117.

Curtin, S., & Gangi, J. (2017). *Fuel Cell Technologies Market Report 2016*. Washington, D.C.

Dhez, O., Ade, H., & Urquhart, S. G. (2003). Calibrated NEXAFS spectra of some common polymers. *Journal of Electron Spectroscopy and Related Phenomena*, *128*(1), 85–96.

Dole, M. (1972). *The Radiation Chemistry of Macromolecules*. New York and London: Academic

Press.

Du, M., Jacobsen, C. (2018). Relative merits and limiting factors for X-ray and electron microscopy of thick, hydrated organic materials. *Ultramicroscopy*, *184*, 293-309.

Egerton, R. F. (1980). Chemical measurements of radiation damage in organic samples at and below room temperature. *Ultramicroscopy*, *5*(1–3), 521–523.

Egerton, R. F. (1982). Organic mass loss at 100 K and 300 K. *Journal of Microscopy*, *126*(April), 95–100.

Egerton, R. F. (2011). *Electron Energy-Loss Spectroscopy in the Electron Microscope*. *Reports on Progress in Physics* (3rd edition, Vol. 72). Boston, MA: Springer US.

Egerton, R. F. (2012). Mechanisms of radiation damage in beam-sensitive specimens, for TEM accelerating voltages between 10 and 300 kV. *Microscopy Research and Technique*, *75*(11), 1550–1556.

Egerton, R. F. (2013). Control of radiation damage in the TEM. *Ultramicroscopy*, *127*, 100–108.

Egerton, R. F., Konstantinova, T., & Zhu, Y. (2015). Analysis Of Beam-Sensitive Materials By Electrons And X-Rays. In *Advances in Imaging and Electron Physics* (Vol. 191, pp. 70–80).

Egerton, R. F., Lazar, S., & Libera, M. (2012). Delocalized radiation damage in polymers. *Micron*, *43*(1), 2–7.

Egerton, R. F., Li, P., & Malac, M. (2004). Radiation damage in the TEM and SEM, *35*, 399–409.

Ehsani, M., Gao, Y., & Emadi, A. (2009). *Modern Electric, Hybrid Electric, and fuel cell vehicles: Fundamentals, Theory and Design* (2nd Edition). Boca Raton, FL: CRC Press Taylor & Francis Group.

Eikerling, M. H., Malek, K., & Wang, Q. (2008). Catalyst Layer Modeling: Structure, Properties and Performance. In J. Zhang (Ed.), *PEM Fuel Cell Electrocatalysts and Catalyst Layers: Fundamentals and Applications* (pp. 381–446). London: Springer London.

Eslamibidgoli, M. J., Huang, J., Kadyk, T., Malek, A., & Eikerling, M. (2016). How theory and simulation can drive fuel cell electrocatalysis. *Nano Energy*, *29*, 334–361.

Evchuk, I. Y., Musii, R. I., Makitra, R. G., & Pristanskii, R. E. (2005). Solubility of polymethyl methacrylate in organic solvents. *Russian Journal of Applied Chemistry*, *78*(10), 1576–1580.

Filmetrics, I. (2016). *Taking the mystery out of Thin-Film measurement*. Provided by Filmetrics, available for download: https://wcam.engr.wisc.edu/Public/Tools/Analysis/Filmetrics%20F 20%20technical%20reference.pdf

Fisher, W. K., & Corelli, J. C. (1981). Effect of ionizing radiation on the chemical composition, crystalline content and structure, and flow properties of polytetrafluoroethylene. *Journal of Polymer Science: Polymer Chemistry Edition*, *19*(10), 2465–2493.

Forsythe, J. S., & Hill, D. J. T. (2000). Radiation chemistry of fluoropolymers. *Progress in Polymer Science (Oxford)*, *25*(1), 101–136.

Fukushima, K., Katoh, M., & Fukami, a. (1982). Quantitative measurements of radiation damage to hydrated specimens observed in a wet gas environment. *Journal of Electron Microscopy*, *31*(2), 119–126.

Fuller, T. J., & Dobulis, B. T. (2015). Sulfonated perfluorosulfonic acid polyelectrolyte membranes. United States Patent # 8993193 B2.

Geloni, G. (2018). *Self seeded Free-Electron Lasers*. In: Jaeschke, E., Khan, S., Schneider, J., Hastings, J.: Synchrotron Light Sources and Free-Electron Lasers. Springer Reference.

George, M. G., Wang, J., Banerjee, R., & Bazylak, A. (2016). Composition analysis of a polymer electrolyte membrane fuel cell microporous layer using scanning transmission X-ray microscopy and near edge X-ray absorption fine structure analysis. *Journal of Power Sources*, *309*, 254–259.

Ghassemzadeh, L., Kreuer, K. D., Maier, J., & Müller, K. (2010). Chemical degradation of Nafion membranes under mimic fuel cell conditions as investigated by solid-state NMR spectroscopy. *Journal of Physical Chemistry C*, *114*(34), 14635–14645.

Giannuzzi, L., & Stevie, F. A. (1999). A review of focused ion beam milling techniques for TEM specimen preparation. *Micron*, *30*(3), 197–204.

Gianoncelli, A., Vaccari, L., Kourousias, G., Cassese, D., Bedolla, D. E., Kenig, S., … Kiskinova,

M. (2015). Soft X-Ray Microscopy Radiation Damage On Fixed Cells Investigated With Synchrotron Radiation FTIR Microscopy. *Scientific Reports*, *5*(May), 1–11.

Gierke, T. D., & Hsu, W. Y. (1982). The Cluster—Network Model of Ion Clustering in Perfluorosulfonated Membranes, (14), 283–307.

Glaeser, R. M., & Taylor, K. A. (1978). Radiation damage relative to transmission electron microscopy of biological specimens at low temperature: a review. *Journal of Microscopy*, *112*(1), 127–138.

Gordon, R. B., Bertram, M., & Graedel, T. E. (2006). Metal stocks and sustainability. *Proceedings of the National Academy of Sciences*, *103*(5), 1209–1214.

Gröger, O., Gasteiger, H. A., & Suchsland, J.-P. (2015). Review—Electromobility: Batteries or Fuel Cells? *Journal of The Electrochemical Society*, *162*(14), A2605–A2622.

Grove, W. R. (1839). XXIV. On voltaic series and the combination of gases by platinum. *Philosophical Magazine Series 3*, *14*(86–87), 127–130.

Grubb, D. T. (1974). Radiation damage and electron microscopy of organic polymers. *Journal of Materials Science*, *9*(10), 1715–1736.

Gruger, A., Régis, A., Schmatko, T., & Colomban, P. (2001). Nanostructure of Nafion® membranes at different states of hydration: An IR and Raman study. *Vibrational Spectroscopy*, *26*(2), 215–225.

Gschrey, M., Schmidt, R., Kaganskiy, A., Rodt, S., & Reitzenstein, S. (2014). Study of high-resolution electron-beam resists for applications in low-temperature lithography. *Journal of Vacuum Science & Technology B, Nanotechnology and Microelectronics: Materials, Processing, Measurement, and Phenomena*, *32*(6), 061601.

Guay, D., Stewart-Ornstein, J., Zhang, X., & Hitchcock, A. P. (2005). In Situ Spatial and Time-Resolved Studies of Electrochemical Reactions by Scanning Transmission X-ray Microscopy. *Analytical Chemistry*, *77*(11), 3479–3487.

Guttmann, P., Niemann, B., Rehbein, S., Knöchel, C., Rudolph, D., & Schmahl, G. (2003). The transmission X-ray microscope at BESSY II. *Journal de Physique IV (Proceedings)*, *104*,

85–90.

Hamill, W. H. (1969). A Model for the Radiolysis of Water. *Journal of Physical Chemistry*, *73*(5), 1341–1347.

Hart, J. L., Lang, A. C., Leff, A. C., Longo, P., Trevor, C., Twesten, R. D., & Taheri, M. L. (2017). Direct Detection Electron Energy-Loss Spectroscopy: A Method to Push the Limits of Resolution and Sensitivity. *Scientific Reports*, *7*(1), 1–14. http://doi.org/10.1038/s41598-017-07709-4

Henderson, R. (1995). The potential and limitations of neutrons, electrons and X-rays for atomic resolution microscopy of unstained biological molecules. *Quarterly Reviews of Biophysics*, *28*(02), 171.

Henke, B. L. L., Gullikson, E. M. M., & Davis, J. C. C. (1993). X-Ray Interactions: Photoabsorption, Scattering, Transmission, and Reflection at E = 50-30,000 eV, Z = 1-92. *At. Data Nucl. Data Tables*, *54*(2), 181–342.

Hino, R., Matsui, K., & Yan, X. L. (2011). *The Role of Hydrogen in the World Economy*, *Nuclear Hydrogen Production Handbook*, 4–46. Taylor & Francis Group, LLC.

Hitchcock, A. (2018). X-ray Microscopy Bibliography. Retrieved June 21, 2018, from http://unicorn.mcmaster.ca/xrm-biblio/xrm_bib.html

Hitchcock, A. P. (2012). Soft X-Ray Imaging and Spectromicroscopy. In G. Van Tendeloo, V. D. Dyck, & S. J. Pennycook (Eds.), *Handbook on Nanoscopy Vol.II* (pp. 745–791). Wiley-VCH Verlag GmbH & Co. KGaA.

Hitchcock, A. P. (2015). Soft X-ray spectromicroscopy and ptychography. *Journal of Electron Spectroscopy and Related Phenomena*, *200*, 49–63.

Hitchcock, A. P., Morin, C., Tyliszczak, T., Koprinarov, I. N., Ikeura-Sekiguchi, H., Lawrence, J. R., & Leppard, G. G. (2002). Soft X-ray microscopy of soft matter - Hard information from two softs. *Surface Review and Letters*, *9*(1), 193–201.

Hitchcock, A. P., & Toney, M. F. (2014). Spectromicroscopy and coherent diffraction imaging: focus on energy materials applications. *Journal of Synchrotron Radiation*, *21*(Pt 5), 1019–

30.

Holdcroft, S. (2013). Fuel Cell Catalyst Layers: A Polymer Science Perspective. *Chemistry of Materials*, *26*(1), 381–393.

Howells, M., Jacobsen, C., Warwick, T., & Van den Bos, A. (2007). Principles and Applications of Zone Plate X-Ray Microscopes. In *Science of Microscopy* (Vol. 1984, pp. 835–926). New York, NY: Springer New York.

Huang, J., Li, Z., & Zhang, J. (2017). Review of characterization and modeling of polymer electrolyte fuel cell catalyst layer: The blessing and curse of ionomer. *Frontiers in Energy*, *11*(3), 334–364.

Hujsak, K. A., Roth, E. W., Kellogg, W., Li, Y., & Dravid, V. P. (2018). High speed/low dose analytical electron microscopy with dynamic sampling. *Micron*, *108*(March), 31–40.

Ishii, I., & Hitchcook, A. P. (1988). The oscillator strengths for C1s and O1s excitation of some saturated and unsaturated organic alcohols, acids and esters. *Journal of Electron Spectroscopy and Related Phenomena*, *46*(1), 55–84.

Jacobsen, C., Wirick, S., Flynn, G., & Zimba, C. (2000). Soft x-ray spectroscopy from image sequences with sub-100 nm spatial resolution. *Journal of Microscopy*, *197*(Pt 2), 173–84.

Karan, K. (2017). PEFC catalyst layer: Recent advances in materials, microstructural characterization, and modeling. *Current Opinion in Electrochemistry*, *5*(1), 1–9.

Kaznatcheev, K. V., Karunakaran, C., Lanke, U. D., Urquhart, S. G., Obst, M., & Hitchcock, a. P. (2007). Soft X-ray spectromicroscopy beamline at the CLS: Commissioning results. *Nuclear Instruments and Methods in Physics Research Section A: Accelerators, Spectrometers, Detectors and Associated Equipment*, *582*(1), 96–99.

Kilcoyne, A. L. D., Tyliszczak, T., Steele, W. F., Fakra, S., Hitchcock, P., Franck, K., … Ade, H. (2003). Interferometer-controlled scanning transmission X-ray microscopes at the Advanced Light Source. *Journal of Synchrotron Radiation*, *10*, 125–136.

Kimoto, K., Asaka, T., Nagai, T., Saito, M., Matsui, Y., & Ishizuka, K. (2007). Element-selective imaging of atomic columns in a crystal using STEM and EELS. *Nature*, *450*(7170), 702–

704.

Kirkland, A. I., Chang, S. L.-Y., & Hutchison, J. L. (2007). Atomic Resolution Transmission Electron Microscopy. In *Science of Microscopy* (pp. 3–64). New York, NY: Springer New York.

Klein, R. J., Fischer, D. A., & Lenhart, J. L. (2008). Systematic oxidation of polystyrene by ultraviolet-ozone, characterized by near-edge X-ray absorption fine structure and contact angle. *Langmuir*, *24*(15), 8187–8197.

Knapek, E., & Dubochet, J. (1980). Beam damage to organic material is considerably reduced in cryo-electron microscopy. *Journal of Molecular Biology*, *141*(2), 147–161.

Koprinarov, I. N., Hitchcock, A. P., McCrory, C. T., & Childs, R. F. (2002). Quantitative Mapping of Structured Polymeric Systems Using Singular Value Decomposition Analysis of Soft X-ray Images. *The Journal of Physical Chemistry B*, *106*(21), 5358–5364.

Kuijper, M., van Hoften, G., Janssen, B., Geurink, R., De Carlo, S., Vos, M., … Storms, M. (2015). FEI's direct electron detector developments: Embarking on a revolution in cryo-TEM. *Journal of Structural Biology*, *192*(2), 179–187.

Kusoglu, A., & Weber, A. Z. (2017). New Insights into Perfluorinated Sulfonic-Acid Ionomers. *Chemical Reviews*, *117*(3), 987–1104.

Lamvik, M. K. (1991). Radiation damage in dry and frozen hydrated organic material. *Journal of Microscopy*, *161*(1), 171–181.

Lappan, U., Geißler, U., Scheler, U., & Lunkwitz, K. (2003). Identification of new chemical structures in poly(tetrafluoroethylene-co-perfluoropropyl vinyl ether) irradiated in vacuum at different temperatures. *Radiation Physics and Chemistry*, *67*(3–4), 447–451.

Le Guillou, C., Remusat, L., Bernard, S., Brearley, A. J., & Leroux, H. (2013). Amorphization and D/H fractionation of kerogens during experimental electron irradiation: Comparison with chondritic organic matter. *Icarus*, *226*(1), 101–110.

Lee, V., Susac, D., Kundu, S., Berejnov, V., Atanasoski, R. T., Hitchcock, A. P., & Stumper, J. (2013). STXM Characterization of Nanostructured Thin Film Anode Before and After Start-

Up Shutdown and Reversal Tests. *ECS Transactions*, *58*(1), 473–479.

Lehrer, C., Frey, L., Petersen, S., Mizutani, M., Takai, M., & Ryssel, H. (2000). Defects and gallium-contamination during focused ion beam micro machining. In *2000 International Conference on Ion Implantation Technology Proceedings. Ion Implantation Technology - 2000 (Cat. No.00EX432)* (pp. 695–698). IEEE.

Leontowich, A. (2012). *Tunable Focused X-rays for Patterning and Lithography*. PhD Thesis, McMaster University.

Leontowich, A. F. G. (2013). Utility of the G value and the critical dose to soft X-ray radiation damage of polyacrylonitrile. *Radiation Physics and Chemistry*, *90*, 87–91.

Leontowich, A. F. G., & Hitchcock, A. P. (2012). Secondary electron deposition mechanism of carbon contamination. *Journal of Vacuum Science & Technology B, Nanotechnology and Microelectronics: Materials, Processing, Measurement, and Phenomena*, *30*(3), 030601.

Leontowich, A. F. G., Hitchcock, A. P., & Egerton, R. F. (2016). Radiation damage yields across the carbon 1s excitation edge. *Journal of Electron Spectroscopy and Related Phenomena*, *206*, 58–64.

Leontowich, A. F. G., Hitchcock, A. P., Tyliszczak, T., Weigand, M., Wang, J., & Karunakaran, C. (2012). Accurate dosimetry in scanning transmission X-ray microscopes via the cross-linking threshold dose of poly(methyl methacrylate). *Journal of Synchrotron Radiation*, *19*, 976–987.

A.F.G. Leontowich, R. Berg, C.N. Regier, D.M. Taylor, J. Wang, D. Beauregard, J. Geilhufe, J. Swirsky, J. Wu, C. Karunakaran, A P. Hitchcock and S.G. Urquhart, *Cryo scanning transmission X-ray microscope optimized for spectrotomography*, Rev. Sci Inst. (submitted May 2018).

Leontowich, A. F. G., Tyliszczak, T., & Hitchcock, A. P. (2011). Measurement of the point spread function of a soft x-ray microscope by single pixel exposure of photoresists. *Proc. of SPIE*, *8077*, 80770N1-8.

Li, J., & Stöver, H. D. H. (2010). Pickering Emulsion Templated Layer-by-Layer Assembly for

Making Microcapsules. *Langmuir*, *26*(19), 15554–15560.

Lopez-Haro, M., Guétaz, L., Printemps, T., Morin, A., Escribano, S., Jouneau, P., … Gebel, G. (2014). Three-dimensional analysis of Nafion layers in fuel cell electrodes. *Nature Communications*, *5*(1), 5229.

Lunkwitz, K., Lappan, U., & Scheler, U. (2004). Modification of perfluorinated polymers by high-energy irradiation. *Journal of Fluorine Chemistry*, *125*(6), 863–873.

Ma, Y., Chen, C. T., Meigs, G., Randall, K., & Sette, F. (1991). High-resolution K-shell photoabsorption measurements of simple molecules. *Physical Review A*, *44*(3), 1848–1858.

Malek, K., Mashio, T., & Eikerling, M. (2011). Microstructure of Catalyst Layers in PEM Fuel Cells Redefined: A Computational Approach. *Electrocatalysis*, *2*(2), 141–157.

Mauritz, K. A., & Moore, R. B. (2004). State of understanding of Nafion. *Chemical Reviews*, *104*(10), 4535–4585.

McNeill, C. R., Watts, B., Swaraj, S., Ade, H., Thomsen, L., Belcher, W., & Dastoor, P. C. (2008). Evolution of the nanomorphology of photovoltaic polyfluorene blends: sub-100 nm resolution with x-ray spectromicroscopy. *Nanotechnology*, *19*, 424015.

Meents, A., Gutmann, S., Wagner, A., & Schulze-Briese, C. (2010). Origin and temperature dependence of radiation damage in biological samples at cryogenic temperatures. *Proceedings of the National Academy of Sciences of the United States of America*, *107*(3), 1094–1099.

Melo, L. G. A., Hitchcock, A. P., Jankovic, J., Stumper, J., Susac, D., & Berejnov, V. (2017). Quantitative Mapping of Ionomer in Catalyst Layers by Electron and X-ray Spectromicroscopy. *ECS Transactions*, *80*(8), 275–282.

Melo, L. G. A., Hitchcock, A. P., Berejnov, V., Susac, D., Stumper, J., & Botton, G. A. (2016). Evaluating focused ion beam and ultramicrotome sample preparation for analytical microscopies of the cathode layer of a polymer electrolyte membrane fuel cell. *Journal of Power Sources*, *312*, 23–35.

Melo, L. G. D. A., Botton, G. A., & Hitchcock, A. P. (2015). Quantification of the critical dose

for radiation damage to perfluorosulfonic acid membranes using soft X-ray microscopy, *21*(1220), 2443–2444.

Migunov, V., Ryll, H., Zhuge, X., Simson, M., Strüder, L., Batenburg, K. J., … Dunin-Borkowski, R. E. (2015). Rapid low dose electron tomography using a direct electron detection camera. *Scientific Reports*, *5*, 1–5.

More, K., & Reeves, S. (2005). TEM Specimen Preparation of Partially-Embedded Electrodes From Proton Exchange Membrane Fuel Cell Membrane Electrode Assemblies. *Microscopy and Microanalysis*, *11*(S02), 2104–2105.

Nagaishi, R., & Kumagai, Y. (2011). Radiolysis of Water. *Nuclear Hydrogen Production Handbook*, 177–187.

Norrman, K., Ghanbari-Siahkali, A., & Larsen, N. B. (2005). 6 Studies of spin-coated polymer films. *Annual Reports Section "C" (Physical Chemistry)*, *101*(October 2005), 174.

Ohta, T., Seki, K., Yokoyama, T., Morisada, I., & Edamatsu, K. (1990). Polarized XANES Studies of Oriented Polyethylene and FIuorinated PolyethyIenes. *Physica Scipta*, *41*(4), 150–153.

Okudaira, K. K., Yamane, H., & Ito, K. (2002). Photodegration of Poly(tetrafluoroethylene) and poly(vinylidene fluoride) thin films by inner shell excitation. *Surface Review and Letters*, *9*(1), 335–340.

Orthacker, A., Schmied, R., Chernev, B., Fröch, J. E., Winkler, R., Hobisch, J., … Plank, H. (2014). Chemical degradation and morphological instabilities during focused ion beam prototyping of polymers. *Physical Chemistry Chemical Physics : PCCP*, *16*(4), 1658–66.

Paul, D., Fraser, A., & Karan, K. (2011). Towards the understanding of proton conduction mechanism in PEMFC catalyst layer: Conductivity of adsorbed Nafion films. *Electrochemistry Communications*, *13*(8), 774–777.

Paul, D. K., Giorgi, J. B., & Karan, K. (2013). Chemical and Ionic Conductivity Degradation of Ultra-Thin Ionomer Film by X-ray Beam Exposure. *Journal of the Electrochemical Society*, *160*(4), F464–F469.

Peron, J., Mani, A., Zhao, X., Edwards, D., Adachi, M., Soboleva, T., … Holdcroft, S. (2010). Properties of Nafion® NR-211 membranes for PEMFCs. *Journal of Membrane Science*, *356*(1–2), 44–51.

Popovici, D., Sacher, E., & Meunier, M. (1998). Photodegradation of teflon AF1600 during XPS analysis. *Journal of Applied Polymer Science*, *70*(6), 1201–1207.

Rae, P. J., & Dattelbaum, D. M. (2004). The properties of poly(tetrafluoroethylene) (PTFE) in compression. *Polymer*, *45*(22), 7615–7625.

Rhodes, C. J. (2016). The 2015 Paris climate change conference: COP21. *Science Progress*, *99*(1), 97–104.

Rightor, E. G., Hitchcock, A. P., Ade, H., Leapman, R. D., Urquhart, S. G., Smith, A. P., … Warwick, T. (1997). Spectromicroscopy of Poly(ethylene terephthalate): Comparison of Spectra and Radiation Damage Rates in X-ray Absorption and Electron Energy Loss. *The Journal of Physical Chemistry B*, *101*(11), 1950–1960.

Rodriguez, J. A., Eisenberg, D. S., & Gonen, T. (2017). Taking the measure of MicroED. *Current Opinion in Structural Biology*, *46*, 79–86.

Roth, J., Eller, J., & Buchi, F. N. (2012). Effects of Synchrotron Radiation on Fuel Cell Materials. *Journal of the Electrochemical Society*, *159*(8), F449–F455.

Samuel, A. H., & Magee, J. L. (1953). Theory of radiation chemistry. II. Track effects in radiolysis of water. *The Journal of Chemical Physics*, *21*(6), 1080–1087.

Schäfer, T., Michel, P., Claret, F., Beetz, T., Wirick, S., & Jacobsen, C. (2009). Radiation sensitivity of natural organic matter: Clay mineral association effects in the Callovo-Oxfordian argillite. *Journal of Electron Spectroscopy and Related Phenomena*, *170*(1–3), 49–56.

Scheiba, F., Benker, N., Kunz, U., Roth, C., & Fuess, H. (2008). Electron microscopy techniques for the analysis of the polymer electrolyte distribution in proton exchange membrane fuel cells. *Journal of Power Sources*, *177*(2), 273–280.

Schlossmacher, P., Klenov, D. O., Freitag, B., von Harrach, S., & Steinbach, A. (2010).

Nanoscale Chemical Compositional Analysis with an Innovative S/TEM-EDX System. *Microscopy and Analysis*, *24(7)*, S5–S8.

Schulze, M., Bolwin, K., Gülzow, E., & Schnurnberger, W. (1995). XPS analysis of PTFE decomposition due to ionizing radiation. *Fresenius' Journal of Analytical Chemistry*, *353*(5–8), 778–784.

Schulze, M., Lorenz, M., Wagner, N., & Guelzow, E. (1999). XPS analysis of the degradation of Nafion. *Fresenius' Journal of Analytical Chemistry*, *365*(1–3), 106–113.

Sezen, M., Plank, H., Fisslthaler, E., Chernev, B., Zankel, A., Tchernychova, E., … Pölt, P. (2011). An investigation on focused electron/ion beam induced degradation mechanisms of conjugated polymers. *Physical Chemistry Chemical Physics*, *13*, 20235.

Sezen, M., Plank, H., Nellen, P. M., Meier, S., Chernev, B., Grogger, W., … Poelt, P. (2009). Ion beam degradation analysis of poly(3-hexylthiophene) (P3HT): can cryo-FIB minimize irradiation damage? *Physical Chemistry Chemical Physics : PCCP*, *11*, 5130–5133.

Shapiro, D. A., Yu, Y. S., Tyliszczak, T., Cabana, J., Celestre, R., Chao, W., … Padmore, H. A. (2014). Chemical composition mapping with nanometre resolution by soft X-ray microscopy. *Nature Photonics*, *8*(10), 765–769.

Shinotsuka, H., Tanuma, S., Powell, C. J., & Penn, D. R. (2015). Calculations of electron inelastic mean free paths. X. Data for 41 elemental solids over the 50eV to 200keV range with the relativistic full Penn algorithm. *Surface and Interface Analysis*, *47*(9), 871–888.

Sieminski, A. (2017). *Annual Energy Outlook 2017*. Independent Statistics & Analysis. U.S. Energy Information Administration.

Siroma, Z., Kakitsubo, R., Fujiwara, N., Ioroi, T., Yamazaki, S. ichi, & Yasuda, K. (2009). Depression of proton conductivity in recast Nafion® film measured on flat substrate. *Journal of Power Sources*, *189*(2), 994–998.

Sorrentino, A., Nicolás, J., Valcárcel, R., Chichón, F. J., Rosanes, M., Avila, J., … Pereiro, E. (2015). MISTRAL: a transmission soft X-ray microscopy beamline for cryo nano-tomography of biological samples and magnetic domains imaging. *Journal of Synchrotron*

Radiation, *22*(4), 1112–1117.

Srinivasan, R. (1986). Ablation of polymers and biological tissue by ultraviolet lasers. *Science*, *234*(4776), 559–565.

Stöhr, J. (1992). *NEXAFS Spectroscopy*. Springer Series in Surface Sciences (Vol. 25). Springer-Verlag Berlin Heiderlberg.

Susac, D., Berejnov, V., Hitchcock, A. P., & Stumper, J. (2011). STXM Study of the Ionomer Distribution in the PEM Fuel Cell Catalyst Layers. In *ECS Transactions* (Vol. 41, pp. 629–635).

Susac, D., Berejnov, V., Stumper, J., & Hitchcock, A. P. (2012). STXM Characterization of PEM Fuel Cell Catalyst Layers. *ECS Transactions*, *50*(2), 405–413.

Suzuki, T. (2016). Fuel Cell Stack Technology of Toyota. *ECS Transactions*, *75*(14), 423–434.

Tahir, D., & Sari, N. H. (2015). Stopping powers and inelastic mean free path of 200eV-50keV electrons in polymer PMMA, PE, and PVC. *Applied Radiation and Isotopes*, *95*, 59–62.

Takamatsu, T., & Eisenberg, A. (1979). Density and Expansion Coefficients of Nafion. *J. App. Poly. Sci.*, *24*(11), 2221–2235.

Tavares, P. F., Leemann, S. C., Sjöström, M., & Andersson, Å. (2014). The max iv storage ring project. *Journal of Synchrotron Radiation*, *21*(5), 862–877.

The World Bank. (2014). CO2 emissions from transport (% of total fuel combustion). Retrieved from: https://data.worldbank.org/indicator/EN.CO2.TRAN.ZS

Thibault, P., Dierolf, M., Menzel, A., Bunk, O., David, C., & Pfeiffer, F. (2008). High-Resolution Scanning X-ray Diffraction Microscopy. *Science*, *321*(5887), 379–382.

Thibault, P., Guizar-Sicairos, M., & Menzel, A. (2014). Coherent imaging at the diffraction limit. *Journal of Synchrotron Radiation*, *21*(5), 1011–1018.

Thiele, S., Fürstenhaupt, T., Banham, D., Hutzenlaub, T., Birss, V., Ziegler, C., & Zengerle, R. (2013). Multiscale tomography of nanoporous carbon-supported noble metal catalyst layers. *Journal of Power Sources*, *228*, 185–192.

Thomas, C. E. (2009). Fuel cell and battery electric vehicles compared. *International Journal of Hydrogen Energy*, *34*(15), 6005–6020.

Tyliszczak, T., & Hitchcock, P. (2000). STXM_Control is written in C++, 1st version completed in 2000. Since 2014 the ALS version has been modified to run on Windows 7. The pre-2014 version, with minor modifications, is run on Windows XP at the CLS.

Tzvetkov, G., & Fink, R. (2008). Temperature-dependent X-ray microspectroscopy of phase-change core–shell microcapsules. *Scripta Materialia*, *59*(3), 348–351.

Tzvetkov, G., Späth, A., & Fink, R. H. (2014). Soft X-ray induced damage in PVA-based membranes in water environment monitored by X-ray absorption spectroscopy. *Radiation Physics and Chemistry*, *103*, 84–88.

Uchida, H., Song, J. M., Suzuki, S., Nakazawa, E., Baba, N., & Watanabe, M. (2006). Electron tomography of Nafion ionomer coated on Pt/carbon black in high utilization electrode for PEFCs. *The Journal of Physical Chemistry. B*, *110*(27), 13319–21.

Urquhart, S. G., & Ade, H. (2002). Trends in the carbonyl core (C 1S, O 1S) --> pi*c=o transition in the near-edge X-ray absorption fine structure spectra of organic molecules. *Journal of Physical Chemistry B*, *106*(34), 8531–8538.

Urquhart, S. G., Hitchcock, A. P., Priester, R. D., & Rightor, E. G. (1995). Analysis of polyurethanes using core excitation spectroscopy. Part II: Inner shell spectra of ether, urea and carbamate model compounds. *Journal of Polymer Science Part B: Polymer Physics*, *33*(11), 1603–1620.

Wang, C., Krishnan, V., Wu, D., Bledsoe, R., Paddison, S. J., & Duscher, G. (2013). Evaluation of the microstructure of dry and hydrated perfluorosulfonic acid ionomers: microscopy and simulations - SUP. *Journal of Materials Chemistry A*, *1*(3), 938.

Wang, J. (2008). *Radiation chemistry by soft X-ray spectromicroscopy*. PhD Thesis, McMaster University.

Wang, J., Botton, G., West, M., & Hitchcock, A. P. (2009). Quantitative evaluation of radiation damage to polyethylene terephthalate by soft X-rays and high-energy electrons. *The Journal*

of Physical Chemistry Bournal of Physical Chemistry. B, *113*(7), 1869–76.

Wang, J., Morin, C., Li, L., Hitchcock, A. P., Scholl, A., & Doran, A. (2009). Radiation damage in soft X-ray microscopy. *Journal of Electron Spectroscopy and Related Phenomena*, *170*(1–3), 25–36.

Wang, J., Stöver, H. D. H., Hitchcock, A. P., & Tyliszczak, T. (2007). Chemically selective soft X-ray patterning of polymers. *Journal of Synchrotron Radiation*, *14*(2), 181–190.

Warkentin, M., Hopkins, J. B., Badeau, R., Mulichak, A. M., Keefe, L. J., & Thorne, R. E. (2013). Global radiation damage: Temperature dependence, time dependence and how to outrun it. *Journal of Synchrotron Radiation*, *20*(1), 7–13.

Warwick, A., Padmore, H. A., & Ade, H. (1998). Bend magnet beam line for scanning transmission X-ray microscopy at the Advanced Light Source. In I. McNulty (Ed.), *Proc. SPIE 3449, X-ray Microfocusing: Applications and Techniques* (pp. 12–18).

Warwick, T., Ade, H., Kilcoyne, D., Kritscher, M., Tylisczcak, T., Fakra, S., … Padmore, H. (2002). A new bend-magnet beamline for scanning transmission X-ray microscopy at the advanced light source. *Journal of Synchrotron Radiation*, *9*(4), 254–257.

Williams, D. B., & Carter, C. B. (2009). *Transmission Electron Microscopy. Springer New York*. Springer Science.

Williams, D. B., & Carter, C. B. (2016). *Transmission Electron Microscopy*. (C. B. Carter & D. B. Williams, Eds.) Cham: Springer International Publishing.

Willmott, P. (2011). *An introduction to synchrotron radiation : techniques and applications*. West Sussex, England: John Wiley & Sons, Inc.

Wilson, A., Marcinkoski, J., & Papageorgopoulos, D. (2016). *Fuel Cell System Cost - 2016. DOE Hydrogen and Fuel Cells Program Record Record*. Retrieved from hydrogen.energy.gov

Wilson, M. S., & Gottesfeld, S. (1992). Thin-film catalyst layers for polymer electrolyte fuel cell electrodes. *Journal of Applied Electrochemistry*, *22*(1), 1–7.

Wu, J., Melo, L. G. A., Zhu, X., West, M. M., Berejnov, V., Susac, D., … Hitchcock, A. P. (2018). 4D imaging of polymer electrolyte membrane fuel cell catalyst layers by soft X-ray spectro-

tomography. *Journal of Power Sources*, *381*, 72–83.

Xing, W. (2008). Catalyst Layer Composition Optimization. In J. Zhang (Ed.), *PEM Fuel Cell Electrocatalysts and Catalyst Layers* (pp. 1003–1040). London: Springer London.

Yakovlev, S., Balsara, N. P., & Downing, K. H. (2013). Insights on the study of nafion nanoscale morphology by transmission electron microscopy. *Membranes*, *3*(4), 424–439.

Yakovlev, S., & Libera, M. (2006). Cryo-STEM EELS of Nafion Saturated with an Organic Solvent. *Microscopy and Microanalysis*, *12*(S02), 996–997.

Yan, Z. B., Hayes, R., Melo, L. G. A., Goward, G. R., & Hitchcock, A. P. (2018). X-ray Absorption and Solid-State NMR Spectroscopy of Fluorinated Proton Conducting Polymers. *The Journal of Physical Chemistry C*, *122*(6), 3233–3244.

Yano, J., & Yachandra, V. K. (2009). X-ray absorption spectroscopy. *Photosynthesis Research*, *102*(2), 241–254.

Yumoto, H., Mimura, H., Koyama, T., Matsuyama, S., Tono, K., Togashi, T., … Yamauchi, K. (2013). Focusing of X-ray free-electron laser pulses with reflective optics. *Nature Photonics*, *7*(1), 43–47.

Zailer, I., Frost, J. E. F., Chabasseur-Molyneux, V., Ford, C. J. B., & Pepper, M. (1996). Crosslinked PMMA as a high-resolution negative resist for electron beam lithography and applications for physics of low-dimensional structures. *Semiconductor Science and Technology*, *11*(8), 1235–1238.

Zamel, N. (2016). The catalyst layer and its dimensionality - A look into its ingredients and how to characterize their effects. *Journal of Power Sources*, *309*, 141–159.

Zawodzinski, T. A., Derouin, C., Radzinksi, S., Sherman, R. J., Smith, V. T., Springer, T. E., & Gottesfeld, S. (1993). Water Uptake by and Transport Through Nafion® 117 Membranes. *Journal of The Electrochemical Society*, *140*(4), 1041.

Zhang, S., Yuan, X. Z., Hin, J. N. C., Wang, H., Friedrich, K. A., & Schulze, M. (2009). A review of platinum-based catalyst layer degradation in proton exchange membrane fuel cells. *Journal of Power Sources*, *194*(2), 588–600.

Zhang, X., Jacobsen, C., Lindaas, S., & Williams, S. (1995). Exposure strategies for polymethyl methacrylate from in situ x-ray absorption near edge structure spectroscopy. *Journal of Vacuum Science & Technology B: Microelectronics and Nanometer Structures*, *13*(4), 1477.

Zhong, X., Yu, L., Sun, J., Zhang, Y. (1993). Radiation stability of PTFE irradiated under various conditions. *Polymer Degradation and Stability, 39*(2), 187-191.

Ziegler, C., Schedel-Niedrig, T., Beamson, G., Clark, D. T., Salaneck, W. R., Sotobayashi, H., & Bradshaw, A. M. (1994). X-Ray Absorption Study of Highly Oriented Poly(tetrafluoroethylene) Thin Films. *Langmuir*, *10*(12), 4399–4402.

Ziegler, C., Thiele, S., & Zengerle, R. (2011). Direct three-dimensional reconstruction of a nanoporous catalyst layer for a polymer electrolyte fuel cell. *Journal of Power Sources*, *196*(4), 2094–2097.

Zils, S., Timpel, M., Arlt, T., Wolz, a., Manke, I., & Roth, C. (2010). 3D Visualisation of PEMFC Electrode Structures Using FIB Nanotomography. *Fuel Cells*, *10*(6), 966–972.

Zook, L. A., & Leddy, J. (1996). Density and Solubility of Nafion: Recast, Annealed, and Commercial Films. *Analytical Chemistry*, *68*(21), 3793–3796.

Zubavichus, Y., Fuchs, O., Weinhardt, L., Heske, C., Umbach, E., Denlinger, J. D., & Grunze, M. (2004). Soft X-Ray-Induced Decomposition of Amino Acids: An XPS, Mass Spectrometry, and NEXAFS Study. *Radiation Research*, *161*(3), 346–358.

Appendix A

This appendix lists all software packages used in this thesis.

1.   aXis2000, version 25-July-2017

All STXM data was analyzed with the software aXis2000, which is written in Interaction Data Language (IDL). It is available free for non-commercial use from: http://unicorn.mcmaster.ca/aXis2000.html.

2.   Microsoft Office, 2016

The processing program Word was used to prepare publications. PowerPoint was used to prepare presentations, reports and figures for publications. Excel application was used for data analysis.

3.   SigmaPlot 6.0

SigmaPlot (by Synstat) was used to plot all spectroscopy data, perform data fitting and generate publication quality graphs.

4.   STXM_Control

This program is written in C++, 1st version 2000. Since 2014 the ALS version has been modified to run on Windows 7. The pre-2014 version, with minor modifications, is run on Windows XP at the CLS. This program controls all the STXM microscopes used in this thesis. It was written and developed by Dr. Tolek Tyliszczak and Peter Hitchcock.

5.   Matlab, 2016

This program (by Mathworks) was used for additional data fitting.

Appendix B – Supplemental info to Chapter 4

Supplemental Information to

Effect of UV radiation damage in air on polymer film thickness, studied by soft X-ray spectromicroscopy

Lis G.A. Melo*[1], Adam P. Hitchcock[1], Darija Susac[2], Juergen Stumper[2] and Viatcheslav Berejnov[2]

[1] Dept. Chemistry and Chemical Biology, McMaster University, Hamilton, ON Canada L8S 4M1

[2] Automotive Fuel Cell Corporation Corp., 9000 Glenlyon Parkway, Burnaby, BC, Canada V5J 5J8

Contents:

S1. Same areas studied by STXM and UV-SR

S2. Thickness determination using Scanning Transmission X-ray Microscopy (STXM)

S3. Raw UV-SR data (Reflectance and refractive index)

S4. Additional STXM data analysis and peak assignments

S5. Correlating UV-SR and STXM thickness measurements

S6. Analysis of thickness decay data $h(t)$ for PMMA and PS polymers

S1. Same areas studied by STXM and UV-SR

The polymer film was mounted on SiNx windows and covered the thin SiNx film in areas with and without the underlying Si frame as shown in Figure S1a. The part of the polymer film deposited on the window area (i.e. without underlying Si) was used for STXM and UV-SR correlation measurements. This area is highlighted in Fig. S1a and shown in Fig. S1b,c before STXM and UV-SR measurements, respectively. This allows measurements by both instruments on areas of the polymer films which are at the same position within a few tens of microns. Fig 1c highlights the area (blue square) used to acquire UV-SR measurements and Fig. S1d highlights

the same area (blue square) that was used to acquire STXM measurements for the thickness determination.
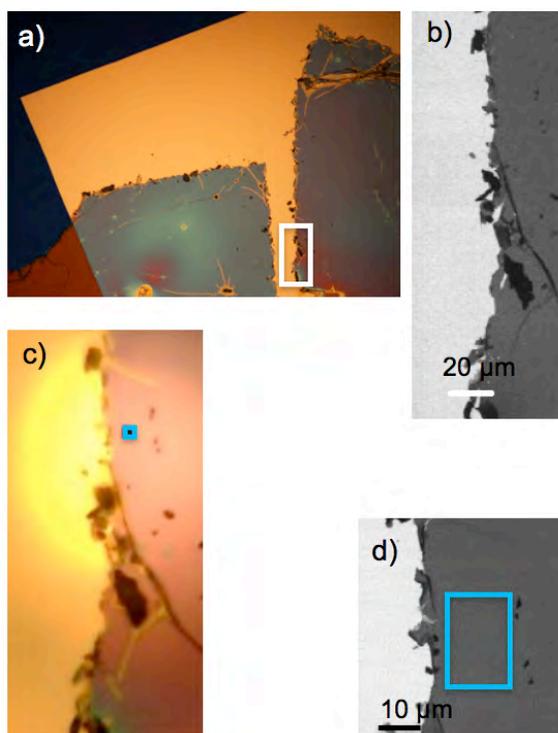
Figure S1 (a) is an optical microscope image of a PS samples in reflective mode using 5X magnification. The white square indicates the region of interest shown in higher magnification in (b) and (c). (b) STXM image at 285.2 eV of the region indicated in (a). (c) Image in reflection mode taken from the Filmetrics equipment. The blue square indicates the region of the UV-SR measurement. (d) Higher magnification of the STXM image at 285.2 eV. The blue square indicates the selected region from the stack for thickness determination (excluding dust particles).

S2. Thickness determination using Scanning Transmission X-ray Microscopy (STXM)

The sample is raster scanned in X and Y at a Z-value corresponding to the focus of a stationary X-ray beam. $I(E,x,y)$, the transmitted intensity at each (X,Y) pixel and photon energy, E is measured and converted to optical density, OD, using the Lambert-Beer law,

$$OD(E) = -\ln\big(I(E)/I_o(E)\big)$$

where $I(E)$ is the intensity transmitted through the sample and $I_0(E)$ is the intensity of the incident photon beam at photon energy E. For material in the probe area composed of multiple chemical species (components), the measured OD is a linear combination of the absorption of all components:

$$OD(E) = \sum_i OD1(E)_i h_i$$

where $OD1(E)_i$ is the reference spectrum of component i obtained from experiment, and h_i is the effective thickness of component i (where the term "effective" is used to describe the situation where the component is distributed non-uniformly along the beam direction, Z coordinate). If the $OD1(E)_i$ for each component are known, then h_i can be determined by least square fitting the measured OD spectrum with the relevant $OD1_i$ spectra. A valid reference spectrum must be obtained for each pure component. The reference spectra on a relative intensity scale are converted to an absolute $OD1(E)_i$ intensity scale (optical density per 1 nm thickness) by scaling the measured spectrum of the pure component outside of the near edge region to the spectrum of the component mass absorption coefficient $\mu_i(E)$:[S.1]

$$OD1_i = \mu_i(E)\rho_i$$

where ρ_i is the gravimetric density of the pure component, i. Outside of the near edge spectral region, the component mass absorption coefficient $\mu_i(E)$ is the sum of the atomic mass absorption coefficients $\mu_a(E)$ of each element present in the component species[S.2]

$$\mu_i(E) = \left(N_A / M_r\right)\sum_q x_q \mu_{a,q}(E)$$

where M_r is the molecular mass, N_A is Avogadro's number, q is the index of the element, and x_q is the number of times element q is found in the molecular formula or repeat unit of the component (see Scheme 1 in the paper). The molecular mass and x_q are known and the elemental spectra $\mu_{a,q}(E)$ are tabulated[S.2] so the component mass absorption coefficient $\mu_i(E)$ can be calculated. The $OD_i(E)$ spectrum of a single pure component is derived by a least square fit (LSF) of the measured relative spectrum to the product $\mu_i(E)\rho_i$ in the pre and post edges of the appended multi edge spectra (the number of edges depends on the chemical formula; C 1s, O 1s and/or F 1s in this study). The resulting LSF coefficients a_i and b_i are then used to compute the reference spectrum $OD1_i(E)$ of component i:

$$OD_i(E) = a_i + b_i OD1_i(E)$$

using computer algebra software Mathematica 8.0 (Wolfram Research Inc., IL).

Image sequences or stacks were recorded at specific edges (C 1s, O 1s, F 1s) to increase the accuracy of the STXM thickness determination. The same area was measured for several edges i.e. C 1s for all 3 polymers, O 1s for PMMA and F 1s for PFSA. The measured stacks for each polymer were appended. I_0 was recorded for each Y pixel line of the (X,Y) image and used to convert the transmitted intensity to optical density per each Y line of pixels (this method allow to bypass the X-ray beam instabilities with characteristic time $\sim$ of the Y-line scan time). The $OD_{X,Y}(E)$ spectrum was then divided by the $OD1(E)$ reference spectrum for that particular polymer to get a thickness map, $h(\mathrm{x,y})=OD(E,x,y)/OD1(E)$, in which each pixel provides an independent thickness measurement.

S3. Raw UV-SR data (Reflectance and refractive index)

The measured raw $R(\lambda)$ spectra for PMMA and PS are presented in Figures S2 and S3. The raw spectra change significantly over the 30 min exposure time and were used to calculate the thickness and refractive index.
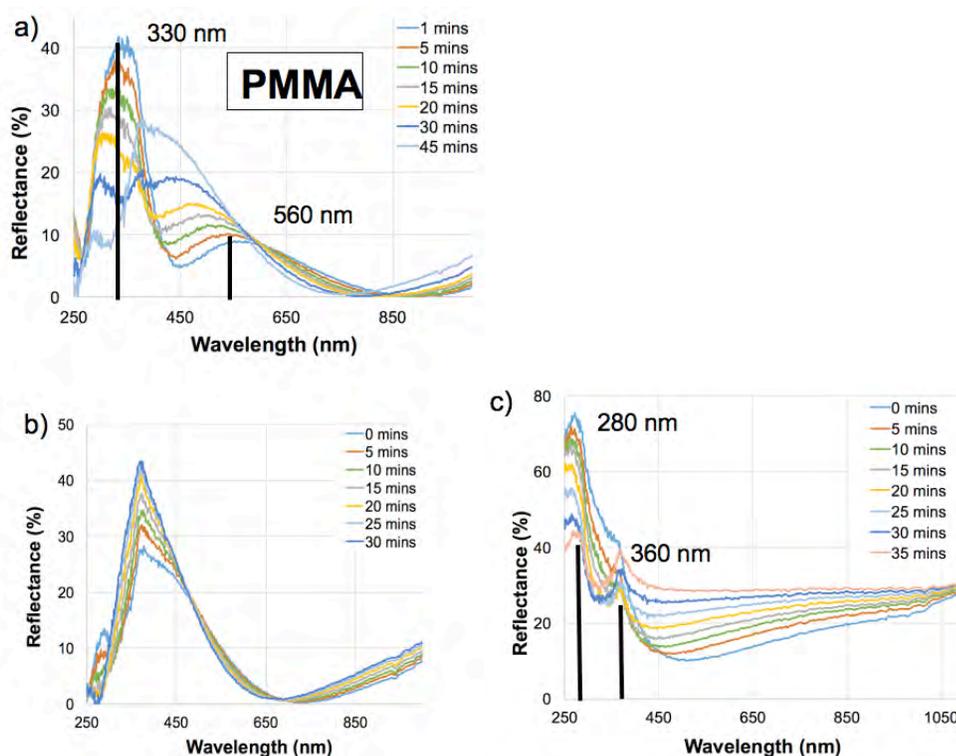
Figure S2 Reflectance spectra for PMMA, recorded over time intervals between 1 and 45 min for (a) a 91nm thick PMMA film spun cast from a 3 wt% toluene solution and transferred on to a 75 nm SiN$_x$ window. (b) Raw reflectance data from a 48 nm thin PMMA film based on a 2 wt% toluene solution. This is the raw data used for the results shown in Figure 3. To show the substrate effect, (c) is the raw data for the 80 nm PMMA film on the Si frame used in Figure 5.
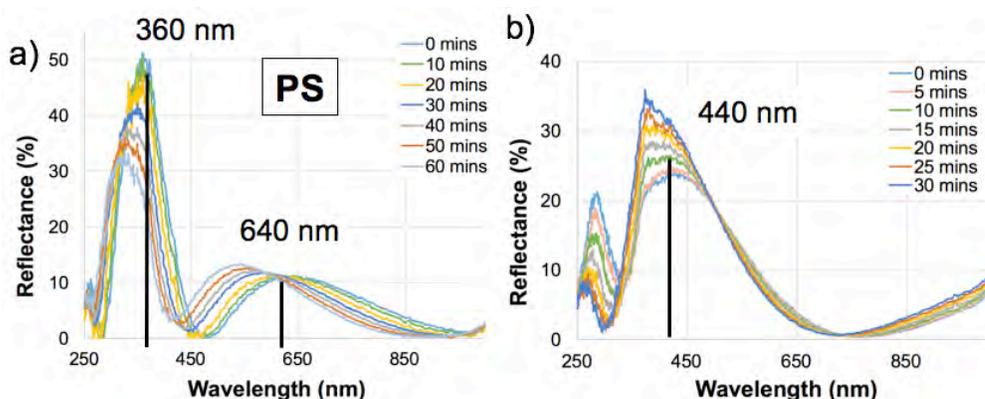
Figure S3 Reflectance spectra for PS, recorded over time intervals between 1 and 45 min for (a) 110 nm thick PS film spun cast from a 2 wt% toluene solution and transferred on to a 75 nm SiN$_x$ window. (b) Raw reflectance data from a 49 nm thin PS film spun cast from a 1 wt% toluene solution and transferred on to a 75 nm SiN$_x$ window. This is the raw data used for the results shown in Figure 4.

The refractive index values for each datapoint in Figure 5 is shown in Figure S4. As shown, the error increases for the film as the thickness decreases. There is also evidence of the PMMA refractive index changing due to exposure of UV.
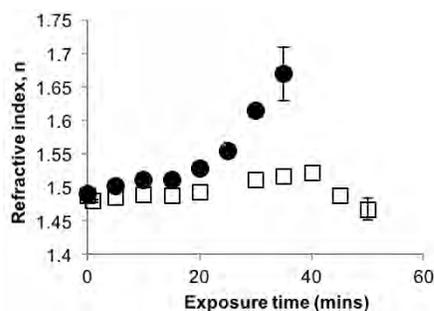
Figure S4 plots the refractive index values for each of the points of Figure 5, determined using method ii. □ = PMMA on 75 nm SiNx on a Si frame, ● = PMMA on a Si wafer with native oxide.

S4. Additional STXM data analysis and peak assignments

Figure S5 presents the (a) optical image taken from the UV-SR instrument, (b) optical image taken from an optical microscope after the 5 mins exposure from UV-SR and (c) STXM image at 285.2 eV depicting the areas where there was UV exposure. Spectra shown in (d) and (e) are the C 1s and O 1s for the 5 min PS exposed sample to UV. The spectral assignment for the C 1s and O 1s NEXAFS spectra shown in Figure 6 and S5 is summarized in Table S1 for PS.
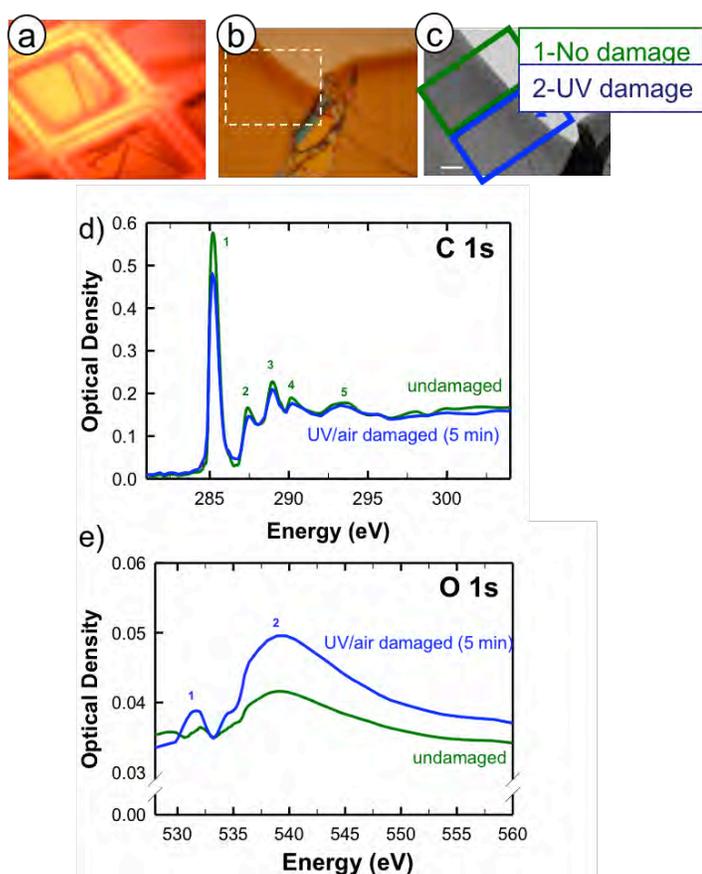
Figure S5 Characterization of a PS thin film after 5 min exposure to UV-SR illumination. (a) visible light image (15x) recorded during the measurements. (b) visible light image (50x) of the same area after the UV-SR measurements. (c) STXM transmission image at 285.2 eV (C 1s $\rightarrow$ $\pi*_{C=C}$ transition) of the same area. The intensity of the 285.2 eV peak is only slightly reduced. (d) STXM C 1s spectra of the damaged (blue) and undamaged (green) areas as indicated in (c). (e) STXM O 1s spectra of the damaged (blue) and undamaged (green) areas as indicated in (c).

Table S1 Energies and tentative assignments of features in the C 1s and O 1s spectra of unexposed and 30 min UV/air damaged polystyrene (PS).

	undamaged			UV/air damaged	
#	Energy (eV)	Assignment	#	Energy (eV)	Assignment
C 1s					
1	285.2	$1\pi^*$	1	285.2	$\pi^*_{C=C}$
2	287.5	exciton	2	286.6	$\pi^*_{C=O}$
3	288.9	$2\pi^*$			
4	290.4		3	288.5	σ^*_{C-O}
5	293.4	$\sigma^*_{C=C}$	4	293.6	$\sigma^*_{C=C}$
O 1s					
	-		1	531.6	$\pi^*_{C=O}$
	-		2	539.0	σ^*_{C-O}

Figure S6 compares the (a) undamaged *OD1(E)* spectrum for PS and the (b) new *OD1(E)* spectrum with the respective theoretical spectra. For (b), a new theoretical spectrum was generated by changing the net-chemical formula to incorporate oxygen for the PS that was damaged by UV-SR during the 30 min exposure. A relatively good match between the pre and post-edge indicates the new formula is adequate.
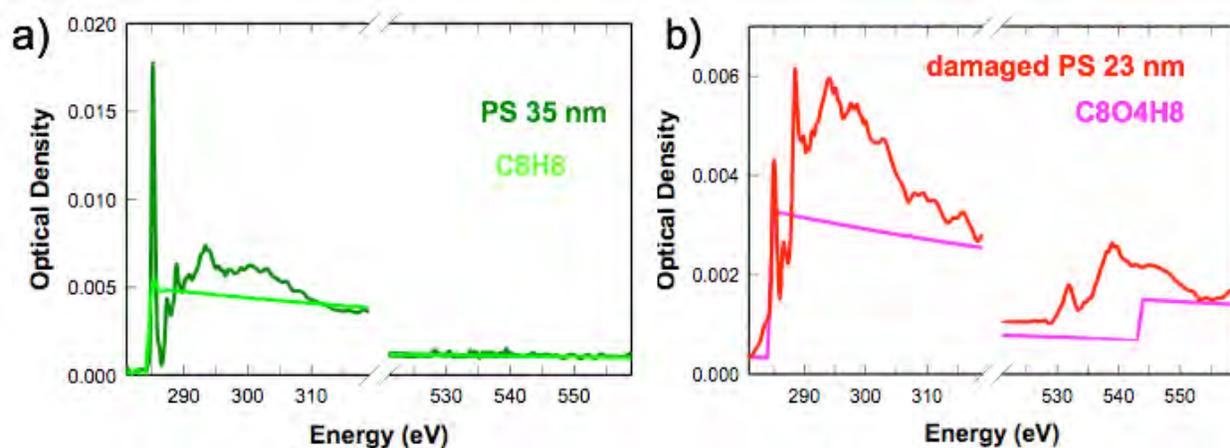
Figure S6 X-ray absorption spectra of (a) undamaged and (b) 30 min UV/air damaged PS in the C 1s and O 1s regions fit to OD/h curves, where h = 35 nm for undamaged PS (C_8H_8, d=1.04 g/mL) and h = 23 nm for 30 min UV/air damaged PS ($C_8O_4H_8$, d=1.04). The elemental composition for the damaged PS was derived as outlined in the main paper.

Figure S7 presents the PMMA exposed to 5 mins during the UV-SR measurements with images taken (a) from the objective lenses in the UV-SR instrument, (b) from an optical microscope after the 5 mins exposure from UV-SR and (c) with STXM at 288.4 eV depicting the areas where there was UV exposure. Spectra shown in (d) and (e) are the C 1s and O 1s for the 5 min PS exposed sample to UV. Table S2 shows the spectral assignment for damaged and non damaged PMMA. Figure S8 presents the quantification of the (a) undamaged and (b) 30 min damaged *OD1(E)* spectrum overlaid with the PMMA chemical formula in (a) and (b) new net-chemical formula for the 30 min UV/air radiation damaged area calculated as $C_5O_4H_8$, obtained by the same method used to analyze the composition of the damaged PS.
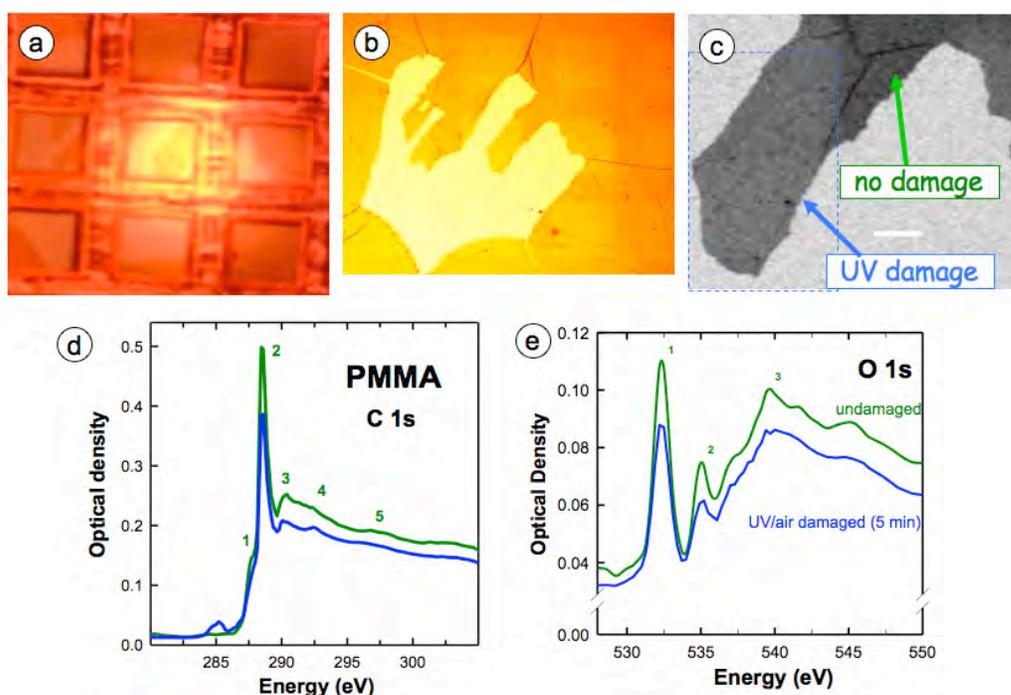
Figure S7 Characterization of a PMMA thin film after 5 min exposure to UV-SR illumination. (a) visible light image (15x) recorded during the measurements. (b) visible light image (50x) of the same area after the UV-SR measurements. (c) STXM transmission image at 288.4 eV (C 1s(C=O) $\rightarrow \pi^*_{C=O}$ transition) of the same area. (d) STXM C 1s spectra of the damaged (blue) and undamaged (green) areas indicated in (c). (e) STXM O 1s spectra of the damaged (blue) and undamaged (green) areas indicated in (c).

Table S2 Energies and tentative assignments of features in the C 1s and O 1s spectra of unexposed and 30 min UV/air damaged polystyrene (PMMA).

	undamaged			UV/air damaged	
#	Energy (eV)	Assignment	#	Energy (eV)	Assignment
C 1s					
1	287.6	σ^*_{C-H}	1	286.7	$\pi^*_{C=O}$
2	288.45	$\pi^*_{C=O}$			
3	290.2		2	288.6	$\pi^*_{O-C=O}$
4	291.9	σ^*_{C-C}	3	294.1	σ^*_{C-C}
5	295.9	$\sigma^*_{C=O}$	2	298.0	$\sigma^*_{C=O}$
O 1s					
1	532.3	O 1s(C=O) →$\pi^*_{C=O}$	1	532.2	$\pi^*_{C=O}$
2	535.2	O 1s(O-C=O)→ $\pi^*_{C=O}$	2	534.9	σ^*_{C-O}
3	540.3	$\sigma^*_{C=O}$	3	539.6	$\sigma^*_{C=O}$
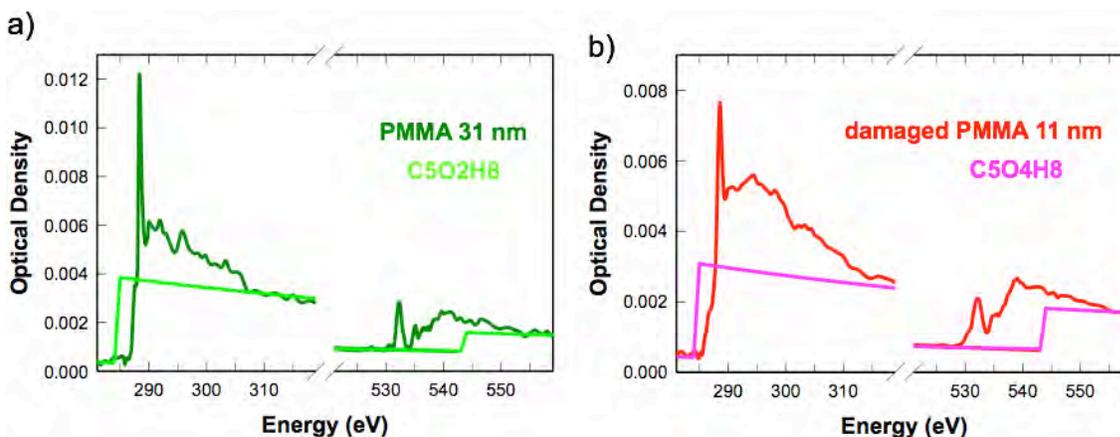
Figure S8 X-ray absorption spectra of (a) undamaged and (b) 30 min UV/air damaged PMMA in the C 1s and O 1s regions fit to OD/h curves, where h = 31 nm for undamaged PMMA ($C_5O_2H_8$, d=1.18 g/mL) and h = 11 nm for 30 min UV/air damaged PMMA ($C_5O_4H_8$, d=1.18). The elemental composition for the damaged PMMA was derived as outlined in the main paper.

Spectral assignment for PFSA sample is shown in Table S3 and the raw UV-SR data as a function of exposure time is shown in Figure S9. The raw spectra are consistently similar as the exposure time increases, indicating that PFSA is not sensitive to the same UV radiation as PS and PMMA.

Table S3 Energies and tentative assignments of features in the C 1s and F 1s spectra of perfluoro-sulfonic acid (PFSA).

#	Energy (eV)	Assignment		#	Energy (eV)	Assignment
	undamaged				undamaged	
C 1s				F 1s		
1	289.1	$\sigma^*_{C=O}$		1	689.9	σ^*_{C-F} ($\perp$)
2	292.4	σ^*_{C-F} $\perp$		2	693.9	σ^*_{C-F} (//)
3	295.5	σ^*_{C-F} (//)		3	704.6	MS[a] xanes
4	298.6	σ^*_{C-C}		4	722	MS[a] xanes
5	307	σ^*_{C-C}				

[a] MS = multiple scattering
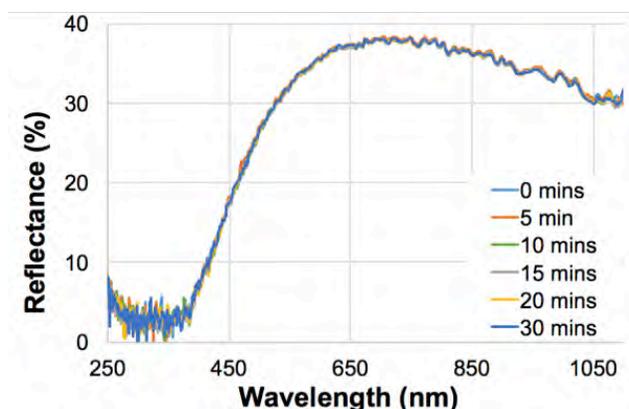

Figure S9 Reflectance spectra recorded over time intervals between 0-30 m for a 52 nm thick PFSA film spun cast from a 2 wt% solution in an aqueous isopropanol mixture. The curves overlap within the noise level. This is the raw data used in determining the thicknesses reported in Figure 2.

S5. Correlating UV-SR and STXM thickness measurements

The linear correlation analysis between UV-SR and STXM thickness for PS, PMMA and PFSA films from Figure 9 is shown in Figure S10 with the values in Table S4.
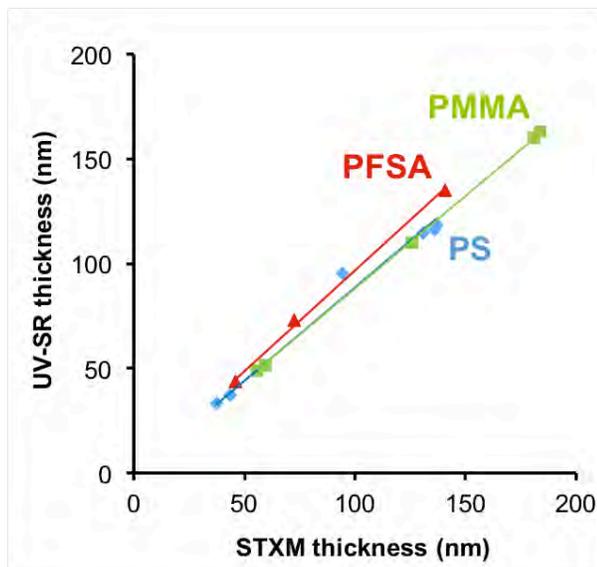
Figure S10 Absolute thicknesses (nm) of 3 polymeric thin films (PS, PMMA, PFSA spun coated and deposited on a 75 nm thick SiNx window) determined by UV-SR plotted against the thicknesses of the same areas determined by STXM (see Table 2 for numerical values), in both cases, using minimal exposure conditions. The straight lines are linear fits with the slopes and regression coefficients indicated in Supplemental Table S4.

Table S4 Linear regression of the UV-SR and STXM thickness results presented graphically in Figure S9.

Sample	Slope	Standard error of slope	R^2
PS	0.885	0.0222	0.9969
PMMA	0.881	0.0038	0.9999
PFSA	0.967	0.0144	0.9995

S6. Analysis of thickness decay data $h(t)$ for PMMA and PS polymers

Part 1: obtaining phenomenological trends of all experimental data

Figure S11 represents the full raw data set obtained for different initial thicknesses

$h_0 = h(t = 0)$ for both polymers PMMA and PS. Below we present an analysis aiming to

find trends describing functionality of $h(t)$ and its phenomenological parameters.
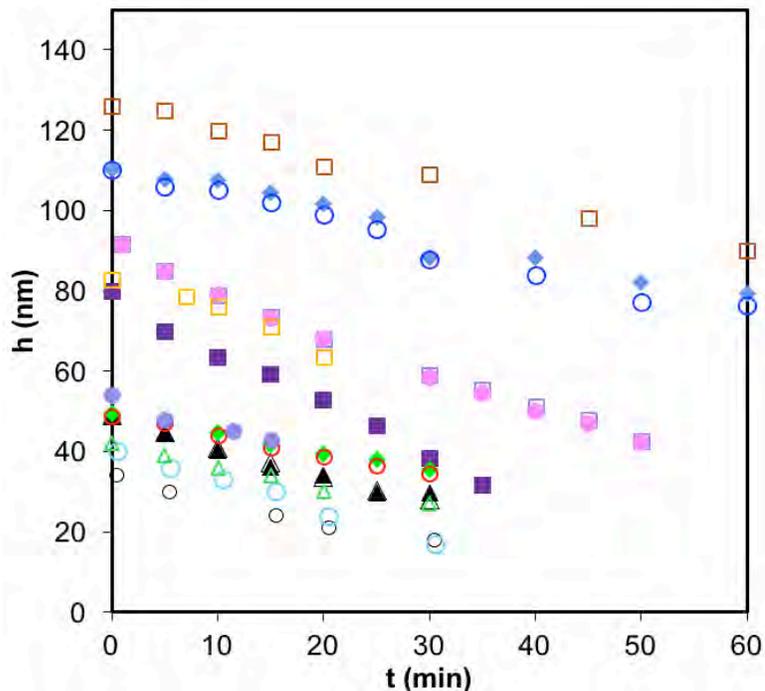
Figure S11: Raw h(t) data measured by UV-SR for different initial thicknesses h_0 and different polymers (PMMA, PS) with respect to the UV radiation time applied: ○ = method-ii PS 110nm (Fig. 4), ○= method-ii PS 40 nm (Fig. 2), △ = method-ii PS 42 nm, ◆ = method-i PS 49 nm (Fig. 4), ○= method-ii PS 49 nm (Fig. 4), ◆ = method-i PS 110 nm (Fig. 4), □= method-ii PS on Si 83 nm, □ = method-ii PS 126 nm, ○ = method-ii PMMA 34 nm (Fig. 2), □ = method-ii PMMA 92 nm (Fig. 3), ● = method-i PMMA 91 nm (Fig. 3), △ = method-ii PMMA 49 nm (Fig. 3), ▲= method-i PMMA 49 nm (Fig. 3), ■ = method-i PMMA on Si (Fig. 5), ● = method-ii PMMA 54 nm.

Following the reviewer's suggestion, we tested all the data in Figure S11 against the

following approximation function:

$$h(t) = h_0 e^{-bt},\qquad\qquad \text{(S1)}$$

were h_0 and b are some phenomenological parameters calculated for each given data set by

applying the least square fit for S1 approximation. If the approximation S1 is satisfactory, then by

introducing a new scale for Figure S11, all data points collapse making the obscured mathematical law of the exponential functionality look more pronounced. Figure S12 represents the same data in Figure S11 plotted with the new dimensionless axes X and Y scaled as: $X = t*b$

and $Y = h(t)/h_0$, respectively, where both h_0 and b were found for each given data set by the least square fit of S1. Table S5 presents these parameters for a linear and exponential fit.

Table S5 Comparison of the phenomelogical parameters of a linear and exponential approximation for all PS and PMMA data points in Figure S11.

	Material	Method	h0*	h0#	b*	b#
○	PS	ii	109.9	110.9	-0.613	-0.007
◆	PS	i	111.2	112.1	-0.6125	-0.006
☐	PS/Si	ii	84.4	84.9	-0.959	-0.013
☐	PS	ii	126.2	127.1	-0.614	-0.006
◆	PS	i	49.6	49.9	-0.482	-0.011
○	PS	ii	49.0	49.3	-0.495	-0.012
△	PS	ii	41.5	42.0	-0.511	-0.015
○	PS	ii	40.7	42.9	-0.771	-0.029
●	PMMA	i	89.3	92.2	-0.974	-0.015
☐	PMMA	ii	89.4	92.2	-0.955	-0.015
■	PMMA/Si	i	78.2	82.2	-1.316	-0.025
▲	PMMA	i	47.5	48.1	-0.661	-0.018
△	PMMA	ii	48.3	49.1	-0.709	-0.019
○	PMMA	ii	33.2	33.8	-0.540	-0.022

* Linear approximation

\# exponential approximation
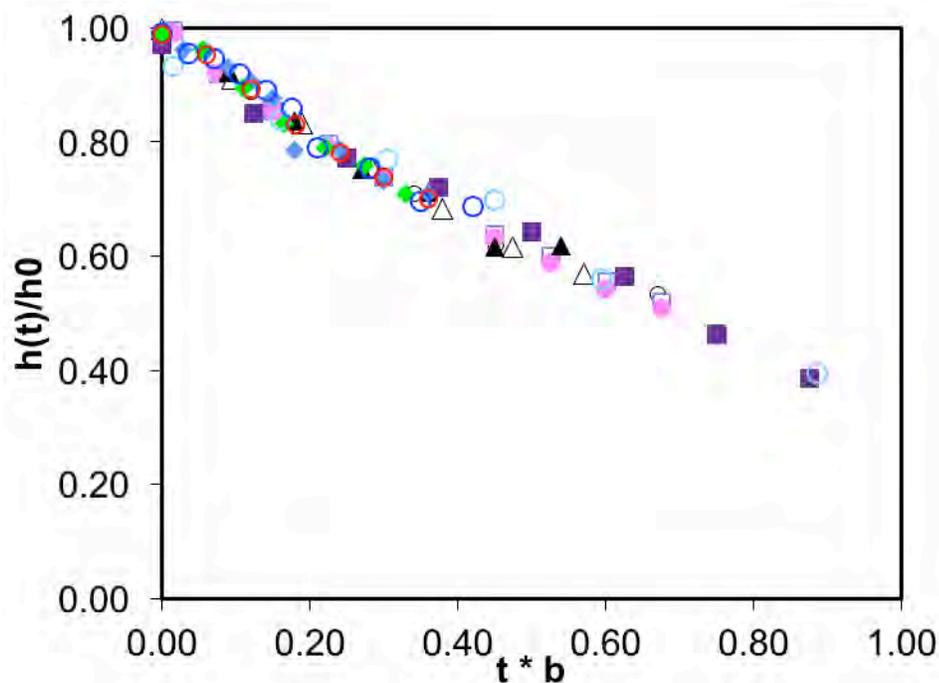
Figure S12   Same data as in Figure S11 plotted with new scaled coordinated $X = t*b$ and

$Y = h(t)/h_0$, where coefficients h_0 and b were found for each given data set as in Table S5 of

Figure S11 by the least square fitting with S1 approximation. The slight exponential non-linearity is apparent. ○ = method-ii PS 110nm (Fig. 4), ○= method-ii PS 40 nm (Fig. 2), ◆ = method-i PS 49 nm (Fig. 4), ○= method-ii PS 49 nm (Fig. 4), ◆ = method-i PS 110 nm (Fig. 4), ○ = method-ii PMMA 34 nm (Fig. 2), □ = method-ii PMMA 92 nm (Fig. 3), ● = method-i PMMA 91 nm (Fig. 3), Δ = method-ii PMMA 49 nm (Fig. 3), ▲= method-i PMMA 49 nm (Fig. 3), ■ = method-i PMMA (Fig. 5), ●= method-ii PMMA 54 nm.

The natural logarithm is applied to Y axis in Figure S12 and is shown in Figure 10. The

overall trend looks more linear than in Figure S12, confirming that the natural logarithm function

is the appropriate experimental approximation.

With the given intervals of X and Y, the collapsed exponential trend looks very similar to

a linear approximation (due to the small values of phenomenological coefficient b, $b*t<1$, where

time t is large and change in the interval (0,3600 s) as shown in Table S5.

Part 2: Theoretical analysis of experimental trends

We assume that all data points in Figure S11 is a monotonous decaying data.

The speed of the thickness decay can be written as: $dh(t)/dt$. This could be named as the

rate of the thickness decay and denoted by R:

$$\frac{dh(t)}{dt} = R, \text{ where } R < 0 \qquad\qquad (S2)$$

Which type of functionality of R describes the data in Figure S11? The data in Figure S11 is

presented as a function of $h(t)$, which is a particular solution of the S2 differential equation.

Therefore, the function R must be constructed such that the solution of S2 will give us the exact

$h(t)$ functionality discovered in Part1.

In the Part1 we found that from experimental point of view, the exponent with a negative

power $h_0 e^{-bt}$ is a good approximation of the experimental $h(t)$. At the same time, we noticed that

b is small and another type of approximation – a linear approximation $h(t) = h_0 - at$ - is also

reasonable.

Here both cases are considered. First, the differential equation S2 is solved for $R = -a$

and then for $R = -h(t)b$.

The rate R is a constant:

$$\frac{dh(t)}{dt} = -a. \qquad\qquad (S3)$$

Integrating and finding the constant of integration for a linear model of $h(t)$:

$$h(t) = h_0 - at, \text{ where } h_0 = h(t = 0). \qquad (S4)$$

The rate R is proportional to the thickness:

$$\frac{dh(t)}{dt} = -h(t)b \qquad\qquad (S5)$$

Integrating and finding the constant of integration for the exponential model of $h(t)$:

$h(t) = h_0 e^{-bt}$, with similar $h_0 = h(t = 0)$.   (S6)

From the analysis of the experimental data, a is between ~0.5 and ~1, while b is between ~0.006 and ~0.03, i.e. $b<<1$. Therefore, we could represent a solution for equation S5 as a Taylor series with respect to the small parameter b:

$$h(t) = h_0 e^{-bt} = h_0 \left(1 - bt + \frac{b^2 t^2}{2} + O(b^2) \right),   \quad (S7)$$

where $O(b^2)$ is a second order residue. With the first order accuracy, the exact solution S6 can be replaced with;

$$h(t) \approx h_0(1 - bt).   \quad (S8)$$

There are two different types of the decay rate: $R = -a$ and $R = -h(t)b$, which produce different equations and thus different particular solutions: linear S4 and exponential S6, respectively. The exponential solution S6 due to given experimental conditions ($b<<1$) can be further reduced to the linear equation S8. Comparing S4 and S8:

$$a = h_0 b.   \quad (S9)$$

where a is a constant rate of the thickness decay and its dimension is [length/time]. Parameter b is a reciprocal of time; thus, $\tau = 1/b$ and its dimension is [time]. Now S9 can be rewritten as the rate for both models of R:

$$a = h_0 / \tau.   \quad (S10)$$

Part3: analysis of relationship for phenomenological parameters a, h_0, and b

Differential equations S3 and S5 describe dynamics of the change of thickness decay rate depending on the implemented model of R. The solutions S4 and S6 gives us two evolutions of how the thickness may decay with respect to the time. These two solutions depend on a few coefficients: a, h_0 and b (the last one is $1/\tau$), which are the phenomenological parameters for the experimental data. Is there a particular relationship between these parameters, with respect to the

raw data obtained in Figure S11? Are there additional relationships related to equations S9 and S10?

Figure S13 shows h_0 and τ (which is $1/b$) calculated for each dataset of Figure S11 for PMMA and PS. In Figure S13 there are two distinct correlations of characteristic time of the decay, τ, with respect to the initial thickness of the layer, h_0.
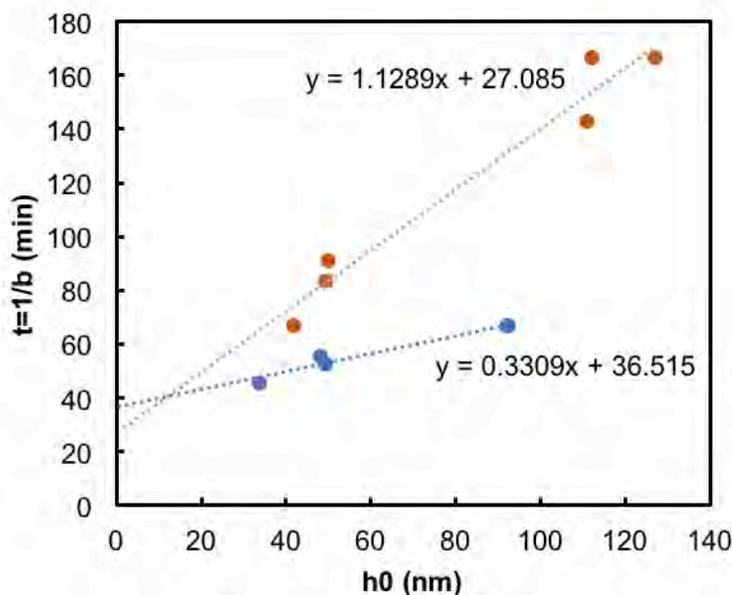

Figure S13 Least square fit coefficients h_0 and $\tau=1/b$ obtained for the thickness decay rate model $R = -h(t)b$ with solution $h(t) = h_0 e^{-bt}$ for all data sets presented in Figure S11 where ● denotes all PMMA and ● all PS samples.

Both correlations PMMA and PS overlap when $h_0 \to 0$ giving the characteristic time

$\tau \approx 15$ min, which is *independent from the material*. The same data as in Figure S13 can be re-

plotted in terms of the characteristic decay rate a (S9, S10).

Similar to Figure S13 both correlations for PMMA and PS overlap when $h_0 \to 0$ giving a

characteristic decay rate $a \approx 0.5$ nm/min which is *independent on the material*. The data in

Figure S13 and Figure S14 are inverted with respect to the polymer material, indicating that the lower characteristic time corresponds to higher decay rate.
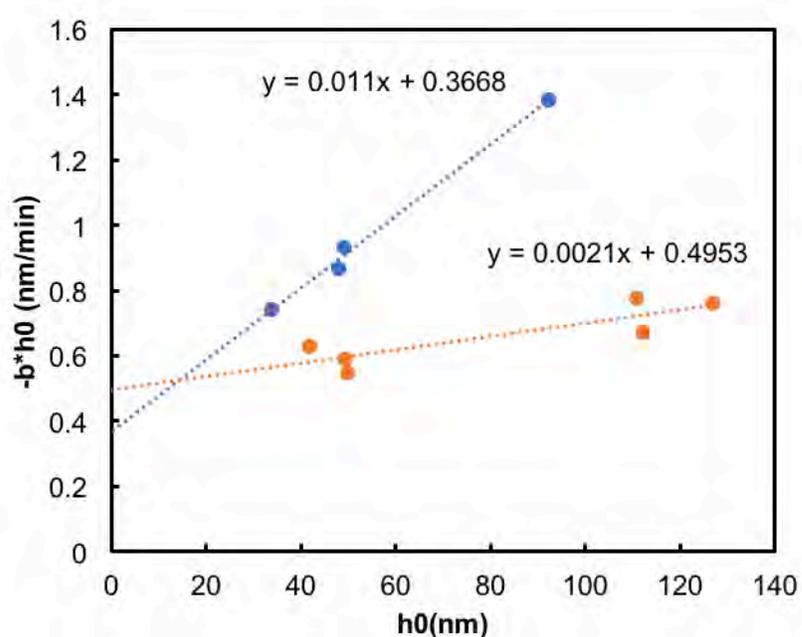
Figure S14 Same data as in Figure S13 re-plotted against the characteristic decay rate $a = h_0\,b$ (S9) where ● denotes all PMMA and ● all PS samples.

References

S.1 Hitchcock, A. P. Soft X-Ray Imaging and Spectromicroscopy. In *Handbook on Nanoscopy Vol.II*; Tendeloo, G. Van, Dyck, V. D., Pennycook, S. J., Eds.; Wiley-VCH Verlag GmbH & Co. KGaA, 2012; pp 745–791.

S.2 Henke, B. L. L.; Gullikson, E. M. M.; Davis, J. C. C. X-Ray Interactions: Photoabsorption, Scattering, Transmission, and Reflection at E = 50-30,000 eV, Z = 1-92. *At. Data Nucl. Data Tables* **1993**, *54* (2), 181–342